

**Performance and Value of Geometric Solar Arrays Subject to Cyclical  
Electricity Prices and High Solar Penetration**

by

Adrian Benoit Gordon Boivin

B.A.Sc., The University of British Columbia, 2016

A THESIS SUBMITTED IN PARTIAL FULFILLMENT OF  
THE REQUIREMENTS FOR THE DEGREE OF  
MASTER OF APPLIED SCIENCE

in

THE COLLEGE OF GRADUATE STUDIES  
(Electrical Engineering)

The University of British Columbia

(Okanagan)

October 2019

© Adrian Benoit Gordon Boivin, 2019

## Committee Recommendation Form

The following individuals certify that they have read, and recommend to the College of Graduate Studies for acceptance, a thesis/dissertation entitled:

Performance and Value of Geometric Solar Arrays Subject to Cyclical Electricity Prices and High Solar Penetration

---

submitted by \_\_\_\_\_ in partial fulfillment of the requirements of

Adrian Benoit Gordon Boivin

the degree of \_\_\_\_\_ .

Master of Applied Science

Dr. Jonathan F. Holzman

---

**Supervisor**

Dr. Wilson Eberle

---

**Supervisory Committee Member**

Dr. Liwei Wang

---

**Supervisory Committee Member**

Dr. Alexander Uhl

---

**University Examiner**

## Abstract

The shift away from fossil-fuel-based electricity generation due to environmental concerns has raised substantial interest in photovoltaic generation. However, the intermittent nature of photovoltaic generation has raised significant concerns when it is implemented at high penetration levels. As the production of photovoltaic electricity is based on the sun's position and weather conditions, rather than electricity demand, large amounts of photovoltaic generation can lead to dramatically fluctuating electricity prices and electrical grid instability. This work examines the optimization of solar generating arrays using a value-based metric, in order to maximize the profit obtained rather than maximizing the power generated as is traditionally done. Such an optimization can serve to reduce the negative societal effects of high photovoltaic penetration while increasing the economic benefits of the array. This optimization is applied here to geometric solar arrays, being simple, infinitely tileable geometric arrangements of square crystalline silicon solar cells. The optimal configuration under present conditions in southern California is found to be rows of solar cells facing  $15^\circ$  west of south, angled at  $21^\circ$  above horizontal, and with a spacing between rows equal to 136% of the height of the rows. While this work does not provide sufficient investigation into the long-term trends of value-based metrics to provide a recommendation for new photovoltaic installations, it strongly supports the use of such metrics for analysis and sets a base for the additional research necessary to incorporate them optimally into future design work.

## Lay Summary

This work investigates a problem frequently seen in areas with large amounts of solar generation. Often, such areas suffer from generating too much electricity during the day and not enough electricity during the mornings and evenings, leading to imbalances in the electrical grid. In this work, solar generating arrays are compared based on the revenue they produce, rather than trying to increase the power they generate. It is hoped that this comparison will lead to solar generating arrays that generate more electricity during times when prices are high, and the additional electricity is likely more useful. Several solar generating arrays with shapes that allow them to trap sunlight in different ways were compared. The best solar generating array under current conditions is found to be similar to what is already widely used, but the information collected may prove helpful in designing high-performance arrays in the future.

## Preface

The work presented in this thesis was carried out in the University of British Columbia's Integrated Optics Laboratory under the supervision of J. F. Holzman.

The simulation presented in Chapter 3 of this work has been previously published as a journal article. Portions of Chapter 3 are reproduced from A. B. Boivin, T. M. Westgate and J. F. Holzman, "Design and performance analyses of solar arrays towards a metric of energy value," *Sustainable Energy & Fuels*, vol. 2, no. 9, pp. 2090-2099, 2018. (<https://pubs.rsc.org/en/content/articlehtml/2018/se/c8se00333e>), with permission from the Royal Society of Chemistry. The results of Chapter 3 have also been published as a conference proceeding; A. B. Boivin, T. M. Westgate and J. F. Holzman, "A linear solar cell array for prolonged and high-value light capture," Proc. SPIE Volume 10527, Physics, Simulation, and Photonic Engineering of Photovoltaic Devices VII; 105270O (2018). <https://doi.org/10.1117/12.2289175>, and are reprinted with permission. The simulation presented in Chapter 4 of this work is in the process of being submitted as a journal article; A. B. Boivin and J. F. Holzman, "A treatise on the revenue and infrastructure of solar arrays". In all three of these works, I was the primary investigator, designed and performed the simulations and experiments, and wrote the manuscripts. J. F. Holzman and T. M. Westgate provided assistance with theory and editing of the manuscripts.

The theory of value-based metrics on which this research is based was developed jointly by myself and J. F. Holzman. I developed the simulations used in this work based on previous work on the analysis and simulation of three-dimensional photovoltaic devices by T. M. Westgate, B. W. D. Veerman, M. H. Bergen, X. Jin, B. Born, and M. Bernier. This manuscript was reviewed by J. F. Holzman and T. M. Westgate.

# Table of Contents

Abstract.....	iii
Lay Summary.....	iv
Preface .....	v
Table of Contents.....	vi
List of Tables .....	ix
List of Figures.....	x
Acknowledgements.....	xv
Dedication.....	xvi
1: Introduction.....	1
2: An Overview of Photovoltaic Generation.....	3
2.1: The Photovoltaics Industry .....	3
2.1.1: Overview of Photovoltaic Technologies.....	4
2.1.2: Overview of Crystalline Silicon Photovoltaics .....	10
2.1.3: Surface texturing and three-dimensional photovoltaics .....	16
2.1.4 Economics of Photovoltaics.....	21
2.1.5: Intermittent Generation and the “Duck Curve” .....	26
2.2: An Examination of the Photovoltaic Process.....	32
2.2.1: The Nature of Sunlight.....	32
2.2.2: Optical Properties of Solar Cells and 3DPV .....	37
2.2.3: Electrical Properties of Photovoltaics .....	41

3: Preliminary Validation with a Simplified Simulation.....	51
3.1: The Three-Dimensional Solar Generating Arrays .....	52
3.1.1: The Flat-Panel Array.....	53
3.1.2: The Angled-Panel Array .....	53
3.1.3: The V-Groove Array.....	56
3.1.4: The U-Groove Array.....	57
3.1.5: Practical Implementation of the Arrays .....	59
3.2: Design of the Simplified Simulation.....	64
3.2.1: Energy Value Density and Electricity Price .....	64
3.2.2: Setup of the Simplified Simulation.....	65
3.2.3: Experimental Characterizations .....	67
3.2.4: Design of the Analytical Model.....	73
3.3: Simplified Simulation Results .....	85
3.3.1: Discussion.....	91
4: Array Analysis with a Rigorous Simulation Approach.....	94
4.1: Experimental Derivation of Solar Cell Parameters.....	95
4.1.1: Preliminary Analysis of Lab-Generated I/V Curves.....	98
4.1.2: Collection and Analysis of Solar I/V Curves.....	105
4.2: Design of the Rigorous Simulation.....	113
4.2.1: A Model for Atmospheric Light .....	116
4.2.2: Optical Power with Diffuse and Polarized Light.....	120

4.2.3: Relative Profit Density as a Metric for Array Performance.....	137
4.2.4: Conversion of Optical Power to Relative Profit Density .....	139
4.3: Results.....	141
4.3.1: Experimental Validation of the Simulation .....	142
4.3.2: Array Optimization under the Relative Profit Density Metric.....	146
4.3.3: The Cost-Dependent Viability of Solar Arrays.....	150
4.3.4: Discussion .....	158
5: Conclusion .....	162
Bibliography .....	165
Appendix A.....	177
Appendix B .....	181
Appendix C .....	184

## List of Tables

Table 3.1: The formulas for unit cell installation area and silicon area for each of the four geometric solar arrays. ....	63
Table 4.1: The curve-fitting parameter results of the three tested lab-generated curves, along with the averaged values for each parameter to be used in simulation. ....	101
Table 4.2: Value of the geometry-dependent cost density at the crossover point for the five years of the study if rotation is fixed at zero. Allowing rotation to vary would likely result in a slight reduction in all these values. ....	157
Table C.1: Relative profit density of the Flat-Panel Array, in $\$/\text{m}^2/\text{y}$ , as a function of the year and geometry-dependent cost density, in $\$/\text{m}^2/\text{y}$ .....	184
Table C.2: Optimal V-Angle of the V-Groove Array without rotation, in degrees, as a function of the year and geometry-dependent cost density, in $\$/\text{m}^2/\text{y}$ .....	185
Table C.3: Optimal relative profit density of the V-Groove Array without rotation, in $\$/\text{m}^2/\text{y}$ , as a function of the year and geometry-dependent cost density, in $\$/\text{m}^2/\text{y}$ .....	185
Table C.4: Optimal width of the U-Groove Array without rotation, normalized to the solar cell side length, as a function of the year and geometry-dependent cost density, in $\$/\text{m}^2/\text{y}$ .....	186
Table C.5: Optimal relative profit density of the U-Groove Array without rotation, in $\$/\text{m}^2/\text{y}$ , as a function of the year and geometry-dependent cost density, in $\$/\text{m}^2/\text{y}$ , including only widths of 1-10, 100, and infinite times the solar cell side length. ....	186
Table C.6: Optimal Tilt Angle of the Angled-Panel Array without rotation, in degrees, as a function of the year and geometry-dependent cost density, in $\$/\text{m}^2/\text{y}$ .....	186
Table C.7: Optimal spacing of the Angled-Panel Array without rotation, in mm, as a function of the year and geometry-dependent cost density, in $\$/\text{m}^2/\text{y}$ .....	187
Table C.8: Optimal relative profit density of the Angled-Panel Array without rotation, in $\$/\text{m}^2/\text{y}$ , as a function of the year and geometry-dependent cost density, in $\$/\text{m}^2/\text{y}$ .....	187
Table C.9: Results of the rotation-dependent analysis of the V-Groove Array. ....	188
Table C.10: Results of the rotation-dependent analysis of the U-Groove Array. ....	188
Table C.11: Results of the rotation-dependent analysis of the Angled-Panel Array. ....	188

# List of Figures

Fig. 2.1: A comparison between the structures of a typical commercial monocrystalline silicon solar cell, as will be used in this study (left), and a high-performance HIT monocrystalline silicon solar cell with textured glass and rear interfaces (right). ..... 16

Fig. 2.2: Examples of established 3DPV geometries. The first row shows examples that are typically used with thin-film technology and could not be created with standard square, rigid solar cells, while the second row shows examples that are compatible with standard crystalline silicon technology. a) Corrugation incorporating curved solar cells [67]. b) Inverted four-sided pyramids using triangular solar cells [69]. c) Curved solar cells shaped into cylinders [70]. d) V-shaped corrugation [72]. e) Retroreflector-based corner cubes [78]. f) An example of a solar tower [79]..... 20

Fig. 2.3: A simplified example of the Duck Curve problem. The demand curve is shown, together with solar generation curves at three different levels of solar penetration, represented by solid lines, long dashes, and short dashes respectively. The net demand resulting from this that must be met by traditional generation is also shown. .... 28

Fig. 2.4: A plot of hourly electricity price in the vicinity of Bakersfield, CA on May 1, 2018, showing the characteristic bimodal peaks and low midday price of the “Duck Curve”. Pricing data is day-ahead locational marginal pricing obtained from the CAISO OASIS database [98] and averaged across California with negative values treated as zero, as described in section 4.2. .... 29

Fig. 2.5: A comparison of the AM0 extraterrestrial solar spectrum and the global, direct, and diffuse variations of the standardized AM1.5 solar spectrum, as well as the black body approximation of the solar spectrum. Data from the standardized spectra obtained from [118]-[119]. .... 35

Fig. 2.6: Complex refractive indices of aluminum, glass, and silicon in the visible spectrum, as the refractive index ( $n$ ) and extinction coefficient ( $\kappa$ ), obtained from [123]. The extinction coefficient of glass is omitted here, as it is essentially zero across the range shown. .... 38

Fig. 2.7: Ideal reflectance at normal incidence for air/glass, glass/silicon, and silicon/aluminum interfaces within the visible spectrum. .... 39

Fig. 2.8: The electronic band structure of silicon, showing the conduction bands in red and the valence bands in black. The primary and secondary indirect bandgaps and the direct bandgap are marked. The band structure is obtained from [127]. .... 43

Fig. 2.9: The absorption coefficient of silicon, clearly showing the primary indirect bandgap at 1100 nm and the direct bandgap at 360 nm as significant drops in absorption. The secondary indirect bandgap at 500 nm is less distinct, but can also be observed. .... 44

Fig. 2.10: A double-diode model of a solar cell, consisting of a current source, two diodes representing recombination losses, and two resistors representing ohmic losses. .... 46

Fig. 2.11: A typical solar cell I/V curve. The maximum power point is marked with a red diamond, and the fill factor is the ratio between the areas of the two blue rectangles. .... 48

Fig. 3.1: A diagram demonstrating the Flat-Panel Array. A unit cell of the array is shown highlighted in red.....	53
Fig. 3.2: A diagram demonstrating the Angled-Panel Array, with its four geometrical parameters illustrated. The south direction is indicated by S. A unit cell of the array, which includes the non-photovoltaic back side of the front solar cell, is shown highlighted in red. ....	54
Fig. 3.3: A diagram demonstrating the V-Groove Array, with its three geometrical parameters illustrated. A unit cell of the array is shown highlighted in red. ....	56
Fig. 3.4: A diagram demonstrating the U-Groove Array, with its three geometrical parameters illustrated. A unit cell of the array is shown highlighted in red. ....	58
Fig. 3.5: A diagram of the coordinate systems used in this analysis. The Cartesian coordinate system is shown offset from the cardinal directions by the rotation angle, $\rho$ , and the sun's position is referenced to the cardinal directions through the zenith angle, $\theta$ , and the azimuth angle, $\phi$ . The size and location of the sun are not to scale. ....	67
Fig. 3.6: An SEM image of the front of the selected solar cells. A silver finger contact is shown running across the middle of the image. The irregular diamond-shaped patterning, on the order of a few microns in size, is inverted pyramid microtexturing, characteristic of alkaline etch texturing on a monocrystalline silicon substrate.....	69
Fig. 3.7: A cross-section SEM capture of the solar cell, with certain thicknesses indicated. The irregularly-patterned layer to the left is the aluminum back contact, while the white-coloured layer to the right is a silver finger front contact, which is out of focus in the upper half of the capture due to lying behind the fractured edge. The inset in the upper left shows detail of the front surface texturing. Lines within the bulk silicon are angles formed during fracturing, and likely do not represent differences in composition.....	70
Fig. 3.8: An image showing a fabricated (a) solar cell together with the components used in its fabrication: b) An unmodified solar cell, c) a square of low-iron glass, d) a square of EVA film, e) a section of lead/tin tab wire, f) a tube of solder paste. Note the darker colouration of the final solar cell, indicating that encapsulation has improved the performance of the anti-reflection coating. ....	71
Fig. 3.9: Hourly electricity price on the sample day of March 20, 2017, demonstrating the distinctive “Duck Curve” profile. Reprinted with permission from the Royal Society of Chemistry. ....	86
Fig. 3.10: Instantaneous power density and accumulated value density for the optimized configurations of the three arrays as a function of time on March 20, 2017. Reprinted with permission from the Royal Society of Chemistry. ....	87
Fig. 3.11: Daily energy value densities for the optimal configurations of the three arrays, normalized to the case of a Flat-Panel Array with zero reflectance, for the period from July 1, 2012 to June 30, 2018. Reprinted with permission from the Royal Society of Chemistry.....	89

Fig. 3.12: Accumulated yearly energy value densities for the optimal configurations of the three arrays, plotted from July 1, 2012, to June 30, 2018. The solid curves are unnormalized and plotted against the left axis, while the dotted curves are normalized to a Flat-Panel Array with zero reflectance and plotted against the right axis. Note that the unnormalized V-Groove Array is difficult to see in this figure, as it is largely hidden by the very similar curve for the unnormalized U-Groove Array. Reprinted with permission from the Royal Society of Chemistry. .... 91

Fig. 4.1: Estimated silicon IQE curve derived from [60], [134]-[136]. ..... 97

Fig. 4.2: Normalized spectral responsivity curve based on the IQE curve presented in Fig. 4.1. .... 97

Fig. 4.3: The effects of varying solar cell parameters on the shape of the I/V curve, compared to a reference curve shown in black. The variations are generally by a factor of 10, with a few exceptions where the curve is too sensitive to that parameter. The dotted black line additionally shows both saturation currents being varied to cancel out their effects on the open-circuit voltage. ... 99

Fig. 4.4: The system for measuring solar cell I/V curves designed by T. Westgate. .... 100

Fig. 4.5: The circuit schematic for the I/V curve measurement setup. The upper section is the measurement circuit, which is implemented four times for four solar cell channels (of which only three are used for this experiment). The solar cell is connected on the left, across a small current sense resistor and a MOSFET serving as a variable load. The voltage is output directly to the DAQ units, while the differential voltage across the current sense resistor is passed through an instrumentation amplifier to measure the current. The lower left circuit controls the variable load, while the lower right circuit is the voltage supply connection. Both of these are implemented twice, once per circuit board. .... 101

Fig. 4.6: A comparison of the halogen floodlamp spectrum, shown in orange, with the AM1.5 spectrum [118], shown in blue, with both spectra normalized. Note that the sharp IR cutoff of the floodlamp spectrum is a limitation of the spectrometer used, and is not characteristic of the floodlamp itself. .... 102

Fig. 4.7: The I/V curves derived from the preliminary lab experiments. Curves #1, #2 and #3 are shown in blue, green, and red respectively. The solid lines represent the experimental data; the dotted lines represent the curve-fit parameters; and the dashed lines represent the curves with final selected parameters. The large discrepancies between the experimental and final curves for the blue and green captures can be explained by excessive experimental series resistance and increased surface recombination, respectively. .... 103

Fig. 4.8: The ARIES experimental setup. The three simulated arrays are shown to the left, with the Flat-Panel Array furthest from the camera. The upper centre of the image shows the I/V curve measuring circuit described in section 4.1.1, with the power supply and computer controlling it shown to the right. .... 107

Fig. 4.9: The power captured by each array over the course of the day for the three arrays in the ARIES experiment. .... 108

Fig. 4.10: The curve-fit values for the first saturation current obtained from the ARIES experiments. The black and red lines show simulated results at ambient temperature and at 7 K above ambient temperature respectively, scaled to match the experimental data.....	109
Fig. 4.11: The curve-fit values for the second saturation current obtained from the ARIES experiments. ....	110
Fig. 4.12: The curve-fit values for the photocurrent obtained from the ARIES experiment, normalized to the simulated photocurrent using the spectral responsivity scaling factor previously obtained in section 4.1.1. Shadowing from hills and from afternoon clouds are indicated by A and B, respectively.....	111
Fig. 4.13: A comparison of the experimental photocurrents obtained in the ARIES experiment, shown as solid lines, against the simulated photocurrents under identical conditions, shown as dotted lines. ....	143
Fig. 4.14: A comparison of the experimental first saturation currents obtained from the ARIES experiment against simulated first saturation currents given a solar cell resistive heating of 10 K/(1000 W/m <sup>2</sup> ) and 25 K/(1000 W/m <sup>2</sup> ).....	144
Fig. 4.15: A comparison of the experimental second saturation currents obtained from the ARIES experiment against simulated second saturation currents given a solar cell resistive heating of 10 K/(1000 W/m <sup>2</sup> ) and 25 K/(1000 W/m <sup>2</sup> ).....	145
Fig. 4.16: A comparison of the experimental solar cell electrical powers obtained from the ARIES experiment, represented by solid lines, against simulated electrical powers with and without incident direct solar illumination, represented by dotted and dashed lines respectively. ....	146
Fig. 4.17: The optimal configuration of the V-Groove Array at varying values of $C_{geo,y}$ . The solid line represents the detailed analysis run with a fixed $\rho_{VG}$ , while outlined points represent investigations where $\rho_{VG}$ was left free to vary.....	147
Fig. 4.18: The optimal configuration of the U-Groove Array at varying values of $C_{geo,y}$ . The solid line represents the detailed analysis run with a fixed $\rho_{VG}$ , while the outlined points represent investigations where $\rho_{VG}$ was left free to vary. Note that the actual value of $W_{UG}/a$ at $C_{geo,y} = 1.5$ $\$/m^2/y$ is at least 10, but could be as high as 99. ....	148
Fig. 4.19: The optimal configuration of the Angled-Panel Array at varying values of $C_{geo,y}$ . Solid lines represent the detailed analysis run with a fixed $\rho_{AP}$ , while outlined points represent investigations where $\rho_{AP}$ was left free to vary. ....	149
Fig. 4.20: The photocurrent collected by each solar cell of the array configurations optimized to $C_{geo,y} = 0, 5, \text{ and } 7$ $\$/m^2/y$ on March 20, 2018. ....	152
Fig. 4.21: The generated electrical power density of each of the array configurations optimized to $C_{geo,y} = 0, 5, \text{ and } 7$ $\$/m^2/y$ on March 20, 2018. The Flat-Panel Array is difficult to distinguish in this figure, being nearly identical to the V-Groove Array at $C_{geo,y} = 5$ $\$/m^2/y$ during the middle of the day and the Angled-Panel Array at $C_{geo,y} = 0$ $\$/m^2/y$ during the morning and evening.....	153

Fig. 4.22: A comparison of the generated power of the Angled-Panel Array optimized to $C_{geo,y} = 5$ $\$/m^2/y$ on March 20, 2018, shown in orange at high-resolution settings and in blue at high-simulation-efficiency settings. The inset shows a closer view of the mid-day period to illustrate the quantization noise introduced at high-simulation-efficiency settings. ....	154
Fig. 4.23: The daily relative profit densities of the optimal array configurations at $C_{geo,y}$ values of 0, 5, and 7 $\$/m^2/y$ , over the five-year period of study. Curves shown here are normalized by subtracting the relative profit densities of a Flat-Panel Array at the same $C_{geo,y}$ value. ....	155
Fig. 4.24: Relative profit density improvement over the Flat-Panel Array as a function of $C_{geo,y}$ for optimal configurations of the three other arrays. Solid lines represent the optimal configurations with fixed $\rho$ values, while outlined points represent the optimal configurations with optimized $\rho$ values. ....	156
Fig. 4.25: A comparison of the value of $C_{geo,y}$ at the crossover point and the average electricity price over the five year period studied. A strong correlation between the two values can be seen. ....	158
Fig. A.1: The monthly-averaged day-ahead hourly locational marginal pricing, for the year of July 1, 2013-June 30, 2014, in the region bounded by 34°N, 36°N, 118°W, and 120°W. ....	177
Fig. A.2: The monthly-averaged day-ahead hourly locational marginal pricing, for the year of July 1, 2014-June 30, 2015, in the region bounded by 34°N, 36°N, 118°W, and 120°W. ....	178
Fig. A.3: The monthly-averaged day-ahead hourly locational marginal pricing, for the year of July 1, 2015-June 30, 2016, in the region bounded by 34°N, 36°N, 118°W, and 120°W. ....	178
Fig. A.4: The monthly-averaged day-ahead hourly locational marginal pricing, for the year of July 1, 2016-June 30, 2017, in the region bounded by 34°N, 36°N, 118°W, and 120°W. ....	179
Fig. A.5: The monthly-averaged day-ahead hourly locational marginal pricing, for the year of July 1, 2017-June 30, 2018, in the region bounded by 34°N, 36°N, 118°W, and 120°W. ....	179
Fig. A.6: The monthly-averaged day-ahead hourly locational marginal pricing, for four months of the year of July 1, 2017-June 30, 2018. This figure compares data averaged over the entire state of California, represented by dotted lines, to data collected in the region bounded by 34°N, 36°N, 118°W, and 120°W, represented by solid lines. The accentuation of the Duck Curve effect in a region with large quantities of solar generation is clearly visible. ....	180
Fig. B.1: Relative profit density improvement over the Flat-Panel Array as a function of $C_{geo,y}$ for optimal configurations of the three other arrays, for the year of July 1, 2013 to June 30, 2014. ....	181
Fig. B.2: Relative profit density improvement over the Flat-Panel Array as a function of $C_{geo,y}$ for optimal configurations of the three other arrays, for the year of July 1, 2014 to June 30, 2015. ....	182
Fig. B.3: Relative profit density improvement over the Flat-Panel Array as a function of $C_{geo,y}$ for optimal configurations of the three other arrays, for the year of July 1, 2015 to June 30, 2016. ....	182
Fig. B.4: Relative profit density improvement over the Flat-Panel Array as a function of $C_{geo,y}$ for optimal configurations of the three other arrays, for the year of July 1, 2016 to June 30, 2017. ....	183

## Acknowledgements

This work owes its existence to the numerous individuals who have guided and supported me throughout the course of my Masters degree, and it is important to acknowledge their contributions and thank them for their assistance.

I would like to thank my supervisor, Dr. Jonathan Holzman, for all that he has done to support this research. His extensive knowledge and unfailing insight have helped me past countless stumbling blocks over the development of this work, and his guidance has led my professional and personal life in directions I would never have thought possible. His constant enthusiasm and passion for learning continue to inspire me to reach new heights.

I would like to express my gratitude to Dr. Wilson Eberle and Dr. Liwei Wang for serving on my committee, and to Dr. Alexander Uhl for acting as my university examiner.

I would like to thank Mitch Westgate, whose research provided the motivation for this work, and whose advice in all solar-related matters I frequently relied on. I would additionally like to extend my gratitude to all the other students during my time in the Integrated Optics Laboratory, for their friendship and for putting up with my constant complaining about simulation errors. Thank you, Dr. Brandon Born, Mark Bergen, Ana Ciocoiu, Naomi Fredeen, Luke Herman, Ilija Hristovski, Nikolai Lesack, Jason Reich, Salman Alfihed, and all the other members past and present of the Integrated Optics Laboratory.

I would like to express my thanks to UBC Okanagan's School of Engineering for providing me with the facilities and resources necessary to conduct my research, and to David Zinz, Tim Giesbrecht and David Arkinstall for their assistance with technical matters related to my work.

Finally, I would like to thank my family, Ray Boivin, Linda Boivin, and Maya Boivin, for their unfailing support encouragement as I struggled through these three long years of research.

## Dedication

To my parents, Linda and Ray, without whose love and support I would  
never have made it this far.

# 1: Introduction

Solar electricity generation has emerged as one of the top technologies in the search for renewable energy generation. While large-scale solar electricity generating stations tend to use concentrated solar power or concentrated photovoltaics, and a wide range of photovoltaic materials are beginning to hit the market, crystalline-silicon-based photovoltaics continue to have a dominant presence within the field of solar electricity generation due to their low cost, comparative ease of installation, and ability to be scaled for any application from large commercial arrays to small, personal systems in backyards or on rooftops. This trend is leading to a shift in the power transmission industry paradigm, where a small number of large-capacity electricity generating stations traditionally supply power to a large number of small-scale consumers.

However, the proliferation of distributed solar electricity generation is not without its challenges. Chief among these is the fact that, by generating electricity solely during the day, solar electricity generation is overturning one of the fundamental principles of the old paradigm, namely that in the electricity industry, consumers act and suppliers react. With the supply and demand relationship for electricity being driven from both sides, symptoms such as wildly fluctuating electricity prices, electricity surpluses and deficits, and increased power grid instability are beginning to be seen.

The problem is at its core an economic one. More renewable energy generation is desperately needed, and governmental incentives are often used to promote its development. However, these same incentives are counteracting the typical laws of supply and demand that prevent such problems from developing. As solar cells within geographic proximity tend to have their electricity generation be highly coordinated due to the sun position and weather being generally consistent over small areas, the supply of electricity can increase drastically during sunny weather, subsequently lowering the value of that electricity. This economic pressure would normally serve to lower the quantity of solar electricity generation to a sustainable level. While the incentives are undoubtedly useful at countering the underlying environmental problems at the root of the push for renewable energy generation, their presence here is exacerbating the instability. It is no

longer sufficient for solar electricity generation to simply aim to produce as much power as possible with no attention given to when that power is generated. A shift is needed from comparing photovoltaic systems based on their efficiency to a different metric more in line with their societal and economic impacts.

This thesis serves to introduce a value-based metric in lieu of the standard power-based metric. This metric is used to carry out performance analyses of various geometric solar arrays and their configurations with the goal of identifying the ideal array and implementation under present conditions. We comment on how the ideal array and its configuration may differ in the future based on trends in infrastructure and electricity price. Chapter 2 of this thesis presents some necessary background on photovoltaic technology, geometric solar arrays, the current state of the photovoltaics industry, and the processes behind photovoltaic generation. Chapter 3 describes the initial, simplified simulation that was used to validate the concept of value-based metrics as well as the performance of the geometric solar arrays themselves. Chapter 4 introduces a more detailed and rigorous simulation and uses its results to draw conclusions about the ideal geometric solar arrays under conditions of high solar penetration.

## 2: An Overview of Photovoltaic Generation

Our planet is facing an environmental crisis [1]. Rising levels of greenhouse gases are triggering a rapid increase in the global temperature, resulting in climactic instability that threatens the future of humanity. A significant portion of these greenhouse gases can be traced back to the burning of fossil fuels for electricity production, and this quantity is likely to increase as the transportation industry shifts from internal combustion engines to electric vehicles relying on grid-charged batteries [2]. A shift from conventional, fossil-fuel-using electricity generation to renewable energy sources is desperately needed.

However, significant problems still exist in the fields of renewable energy generation that need to be solved before they can fully replace conventional electricity generation. Photovoltaic generation is one of the most widely used forms of renewable electricity generation, and one that in a single hour could produce almost enough electricity to power the entire planet for a year [3]. However, this bombastic claim is one that does not reflect the current state of the photovoltaic industry. Despite the potential of photovoltaics, low efficiencies, high costs, and the inherent intermittency of sunlight are still significant barriers to its widespread implementation.

### 2.1: The Photovoltaics Industry

Terrestrial photovoltaics have been a commercially viable technology since the mid-1970s, but despite this the field is by no means stagnant [4]. Constant innovation in materials, fabrication methods, installation, and integration within the electrical grid combine to move closer to a level of photovoltaics that can compete with conventional electricity generation while maintaining the stability and reliability of the electrical grid even at high levels of market penetration. As a foundation for the work on three-dimensional photovoltaics that will be explored in this thesis, the following subsections summarize the current state of the photovoltaic industry. This includes a summary of the currently-available semiconductor materials that are used for solar cells, an examination of the materials and structural layouts used to create a solar cell, an explanation of the established use of nano-, micro-, and macro-scale geometries to improve the light collection of solar cells,

a review on how the economic performance of solar generating arrays can be determined and compared, and a discussion of the problem of intermittent generation as it applies to photovoltaics. This background information should provide an adequate knowledge base on which to build additional innovations of photovoltaic devices.

### 2.1.1: Overview of Photovoltaic Technologies

The selection of a photovoltaic material is a tradeoff, an optimization problem between several parameters. Installation cost (including materials and fabrication) and efficiency are commonly viewed as the primary factors to consider, but additional properties, such as the lifespan of the material and the environmental cost of fabrication and disposal of the solar cells, also factor into the decision [5]. High-performance solar cells can be created using direct-bandgap semiconductors such as gallium arsenide and advanced fabrication techniques including multi-junction construction, but these improvements quite literally come at a cost, increasing the per-area cost of solar cells at a rate that cannot be matched by the increase in efficiency. Low-cost solar cells can be created using inexpensive materials such as organic semiconductors and simplified fabrication techniques including thin-film construction, but these cost-saving methods lower the efficiency of the solar cells, reducing their viability for many applications. Materials that perform well at low costs have thus far encountered issues with longevity and toxicity and require further research to become viable for widespread use. For this reason, despite ongoing advances on all three fronts, the photovoltaics industry continues to be dominated by a middle-of-the-road material whose efficiency and cost are neither exceptional nor terrible: Silicon.

The fundamental operation of a solar cell is dependent on first leveraging a photon to excite a bound electron to a higher energy state. Doing so creates both an excited electron, as well as a hole, which is to say a gap in the steady-state arrangement of bound electrons that can be treated as a separate particle. It is then necessary to separate the electron and hole, typically by means of the bias voltage of a diode junction. At this point, the electron and hole are attracted to each other, and work can be performed as they travel to recombine, which is referred to as electrical current. More details on the processes involved will be covered

later in this thesis, in section 2.2.3, but this simplified explanation is sufficient to point out the main methods by which the current (and thereby the efficiency) can be increased: increasing the number of incident photons, increasing the probability that a photon excites an electron, increasing the amount of energy transferred from the photon to the electron, and decreasing the probability of the electron dropping back to a lower energy state before leaving the solar cell.

In terms of solar cell materials, variations in semiconductor material are typically related to the absorption and recombination probabilities, while the probability of incident photons is more closely tied to external structures. Such structures, including anti-reflection coatings, mechanical actuation, and the light concentrators used in concentrated photovoltaics (CPV), can be applied equally to any form of solar cell. The case of CPV is worth special consideration, as light concentration lends itself well to the use of smaller, more efficient solar cells [6]. However, it is not practical in many applications due to the complex light-concentrating system, which requires precise calibration, takes up a large amount of space, and may increase the cost enough to offset the reduction in photovoltaic surface area.

The probability that a photon excites an electron is chiefly linked to the bandgap of the semiconductor used. Photons with an energy above the bandgap will typically interact with the electrons, while photons with an energy below the bandgap will typically continue through the semiconductor unimpeded. The selection of a semiconductor bandgap must also take into account that the higher above the bandgap the energy of a photon is, the more energy becomes lost as heat rather than being transferred to the electron, as the final energy of the electron is typically equal to the bandgap energy. Therefore, a lower bandgap would allow more photons to be captured and excite electrons but would also reduce the energy obtained from each photon. This creates a fundamental efficiency limit for any standard photovoltaic device of a given idealized bandgap operating under a given illumination spectrum, known as the Shockley-Queisser Limit [7]. For the standard AM1.5G terrestrial spectrum, the maximum of this limit is 33.16% for a semiconductor with a bandgap of 1.34 eV, with a smaller local maximum of 32.85% at 1.15 eV. The limit does not change

consistently with varying bandwidth due to atmospheric absorption lines in the spectrum, but generally, bandgaps close to these two peaks are ideal.

The principal solution to the problem posed by the Shockley-Queisser Limit is known as a multijunction solar cell [8]. By stacking multiple semiconductor diode junctions, such that the ones with the highest bandgap are on top, incident photons will pass through each semiconductor layer until they reach one with a sufficiently low bandgap, at which point they will excite an electron with minimal loss of energy. The tradeoff, of course, is cost. By adding more semiconductor layers, the structural complexity and therefore the manufacturing cost of the solar cell is greatly increased. For this reason, while the efficiency records for photovoltaics are typically set by multijunction cells using high-efficiency high-cost materials, a more common motivation for use of this technique is to boost the efficiency of low-efficiency low-cost materials to useable levels [9].

Another factor in the probability that a photon is absorbed by the semiconductor is the thickness of the semiconductor [10]. A thicker semiconductor layer with a longer photon path leads to more chances for absorption, but also requires more material and therefore higher manufacturing costs. Conversely, thin-film solar cells use much thinner semiconductor layers as their name suggests, allowing them to contain less material, lowering one of the primary manufacturing costs of the solar cells. However, this allows a significant percentage of photons to pass straight through the solar cell, reducing efficiency. This effect is also closely linked to whether the semiconductor used has a direct or indirect bandgap. An indirect bandgap means that a photon-electron interaction is less likely to excite the electron, and therefore photons will in general travel deeper into the solar cell before being absorbed [11]. Therefore, a thicker solar cell (and therefore more materials and a higher cost) is generally required to achieve the same efficiency as a direct bandgap semiconductor would have.

The semiconductor material used for a solar cell is also closely tied to the recombination probability. While absorption can be manipulated by adjusting the thickness of the solar cell, a thicker solar cell also means that electrons and holes must travel further through the solar cell to reach the contacts, leading to additional

chances for recombination. This recombination is related to the semiconductor's charge carrier mobilities and lifetimes, and can also be influenced by the presence of defects within the semiconductor.

The most common non-silicon solar cell type is the cadmium telluride (CdTe) thin-film solar cell [12]. As a thin-film material, CdTe cells have lower manufacturing costs but a lower efficiency compared to most silicon solar cells, up to a record of 21% for solar cells, or 18.6% for complete modules [13]. Their small temperature coefficients give them reduced sensitivity to extreme temperature conditions, which, coupled with their strong performance in high humidity, make them a common choice in tropical regions [14]. However, in most applications the toxic cadmium content reduces their desirability [15]. Another common thin-film solar cell, copper indium gallium selenide or CIGS, has higher efficiency than CdTe solar cells [14], up to records around 23.35% for cells or 19.2% for modules [13], which is excellent for thin-film solar cells but still lower than crystalline solar cells, but its complex manufacturing process raises its cost to be comparable to silicon solar cells. CIGS solar cells also often use cadmium sulfide in a buffer layer, leading to similar environmental concerns to those seen with CdTe solar cells [16]. A third group of similar thin-film solar cell types, consisting of copper zinc tin sulfide (CZTS), copper zinc tin selenide (CZTSe), and their alloy, is in development as an attempt to avoid the negative environmental impact of cadmium in CdTe and CIGS solar cells [17]. However, a more complex crystalline structure causes CZT(S/Se) solar cells to have increased lattice defects and therefore a lower efficiency than the other two thin-film materials, with record values around 11.3% for solar cells [13], requiring further improvements to the fabrication process before they can become competitive as a thin-film solar cell variety [18].

Gallium arsenide solar cells, another common solar cell material, have thus far demonstrated the highest efficiency of any single-junction solar cell under terrestrial illumination [19], 29.1% for solar cells and 25.1% for modules [13]. Their direct bandgap of 1.424 eV is nearly ideal. However, the exceptionally high cost of these solar cells, together with toxicity concerns due to the arsenic content, generally restricts their use to space-based applications, where the efficiency-to-mass ratio becomes important and toxicity is less of a concern [20]. Solar cells fabricated from other similar III-V semiconductors, such as indium phosphide

solar cells, face similar issues. One situation where this class of materials are commonly seen is the use of III-V ternary alloys in high-efficiency multijunction solar cells, where the use of three elements instead of two allows the bandgap to be tuned by adjusting the ratio between them [21]. A typical example is an InGaP/InGaAs/Ge triple-junction, which uses two III-V ternary alloys to capture different halves of the visible spectrum on top of a germanium layer to capture near-infrared light. Again, cost is prohibitive in bringing these solar cells to standard markets.

Recently, a lot of attention has been paid to perovskite solar cells [22]. These diverse semiconductors have in common a crystalline structure with the formula  $ABX_3$ , where B and X are monoatomic ions and A is a small organic molecular ion. Semiconductors of this type have been found to have a low manufacturing cost and a high efficiency, with records of 20.9% for cells and 11.6% for modules as of October 2018 [13], making them very promising for commercial solar installations. However, additional practical concerns still need to be overcome before widespread implementation becomes possible, as the materials used tend to be toxic [23] and have short lifespans, undergoing rapid deterioration in the presence of bright light or humidity [24].

Several other photovoltaic types have been the focus of recent research and are worth mentioning, although they are generally limited to specific applications. Organic or polymer solar cells have low manufacturing costs and are very environmentally friendly, but due to the difficulty in achieving crystalline arrangements of large molecules they have low efficiency, with a record of 11.2% for cells [13], and fabricating larger solar cells from them is challenging [25]. Quantum dot solar cells use the geometry of nanoparticles to tune the bandgap to trap light, making them ideal for multijunction solar cells [26], but also leading to challenges with manufacturing costs and charge carrier transport [27], due to their nanoporous surfaces being difficult to adequately passivate. Dye-sensitized solar cells, consisting of a photosensitive dye embedded within a three-dimensional porous matrix, also have a unique light-trapping mechanism that makes the solar cell partially transparent and particularly effective in low-light environments [28], but they tend to have low

efficiency, with a record of 11.9% for cells [13], and a short lifespan [29]. All three of these would require substantial improvements before they could see significant use in the commercial photovoltaics market.

Silicon is the second most common element on Earth, after oxygen. Large quantities of silicon in the form of silicon dioxide, commonly found in nature as sand or quartz, are easily obtainable, and metallurgical grade silicon is relatively inexpensive. However, the presence of impurities even at very low concentrations can negatively affect the photovoltaic properties of the solar cell, and extensive purification is needed to generate silicon for use as a photovoltaic semiconductor [30]. The cost of electronic grade silicon that can be reliably used for solar cells is primarily due to the various processing steps, including the generation of trichlorosilane and the Siemens process, needed to provide the requisite purity for efficient photovoltaic generation [31]. Silicon has poor temperature-dependence, and suffers significantly decreased performance in high-heat conditions. It has an indirect bandgap of 1.12 eV, slightly lower than the optimal single-junction bandgap of 1.34 eV [32]. The indirect nature of the bandgap means that solar cells using silicon have a very significant tradeoff between the thickness and therefore cost of the semiconductor layer and its efficiency, causing them to achieve neither exceptional efficiency nor exceptionally low cost. However, despite these drawbacks, silicon solar cells still experience adequate performance in cost and efficiency, and their long lifespan and low toxicity together with a well-established manufacturing infrastructure lead to their dominance in the photovoltaics industry [5]. As of 2017, 95% of all global photovoltaics production consisted of silicon solar cells [33].

While it is true that certain of the emergent photovoltaic technologies mentioned here may be able to challenge silicon solar cells in the near future, it is undeniable that silicon is at present dominant within the photovoltaics industry. As the research presented here focuses on non-material improvements to photovoltaics, silicon solar cells will be considered exclusively for the remainder of this thesis.

## 2.1.2: Overview of Crystalline Silicon Photovoltaics

Even within the area of silicon, there are several varieties of solar cells that must be compared. The size of silicon crystals within the solar cell can be adjusted, and the layers of the solar cell, including the junction itself and any protective, conductive, passivation, or reflection-controlling layers, can vary between different solar cells. The options available here will be discussed in this section.

The main distinction between types of silicon solar cells is the size of silicon crystals within the solar cell [34]. Monocrystalline silicon solar cells have the largest crystals, followed by polycrystalline, nanocrystalline, and finally amorphous silicon solar cells.

Monocrystalline silicon solar cells are the most efficient form of silicon solar cells, and make up around 33% of all solar cells sold [33]. As the name suggests, monocrystalline silicon solar cells are formed from a single crystal of silicon, and are fabricated by cutting a slice from an ingot of monocrystalline silicon [35]. The fabrication of this ingot, achieved via the Czochralski process, accounts for the comparatively high cost of monocrystalline silicon solar cells, but the single crystal results in high generation efficiency, up to 26.7% for solar cells or 24.4% for modules [13].

Polycrystalline silicon solar cells are the most common type of solar cells, making up around 62% of all solar cells sold. They are created by growing numerous small silicon crystals together to form a piece of silicon with distinct crystal grain boundaries. This is a significantly less expensive fabrication process than what is used for monocrystalline silicon solar cells [35]. However, the crystal grain boundaries formed by this process lower the silicon's conductivity and provide sites for electron-hole recombination, reducing the solar cell's efficiency to a record of 22.3% for solar cells and 19.9% for modules [13]. Additionally, the random orientation of the crystals leads to challenges in applying texturing to the solar cells.

Collectively, monocrystalline and polycrystalline silicon solar cells are referred to as crystalline silicon solar cells, and differ significantly from nanocrystalline and amorphous silicon solar cells. In these solar cells, the silicon crystals are very small or nonexistent, such that the silicon conductivity is extremely low.

For this reason, these solar cells are better used as thin-film solar cells, despite the low light absorption of silicon. This results in very low efficiency which is decreased further by the non-crystalline nature of the semiconductor, which leads to internal nano-voids and grain boundaries that contribute to surface recombination [36], with the record efficiencies being 11.9% for nanocrystalline silicon solar cells and 10.2% for amorphous silicon solar cells [13]. This makes them less desirable for power generation, but their extremely low cost and high reliability are still desirable in many applications, such as low-power electronics [37].

The research presented here focuses primarily on monocrystalline silicon solar cells, due to their heightened efficiency and still significant market share, but the results can equally well apply to polycrystalline silicon solar cells. The greatly reduced efficiency and market share of nanocrystalline and amorphous silicon solar cells makes results related to them less relevant to this research, and therefore they will not be considered.

For a silicon solar cell to work properly, a diode junction must be established within the silicon layer. This is done through the use of dopants, with boron and phosphorus typically used for P-type and N-type doping, respectively [34]. With the notable exception of back-contact solar cells, the diode junction is typically vertically oriented, with one layer at the top surface of the solar cell and the other at the bottom surface. The standard silicon solar cell uses a P-type silicon substrate with a thin N-type upper layer forming a simple P-N junction. The inverse of this is also widely used, using an N-type substrate and a thin P-type layer [38]. N-type substrates offer increased carrier lifetimes within the bulk of the semiconductor and reduced susceptibility to impurities, but P-type substrates remain the most common due to historically higher efficiency and better radiation resistance, which have led to increased manufacturing capacity [39]. In addition, the diffusion of aluminum from the low-cost, large-area contacts typically used on the back of the solar cell into the silicon can result in P-type doping, complicating the contact design for N-type substrate solar cells [40]. The inclusion of additional dopant layers can be used to create a stronger electric field within the solar cell, encouraging the movement of electrons out of the cell. For example, a back surface field (BSF) solar cell uses a P-type substrate with a purposefully aluminum-doped P+ region along

the back surface [41]. It is also common for solar cells with grid-shaped rather than planar contacts to have more heavily doped regions near the contacts to promote lateral charge carrier transit towards the contacts [42].

There are a few more advanced silicon diode junction configurations that are worth discussing. In the previously-mentioned back-contact solar cells, the P- and N-type regions are horizontally rather than vertically spaced. This allows for all electrical connections to be kept on the back of the solar cell, removing the challenge of incident light being blocked by the front contacts [43]. However, this improvement leads to a much higher cost and more complicated fabrication process [44]. A similar high-cost high-efficiency variation is the heterojunction with intrinsic thin-layer (HIT) solar cell [30]. This type of solar cell builds upon the previously-discussed P-N-N+ geometry by using amorphous thin-film silicon for the outer layers, and placing intrinsic amorphous silicon layers between the three doped layers. This results in improved surface passivation, as the intrinsic silicon layers block recombination at the borders of the crystalline silicon, allowing the contacts to be designed with less focus on passivation concerns. Additionally, HIT solar cells exhibit improved high-temperature performance compared to a standard crystalline silicon diode junction. Once again, however, these improvements require increased fabrication costs.

Additional layers on a solar cell may not directly contribute to electron excitation, but they serve important purposes in the overall operation of the solar cell. Conductive layers are needed to collect the charge carriers on opposite sides of the solar cell. Reflection management layers are often used, both on the front surface to discourage the reflection of light away from the solar cell, and on the rear surface to encourage the reflection of any photons that pass through the solar cell, so that they will pass through again and have a second chance to excite a photon. Surface passivation is necessary to reduce the recombination of electrons and holes along the surface of the solar cell, which is a major loss mechanism for photovoltaics. Finally, structural and protection layers are required to ensure the long-term stability of the solar cell.

Conductive layers for a typical crystalline silicon solar cell consist of a grid of narrow metal fingers connecting larger busbars on the front surface, and a solid plane of metal on the back surface [37]. The use

of a grid here is also a tradeoff. The front conductive layer needs to let light pass through it into the solar cell, but requiring the electrons to travel laterally through the semiconductor material to reach the conductive layer greatly increases the losses due to recombination. A grid of narrow fingers allows the conductor to come close to all parts of the surface, while only blocking a small fraction of the area. Silver is typically used for this grid, as the thin fingers require a very high conductivity to avoid adding significant resistance to the solar cell [40]. A better solution would be to use a transparent conducting oxide such as indium tin oxide (ITO), which provides complete conductivity coverage of the solar cell without blocking substantial amounts of light [30]. However, in addition to the high expense of ITO, there is a further tradeoff with thinner layers being insufficiently conductive due to their higher resistivity compared to metals, and thicker layers having problems with transparency [45]. The rear conductive layer is much simpler to design, as there is no need for light to pass through it. The use of a solid layer means that the effect of conductance on the total resistance is reduced, and can further be lowered by using a thicker layer, encouraging the use of a cheaper but less conductive material such as aluminum here [40]. This rear conductive layer can also serve as a reflector, thanks to aluminum's high broadband reflectivity across the visible and near-infrared spectrum [46]. However, aluminum is not particularly effective as a passivation layer, so significant amounts of surface recombination can occur at the silicon-aluminum interface. To combat this, certain solar cells such as passivated emitter rear contact (PERC) solar cells have a passivation layer of aluminum oxide between the silicon and the back conductive plane, with small gaps in the passivation layer serving as electrical contacts [34]. This causes similar issues to what the front-contact grid experiences with lateral charge transport, but it is still more efficient than the alternative so long as highly-doped silicon regions around the contact points are used as previously discussed. However, the increased cost means that this is primarily limited to higher-end solar cells.

Bare silicon, being semi-metallic with a large refractive index, reflects more than 30% of incident light across the visible spectrum, and therefore must use some form of anti-reflection layer to allow it to achieve reasonable photovoltaic efficiency. The methods to reduce reflectivity from the front surface of a solar cell

include surface texturing, which will be discussed in the following section, and antireflective coatings, with the two often being used in combination. The simplest antireflective coating is a layer with a refractive index that is intermediate between that of the silicon and the outer protective layers, optimally being the geometric mean of their refractive indices [47]. However, a single layer like this will only reduce the reflectance by around 50%. A more effective solution is to use a quarter-wave layer, whose thickness is a quarter of the wavelength of the desired light, such that reflections off the front and back of the layer interfere destructively and cancel out [48]. As sunlight forms a broadband spectrum rather than a single wavelength, this solution is obviously not ideal, but its high effectiveness for low cost still makes it a widely-used option. This is the reason why solar cells are commonly blue: they are using a quarter-wave layer that is tuned to capture photons in the green and red portions of the solar spectrum, which are the most common and most efficiently converted by silicon respectively, and as a consequence blue light is not adequately transmitted. For such a layer, the selected material needs a refractive index between that of the silicon and of any protective layers. Several materials, such as silicon dioxide and titanium dioxide, can be used for this purpose, but silicon nitride is most commonly used here, as it has an intermediate refractive index between glass and silicon and also serves the dual purpose of passivating the silicon surface to reduce surface recombination [49]. As silicon nitride is an insulating material, it can block the connection of the contacts to the silicon, and it is therefore typically only used between the contacts.

Other, more complex forms of antireflective coatings are also possible. Multiple layers of quarter-wave thickness with varying refractive indices will outperform a single layer in their ability to capture reflections [50]. Similarly, multiple layers of intermediate refractive index material can couple light more effectively between the two mediums [48]. The logical extension of this, gradient index (GRIN) films, provide a spatially-varying refractive index that allows them to better couple light between silicon and the outer protective layers [51]. This effect can range from simple linear variation across part of the range between the refractive indices of the neighbouring regions, to linear variation across the entire range with perfect

index matching on both interfaces, to more complex nonlinear variation of the refractive index, with each step improving the performance of the antireflective coating but also increasing the cost [52].

One final point of consideration is the protective layers of the solar cell. In order to ensure the long lifetime of a solar cell, it must be protected from the elements. A layer of glass, typically tempered low-iron glass for maximum transparency and safety if broken, is used to shield the solar cell from physical damage and accumulation of debris or dust [53]. By adhering the glass directly to the solar cell, this additionally forms a barrier against humidity and protects the silver contacts from oxidation, while eliminating the chance of unfavorable reflections that could be present if an air gap existed [54]. Ethylene-vinyl acetate (EVA) is often used for this, as it offers easy application, excellent weather resistance, and a refractive index nearly identical to that of glass. However, EVA can be degraded by ultraviolet light, so it can only be used with glass that blocks that portion of the spectrum. Other materials can be used to avoid this problem, such as polyvinyl butyral (PVB), which has better UV stability but degrades in humid conditions, and silicone, which is highly stable under both UV and humidity but has a higher price.

For the purpose of this study, it would be preferable to use a standard silicon solar cell, such as is commonly used in industry. A monocrystalline solar cell will be used to allow for more ideal behaviour of the diode junction, but otherwise the standard layers of a silicon solar cell will be assumed. The cross-section of such a solar cell is shown in Fig. 2.1, contrasted against a high-performance silicon solar cell for comparison purposes. The layers of this standard solar cell consist of, from front to back: A tempered, low-iron glass protective layer, an EVA bonding layer, a silver finger mesh front-contact layer, a silicon nitride quarter-wave anti-reflective and passivation layer, a P-substrate silicon P-N junction, and an aluminum back-contact and reflector layer. This will allow the results of this study to closely approximate what can easily be done with current manufacturing capabilities.

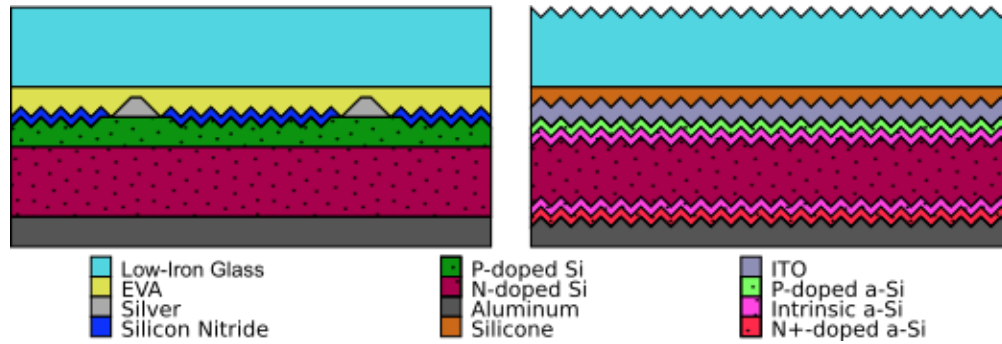


Fig. 2.1: A comparison between the structures of a typical commercial monocrystalline silicon solar cell, as will be used in this study (left), and a high-performance HIT monocrystalline silicon solar cell with textured glass and rear interfaces (right).

### 2.1.3: Surface texturing and three-dimensional photovoltaics

On a flat surface, the minimum reflectance of unpolarized specular light comes when the light arrives along the direction of the surface normal. In photovoltaics, this means that an optimally-functioning solar cell is one that has its surface normal pointed directly at the sun. In practice, this is difficult to achieve. However, the performance of solar cells under light arriving at a steeper angle can be improved through the use of a non-flat surface.

For a solar cell to remain pointed at the sun at all times, it is necessary to include a mechanically-actuated sun-tracking system, which detects the location of the sun and orients the solar cell to point towards it [55]. While this is a commonly seen implementation, there are some important concerns that must be considered for such an application.

The first such concern with sun-tracking is that of efficiency [56]. The need to detect the sun's position and mechanically re-orient the solar cell requires an input of electrical energy, which must be subtracted from the total energy output of the solar cell in order to calculate its overall efficiency. Any improvements in the efficiency of the solar cell due to the sun-tracking will be reduced and potentially offset by this.

Secondly, there is the effect of shadowing. While the total area of photovoltaic surfaces in a given solar generating array will always remain constant, the installation area projected onto the sun-facing plane varies as a function of the sun's location in the sky. This means that if this solar generating array contains multiple

individually-actuated panels, which is a necessity for large arrays of sun-tracking solar cells, either these panels will be widely-spaced, leading to large gaps between them and therefore an inefficient use of land area when the sun is directly overhead, or they will be tightly packed, causing them to cast shadows onto each other when low-angled sunlight causes these panels to move into a more vertical orientation [57]. Partial shadowing of solar panels can have significant negative effects on the performance of the solar generating array, disproportionately to the direct loss of generation expected due to reduced illumination [58]. Dark solar cells in series with illuminated ones act as large resistors, dropping the power output and potentially heating up to the point of damaging themselves, while dark solar cells in parallel act as bridging diodes, dragging down the output voltage. For the most part, external protection diodes can be used to mitigate these concerns, but the diodes themselves introduce power loss into the system during partial shadowing conditions, and they cannot offset partial shadowing within a single solar cell, only between solar cells. For this reason, close proximity of mechanically actuated solar panels is typically undesirable.

Thirdly, the practical concerns of a mechanical actuation system must also be considered [59]. Such a system tends to be physically large with a significant vertical profile, which limits its use in space-constrained or high-wind locations. Additionally, the system itself could add substantially to the cost of the solar generating array, and the presence of moving parts generally results in additional maintenance requirements over the lifetime of the solar generating array, which also come with associated costs. This, too, must be factored against the improved efficiency of the solar generating array to determine if the sun-tracking system is actually beneficial.

Taken together, these constraints on the use of a sun-tracking system mean that it is common in specific applications, but rare in others. For example, an installation within active farmlands can afford to have widely spaced panels, as the area between the solar panels can be useful for other purposes such as animal grazing. Such an installation would therefore be likely to use a sun-tracking system. Meanwhile, in a rooftop installation, where space is at a premium and maintenance access and wind are significant concerns, the use of a sun-tracking system is unlikely.

For applications where sun-tracking systems are impractical, as well as to further benefit applications where they are not, surface texturing can be used to reduce the reflectance, specifically the steep-angle reflectance but also to a lesser extent the normal reflectance, of the solar cell [60]. Surface texturing consists of small topographical features on the surface of the solar cell. There are two main mechanisms by which texturing can reduce reflection. Nanotexturing, with a scale comparable to the light's wavelength, acts as a GRIN anti-reflection coating, without the need for a precisely varying refractive index. Meanwhile, microtexturing, which is significantly larger than the wavelength of light, collects additional light by providing alternate surface normals and capturing reflections. The two types of surface texturing can even be used in tandem, thanks to the vastly different scale between them [61].

Nanotexturing, on the scale of the wavelength of light, is an approach that can obtain low reflectances through the use of three-dimensional geometries using a similar mechanism to that of anti-reflection coatings [47]. Due to its small size compared to the wavelength, the nanotexturing effectively has a homogeneous refractive index that transitions from entirely that of the outer layer to entirely that of the substrate as the light passes through it, effectively acting as a GRIN anti-reflection coating without the need to actually have a spatially-varying refractive index. This also removes the dependence of GRIN coatings of finding a suitable material that has a refractive index in the desired range, as only the two edges of the refractive index change are needed for nanotexturing. Common shapes used here include nanowires [62], which can be easily fabricated through deposition, and moth's-eye structures [50], which are more complicated to fabricate but provide a more uniform and predictable refractive index transition. The use of silicon nanowires directly on top of the silicon diode substrate, commonly referred to as black silicon, is a commonly-used low-cost nanotexturing technique, but having the nanowires be electrically contiguous with the diode junction leads to significant surface recombination, and a greater reliance on passivation techniques to counteract this [63].

Microtexturing refers to texturing that is significantly larger in scale than the wavelength of light, which reduces reflections through a significantly different mechanism. In this case, the textured surface provides

surface normals pointing in several different directions. Due to this, light that is incident on the solar cell at a steep angle is likely to be more directly incident onto the texturing features, reducing its immediate reflection. Additionally, there is the chance that that reflection would be incident onto another part of the texturing, allowing it to be recaptured.

While such texturing can be accomplished through other materials placed on top of the silicon substrate of a solar cell [64], it is more frequently achieved through directly etching the substrate to change its shape. In selecting the method of etching, light trapping must be balanced against the increased surface recombination that results from a more highly textured surface. For a monocrystalline solar cell, the ideal method to use here is an anisotropic alkaline etch [60], as this cuts along the crystalline planes of the silicon wafer to create a semi-regular texture consisting of four-sided pyramids of varying size and position that are highly effective at trapping incident light. For polycrystalline silicon, however, this method is much less effective due to the randomly-oriented crystal grains, which may be altered unpredictably by the anisotropic etch [65]. An isotropic acidic etch is more commonly used here, which creates a randomized texture of shallow, rounded features. Unfortunately, the shallowness of the features created by this method lowers their ability to capture light. An alternative method is reactive ion etching, which creates similarly randomized, rounded texturing, but with both finer detail and a higher aspect ratio. While this method outperforms acidic etching, the highly porous surface created by this type of etch causes an increase in surface recombination, and the higher price of reactive ion etching also lowers its desirability. All of these three methods can be combined with masking to apply regular patterns to the resulting texture [66], heightening their performance further at the cost of an additional processing step during fabrication.

The principles of microtexturing can also be applied at a larger scale. Instead of small surface features forming a three-dimensional geometry on the surface of the solar cell, the solar cells themselves can be arranged to form a three-dimensional array that collects light from lower angles at direct incidences and promotes inward reflections, a technique that is referred to here as three-dimensional photovoltaics, or 3DPV. This is easiest to perform using thin-film solar cells, as they can be designed in irregular or curved

shapes. This easily allows for such geometric arrangements as a hemisphere-based corrugation [67], inverted cones [68] or pyramids [69], cylinders [70], or even more complex optimized structures [71], some examples of which are shown in Fig. 2.2 a)-c). These techniques are frequently used to offset the established low efficiency of thin-film solar cells.

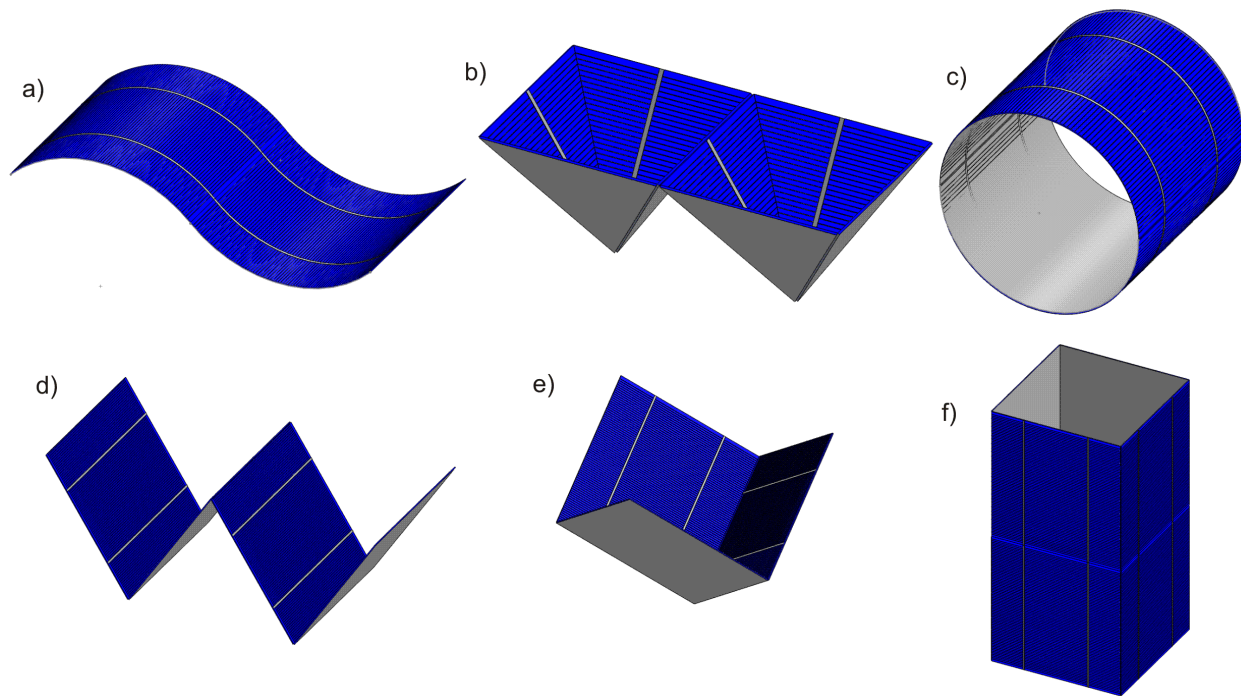


Fig. 2.2: Examples of established 3DPV geometries. The first row shows examples that are typically used with thin-film technology and could not be created with standard square, rigid solar cells, while the second row shows examples that are compatible with standard crystalline silicon technology. a) Corrugation incorporating curved solar cells [67]. b) Inverted four-sided pyramids using triangular solar cells [69]. c) Curved solar cells shaped into cylinders [70]. d) V-shaped corrugation [72]. e) Retroreflector-based corner cubes [78]. f) An example of a solar tower [79].

Silicon solar cells, however, are not nearly as flexible as their thin-film counterparts, both literally and figuratively. They are almost exclusively available as squares and rectangles, with triangular shapes generally being available only for large solar panels, where they are created as a grid of smaller square solar cells with empty space along the angled edge. While irregularly-shaped solar cells are certainly possible, the fabrication of such solar cells would mean that the established silicon solar cell manufacturing capability could not be adequately leveraged, resulting in substantially higher manufacturing costs. Any 3DPV array

intended for use with silicon solar cells should therefore consist solely of square or rectangular flat solar cells.

A few 3DPV geometries that are compatible with silicon solar cells have been the subject of previous research. The most common of these is V-shaped corrugation [72], shown in Fig. 2.2 d), which consists of rows of solar cells tilted alternately towards the east and west. While this geometry was originally intended for use with silicon solar cells [73], it has since seen much more widespread research with lower-efficiency solar cells such as organic solar cells [74]-[75]. Such use often revolves around the opposing sides being constructed of different solar cells [76]-[77], such that light reflecting off one type of solar cell is then incident on a different type, effectively creating a multijunction solar cell without the need for the two junctions to be directly stacked on top of each other. While this reduces the fabrication complexity and thereby the cost of the multijunction solar cell implementation, which is considered one of its major challenges, the resulting tandem solar cell is highly angle-dependent, and the position of the sun could frequently mean that only one of the two solar cells is actually illuminated.

Other silicon-compatible 3DPV geometries that have been previously studied include the corner-cube array [78], shown in Fig. 2.2 e), which uses solar cells within corner-cube-shaped retroreflectors to allow for up to three reflections before incident light can be rejected by the solar generating array, as well as solar towers [79], shown in Fig. 2.2 f), which apply the 3DPV concept to maximize per-area light collection for applications with highly restricted available installation area. However, the lack of detailed study into this area of photovoltaic design leads to the possibility that certain legitimately useful 3DPV geometries have been overlooked.

#### 2.1.4 Economics of Photovoltaics

Any discussion of photovoltaics must eventually turn to the subject of economics. While environmental concerns and intermittent generation can be seen as driving motivations for and against the use of photovoltaics respectively, ultimately it is the economic profitability that determines whether a given solar

generating array will be constructed. The initial costs of installation must be weighed against the ongoing value generated by the array over its lifespan to determine if a net profit can be achieved.

As with any form of electricity generating station, solar generating arrays must contend with the issue of high startup cost. The installation cost for photovoltaics is often trivialized to be the fabrication and materials cost for the solar cells themselves, and while this does continue to be a large fraction of the total installation cost, it should be recognized that the solar cells are currently only about half of the total equipment cost for a solar generating array, and the equipment cost itself is often outstripped by the soft costs associated with labour, taxes, permits, and developer overhead [80].

The support structure of the solar panels is often overlooked in calculating the installation cost. In fact, some form of support structure is necessary for any significant solar generating array. Even a configuration that consists solely of horizontally-oriented solar cells on a flat surface must be kept elevated. The inefficiencies of solar cells manifest themselves through the generation of heat, and high heat can negatively impact the efficiency of and eventually lead to failure of the solar cells, so maintaining sufficient airflow around the solar cells to allow for cooling is of critical importance [81]. For solar cells oriented at an angle, placed on uneven or sloped surfaces, or requiring mechanical actuation, the complexity and cost of the support structure can increase accordingly.

The cost of electronic components can also form a significant portion of the total installation cost. The current output of a solar cell varies nonlinearly with its voltage, such that maximum efficiency can only be attained at a specific voltage, which can vary rapidly due to changing illumination conditions. In order to maintain high efficiency, a Maximum Power Point Tracker (MPPT) is required to both detect the voltage at which maximum power can be achieved and match the solar cell's impedance to ensure this voltage is maintained across the solar cell's terminals [82]. Further electronics are then required to convert the power output into a form usable by the connected system. In particular, for a grid-connected system like the ones theorized over the course of this thesis, an inverter is needed to convert the DC output of the solar cells into AC power suitable for being connected to the grid [83]. On top of the significant cost of these large

electronic components, extensive wiring is needed to connect the solar cells together, particularly in large arrays.

Installation labour costs must also be considered for the installation of a solar generating array [80]. Tying a system into the electrical grid is not a matter that should be taken lightly, due to both the danger of the high voltage involved and the legal aspects of forming a contract with the electrical utility to provide electricity, and highly qualified individuals would need to be employed to navigate both aspects of this. The installation of the solar panels themselves and their support structure is also fairly labour-intensive, as the panels can be extremely large and unwieldy, and correctly-performed installation is necessary to ensure high efficiency and minimal maintenance costs over the lengthy lifespan of the solar generating array. The site, too, must be considered: both the actual cost of the land area that will be used, and the expert advice needed to determine whether the shadowing and typical weather at a given site are sufficiently conducive to photovoltaic generation. Additional soft costs, including taxes, permits, material transportation, and any overhead costs and profits retained by the installation and design companies, will often add up to form a significant portion of the total installation cost.

It is also necessary to include ongoing costs over the lifespan of the solar generating array. While the useable lifespan for crystalline silicon photovoltaics is typically taken to be 25-30 years [84], components may need to be replaced over this time period due to normal wear or accidental damage. Labour costs for maintenance and repairs must also be considered, particularly in climates where snow accumulation could block incident light and eventually damage the solar generating array if not removed swiftly [85]. Dust accumulation, while less immediately damaging than snow, will gradually reduce the efficiency of the solar generating array by blocking incident light, necessitating occasional cleaning of the solar cells to keep them operating optimally [86].

Both maintenance costs and the value of electricity produced and either consumed or sold to the electrical utility can be modeled as time-averaged costs over the lifespan of the solar cell. Given that the electricity value must outweigh the maintenance costs for a solar generating array to be considered viable, the total

lifetime economic performance manifests as a large initial cost, followed by steady revenue over the lifespan of the solar generating array. The revenue is not constant, as it is affected by changing weather conditions and the price of electricity, and gradually declines over the lifespan due to increasing maintenance costs and reduced efficiency on an older solar generating array. However, a simplified economic model could assume constant revenue over the entire lifespan.

This simplified economic model allows two key values to be calculated, which can then be used to compare solar generating arrays. The payback period is the time at which the net economic contributions of the solar generating array becomes zero, which is to say that the initial installation cost has been completely paid off by the subsequent revenue [87]. A shorter payback period is preferred, and if the payback period exceeds the lifespan the array is not economically viable. The levelized cost of energy (LCOE), meanwhile, ignores the revenue to compare instead the total lifetime costs of the solar generating array as well as the total lifetime energy generated [88]. This value can then be compared to the average electricity price over the lifetime of the array, and if it is less than the electricity price, the array is economically viable. This thesis primarily uses a third, related metric, the profit, which is defined as the total value generated by the solar generating array over its entire lifespan, minus all installation and maintenance costs. Generally, more than one of these metrics must be considered when determining the economic benefit of a solar generating array.

One point worth noting here is the presence of government subsidies and grants to promote the installation of photovoltaic generation [89]. Solar electricity is a highly environmentally friendly and renewable form of electricity generation, but its fundamental cost is still worse than many other forms of electricity generation, despite the constant innovation in the field. Due to this, environmentally-focused government initiatives will frequently provide options to either reduce the installation cost of photovoltaics, through direct rebates, tax credits, or low-interest loans, or increase the price at which photovoltaic-generated electricity can be sold, by setting renewable energy policy requirements for the electrical utilities that incentivize them to purchase more renewable energy, thereby increasing the price at which the utility will

be willing to purchase the photovoltaic-generated electricity. Any such opportunities must also be considered when evaluating the economic viability of a solar generating array.

Another point worth noting is that the rates at which solar-generated electricity can be sold to the electrical utility can vary widely based on the power-purchase agreement that is in place. One of the most common types of power-purchase agreements for residential solar generation is Net Energy Metering, where surplus generated power that is not immediately used by the producer can be sold to the electrical utility at the same rate as power would normally be purchased from them [90]. This separates the value of the generated electricity from the actual value of electricity to the grid, and may disconnect it entirely from daily fluctuations, depending on the electricity rate plan involved [91]. These plans can increase the price of electricity in times of typical high demand, or at higher levels of electricity consumption, or even leave the price of electricity constant.

Other power-purchase agreements, more commonly used for commercially-owned solar generating arrays, are of the feed-in tariff type, where the electricity price is agreed upon separately [92]. The value of power used in this agreement can vary widely from case to case. Fixed or time-varying values with no dependence on electricity price are often seen. For those power purchase agreements that do depend on the electricity market price, the price used may be the real-time electricity price, or a longer-term price estimate known as the Market Price Referent [91]. Various bonuses can be added onto this price, with many possible ways the bonus could depend on the price, such as setting a minimum price cap, a multiplicative or additive bonus, or a bonus inversely related to the price. The use of the actual instantaneous grid electricity price with no bonus for a feed-in tariff, as is done in this thesis, is not typically done in industry, but was chosen here due to the focus of this thesis being primarily on societal benefits and not on economics, as will be discussed further in chapter 3.

### 2.1.5: Intermittent Generation and the “Duck Curve”

One of the major challenges still faced by the photovoltaic industry is the fact that photovoltaic generation is fundamentally intermittent. Solar generating arrays will not produce electricity at night, and during the day, their electricity generation varies uncontrollably with the weather conditions and the position of the sun in the sky. As a supplement to other forms of electricity generation, this does not pose a huge concern, but with the increasing pressure to adopt fully renewable electricity generation, the inability to supply electricity when it is demanded is becoming a major problem [93].

The issue of intermittent generation affects most forms of renewable generation. Wind and tidal generation similarly depend on natural conditions and cannot be expected to consistently and constantly generate electricity. Only a few specific types of electricity generation are both renewable and non-intermittent, and these, such as hydroelectric and geothermal generation, are often highly location-specific and cannot be installed at the capacity needed to move to fully renewable electricity generation [94].

Conventional, steam-turbine-based fossil-fuel-powered electricity generation is still widely used and provides a steady, constant source of electricity. These generating facilities are capable of regulating their electricity output, unlike most forms of renewable generation, and can therefore be used to counteract market fluctuations. However, they are typically very slow to change their rate of power generation [95]. In a market dominated by this type of generation, the cumulative demand of thousands of consumers tends to average out enough that these slow ramp times are more than sufficient to match the supply to the demand. Once a significant amount of intermittent generation is added to the system, however, the situation changes drastically.

When an electricity market is dominated by intermittent generation, a worrying trend can be seen in the balance between supply and demand. With electricity consumers being generally insensitive to the needs of the electricity grid, and with intermittent generation being largely unable to regulate their supply, it is up to the remaining conventional generation to ensure that supply and demand remain balanced. However, as

the quantity of intermittent generation increases, the magnitude and speed of supply/demand fluctuations also increase to the point that conventional generation cannot change its output fast enough to offset it.

One specific case of particular concern is the “Duck Curve”. In areas with large amounts of solar electricity generation in particular, specific supply/demand trends emerge due to the daily cycle of solar generation, with the electricity produced peaking during the middle of the day and dropping to zero at night [96]. Meanwhile, electricity demand also exhibits a daily cycle. Use of electricity peaks from the morning hours, when people wake up and begin cooking breakfast, through the midday hours, when regions with sufficient sunlight to support large amounts of solar electricity generation typically experience large amounts of air conditioning usage, and into the evening hours, when people tend to turn on lights, cook dinner, and watch TV [96]. Although the peaks of maximum supply and demand on these two curves generally match up, the demand curve has a much more broad profile, extending further into the morning and evening.

As the level of solar penetration increases, the solar electricity generation will initially offset the peak of the demand curve, but will eventually surpass it [97]. This leads to an electricity surplus during the day, resulting in extremely low or even negative electricity prices. Fig. 2.3 provides a simplified depiction of this trend, shown at three different levels of solar penetration. At higher levels, the net demand that must be offset by other forms of generation becomes increasingly low during the middle of the day, eventually reaching zero, at which point electricity would need to be exported or solar generation would need to be curtailed. These low net demand values during the period of peak generation result in low or negative electricity prices, which are of great concern for photovoltaic generation, as they reduce the profit that can be made, and thereby the ability of the solar generating arrays to reach their payback time. Meanwhile, the lack of solar generation in the evening leads to steep, rapid transitions in the net demand, causing skyrocketing electricity prices and electricity shortages. The combination of these two factors results in a consistent bimodal daily electricity price curve with extremely low electricity prices in the middle of the day and high prices during the morning and evening, shown in Fig. 2.4, with a shape that is said to be

reminiscent of a duck, hence the name “Duck Curve”. Additional examples of this phenomenon can be found in Appendix A.

The simple solution to this problem is to let the market regulate itself. High electricity prices will discourage additional demand, and low electricity prices will discourage additional supply. However, this does not work well in practice for this situation. End consumers are generally sheltered from the instantaneous market prices through their electricity rate plans, and therefore cannot see and respond to the massive fluctuations in supply and demand that actually exist [99]. Even if this were not the case, attempting to use extremely high prices to force people to rearrange their lives is unlikely to have any positive effect, and would likely lead to widespread complaints and protests. Meanwhile, on the generation side, the economic incentive is to move towards conventional generation, which is to say the exact opposite of the environmentally-necessary shift towards renewable generation that is at the core of this problem in the first place.

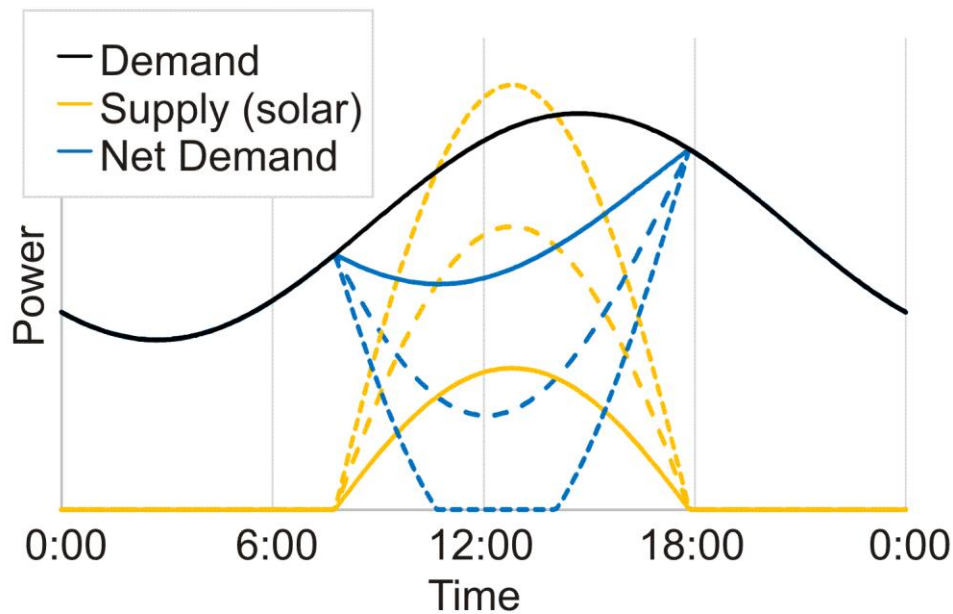


Fig. 2.3: A simplified example of the Duck Curve problem. The demand curve is shown, together with solar generation curves at three different levels of solar penetration, represented by solid lines, long dashes, and short dashes respectively. The net demand resulting from this that must be met by traditional generation is also shown.

Beyond market regulation, the next common approach to fix this problem is curtailment [100]. During times of high intermittent generation, the amount of electricity that will be accepted by the grid is capped so that supply does not exceed demand. This solution is, unfortunately, highly damaging to the intermittent generation suppliers. In addition to simply limiting the amount of intermittent generation that can be supplied to the grid at far below the goal of 100%, this approach also reduces the revenue of intermittent generation, strongly reducing its economic viability and discouraging the installation of additional intermittent generation systems. Clearly such an approach is counterproductive to the end goal of increasing the production of renewable electricity generation, and alternative methods of balancing intermittent generation must be sought.

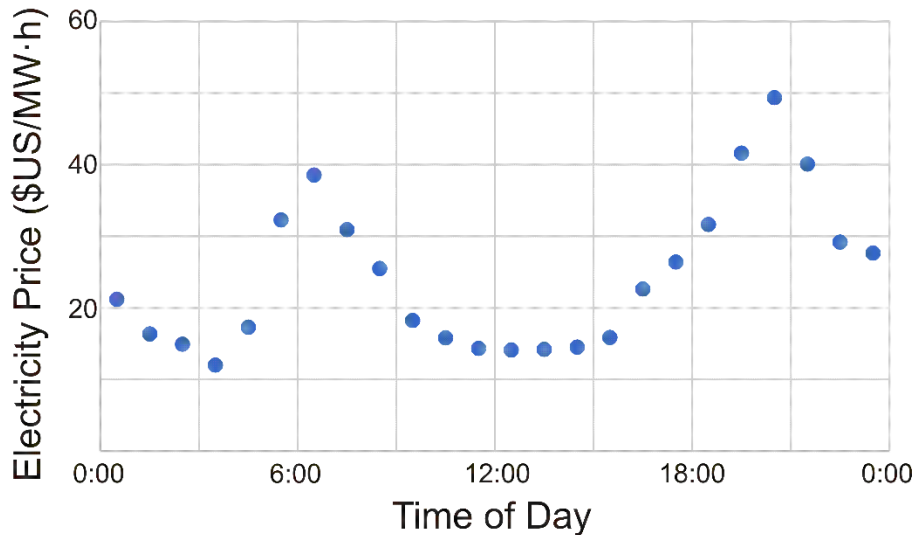


Fig. 2.4: A plot of hourly electricity price in the vicinity of Bakersfield, CA on May 1, 2018, showing the characteristic bimodal peaks and low midday price of the “Duck Curve”. Pricing data is day-ahead locational marginal pricing obtained from the CAISO OASIS database [98] and averaged across California with negative values treated as zero, as described in section 4.2.

Another possibility is through the use of dispatchable power generation. Certain types of conventional generation facilities, such as combined-cycle gas turbine (CCGT) facilities, do have the ability to vary their output power rapidly, and can therefore be used to offset the variation caused by intermittent generation [101]. However, these plants are often less efficient while varying their output power, and to use them to offset intermittent generation it is necessary for them to spend large portions of time with minimal electricity

generation. Taken together, this means that their operating revenue is significantly lower than conventional generation facilities that are not used in this manner, so unless additional economic incentives for providing dispatchable power become available, the revenue from such facilities is typically too low to justify their construction.

The true solution to this problem, therefore, lies in energy storage. The ability to store electricity produced during the high-supply/low-demand hours to then use during the low-supply/high-demand hours is necessary to make intermittent generation feasible on a large scale. Certain forms of renewable generation already have the capability to perform energy storage. Hydroelectric generation, for example, owes its ability to rapidly adjust its generated power to the fact that the water in the reservoir is being stored and can be converted to electricity when needed [102]. However, hydrology concerns such as maintaining consistent lake levels and river flow rates limit how much this can be used, and coupled with the aforementioned rarity of hydroelectric sites, it is clear that hydroelectric generation alone cannot solve the energy storage problem. Concentrated solar power, meanwhile, uses energy storage in the form of heat storage [103]. Concentrated sunlight is used to produce steam, which turns a turbine. As the system takes a long time to cool down, electricity generation can continue past sunset into the evening hours. However, while this energy storage does help to offset the “Duck Curve” problem, it only reduces the impact of the CSP generating facility itself, and cannot provide energy storage for other generation facilities. Neither solution can be implemented on a scale capable of solving the problem of intermittent generation.

The inverse approach, energy storage integrated into the consumers rather than the generation, is also a viable strategy here. This technique, referred to as load shifting, works by moving the active times of electrical loads that inherently incorporate energy storage into the periods of high supply and low demand [99]. Loads such as the charging of electric vehicles and industrial refrigeration will therefore be primarily running during the day, and shut off in the evening, helping the electricity demand to better conform to the supply. However, the aforementioned difficulties with economic manipulation of demand still apply here, albeit to a lesser extent. Widespread societal changes would be needed to implement load shifting on a large

scale, and it is unclear what fraction of electrical loads would be compatible with this technique, and therefore how significantly load shifting could reduce the intermittent generation problem. It is obvious, however, that generation- and load-based energy storage alone are not sufficient to fully fix this problem, and dedicated energy storage is required for renewable electricity generation to achieve market dominance.

The primary route of research for energy storage is the use of electrochemical storage, such as batteries [104]. However, there are still many problems that would need to be overcome before grid-connected battery systems could be used on a large scale. Notably, the efficiency of both charging and discharging batteries is quite poor, so a significant portion of the electricity stored in this manner is lost. The cost of the batteries, which can be significant, must also be considered [105], as well as the prevalence of the materials used in their fabrication, where some necessary materials such as lithium may be too rare to allow for the necessary increases in battery production needed. Further development of battery technology is required before they could be widely used in electricity storage.

Other methods of energy storage have also been considered, but are less developed than battery technology and thus are likely to not be useable in the near future. Supercapacitors have thus far been primarily used for short-term power storage, and although their use as a long-term storage device is being developed, it remains a highly experimental technology [106]. Chemical storage, by using the electricity to produce hydrogen that can later be used in a hydrogen fuel cell to generate electricity, is a similarly emerging technology [107]. Very high efficiencies have been seen for hydrogen storage, but additional research is still required to overcome the high system costs and challenges of hydrogen storage associated with this. On the opposite side of the spectrum, pumped hydroelectric and compressed air storage are both well-established and widely-used forms of energy storage, but their poor conversion efficiency, below that achieved with batteries, limits the extent to which they can be economically implemented [108]. All of these technologies would need significant development before they become a true solution to the problem of intermittent generation.

With intermittent generation problems such as the “Duck Curve” gaining prominence, and true solutions still being a long way off, short-term methods to reduce the impact of the problem are desperately needed to bridge the gap until energy storage technology matures to a useable level. The purpose of this thesis is to explore one such short-term method – the use of 3DPV geometries to specifically promote the collection of low-angle sunlight, and thereby extend the useable generation time of photovoltaics and reduce their intermittency.

## 2.2: An Examination of the Photovoltaic Process

In order for a simulation of a photovoltaic array to be developed, it is necessary to first consider the principles of operation of such an array. This section strives to accomplish exactly that, providing an in-depth look at the nature of sunlight and the terrestrial light spectrum, the optical performance of the simplified silicon solar cell identified in section 2.1.2, and the electrical performance of such a solar cell, together with the electrical performance of the external electronics needed to accomplish the optimal capture of photovoltaic-generated electricity. This will serve as a solid foundation on which to build both the simplified simulation of chapter 3, and the detailed simulation of chapter 4.

### 2.2.1: The Nature of Sunlight

The nature of the photons that supply energy input to a photovoltaic system is key to analyzing the performance of such a system. An investigation into the practical nature of photovoltaic generation must therefore begin in the same place as the vast majority of these photons do. The sun, the closest star to Earth, is the source of all but an insignificant amount of the energy that is added to the Earth’s thermodynamic system, and the majority of this energy influx comes in the form of photons [109]. Every second, approximately  $10^{36}$  solar photons of varying energies enter the Earth’s atmosphere [110], where they may be absorbed, reflected, or propagate downward to reach the surface.

The surface temperature of the sun is approximately 5778 K, and the light emitted from the sun can therefore be approximated as black body radiation at that temperature [111]. The exact spectrum output by the sun

differs from the idealized black body spectrum due to temperature variations both across the surface of the sun and within the sun, as well as transmission and absorption through the upper atmosphere of the sun. The actual spectrum of sunlight that reaches the Earth is typically referred to as the AM0 spectrum.

However, the AM0 spectrum is not the spectrum seen on the surface of the Earth. Transmission through the atmosphere will affect the spectrum, with some photons being absorbed, and some being scattered, each at different rates for different wavelengths of light. This effect is related to the total thickness of the atmosphere through which the light must propagate to reach the surface, which is referred to as the air mass. AM1 refers to conditions with light propagating through a single unit of air mass, i.e. with the sun directly overhead. AM1.5, meanwhile, has a 50% longer atmospheric path, corresponding to the sun having a zenith angle, or angular separation from directly overhead, of  $48^\circ$ . AM1.5 is commonly used as the standard incident light spectrum for photovoltaic research, as it is an adequately average example of light spectra at all incident angles.

The curvature of the earth has a profound effect on air mass that must be considered. Firstly, as the sun approaches the horizon, the air mass increases at an increasing rate. However, due to the curvature of the earth, this effect does not approach infinity, but rather reaches a maximum value as the sun reaches the horizon. This maximum value is often taken to be AM38, or 38 times the thickness of the atmosphere [112]. This number, however, is only an approximation, due to the fact that the atmosphere is non-uniform, and the value varies slightly depending on the source. In fact, the earth's atmosphere has different compositions and densities at different elevations, and no clearly-defined upper edge. The lack of an upper edge is the reason that the horizontal air mass is so ill-defined, as on a curved world, the air mass at a given angle is dependent not only on the vertical air mass and the angle, but also on the ratio between the atmosphere thickness and the earth's radius. The difficulty of determining an objective value for this ratio is what makes air mass numbers, particularly at shallow angles of incidence, difficult to determine with any degree of certainty.

The curvature of the earth also means that, rather than the light path through every layer of the atmosphere being increased proportionately when sunlight travels through the atmosphere at a steep angle of incidence, the light path through the lowest layers of the atmosphere is increased much more than the light path through the highest layers. This further complicates the use of air mass in a general sense, as different layers of the atmosphere, with their different densities and compositions, understandably have different absorption and scattering effects on the light passing through them [113]. In an ideal flat-atmosphere case, the intensity of light reaching the earth at a given air mass  $AM$  and wavelength  $\lambda$  would be calculated as

$$I_{\text{Opt}}(AM, \lambda) = I_{\text{AM0}}(\lambda)e^{-\alpha(\lambda)t_{\text{atm}}AM}, \quad (2.1)$$

based on the AM0 light intensity  $I_{\text{AM0}}$ , the thickness of the atmosphere  $t_{\text{atm}}$ , and some wavelength-dependent absorption coefficient  $\alpha$ . The deviation from this ideal case is negligible at steep angles of light incidence, but becomes significant at shallow angles [114].

All of this neglects the fact that the atmosphere, in addition to being vertically-stratified, is also time-varying. Even ignoring the obvious impact of clouds, atmospheric particulates in the form of smoke, pollution-based haze, water vapour, etc. can have a substantial effect on the light that is absorbed or scattered by the atmosphere [115]. The AM spectra are standardized reference spectra, and therefore neglect the effect of these highly-time-variant, unpredictable, and difficult to model effects.

The aforementioned light scattering is also an important phenomenon to be aware of [116]. Typically, rates of light scattering exceed those of light absorption during atmospheric propagation by an order of magnitude. This is important, since unlike absorbed light, scattered light may eventually reach the ground and contribute to photovoltaic generation. This light, referred to as diffuse sky illumination, is typically only a small fraction of the total incident solar illumination. However, in some circumstances, such as in cloudy weather and during the morning and evening, the direct solar illumination can become greatly reduced, while the diffuse sky illumination remains significant. In particular, at sunrise and sunset, direct

solar illumination drops to zero while diffuse sky illumination can remain significant for a slightly longer period.

The presence of diffuse sky illumination also means that the standardized AM1.5 spectrum actually has two variants [117]. AM1.5G, the global AM1.5 spectrum, includes both direct and diffuse illumination, while AM1.5D, the direct AM1.5 spectrum, includes only direct solar illumination. A third spectrum, AM1.5Diff, can be obtained for just the diffuse sky illumination by subtracting the other two spectra. Fig. 2.5 shows all three variations on the AM1.5 spectrum, compared against the AM0 spectrum and the sun's blackbody approximation spectrum.

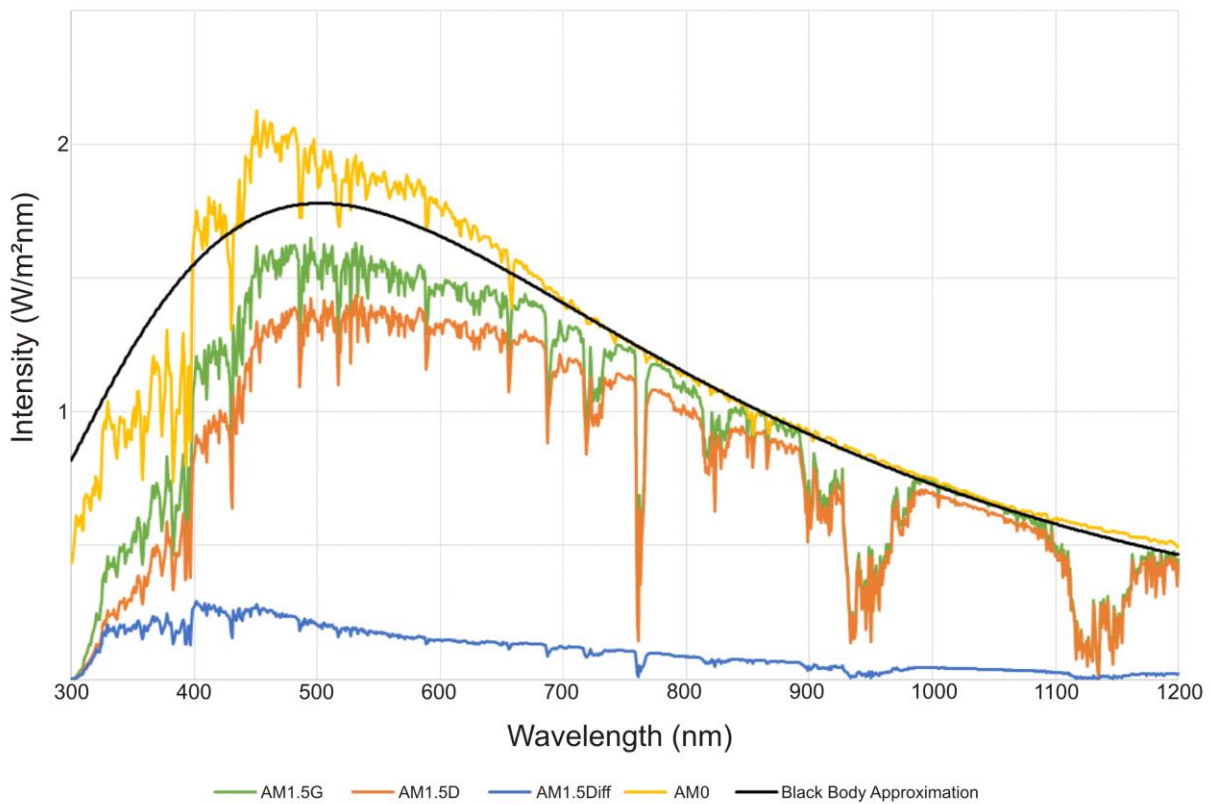


Fig. 2.5: A comparison of the AM0 extraterrestrial solar spectrum and the global, direct, and diffuse variations of the standardized AM1.5 solar spectrum, as well as the black body approximation of the solar spectrum. Data from the standardized spectra obtained from [118]-[119].

Unlike direct solar illumination, diffuse sky illumination cannot be approximated as a collimated light source. Rather, the illumination is spread over the entire sky. An extremely simplified assumption would

be that the illumination on a given point from diffuse sky illumination is uniformly distributed over the entire sky. This is essentially equivalent to treating the sky as a Lambertian source, where the illumination intensity in a given direction is proportional to the cosine of the angle from directly downward [120]. This leads to the property that the diffuse sky illumination from any area of sky is directly proportional to the solid angle of that area of sky.

Of course, the assumption that diffuse sky illumination is constant has long been regarded as inaccurate. Even in the absence of atmospheric non-uniformities such as clouds, the diffuse sky illumination varies based on both angular distance from the sun and angular elevation above the horizon [121]. Diffuse sky illumination is greatest near the horizon, and significantly less intense overhead, with the horizon having a more uniform spectrum and therefore appearing closer to white light than the blue light from overhead. When the sun is at a lower angle, directional dependence increases as well, and sky brightness in both the direction of the sun and the opposite direction is increased. With the sun near or on the horizon, all of these effects are intensified, with the horizon around and directly opposite the sun being much brighter than other regions of the sky. Additionally, the light spectrum is shifted heavily, with the horizon light becoming redder, while the dimmer overhead light loses its blue-dominance.

This change in diffuse sky spectrum is due primarily to the different scattering rates of different colours of light off of airborne particles. Light encountering particles smaller than its wavelength undergoes Rayleigh scattering, which is relatively weak and omnidirectional. However, for particles of similar size to the wavelength, the primary scattering method is Mie scattering, which is somewhat directional, tending to cause mainly small changes in the light propagation direction [122]. Blue light, having a smaller wavelength, experiences a higher degree of Mie scattering for a given set of atmospheric aerosols than red light does. When the sun is overhead, the shallow angles needed to scatter light to an observer favour Mie scattering, causing the sky to appear blue. Conversely, the much longer optical paths associated with the sun near the horizon cause much of the blue light to scatter away from the observer before reaching them, resulting in a red sky colour. Meanwhile, the horizon sky in overhead-sun conditions and the overhead sky

in horizon-sun conditions both require large scattering angles for scattered light to reach the observer, increasing the prominence of Rayleigh scattering and resulting in a more uniform white coloration.

Despite these variations in diffuse sky light, the simplified explanation of the sky having a constant spectrum and uniform Lambertian intensity can still give accurate results, given that diffuse sky light typically only accounts for 10% of the total illumination. The light incident on a solar generating array can therefore be approximated as the sum of two spectral sources: direct solar illumination, incident along a collimated path from the sun; and diffuse sky illumination, incident from all areas of visible sky at a constant angular intensity.

### 2.2.2: Optical Properties of Solar Cells and 3DPV

As previously discussed, the typical solar cell that will be considered for this research consists of the following layers from top to bottom: a protective glass layer; an EVA encapsulation layer; a silver mesh front contact; a silicon nitride quarter-wave anti-reflection layer; the silicon diode junction; and an aluminum back contact. For the purposes of optical properties, the encapsulation layer and the front contact can typically be neglected. The former is typically selected to very closely match the index of refraction of the glass layer, and therefore is typically included as part of that. The latter, meanwhile, is designed so as to cover the minimum possible surface area, such that light interacts minimally with it. Fig. 2.6 shows the complex refractive indices of the glass, silicon, and aluminum layers that must be considered in the optical design of the solar cell. Each complex refractive index shown is comprised of a real component, the refractive index  $n$ , and an imaginary component, the extinction coefficient  $\kappa$ .

Light propagation into the solar cell begins with the light incident on the outer surface, the air-glass interface. Reflection here must be accounted for, although it is quite minimal due to the low refractive index of glass, which is approximately 1.5 across the entire visible spectrum, leading to a reflectance of around 4%, shown in Fig. 2.7. The surface here is generally flat, although texturing on the protective layer is not unheard of [124]. Glass-surface texturing will generally increase light coupling into the solar cell, but runs

additional risks of increasing the optical path and therefore the absorption within the glass layer, as well as trapping environmental contaminants such as dust, which can block incident light. Under the assumption that a flat surface is in use, any specular light reflected off this surface will experience some level of polarization but will remain specular.

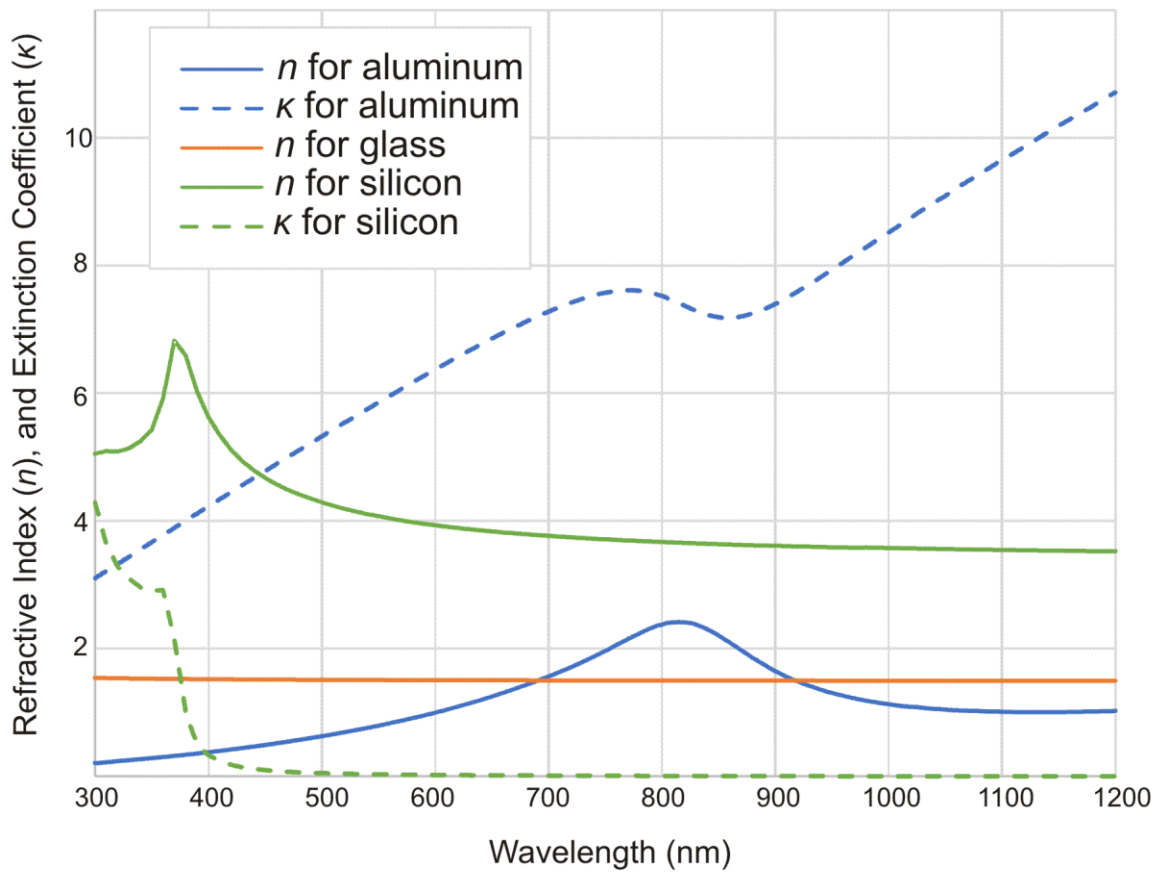


Fig. 2.6: Complex refractive indices of aluminum, glass, and silicon in the visible spectrum, as the refractive index ( $n$ ) and extinction coefficient ( $\kappa$ ), obtained from [123]. The extinction coefficient of glass is omitted here, as it is essentially zero across the range shown.

The transmission of light through glass is near 100% over most of the visible spectrum. In particular, low-iron glass is used here to further increase transmission, averting the slight transmission loss of red and near-infrared light that gives standard glass its greenish tint [53].

The EVA-silicon interface is under normal circumstances the main source of reflection away from the solar cell, with a typical reflectance around 20% as shown in Fig. 2.7, and therefore is almost always textured.

This texturing affects the nature of reflection here, and in the case of a regularly geometric texturing such as inverted pyramids, can result in light being strongly reflected in a few specific directions [125]. This can lead to a complex relationship between the direction of incident direct solar illumination and the directionally-dependent intensity of reflection off the EVA-silicon interface, which is also dependent on the orientation of the texturing relative to the solar module, a property that may be randomly varying between different solar cells. A solar cell with an irregular texturing, conversely, will display more uniform diffuse reflection off the silicon surface that generally does not wildly vary between solar cells. It is worth noting that texturing greatly reduces the angular dependence of reflection on the EVA-silicon interface. Even light that is incident to the interface at a steep angle is likely to be much closer to normal incidence on the specific textured feature it intersects.

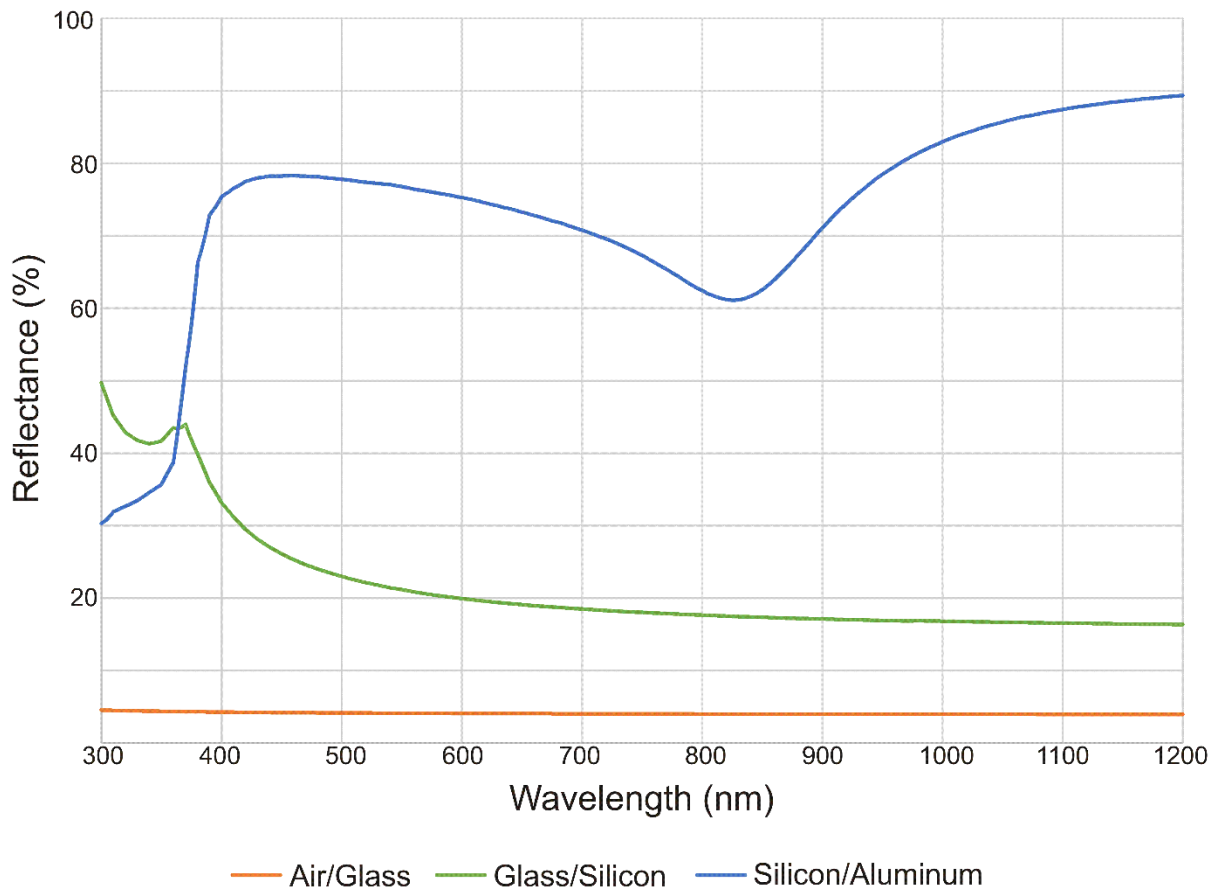


Fig. 2.7: Ideal reflectance at normal incidence for air/glass, glass/silicon, and silicon/aluminum interfaces within the visible spectrum.

Multiple internal reflections within the glass layer would normally be neglected, due to the low reflectance of the air-glass interface allowing most reflected light to exit. However, the scattering effect of the EVA-silicon interface can result in a significant amount of the reflected light hitting the air-glass interface at a steep enough angle to undergo total internal reflection. Such internally-reflected light would then have a second chance at being transmitted into the silicon, and due to the low angular dependence of the textured EVA-silicon interface, the steep angle needed for total internal reflection would not necessarily increase the reflectance of the EVA-silicon interface significantly.

After passing the EVA-silicon interface, the light propagates through the silicon diode junction. While the thickness of the silicon layer is relatively small, even for thick crystalline solar cells, the scattering induced by the texturing significantly increases the average path length of a photon through the silicon. The absorption of the silicon layer is high, with a 176-micron layer (the thickness of the solar cells used later in this thesis) absorbing over 99% of all photons up to 909 nm that pass through it along the shortest possible path. For photons near the bandgap of silicon, absorption becomes lower, dropping to 50% at 1019 nm, and as low as 5.89% at the nominal bandgap of 1100 nm for the same direct path through a 176-micron silicon layer. It is therefore possible for a significant percentage of these photons to propagate through the silicon and reach the back interface.

Among the many purposes of the aluminum backplane of the solar cell is its functionality as a reflector for incident light. Fig. 2.7 shows the reflectance of aluminum in silicon. Aluminum is not a perfect reflector, and its reflectivity is reduced when it is placed within a silicon medium rather than an air medium. While the reflectivity of aluminum in silicon may not be particularly high across the visible spectrum, the region of interest for reflection off the back interface is near the silicon bandgap of 1100 nm, where photons have a high probability of penetrating through the silicon layer, but still have the potential to excite an electron. In this region, the reflectivity of aluminum in silicon is over 85%, sufficiently high to reflect the majority of photons reaching this interface and give them a second propagation through the silicon during which they might be absorbed. The aluminum-silicon interface may be textured, similar to the glass-silicon

interface [126], although the purpose of this texturing is different. Here, the purpose is to diffusely scatter the light that reflects off the surface. For a solar cell with a geometrically-textured front surface and a planar back surface, light that enters into the solar cell is very likely to couple out of the solar cell after only a single pass in and back. By adding an additional scattering step, the chance of multiple internal reflections is greatly increased. For crystalline silicon solar cells, this effect is less necessary due to the high rates of absorption within the solar cell, but is still helpful in trapping weakly-absorbed near-bandgap light.

As the subject of this research is 3DPV, inter-solar-cell reflections must also be considered here. The reflection of light off a solar cell consists primarily of the reflection off the air-glass interface and the reflection off the silicon anti-reflection coating. Other light paths, such as reflection off the silicon-aluminum interface, reflection off the glass-EVA interface, and multiple internal reflections, are negligible in comparison to these two primary reflection sources. As previously mentioned, the reflection off the air-glass interface is a partially-polarized specular reflection, while the reflection off the anti-reflection coating is highly dependent on the type of anti-reflection coating used but may be assumed to be diffuse. The specular reflection can be directed, through the geometry of the three-dimensional structure, to be subsequently incident on another solar cell, where the light could undergo transmission into the solar cell and generate electricity, subject to its modified reflectance based on its partial polarization. The diffuse reflection, meanwhile, propagates in all directions, and the fraction that can be reabsorbed is therefore largely dependent on the aspect ratio of the geometric structure, since deeper and narrower features result in more diffuse light reflected off an arbitrary point on the structure being incident on another point on the structure. Reflections from this second incidence of light may in fact be captured a third time, and so forth.

### 2.2.3: Electrical Properties of Photovoltaics

The electrical properties of a photovoltaic device begin with the interaction of a photon and an electron. This section of this thesis will cover the excitation of that electron and associated creation of a hole, as well as the propagation of that electron and hole through the solar cell and any subsequent recombination or loss

mechanisms that may occur. The ability to interpret the solar cell as a conventional circuit will also be discussed.

As previously mentioned, silicon is an indirect-bandgap semiconductor. This means that the smallest possible energy gap for a stable valence electron to enter an excited state also requires the electron to undergo a significant change in momentum [11]. As momentum must be conserved in any collision, and the momentum of a photon is negligible, a third particle must be involved in indirect-bandgap electron excitation. This particle is a phonon, or a quantized vibration of the crystalline semiconductor lattice. The requirement for a third particle to be involved in this interaction is what lowers the probability of photon absorption taking place in indirect-bandgap materials, and therefore requires the use of a thicker semiconductor layer to achieve adequate efficiency; in any collisions where a phonon is not involved, the electron will immediately drop back to its rest state, emitting a photon identical to the one that was absorbed.

The excitation of an electron can involve either the absorption or emission of a phonon. Since energy must also be conserved, and phonons have a small but significant energy, interactions involving phonon absorption do not require a photon with as much energy as interactions involving phonon emission do to excite an electron. In addition, interactions where the photon energy is nearly minimal must be assisted by phonons with precise energy and momentum values, while higher-energy photons can be assisted by a wider range of phonons. Together, these two effects serve to blur the bandgap, turning what would normally be a sharp cutoff in photon absorption and electron excitation at 1100 nm into a gradual slope.

The indirect bandgap of silicon is not the only opportunity for photon interaction to excite an electron [32]. Additional indirect bandgaps, where higher-energy photons may excite electrons across a higher-energy gap in the band structure, can be found. These can be approximately modeled as a second indirect bandgap at 2.5 eV, or 500 nm, and serve to increase the photon absorption for photons beyond that energy. Additionally, with a high enough photon energy, silicon does have a direct bandgap, beyond which phonons are no longer required to mediate the excitation of an electron. Silicon's direct bandgap is 3.4 eV, or 360 nm. This is unfortunately too high to absorb any photon less energetic than ultraviolet, but it does mean

that the absorption of photons and generation of excited electrons in the ultraviolet range is much more likely than in the visible and near-infrared ranges, a fact which can be clearly seen in silicon's absorption spectrum. Silicon's band structure, shown in Fig. 2.8, and its absorption spectrum, shown in Fig. 2.9, both show the presence of the two indirect bandgaps and the direct bandgap. Note that although the electrons may be excited via a higher-energy bandgap, they will quickly drop back to the energy level of the lowest indirect bandgap, and therefore the resulting electron energy does not differ from that of electrons excited through the lowest indirect bandgap.

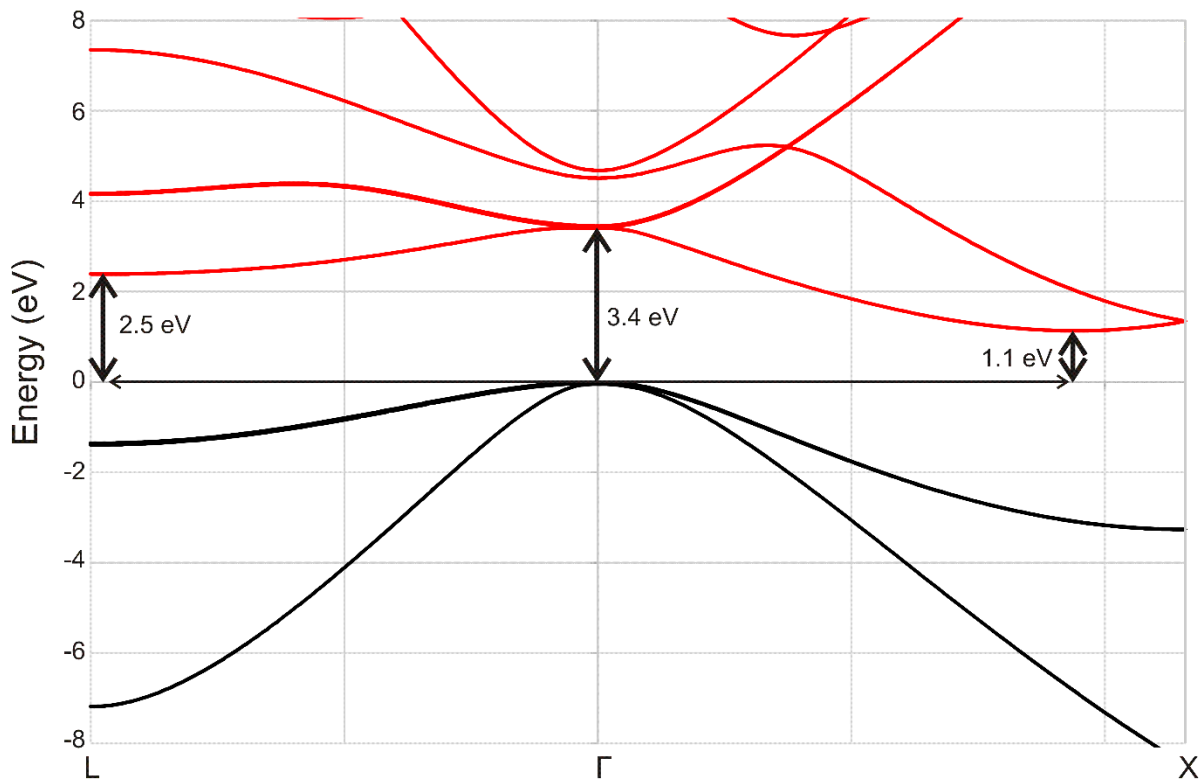


Fig. 2.8: The electronic band structure of silicon, showing the conduction bands in red and the valence bands in black. The primary and secondary indirect bandgaps and the direct bandgap are marked. The band structure is obtained from [127].

In a normal, undoped piece of semiconductor, the excited electron would quickly recombine with the hole that formed when it was excited. In order to extract electricity from this interaction, it is necessary to separate the electron and the hole. The semiconductor diode junction achieves this by forming a bias voltage, essentially tilting the band structure so that electrons drift in one direction while holes drift in the

other direction [128]. If these electrons and holes succeed in reaching the contacts on either side of the solar cell, an electrical current will be formed. However, there are several mechanisms by which the electron may still drop back to its ground state before leaving the solar cell [129].

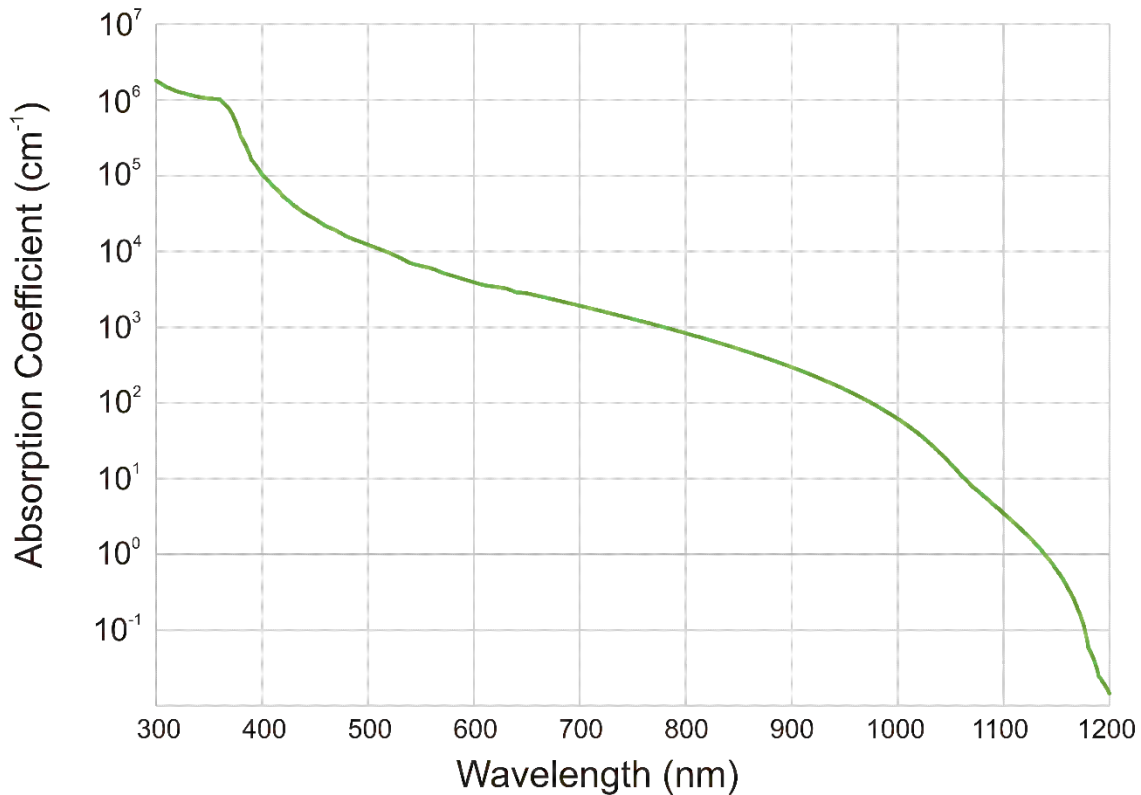


Fig. 2.9: The absorption coefficient of silicon, clearly showing the primary indirect bandgap at 1100 nm and the direct bandgap at 360 nm as significant drops in absorption. The secondary indirect bandgap at 500 nm is less distinct, but can also be observed.

Bulk recombination refers to the recombination of electrons and holes within the bulk semiconductor material, typically the base due to its larger volume, but the same effect occurs in the emitter. Due to the diode junction separating electrons and holes, these regions primarily contain a single type of charge carrier. As one of the charge carriers will be much more common in one region than the other, the effects of this recombination are primarily tied to the charge carrier density of the minority carrier, which is in turn linked exponentially to the bias voltage.

Surface recombination is very similar in principle to bulk recombination. Ideally, the thickness of a solar cell will be small relative to the diffusion length of the charge carriers, such that charge carriers from the diode junction can reach the contacts without experiencing bulk recombination. However, this also means that the charge carriers can reach the surface of the solar cell, where defects in the crystalline structure can assist in recombination. Like with bulk recombination this effect is exponentially linked to the bias voltage, but it can be much more significant unless properly dealt with. Surface passivation helps to reduce the number of crystalline defects on the surface of the solar cell, thereby reducing the severity of surface recombination.

A third area where recombination can occur is within the diode junction itself. Junction recombination affects electrons and holes that have not yet left the diode junction. As both charge carriers are quickly swept out of the junction, they both have similar charge carrier densities here, causing the recombination rate to be exponentially linked to half the bias voltage, making this effect more noticeable at lower voltages relative to the bulk and surface recombinations.

A fourth type of recombination that is frequently overlooked is edge recombination. At the edges of the solar cells, the diode junction overlaps with the surface crystalline defects. The presence of defect states within the diode junction, and the widening of the junction due to these defect states, leads to high rates of recombination exponentially proportional to less than half the bias voltage. As this effect can be greatly reduced by proper creation and passivation of the edges of the solar cell, it is often seen only in commercial solar cells, and overlooked in lab experiments.

Finally, it is important to recognize that ohmic recombination also occurs within the solar cells. The presence of aluminum or carbon impurities or disturbed crystalline states within the diode junction can result in resistive links between the two surfaces of the solar cell, leading to leakage currents within the solar cell.

A common electrical model for a solar cell consists of a current source together with several passive elements representing different loss mechanisms [130], shown in Fig. 2.10. Two diodes serve to short out the current source. The first, with a unity ideality factor, represents the bulk and surface recombination of the solar cell and their exponential dependence on the junction voltage. The second diode has an ideality factor of 2, and represents the junction and edge recombination. The ideality factor of 2 fits well for the junction recombination and its exponential dependence on half the voltage. As the edge recombination is typically exponentially dependent on less than half the voltage, an ideality factor higher than 2 would be preferable to represent this recombination, but for simplicity the two recombination types are typically combined and given a standardized ideality factor. Even simpler models often neglect this second diode altogether, as its effect on the solar cell performance is often negligible. Together, the effect of these two diodes is to sharply limit the output voltage of the solar cell. Voltages beyond 0.7 V are usually not achievable, as the diode current loss in the solar cell exceeds the photogenerated current.

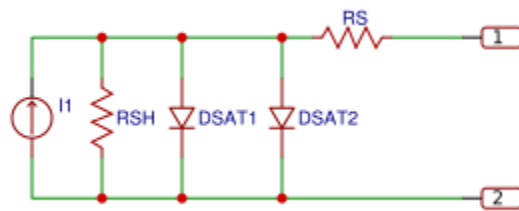


Fig. 2.10: A double-diode model of a solar cell, consisting of a current source, two diodes representing recombination losses, and two resistors representing ohmic losses.

Two resistors are also included in the conventional solar cell model. A shunt resistor in parallel with the current source and the diodes represents the leakage current across the diode junction. Meanwhile, a series resistor on the output of the solar cell represents resistance to lateral electron flow within the semiconductor to reach the contacts, as well as the resistance of the contacts themselves and any solder junctions coupling them into the system wires. Minimizing this resistance is critical to the performance of the solar cell, as even a very small resistance here can substantially reduce the already low output voltage of the solar cell.

The total equation for the current of a solar cell using the double diode model is

$$J_{PV} = I_{Opt} R_{\lambda} - J_{Sat1} \left( e^{\frac{q(V+J_{PV}R_S)}{k_B T}} - 1 \right) - J_{Sat2} \left( e^{\frac{q(V+J_{PV}R_S)}{n_d k_B T}} - 1 \right) - \frac{V + J_{PV} R_S}{R_{sh}}. \quad (2.2)$$

In this equation,  $J_{PV}$  is the photovoltaic current density, and  $V$  is the terminal voltage, which together determine the power output. The optical intensity is  $I_{Opt}$  and the spectral responsivity is  $R_{\lambda}$ , while the product of these two quantities is the photocurrent density,  $J_{PH}$ . The variables  $J_{Sat1}$  and  $J_{Sat2}$  are the first and second saturation current densities, and  $R_S$  and  $R_{sh}$  are the series and shunt area-related resistances (in units of  $\Omega\text{cm}^2$ ). The use of area-related resistance here reflects the fact that both ohmic shunt paths between the surfaces of the solar cell and ohmic series paths into the contacts are distributed over the entire surface of the solar cell, such that a given resistive element applies only to adjacent current-generating elements. This allows the resistances to be used directly with the current densities to calculate voltage. The junction temperature is  $T$ , Boltzmann's constant is  $k_B$ , and  $q$  is the electron charge, such that  $k_B T/q$  is the thermal voltage of the diode junction. The ideality constant for is  $n_d$  the second saturation current, which has been assumed to be equal to 2. Due to the fact that several of the phenomena detailed in this function link the photovoltaic current density and the terminal voltage, the function is implicit and cannot easily be solved analytically.

A typical solar cell current-voltage relationship is shown in Fig. 2.11. The presence of the diode-like losses gives this curve its distinct bent shape, with the diode currents tuning the exact shape of the elbow. Shunt resistance determines the slope of the curve to the left of the elbow, while series resistance determines the slope of the curve to the right of the elbow. The illumination on the solar cell shifts the curve vertically, directly determining the short-circuit current; in complete darkness, this would be zero.

The maximum power point is the point at which the power, the product of the current and voltage, is maximized. For optimal efficiency, the solar cell should be made to operate at this point, which is typically found near the elbow in the I-V curve. The quality of the solar cell can be estimated based on its fill factor, which is the ratio of the maximum power to the theoretically optimum power based on the product of the

open-circuit voltage and the short-circuit current. Lower series resistances and higher shunt resistances are typically indicated by an increase in fill factor.

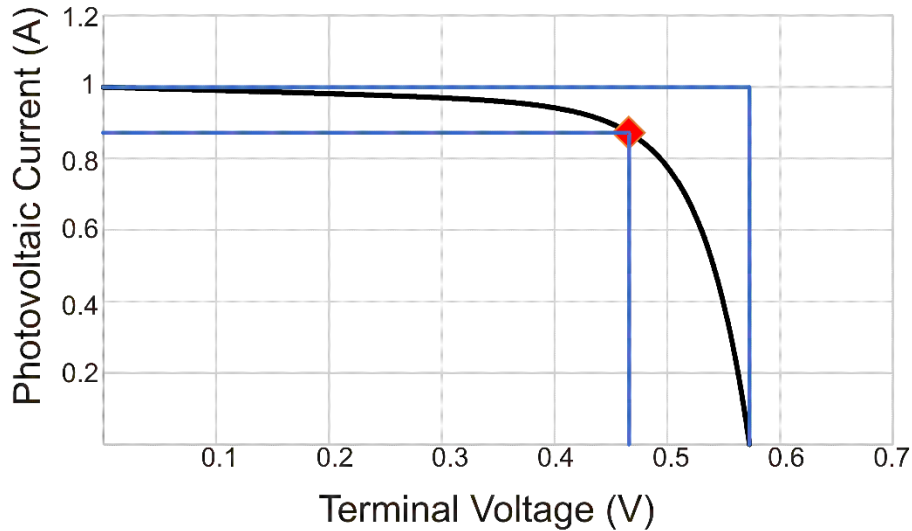


Fig. 2.11: A typical solar cell I/V curve. The maximum power point is marked with a red diamond, and the fill factor is the ratio between the areas of the two blue rectangles.

In large arrays, many solar cells must be connected together in order for substantial amounts of electricity to be generated. In an ideal case, every solar cell would have its own maximum power point tracker, and operate at its maximum power point. Practically, this is not possible due to the high cost of MPPT units. Instead, a large number of solar cells must be connected together and controlled by a single MPPT unit. These solar cells can be connected both in parallel and in series, with each option having its own challenges [58].

Parallel-connected solar cells are forced to all operate at the same voltage. In a perfect case, all of the solar cells in an array would have identical I/V curves, and this would not be a problem. However, manufacturing variations can cause the parameters of different solar cells, and thereby their I/V curves, to vary. More significantly, there is no guarantee that the illumination on two different parallel-connected solar cells will be identical. If two solar cells with significantly different illumination conditions are connected in parallel, it is possible for the more shadowed one to be forced past its open-circuit voltage, causing its total power

output to become negative. To counteract this, blocking diodes are typically added to parallel-connected solar cells in order to block any current that would flow through the cells in the reverse direction. Even with these diodes in place, further challenges arise from the effect that summing multiple I/V curves has on the maximum power point. In addition to the global maximum power point, a system of summed I/V curves can introduce local maximum power points that, despite supplying less power than the global maximum power point, could confuse an MPPT unit with a less-advanced tracking algorithm. Therefore, despite the justification that multiple solar cells in parallel allow the number of MPPT units needed to be reduced, more advanced MPPT units are also required in this case.

The use of solar cells in series can also generate similar effects, but in a way that can prove much more damaging to the solar cells. While overvoltage conditions caused by parallel connections with a highly-illuminated solar cell result in reverse current that is absorbed by the diode-like losses, overcurrent conditions caused by series connections with a highly-illuminated solar cell result in reverse voltage, an effect that causes high current flow through the shunt resistance of the solar cell. This carries a high risk of damaging the solar cell, and also creates a significant negative voltage across the solar cell, negatively affecting the output of the entire string of series-connected solar cells. Bypass diodes are used to avoid this case, allowing a path for current to bypass the solar cell if its generated current is not high enough. Like with parallel connections, series connections can result in local maximum power points, requiring the use of more sophisticated MPPT units.

A standard photovoltaic array consists of both parallel- and series-connected solar cells, often consisting of parallel-connected strings of series-connected cells. These are then connected to a MPPT unit, which algorithmically determines the maximum power point of the array and adjusts the array-facing impedance to match this. There may be a single MPPT unit for the entire array, or several units, with each controlling a smaller group of solar cells [131]. Fewer solar cells per MPPT unit may increase the cost of the array, but this approach also increases the performance of the array under uneven illumination conditions or partial

shading, and distributed electronics approaches are becoming commonplace even for smaller photovoltaic arrays.

Beyond the MPPT units, the generated electricity must be converted to a form that can be used by the desired load. Inverters, in the case of grid-connected systems, or charge controllers, in the case of battery-charging DC systems, are commonly used, and they may be found either integrated with the MPPT unit or as a separate piece of hardware. Collectively, the power conversion electronics typically are comparable with the cost of the photovoltaic modules.

For the evaluation of a 3DPV array, the exact details of these electronics are not needed, and the assumption can be made that their operation is ideal, collecting electricity exactly at the maximum power point, and retaining an efficiency of 100% in converting it to a load-useable form. Therefore, only the electronic performance of the solar cells themselves will need to be included in the models that will be developed in the subsequent chapters.

### 3: Preliminary Validation with a Simplified Simulation

This chapter serves to discuss the first simulation that was used to analyze the performance of solar generating arrays based on a value-centered metric, rather than a power-centered metric. The simulation, while simplified, can be used to investigate the viability of various array geometries under value-based metrics. Admittedly, it cannot be used to draw absolute conclusions on the performance of the arrays.

Commercial simulation software for photovoltaic arrays such as PVSyst and Aurora could potentially be used to perform this research. However, such software is intended for a drastically different purpose than what is performed here, and would not be adequate for this research. In particular, complex geometrical arrangements of solar cells are difficult to adequately model in commercial software, which is generally designed to model simple arrays. Additionally, commercial simulation software obfuscates a large quantity of the internal calculations, making it difficult to apply the power results to an accurately time-varying electricity value rather than a fixed sale price, and making it unclear how many of the solar generation properties of particular interest to this research are handled in the simulation. For these reasons, it was preferable to design a custom simulation for the purposes of this research.

The metric selected for optimization and results for this simulation is energy value density. This metric is defined as

$$Val_y = \int p(t) \mathcal{P}_{\text{gen}}(t) dt , \quad (3.1)$$

the integrated product of time-varying electricity price,  $p$ , in units of United States (US) dollars per watt-hour, and generated electrical power density,  $\mathcal{P}_{\text{gen}}$ , in units of watts per metre-squared. This serves as a simplified estimate of the economic value that can be collected by a given solar generating array for standard units of array area and time period. This metric was selected not as an economic indicator, but as a societal one. By incorporating time-dependent electricity price into the metric, both the total power generated by the array and how well this power temporally matches the daily electricity demand curve can

be evaluated with a single number. The ultimate implication of energy value density is that it can serve as an indicator of how well the array acts to reduce the electricity demand curve to zero, incorporating both the societal goal of eliminating the “Duck Curve” and related electricity supply fluctuations by flattening the demand curve, and the developer-driven goal of generating maximum profit using the solar generating array.

This chapter provides details on the simplified simulation and the results obtained from it. First, the solar generating arrays that are studied in both this and the next chapter are introduced. The details of the simulation, and the simplifications involved, are then discussed. Following this, the simulation results are shown and conclusions are drawn.

### 3.1: The Three-Dimensional Solar Generating Arrays

As beneficial as an exhaustive analysis of possible solar arrays would be, such an analysis is beyond the scope of this work. As such, it is necessary to select representative geometric solar arrays that will be compared. A geometric solar array is defined here as a 3DPV system that is intended to be horizontally extended to fill any available installation area. Four such arrays are chosen, including two well-established array types and two arrays that have the potential to generate significant amounts of electricity during the early-morning and late-evening hours, when electricity prices are significantly above average. This potential is based on the presence of east- and west-facing solar cells in the arrays. These solar cells will be nearly normal to incident light in the early-morning and late-evening hours, contrasted against south-, north-, and upward-facing solar cells, which would have steep angles of incidence in such a situation. Additionally, the presence of both east- and west-facing solar cells introduces the possibility for reflections off of solar cells facing in one direction to be incident on solar cells facing in the opposite direction.

The following subsections introduce the four geometric solar arrays that will be studied here, and present any optimizable parameters that can be adjusted to create different configurations of a given array.

### 3.1.1: The Flat-Panel Array

The Flat-Panel Array, shown in Fig. 3.1, is the simplest possible arrangement of solar cells, and it is used here as a benchmark. It is a planar array of solar cells, each with a side-length of  $a$ . The flat-panel array lies within the horizontal plane with its surface normal directed up. This geometric solar array is the only possible infinitely scalable array that completely averts the possibility of inter-solar-cell shadowing, but conversely, it is the only array that completely eliminates any chance of capturing reflections. As such, it serves as a simple basis for comparison for the other three arrays, and in fact acts as a degenerate case of each of them, as will be shown in the following subsections. Unlike the following three arrays, the Flat-Panel Array has no optimizable parameters that could result in varying configurations, and all such arrays will be identical in terms of theoretical performance.

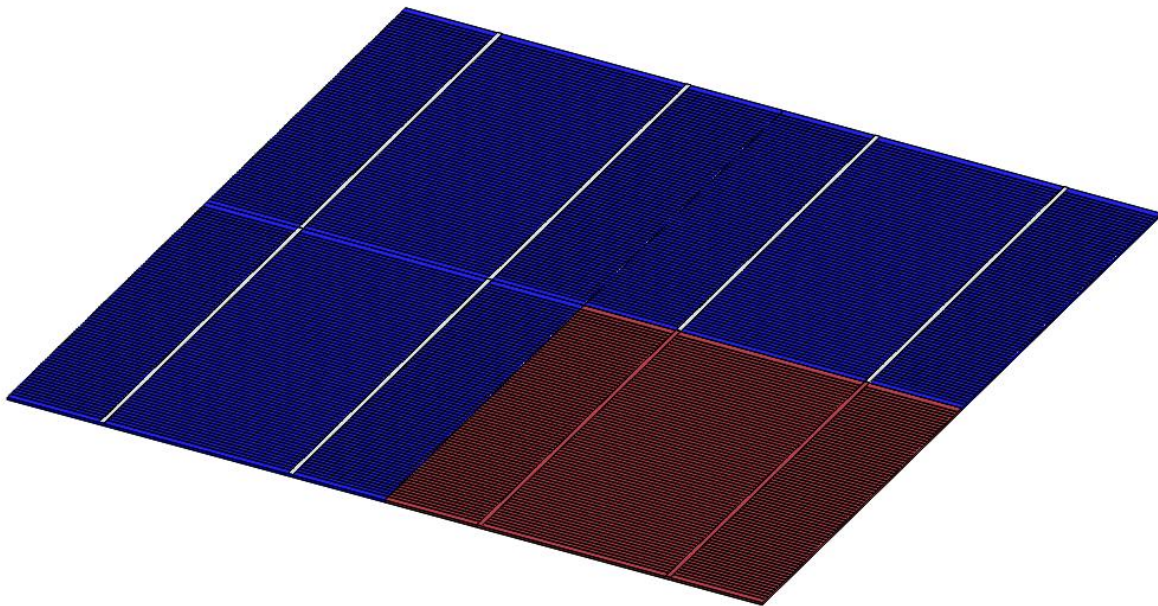


Fig. 3.1: A diagram demonstrating the Flat-Panel Array. A unit cell of the array is shown highlighted in red.

### 3.1.2: The Angled-Panel Array

The Angled-Panel Array, shown in Fig. 3.2, is the second array to be investigated in this study. This array represents the current state-of-the-art in stationary geometric solar arrays. In this array, solar cells are

arranged in rows tilted at an angle from horizontal and oriented to all face in the same direction. Such an arrangement retains a fairly simple structure, but allows sunlight in the middle of the day to be more directly incident on the solar cells due to their tilt. This improvement must then be balanced and optimized against the power losses inherent in each row of solar cells potentially shadowing the row behind it. While the fact that all solar cells face in the same direction precludes the possibility of direct reflections of light between solar cells, diffuse light can still be reflected off the back of an opposing row of solar cells or the ground between rows and illuminate the solar cells.

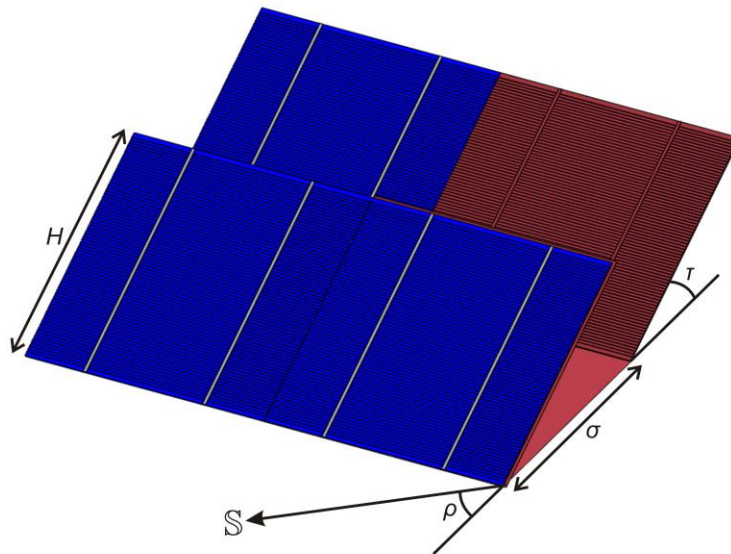


Fig. 3.2: A diagram demonstrating the Angled-Panel Array, with its four geometrical parameters illustrated. The south direction is indicated by  $S$ . A unit cell of the array, which includes the non-photovoltaic back side of the front solar cell, is shown highlighted in red.

Despite, or more accurately due to, its simplicity, the Angled-Panel Array has the highest number of optimizable parameters of any of the geometric solar arrays studied here. The tilt angle of the solar cells,  $\tau_{AP}$ , determines the angle between the solar cells and the ground, while the rotation angle,  $\rho_{AP}$ , determines their orientation with respect to a reference direction, which is selected to be south to match the convention used for azimuth direction in this thesis. The spacing,  $\sigma_{AP}$ , refers to the distance separating the lines of

contact between two adjacent rows of the solar cell and the ground, and the height,  $H_{AP}$ , determines the height of each row. In the case where  $\tau_{AP} = 0$  and  $\sigma_{AP} = H_{AP}$ , the array will be identical to a Flat-Panel Array.

The inclusion of spacing and height as two separate parameters raises an interesting point. At first glance these two parameters could be combined into a single one denoting the ratio between them, the aspect ratio  $N_{AP} = H_{AP}/\sigma_{AP}$ . However, it should be noted that due to the presence of external electronics, particularly blocking and bypass diodes, two adjacent solar cells do not behave identically to a single larger solar cell with the same area. In order to separate this effect from other array properties, it may be beneficial to use the aspect ratio as an optimizable parameter and to incorporate the additional degree of design freedom into a new parameter, the scaling factor, defined as  $S_{AP} = H_{AP}/a$ .

The possible values for the tilt angle range from 0 to  $\pi$  rad, although values larger than  $\pi/2$  rad are unlikely, as such values would have the solar panels pointed downward. The rotation angle can be in any direction, and for the purpose of this analysis, values between  $-\pi$  and  $\pi$  rad will be used. The spacing can be any positive number, and leads to the limiting case of a single, standalone row of solar cells as it approaches infinity. The height, similarly, can be any positive number, although it is restricted to integer multiples of the solar cell side length to avoid using partial solar cells in the design. Restrictions on the derived parameters can be easily obtained from these: the aspect ratio can be any positive number, while the scaling factor can be any positive integer.

With four degrees of freedom in its design, it is clear that optimization of the Angled-Panel Array is a non-trivial task. Due to this, and due to the fact that the purpose of the simplified simulation is to investigate the theoretical viability of the arrays, while the Angled-Panel Array is a widely-used geometric solar array whose viability can be assumed without the need for additional validation, this array will be neglected from the remainder of this chapter, and will be investigated exclusively in the following one. In that chapter, it will be shown that this decision was in fact necessary for additional reasons, as under the conditions presented with the simplified simulation, an optimized Angled-Panel Array degenerates into a Flat-Panel Array.

### 3.1.3: The V-Groove Array

The V-Groove Array, while not commonly used, has been studied extensively. The array, shown in Fig. 3.3, is a corrugated structure that is made up of discrete numbers of silicon solar cells with a side-length of  $a$  arranged into V-shaped grooves. The majority of investigations into the V-Groove Array focus on its ability to capture increased amounts of midday sunlight, due to promoting reflections of light off one solar cell and onto the adjacent one, as well as the ability to leverage this property to create tandem solar cells that combine two different bandgaps, but do not require the additional design complexity of stacking solar cell junctions that is inherent in multijunction solar cells. The interest in the V-Groove Array in this work, however, is due to a different property. As the array includes tilted solar cells facing in two opposing directions, it meets the conditions for improved low-angle performance laid out earlier, and may provide an example of an established solar array geometry that demonstrates increased potential to counteract the “Duck Curve” problem.

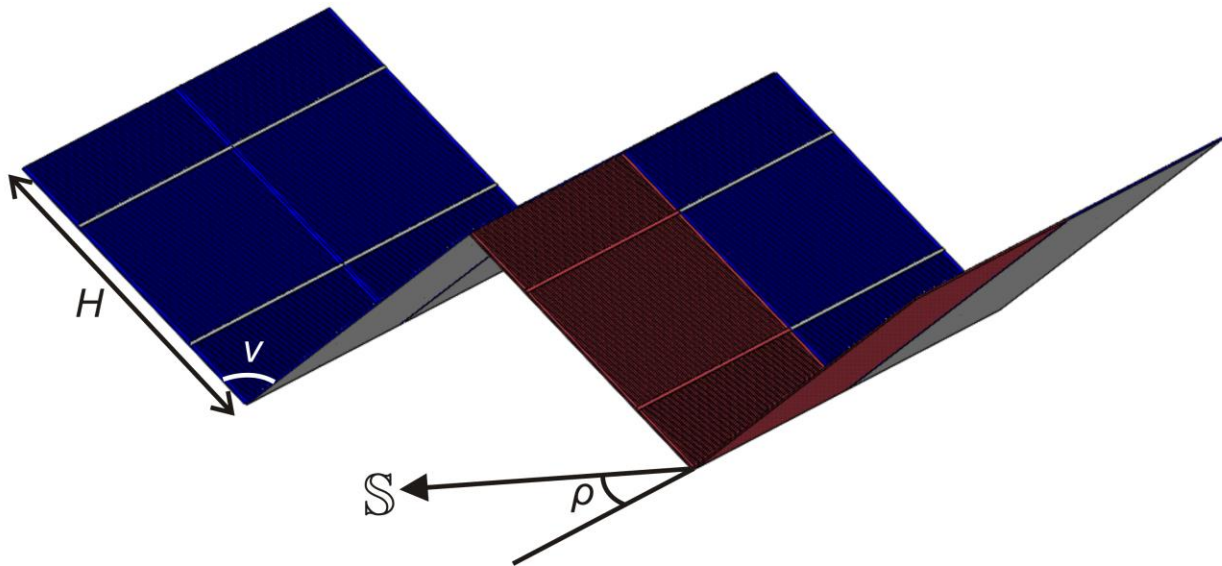


Fig. 3.3: A diagram demonstrating the V-Groove Array, with its three geometrical parameters illustrated. A unit cell of the array is shown highlighted in red.

The key design parameter for the V-Groove Array is the V-angle,  $v_{VG}$ , being the internal angle between the sides of the grooves. Additionally, the V-Groove Array has a rotation angle,  $\rho_{VG}$ , and a scaling factor,  $S_{VG}$ ,

analogous to those discussed with regards to the Angled-Panel Array. Due to the differing nature of intended operation, where the angled panels are intended to face and capture the late-day sun rather than the midday sun, however, the rotation angle is defined slightly differently here, being the separation between the south direction and the direction vector along the rows of solar cells, rather than the one across them. As with the Angled-Panel Array, the scale can also be specified by a different parameter, the height  $H_{VG} = S_{VG} \times a$ .

The V-angle is restricted to values between 0 and  $\pi$  rad, with the former representing the vertical solar cells being perfectly adjacent, and the latter representing degeneration into a Flat-Panel Array. The rotation angle can again have any value; however, due to the rotational symmetry of this array, this value can be further restricted without affecting the results. The rotation angle is therefore chosen to be between  $-\pi/2$  and  $\pi/2$  rad. Similarly to the Angled-Panel Array, the height is restricted to positive integer multiples of the solar cell side length, and the scaling factor is restricted to positive integers.

#### 3.1.4: The U-Groove Array

The U-Groove Array, shown in Fig. 3.4, consists of a planar array of solar cells, on top of which run vertical walls of double-sided solar cells. Such a structure forms U-shaped grooves. This array was designed as part of this research specifically to address the “Duck Curve” problem. Although similar structures consisting of orthogonal cells exist, a semi-infinite linear structure with a flat base is novel to this research. The flat bottom of the array allows for continued performance in high-angled light conditions, while the vertical walls serve as light-trapping mechanisms in the low-angle morning and evening conditions. In such conditions, the opposing solar cells not only face into the sunlight, as with the V-Groove Array, but their perpendicular nature allows for the trapping of reflected light between them, with the number of reflections undergone by any incident light before it reflects off the bottom and exits the array increasing without bound as the angle of incidence becomes closer to horizontal.

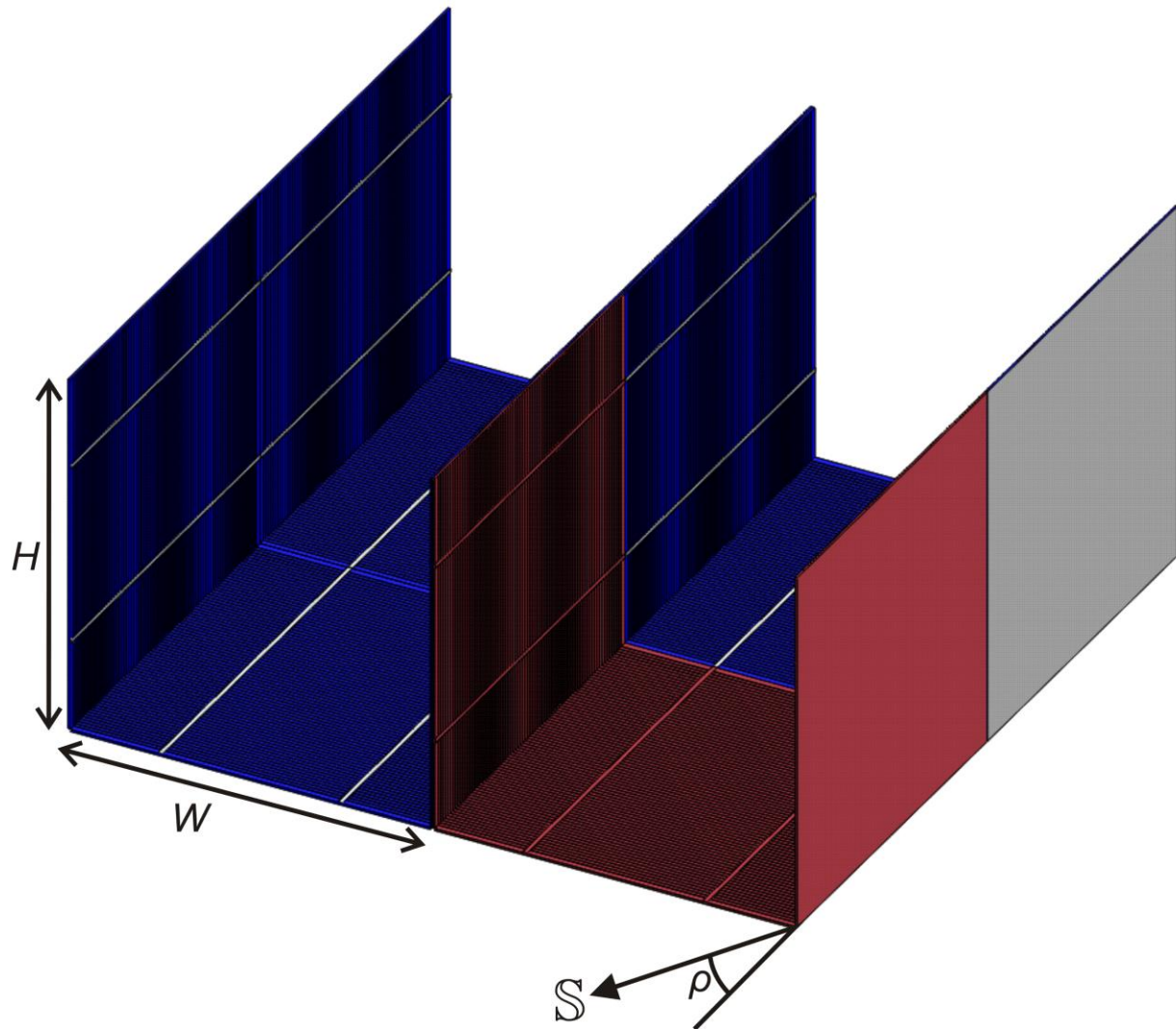


Fig. 3.4: A diagram demonstrating the U-Groove Array, with its three geometrical parameters illustrated. A unit cell of the array is shown highlighted in red.

The key design parameter for the U-Groove Array is the aspect ratio,  $N_{UG}$ . As with the Angled-Panel Array, it is defined as the ratio between the height of the walls and their spacing. A larger aspect ratio results in taller, more closely-spaced walls that are more effective at low-angle light trapping, but do not contribute to the array performance during the day. It is worth noting that the aspect ratio is restricted by the necessity for both the height and spacing of the walls to be whole-number multiples of the solar cell side length. While the height is self-evident, the restriction on the spacing is essentially a design choice. While solar cells extending under the walls would be possible, the non-zero thickness of the walls would result in a

wasted area of the solar cell that could never be illuminated. Additionally, such an approach would greatly extend the size of a unit cell needed for analysis, as will be explained in the following section.

Similarly to the previously-described arrays, the U-Groove Array also has a scale parameter,  $S_{UG}$ , which is defined as the number of solar cells arranged vertically in the walls, and a rotation angle,  $\rho_{UG}$ , which is defined as the angle separating the direction along the walls from the south direction. It is also possible to replace the aspect ratio and scale parameters with height and spacing, similar to the alternate interpretation available for the Angled-Panel Array, where  $H_{UG} = S_{UG} \times a$  and  $\sigma_{UG} = S_{UG} \times a / N_{UG}$ .

The rotation angle can take on any value, and due to this array having identical rotational symmetry to the V-Groove Array, this value can be restricted to between  $-\pi/2$  and  $\pi/2$  rad. The scaling factor can be any positive integer, while both the height and spacing can be any positive multiple of the solar cell side length. Restrictions on the aspect ratio are slightly more complicated here; it can be the ratio of any two positive integers, with the additional stipulation that the integer in the numerator is equal to the scaling factor. The U-Groove Array degenerates into a Flat-Panel array in the case where the aspect ratio approaches 0 or the spacing approaches infinity. Note that this degeneration is much more theoretical than for the other arrays: Practical concerns would restrict the array long before it could reach an infinite spacing between the walls.

### 3.1.5: Practical Implementation of the Arrays

With the arrays and their associated parameters defined, it is a good idea to discuss how they will be practically implemented for the purposes of this analysis.

The size of the array itself is necessary to consider for any detailed analysis, as solar cells near the edge can be subject to different shadows and reflections than those near the middle. As an example, the shadow cast by one wall of a U-Groove Array on the opposing wall is perfectly linear along the directions of the walls except at one end of the array, where the shadow will have a corner, allowing more light to enter the array than normally would. For the purposes of this study, it is assumed that such end effects are negligible on all arrays studied here, and can therefore be ignored. This is a reasonable assumption so long as the array

size is large relative to the size of the array geometry, and light does not enter the array at low angles along the direction of the corrugation. For U- and V-groove Arrays with small values of  $\rho$ , such a circumstance would correspond to the sun being low in the north or south sky, a condition that occurs only at extreme latitudes. In these locations, solar electricity generation is less viable to begin with, reducing the risk of high solar penetration and making them unfavourable candidates for this study.

The site used for the array is therefore also important to consider. Obviously, when the goal is to capture high-value low-angle light in the morning and evening, obstructions that block the horizon would be detrimental to any such array, regardless of its geometry. These arrays are therefore intended for use in open areas: fields, deserts, hilltops, and rooftops would all be suitable locations. However, it is also important to consider the implications of the selected metric when making this decision. This first simulation is optimized based on energy value density, which is per unit area. As the value generated is being optimized per unit area, this simulation does not apply well to sites where the area can be expanded with little marginal cost, i.e., fields and deserts. It can therefore be said that the intended site for these arrays, as optimized in the simplified simulation, is elevated sites with limited space, such as rooftops and hills.

This choice of locations leads to a solution to what would otherwise be a challenging issue to address. In general, optimization of these arrays is complicated by the fact that an array with a larger scaling factor will always outperform an array with a smaller scaling factor. As the optimization metric is in terms of unit area, and idealized simplifications such as the lack of end effect are in place, the actual size of the features that compose the solar array should not matter in most cases. However, the number of solar cells that make up these features definitely does matter, due to the influence of blocking diodes. Any solar cell that would not generate electricity is disconnected from the circuit, and the more solar cells there are per feature, the more selectively this property can remove the losses associated with shaded areas of the feature from the circuit. Given this property, larger structures should always have better performance.

Obviously, there are tradeoffs that prevent an infinitely large array from being used. The challenge here arises from the fact that these tradeoffs are non-quantifiable and largely dependent on the specific installation. Doubling the array size doubles the number of parallel strings of solar cells with blocking diodes that would be required, increasing the array complexity. A larger scale also requires a larger array area in order to minimize non-ideal effects. However, perhaps the most important effect is the implications of increasing the height of the array. A taller array would require a more complex support structure, which would increase the cost, and in the case of thin features such as the U-Groove Array's walls, reduce the ability of the practical array to match an idealized geometry. In addition, a taller array would be more susceptible to wind loading and would be at an increased risk of damage during storms.

The selection of an elevated location for this array provides a strong justification for limiting the scaling factor of the arrays involved, due to the fact that such a location with unrestricted horizon views is likely to experience particularly strong winds [132]. Wind loading will quickly become a problem for any tall arrays in this situation, and the support structures necessary to offset this problem would increase rapidly in complexity and cost as the height increases. For this reason, the decision was made to fix the scaling factor at  $S = 1$  for all arrays in this simulation. This restricts the height of all arrays to be at most a single solar cell. The argument can be made that a realistic implementation is more likely to use one solar panel as the height, rather than one solar cell, and a fixed value of  $S$  around 10 might be more realistic. However, such a decision would greatly increase the number of solar cells per unit cell, and therefore the time and complexity of the simulation necessary. It will therefore be assumed that the scaling applies similarly to all arrays, with the obvious exception of the Flat-Panel Array, and therefore the results obtained with  $S = 1$  would be equally valid at  $S = 10$ .

The location of the arrays in a more general sense must also be considered, as the latitude and longitude of the site determine the path of the sun through the sky throughout the day. The primary area of interest for this study is the state of California, as the high amounts of solar generation already installed there lead to a prominent and widely-discussed "Duck Curve" phenomenon. For the simplified analysis, a central location

within the state that is located at the intersection of lines of latitude and longitude will be an adequate estimate. The selected location is 37°N, 120°W, near the city of Fresno.

As previously mentioned, the electrical components used to connect the solar cells to the grid are assumed to be ideal for the purpose of this simulation. Given the assumptions of negligible end effect and unobstructed horizons, all solar cells within a single row in the direction of the grooves for the V-Groove Array and U-Groove Array will have identical I/V curves. For this reason, these cells can be connected in a series chain without expected losses, and the use of bypass diodes on each solar cell would not have any effect. Obviously, in a realistic scenario these assumptions would not be entirely accurate, and other non-idealities such as partial cloud cover and manufacturing variations could cause different solar cells within the same row to have vastly differing I/V curves, so the use of these diodes in a practical installation would still be required.

Each of these strings of solar cells would require a blocking diode to disconnect any strings that are not generating power, and the strings can then be joined in parallel and connected through a single Maximum Power Point Tracking (MPPT) unit to the load. The MPPT unit carries out impedance matching between the solar cells and load to maximize the transfer of electrical power. The use of a single MPPT unit for each array is a subtle – but potentially important – point for the arrays. This is because the individual strings of solar cells within the V-Groove and U-Groove Arrays will often capture differing levels of optical power throughout the course of a day. Each string would therefore have a different ideal impedance at which it would generate maximum power. In order to take advantage of this, each string of solar cells would have its own MPPT unit here, in a manner similar to a microinverter system (where each solar panel has a unique MPPT unit). Microinverter systems are generally more cost-efficient than a single large inverter, even without the expected variation between strings of solar cells that would be seen in this array [131]. A single inverter was nonetheless used here, as such an implementation would simplify the theoretical installation of the more complex arrays, and similar research has found the improvements in generated power from cell-orientation-based microinverters to be negligible [78].

For the purpose of analysis, it is useful to identify the section of an array that will be studied. The unit cell of a geometric solar array is defined here as the smallest section of the array that contains only whole solar cells, and can be used to build the entire array through only translations within the horizontal plane. Even with these restrictions, it is possible to identify several different unit cells for each array. Figures 3.1-3.4 demonstrate the unit cells selected for use with each array. These unit cells were selected in order to optimally contain reflections within the unit cells. Note that the Angled-Panel Array unit cell includes the (non-photovoltaic) backing of the adjacent row and intermediate ground; these were included to simplify the calculation of diffuse light in chapter 4 of this thesis.

With the unit cells selected, it is possible to define the area of each unit cell, both the installation area and the area of solar cells necessary, in terms of the array parameters. These equations will be useful for determining the cost of the solar arrays later, and are summarized here in Table 3.1.

Table 3.1: The formulas for unit cell installation area and silicon area for each of the four geometric solar arrays.

<b>Array</b>	<b>Installation Area</b>	<b>Silicon Area</b>
Flat-Panel Array	$a^2$	$a^2$
Angled-Panel Array	$a\sigma_{AP} = a^2 S_{AP}/N_{AP}$	$aH_{AP} = a^2 S_{AP}$
V-Groove Array	$2aH_{VG}\sin(\nu_{VG}/2) = 2a^2 S_{VG}\sin(\nu_{VG}/2)$	$2aH_{VG} = 2a^2 S_{VG}$
U-Groove Array	$a\sigma_{UG} = a^2 S_{UG}/N_{UG}$	$a(\sigma_{UG} + 2H_{UG}) = a^2 S_{UG}(2 + 1/N_{UG})$

Several assumptions that will be used in the development of this simulation have therefore been defined surrounding how the arrays will be practically implemented. The solar arrays are assumed to be in a location with limited available area and unobstructed horizons, such as a rooftop, and the location is chosen to be at coordinates of 37°N, 120°W. The installation area is assumed to be sufficiently large relative to the feature size that the effects of the array edges are negligible. The arrays are restricted to have a maximum height of one solar cell, and the smallest tileable area or unit cell is selected for analysis, to reduce the complexity of the simulation. The solar cells are assumed to be connected in series along the linear direction of each array, such that all solar cells with comparable orientation and position are in series, and all strings are

connected together in parallel to a single MPPT unit. These assumptions together make the arrays possible to simulate, while remaining relatively realistic.

## 3.2: Design of the Simplified Simulation

As the purpose of the simplified simulation was merely validation of economic viability of each array, the use of a highly-accurate and detailed simulation for this stage was avoided in favour of a simplified simulation reliant on aggregate quantities for the light involved, in the interest of reducing both design and simulation time. This section examines the details of this simplified simulation, including the assumptions that were made in its creation.

### 3.2.1: Energy Value Density and Electricity Price

An ideal place to start the analysis of this simulation would be with its metric of optimization, the energy value density. As mentioned previously, this metric is the product of generated electrical power density and time-varying electricity price. The majority of this simulation is dedicated to the derivation of the generated electrical power density. This section will therefore elaborate on the source of the other quantity, the time-varying electricity price.

As previously mentioned, the state of California is selected for the location, given its heavy reliance on solar power generation and its growing concern for the “Duck Curve”. Historical electricity price data for California is freely available from the California Independent System Operator (CAISO) through their Open Access Same-Time Information System (OASIS) [98]. For this study, the prices used are derived from the day-ahead locational marginal pricing, which is an hourly estimate of the value of an additional unit of electricity, as estimated a day in advance. As explained in section 2.1.4, an electricity pricing this volatile is rarely used in actual power purchase agreements, due to the understandable risk to the supplier, although it may be used to derive the power purchase agreement price, and to determine the economic benefits of larger electricity purchases. Nonetheless, this pricing will be used directly in this simulation, due to the

need for a more temporally-accurate electricity price in order to adequately assess the societal benefits of the arrays.

The electricity prices were collected from OASIS for locations across California at one hour intervals for a period of six years starting July 1, 2012, and then averaged over all locations, while treating negative prices as zero. This is due to the fact that a sufficiently intelligent grid-connected system would be capable of simply disconnecting from the grid under circumstances where generation would result in losses rather than profits. Although this scenario is unrealistic, due to the aforementioned use of more averaged electricity prices in realistic power purchase agreements, it does coincide well with the actual practice of curtailment, whereby photovoltaic generation is required to shut down during periods of surplus grid power in order to prevent supply from exceeding demand. Examples of the daily electricity price trends found in this data can be seen in Appendix A.

The average was then time-interpolated with the hourly prices taken as the midpoint of each hour to establish a net electricity price for California at two-minute intervals. The intervals were selected to be on odd-numbered minutes, rather than even-numbered ones. This is due to the fact that when summing these data points to produce daily energy value densities, it is simpler for the 12:00 AM transition point between days to be in between data points, rather than directly on a data point that must then be split between the two days.

### 3.2.2: Setup of the Simplified Simulation

The second factor needed to calculate the energy value density is the time-varying generated electrical power per unit area. The generated electrical power is calculated in this simulation using experimental characterizations of a typical square silicon solar cell, having a side-length of approximately  $a = 78$  mm, and the application of these characterizations to an analytical model of the solar arrays. The motivation for this tandem experimental-theoretical approach rather than a fully experimental one is twofold. First, it becomes possible to characterize the performance of arrays with a wide range of geometries and

illumination conditions. Second, it becomes possible to characterize the performance of arrays in terms of their captured, incident, and reflected optical powers—with knowledge of contributions from internal reflections. Such knowledge cannot be gained when the electrical output power alone is measured. The generated electrical power density is defined as a density with respect to the installation area because the generated electrical powers of the arrays scale in proportion to this area.

The generated electrical power density is calculated for the changing illumination conditions over the course of a day. The incident sunlight is defined in terms of an azimuth angle with respect to south,  $\phi$ , and a zenith angle,  $\theta$ , as shown in Fig. 3.5 on a Cartesian coordinate system. The coordinate system has its  $x$ -direction aligned with south, its  $y$ -direction aligned with east, and its  $z$ -direction aligned vertically, upwards. This simplified simulation will not vary the rotation angle,  $\rho$ , for the V-Groove Array and U-Groove Array, as will be discussed later, meaning that the Cartesian coordinate system will also be aligned with the arrays themselves. The direct solar irradiance is defined by a magnitude of  $I_0$  and an incident ray (unit) vector of  $(\alpha, \beta, \gamma)$ . The directional cosines within the ray vector are linked to the azimuth and zenith angles by

$$\alpha = \cos \phi \sin \theta, \quad (3.2)$$

$$\beta = \sin \phi \sin \theta, \quad (3.3)$$

$$\gamma = \cos \theta. \quad (3.4)$$

Given these definitions, the generated electrical power density can be analyzed for varying illumination conditions of the three geometric solar arrays studied in this analysis.

In order to reduce the complexity of this simulation, several additional simplifications will need to be performed. The most notable of these is the reduction of incident sunlight to aggregate quantities. This is to say that all light within the simulation will be treated as monochromatic and unpolarized. Additionally,

diffuse light will be neglected entirely, due to the additional complexity that arises from calculating light paths for diffuse light.

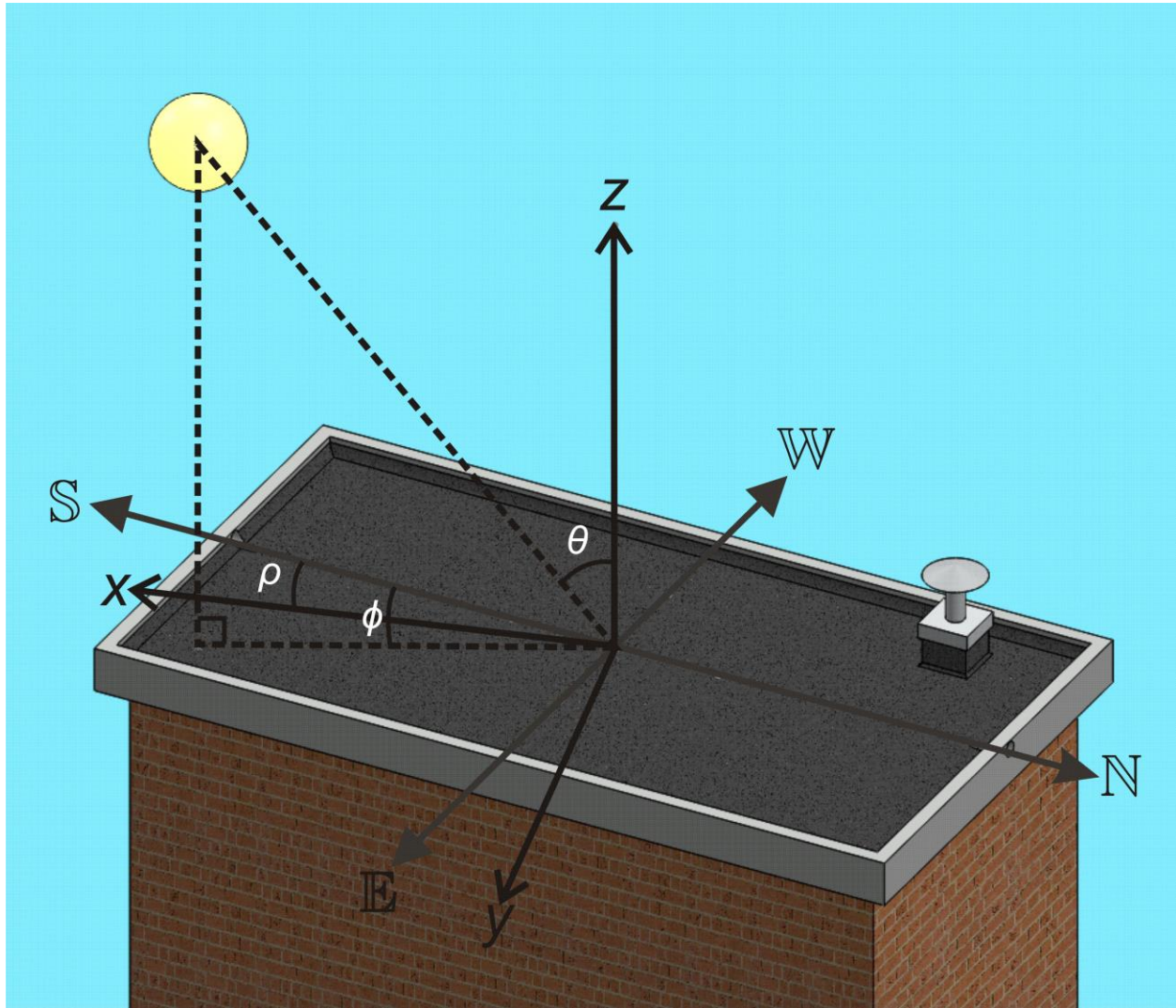


Fig. 3.5: A diagram of the coordinate systems used in this analysis. The Cartesian coordinate system is shown offset from the cardinal directions by the rotation angle,  $\rho$ , and the sun's position is referenced to the cardinal directions through the zenith angle,  $\theta$ , and the azimuth angle,  $\phi$ . The size and location of the sun are not to scale.

### 3.2.3: Experimental Characterizations

In order to provide more accurate results, the design of the first simulation incorporates experimental characterizations, to identify the key parameters of the solar cells used within the three solar arrays, and an

analytical model of the three arrays, to define their performance. The experimental characterizations are presented in this section.

### 3.2.3.1: Preparation of Solar Cells for Experimental Testing

In order for these experimental characterizations to be performed, it is necessary to select a solar cell. For the purpose of this study, TG Solar 18% efficiency monocrystalline silicon solar cells with an area of 3 x 3 inches were selected. SEM images were taken of this solar cell, and are shown in Fig. 3.6-3.7.

Fig. 3.6 shows a close-up image of the solar cell, including one of the conductive metal fingers. The diamond-shaped pattern across the solar cell surface is indicative of alkaline-etched surface texturing, which results in inverted four-sided pyramids of uniform orientation but random position and size.

Fig. 3.7 shows a cross-section of the solar cell. The front fingers and back planar contact are both clearly visible, as is the bulk silicon, and a close-up shows a more detailed view of the pyramidal texturing. Energy dispersive spectrometry (EDS) of the location confirms that the front fingers are silver, while the back contact is aluminum. Unfortunately, analysis of the finer solar cell features is not possible. The dopant density within the bulk silicon is too low to accurately identify and measure the diode junction. Although the blue coloration of the solar cell proves the existence of a front-side anti-reflective coating, this layer could not be directly observed in the images or the EDS captures. Similarly, any back-side passivation layer could not be detected, although the relatively high expected efficiency of 18% would be unlikely if this layer did not exist. The absence of these layers from EDS analysis is, however, understandable, as their expected composition (silicon nitride and aluminum oxide respectively) differs from adjacent layers only through the addition of nitrogen or oxygen, and the low mass of atoms of these elements means that they are unlikely to be accurately detected through EDS analysis.

For these experimental solar cells to adequately match the standardized solar cell design proposed in section 2.2, it was necessary to apply some further modifications to them. Firstly, tab wire was added to the front-side bus bars to allow them to still make electrical contact after the front of the solar cell was covered. The

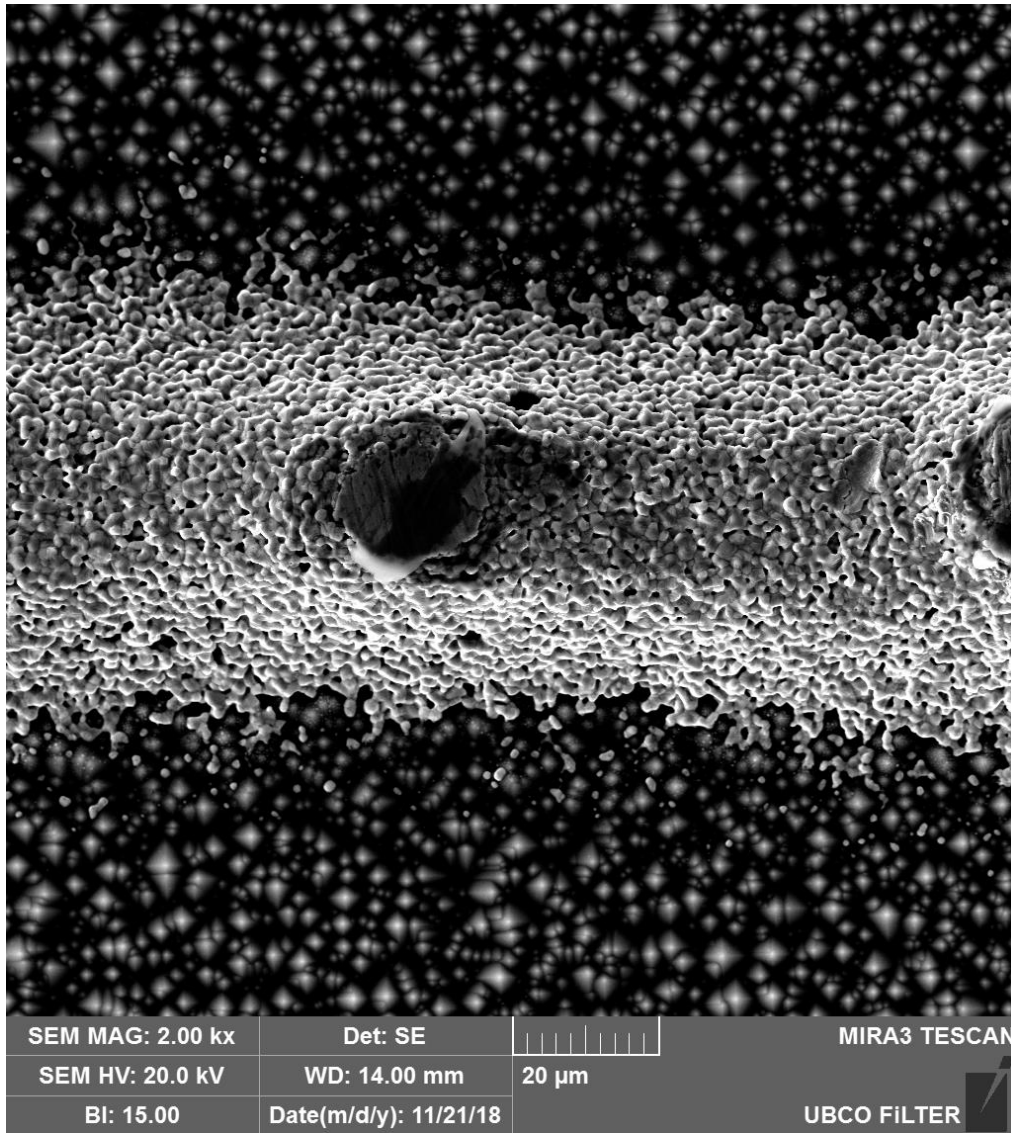


Fig. 3.6: An SEM image of the front of the selected solar cells. A silver finger contact is shown running across the middle of the image. The irregular diamond-shaped patterning, on the order of a few microns in size, is inverted pyramid microtexturing, characteristic of alkaline etch texturing on a monocrystalline silicon substrate.

tab wire used was composed of a lead/tin alloy and was attached using ChipQuik SMDLTLFP solder paste on a hot plate, so as to minimize thermal damage to the solar cell that might occur with traditional soldering. Additionally, encapsulant and protective layers needed to be added to the front of the solar cell due to their effect on the optical performance of the solar cell. Squares of 3 mm thick low-iron glass were selected as a protective layer, and EVA film intended for photovoltaics was selected as an encapsulant layer. The EVA

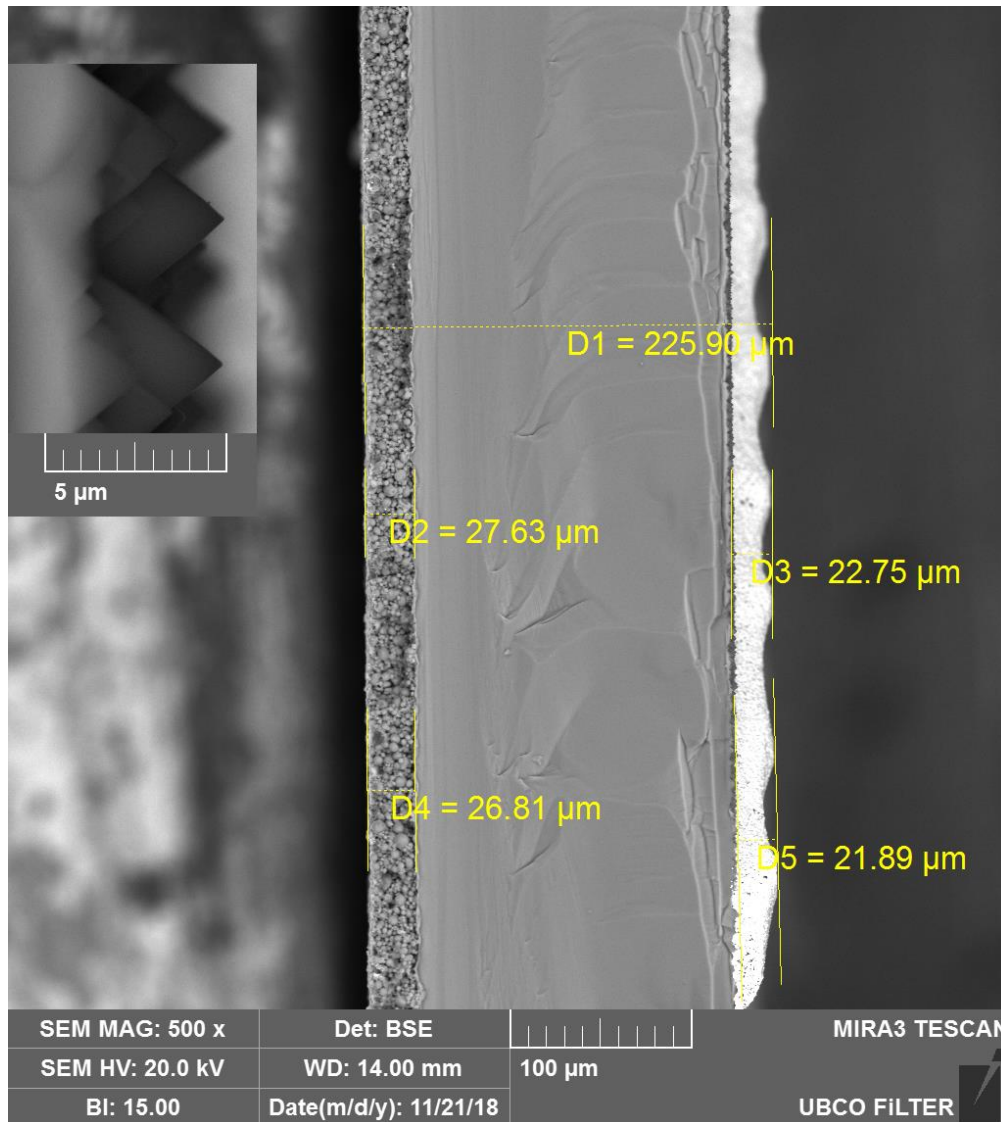


Fig. 3.7: A cross-section SEM capture of the solar cell, with certain thicknesses indicated. The irregularly-patterned layer to the left is the aluminum back contact, while the white-coloured layer to the right is a silver finger front contact, which is out of focus in the upper half of the capture due to lying behind the fractured edge. The inset in the upper left shows detail of the front surface texturing. Lines within the bulk silicon are angles formed during fracturing, and likely do not represent differences in composition.

film needed to be heat-cured in order to become optically transparent, and in order to bond the glass layer to the solar cell. After several trial attempts, optimal clarity with minimum bubbles was obtained by placing the solar cell/EVA/glass assembly in a vacuum oven with weight applied to the top to remove the air from between the layers, applying the vacuum first and then heating the solar cells to approximately 150 °C. A completed solar cell using this method is shown in Fig. 3.8, along with the materials used in its fabrication.

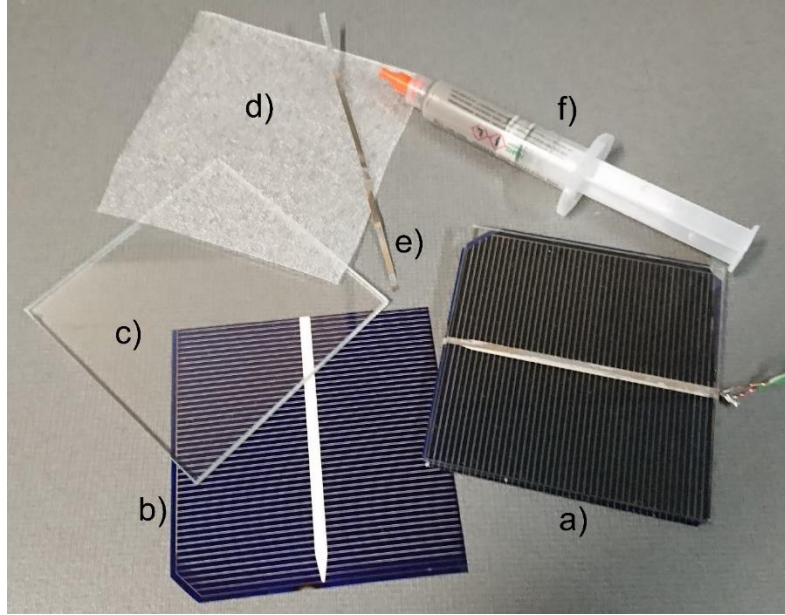


Fig. 3.8: An image showing a fabricated (a) solar cell together with the components used in its fabrication: b) An unmodified solar cell, c) a square of low-iron glass, d) a square of EVA film, e) a section of lead/tin tab wire, f) a tube of solder paste. Note the darker colouration of the final solar cell, indicating that encapsulation has improved the performance of the anti-reflection coating.

### 3.2.3.2: Experimental Derivation of Solar Cell Parameters

The reflectance is the first parameter that needs to be defined for the solar cells – although its generalized understanding presents a challenge. As previously mentioned, there are two primary sources of reflection in the solar cells used for this thesis: the reflection off the glass-air interface, and the reflection off the air-silicon interface. Notably, the air-silicon interface is textured, and therefore exhibits a reflectance better approximated as diffuse. As this simplified simulation ignores diffuse light, this reflection can therefore also be ignored. As such, it is assumed in this simplified simulation that the reflective properties of the solar cell are defined by specular reflection off the glass layer and negligible reflection from the underlying textured surface. With this in mind, the specular reflectance of a solar cell with a protective layer of tempered glass was measured with a 650 nm laser beam at near-normal incidence. It was found to be 3.96%.

The reflectance is applied to the analytical model by defining an effective refractive index of

$$n_{\text{eff}} = \frac{10 + \sqrt{3.96}}{10 - \sqrt{3.96}} \approx 1.497 . \quad (3.5)$$

This value is very close to the established value for the refractive index of low-iron glass at this wavelength, shown in Fig. 2.6 as 1.503. As the refractive index of glass across the visible spectrum has minimal wavelength-dependence,  $n_{\text{eff}}$  can therefore be used as the refractive index for aggregate monochromatic light in glass for this simulation, resulting in a corresponding angular-dependent reflectance for unpolarized light of

$$R(\theta_i) = \frac{1}{2} \left( \frac{\cos \theta_i - \sqrt{n_{\text{eff}}^2 - \sin^2 \theta_i}}{\cos \theta_i + \sqrt{n_{\text{eff}}^2 - \sin^2 \theta_i}} \right)^2 + \frac{1}{2} \left( \frac{\sqrt{n_{\text{eff}}^2 - \sin^2 \theta_i} - n_{\text{eff}}^2 \cos \theta_i}{\sqrt{n_{\text{eff}}^2 - \sin^2 \theta_i} + n_{\text{eff}}^2 \cos \theta_i} \right)^2, \quad (3.6)$$

where  $\theta_i$  is the angle of incidence of light on the solar cell, as measured off its surface normal.

For the purpose of the solar cell parameters themselves, it is necessary to define an electrical model for the solar cells. The double-diode solar cell model from section 2.2.3 will be used as a base, but it will be simplified to a single-diode model by taking the second saturation current to be zero. Additionally, resistive ideality will be assumed, such that the shunt resistance is infinite and the series resistance is zero. The resulting simplified equation is

$$J_{\text{PV}} = I_{\text{Opt}} R_{\lambda} - J_{\text{Sat1}} \left( e^{\frac{qV}{k_B T}} - 1 \right). \quad (3.7)$$

The simplification of this equation makes it explicit, and therefore much easier to solve. It is also apparent that two solar cell parameters remain in the equation that must be defined:  $R_{\lambda}$  and  $J_{\text{Sat1}}$ .

The spectral responsivity cannot be directly used in this case, as it is a highly wavelength-dependent parameter, and this simplified simulation makes the assumption of monochromatic light. Therefore, the related parameter of short-circuit current density will be used instead. Short-circuit current density is defined as

$$J_{\text{SC}} = J_{\text{PV}}(V = 0) = I_{\text{Opt}} R_{\lambda}. \quad (3.8)$$

The short-circuit current can be easily measured by simply shorting together the terminals of the solar cell and measuring the current through them. The short-circuit current was measured for varying levels of incident irradiance. The linear relationship between the short-circuit current density and incident irradiance was established and used to define the short-circuit current density for standard test conditions, i.e., with  $1000 \text{ W/m}^2$  incident irradiance. This gave a short-circuit current density of  $J_{\text{SC,STC}} = 203.5 \text{ A/m}^2$ , for standard test conditions, which is comparable to values seen in the literature [133].

The saturation current density is the final parameter that must be defined for the solar cells within the three solar arrays. It was found by measuring the short-circuit current and open-circuit voltage of the (above) solar cells, for repeated measurements with differing levels of incident irradiance, and using these values within the diode Equation 3.7. This gave a saturation current density of approximately  $J_{\text{sat1}} = 8 \times 10^{-9} \text{ A/m}^2$ , which is typical of values in the literature [134]. Notably, this experiment also showed the saturation current density to vary with the incident optical power. This is likely due to the simplifications made to the diode equation that was used to generate this value, and will therefore not be included in the simulation.

#### 3.2.4: Design of the Analytical Model

The analytical model defines the time-varying captured optical power density and generated electrical power density for the three geometric solar arrays and uses these results to define the accumulated (daily and yearly) energy value densities. For each array, under the illumination conditions for a given time interval, the model is used to compute the captured optical power density for each solar cell in an array as the net power that is not reflected divided by its area, i.e., the solar cell's silicon area. The model is then used to compute the generated electrical power density for each array as the net generated electrical power normalized with respect to the installation area. The product of the electricity price and generated electrical power density is then computed and summed over the course of the day and year to produce the accumulated daily energy value density and yearly energy value density, respectively. The specific details of this analytical model are given within this section.

The generated electrical power density is calculated by first relating the local standard time,  $LST$ , and latitude,  $\Psi$ , to the azimuth angle,  $\phi$ , and zenith angle,  $\theta$ , of the sun's trajectory. The link is made by calculating the Earth's mean anomaly,  $M$ , according to

$$M = (D - 81 \text{ d}) \frac{2\pi}{365 \text{ d} + Lp} , \quad (3.9)$$

where  $D$  is the numerical day of the year, being 1 for January 1, and  $Lp$  is 1 for leap years and 0 otherwise. The Earth's mean anomaly is then used to define the equation of time,  $EOT$ , which quantifies the discrepancy between the apparent solar time,  $AST$ , and local standard time,  $LST$ , caused by the eccentricity of Earth's orbit and the inclination of its axis. The  $EOT$  is

$$EOT = 9.87 \text{ min} \times \sin(2M) - 7.53 \text{ min} \times \cos M - 1.5 \text{ min} \times \sin M . \quad (3.10)$$

The  $EOT$  is used with the local standard time,  $LST$ , the offset due to daylight savings time,  $DST$ , and the angular offset in degrees between the longitude and the time zone meridian,  $\Phi_{\text{offset}}$  (which is assumed here to be  $0^\circ$  due to the selected longitude of  $120^\circ \text{ W}$ ), to give an apparent solar time of

$$AST = LST + EOT - DST + \Phi_{\text{offset}} \frac{4 \text{ min}}{1^\circ} . \quad (3.11)$$

The above definitions are then used to define the declination angle,  $\delta$ , as

$$\delta \approx 23.45^\circ \cdot \frac{\pi \text{ rad}}{180^\circ} \cdot \sin \left( (284 \text{ d} + D) \cdot \frac{2\pi}{365 \text{ d} + Lp} \right) , \quad (3.12)$$

and the hour angle,  $\omega$ , as

$$\omega = (AST - 720 \text{ min}) \cdot \frac{\pi \text{ rad}}{720 \text{ min}} . \quad (3.13)$$

Ultimately, for a given latitude of  $\Psi$ , declination angle of  $\delta$ , and hour angle of  $\omega$ , all in radians, the azimuth angle is defined by

$$\phi = \begin{cases} \arcsin \left( \frac{\cos \delta \sin \omega}{\sqrt{1 - (\sin \psi \times \sin \delta + \cos \psi \times \cos \delta \times \cos \omega)^2}} \right), \cos \omega \geq \frac{\tan \delta}{\tan \psi} \\ \pi - \arcsin \left( \frac{\cos \delta \sin \omega}{\sqrt{1 - (\sin \psi \times \sin \delta + \cos \psi \times \cos \delta \times \cos \omega)^2}} \right), \cos \omega < \frac{\tan \delta}{\tan \psi} \end{cases}, \quad (3.14)$$

and the zenith angle is defined by

$$\theta = \frac{\pi}{2} - \arcsin(\sin \psi \sin \delta + \cos \psi \cos \delta \cos \omega). \quad (3.15)$$

These solar azimuth and zenith angles can then be used to define the captured optical power densities for the three geometric solar arrays that are evaluated in this simplified simulation.

#### 3.2.4.1: Optical Power of the Flat-Panel Array

The captured optical power density of the Flat-Panel Array,  $\mathcal{P}_{\text{cap,FP}}$ , is calculated in a straightforward manner via

$$\mathcal{P}_{\text{cap,FP}} = I_0 (1 - R(\theta)) \cos \theta, \quad (3.16)$$

where  $I_0$  is the incident light irradiance, and  $R(\theta)$  is the reflectance, calculated according to Equation 3.6, for this simple case in which the angle of incidence,  $\theta_i$ , is equal to the zenith angle,  $\theta$ .

#### 3.2.4.2: Optical Power of the V-Groove Array

The captured optical power density of the V-Groove Array is calculated in a more complex manner than that of the Flat-Panel Array because of the consecutive internal reflections off opposing sides of the V-Groove Array. The calculations are carried out with an iterative process that steps through these consecutive reflections. During a given iteration, each solar cell on one side of the V-Groove is illuminated by an incident optical power, according to an incident ray vector, over an illuminated area. The illuminated area is a rectangular strip that spans from a lower edge (closest to the vertex) to an upper edge (furthest from the

vertex) with a width that is equal to the side-length of  $a$ . For the given iteration, the reflected optical power and reflected ray vector are calculated and used to both define the captured optical power (as that not reflected) and project the illuminated area onto the opposing side of the V-Groove (to initiate the next iteration). Since the V-Groove Array's geometry is unvarying in the x-direction, all solar cells on the same side of the V-Groove experience identical illumination conditions. Note also that the alignment of the V-groove array along the x-axis has this process be independent of the directional cosine  $\alpha$ , aside from its use in calculating the reflectance. This is because any reflected optical power exiting a V-groove array unit cell in the x-direction is matched by an identical amount of reflected optical power entering the opposing side of that V-groove array unit cell. Thus, the above iterative process can be carried out for a single unit cell, and the results applied to every unit cell in the array. When both sides of the V-Groove Array receive direct solar illumination, the iterative process is carried out twice: the first process has direct solar illumination and the first iteration on the east-facing solar cell; the second process has direct solar illumination and the first iteration on the west-facing solar cell.

For each iteration, indexed by  $i$ , five intermediate variables are calculated. The variable  $n_{\perp}(i)$  is the component of the incident ray vector projected onto the normal vector to the surface. The variable  $\theta_{yz}(i)$  is the angle between the incident ray vector's projection within the  $yz$ -plane and the  $z$ -axis. It is positive if the  $y$ -component of the incident ray vector and the  $y$ -component of the normal vector to the surface have opposite signs; it is negative if the components have the same signs. The variables  $d_l(i)$  and  $d_u(i)$  are the distances from the V-Groove's vertex to the lower and upper edges of the illuminated area, respectively, normalized with respect to the side-length of  $a$ . The variable  $P_{in}(i)$  is the incident optical power on the given solar cell, being equal to the absolute value of the product of the incident irradiance, illuminated area, and intermediate variable  $n_{\perp}(i)$ . The above intermediate variables are then used to calculate the given iteration's captured optical power contribution for the given solar cell,  $\delta P_{cap}(i)$ , according to

$$\delta P_{cap}(i) = P_{in}(i)(1 - R(\arccos n_{\perp}(i))). \quad (3.17)$$

For the first iteration,  $i = 1$ , the intermediate variables are calculated according to

$$\theta_{yz}(1) = \begin{cases} \arctan(\tan \theta \sin \phi) & \text{east-facing solar cell} \\ -\arctan(\tan \theta \sin \phi) & \text{west-facing solar cell} \end{cases}, \quad (3.18)$$

$$n_{\perp}(1) = \begin{cases} \cos \theta \sin \frac{V_{VG}}{2} + \sin \theta \sin \phi \cos \frac{V_{VG}}{2}, & \text{east-facing solar cell} \\ \cos \theta \sin \frac{V_{VG}}{2} - \sin \theta \sin \phi \cos \frac{V_{VG}}{2}, & \text{west-facing solar cell} \end{cases}, \quad (3.19)$$

$$d_u(1) = 1, \quad (3.20)$$

$$d_1(1) = \max \left( \frac{\sin(\theta_{yz} - V_{VG})}{\sin(\pi - \theta_{yz} - V_{VG})}, 0 \right), \quad (3.21)$$

$$P_{in}(1) = I_0 \cdot n_{\perp}(1) \cdot a^2 (d_u(1) - d_1(1)). \quad (3.22)$$

For subsequent reflections, indexed by  $i$ , the intermediate variables are calculated according to

$$P_{in}(i) = P_{in}(i-1) R(\arccos n_{\perp}(i-1)), \quad (3.23)$$

$$\theta_{yz}(i) = \theta_{yz}(i-1) + V_{VG}, \quad (3.24)$$

$$d_1(i) = d_1(i-1) \frac{\sin \left( \theta_{yz}(i) - \frac{V_{VG}}{2} \right)}{\sin \left( \pi - \theta_{yz}(i) - \frac{V_{VG}}{2} \right)}, \quad (3.25)$$

$$d_u(i) = d_u(i-1) \frac{\sin \left( \theta_{yz}(i) - \frac{V_{VG}}{2} \right)}{\sin \left( \pi - \theta_{yz}(i) - \frac{V_{VG}}{2} \right)}, \quad (3.26)$$

$$n_{\perp}(i) = \sin \left( \theta_{yz}(i) + \frac{V_{VG}}{2} \right) \sqrt{\cos^2 \theta + \sin^2 \theta \sin^2 \phi}. \quad (3.27)$$

A special condition may occur during these iterations when the illumination on a given side of the V-Groove extends above its solar cells. Such a condition is characterized by  $d_u(i) > 1$ . In this condition, the values of the incident optical power and the upper edge of the illuminated area must be adjusted. The adjusted variables are defined off the unadjusted variables according to

$$P_{\text{in}}(i) = P_{\text{in}}'(i) \frac{1 - d_1(i)}{d_u'(i) - d_1(i)}, \quad (3.28)$$

$$d_u(i) = 1, \quad (3.29)$$

where the primed variables denote the unadjusted variables.

The above iterative process has three termination conditions: when reflected light travels away from the opposing side of the V-Groove, which occurs for  $\theta_{yz}(i) + 0.5v_{\text{VG}} > \pi$  rad; when reflected light travels toward but completely misses the opposing side of the V-Groove, which occurs for  $d_l(i) > 1$ ; and when the incident optical power during a given iteration yields  $P_{\text{in}}(i) < P_{\text{in}}(1) \times 10^{-9}$ . When any one of these conditions is reached, the captured optical power density is calculated for the solar cells on both sides of the V-Groove. This is done by summing all of the iterations' captured optical power contributions to each solar cell and dividing the result by the area of the solar cell. This gives a captured optical power density for each solar cell of

$$\mathcal{P}_{\text{cap,VG}}(s) = \frac{1}{a^2} \left( \sum_{i \% 2 = s} \delta P_{\text{cap}}(\text{E}, i) + \sum_{i \% 2 \neq s} \delta P_{\text{cap}}(\text{W}, i) \right). \quad (3.30)$$

The argument list of the iteration values has been expanded here to denote the solar cell that receives direct solar illumination for that iteration sequence: E and W are defined for iterations that had the east-facing and west-facing solar cells receive direct solar illumination, respectively, while  $s = 0, 1$  identifies which side of the array the solar cell of interest is situated on.

### 3.2.4.3: Optical Power of the U-Groove Array

The captured optical power density of the U-Groove Array is calculated in a manner that is a hybrid of those methods used for the other two arrays. For high-angled illumination, at small zenith angles, the bottom of the U-Groove Array plays an important role in redirecting the internal reflections up and out of the array. Thus, such illumination conditions yield low numbers of reflections, making them conducive to relatively straightforward closed-form analyses. For low-angled illumination, at large zenith angles, the U-Groove Array yields large numbers of consecutive internal reflections. Thus, such illumination conditions are analyzed with an iterative process that is similar to that of the V-Groove Array.

The U-Groove Array can be analyzed by considering only a single unit cell of the array. This simplification comes about because the U-Groove, like the V-Groove, runs parallel to the  $x$ -axis. The solar cells on each wall of the array run parallel to the  $x$ -axis and thus experience the same illumination. Likewise, the columns of solar cells on the bottom of the array run parallel to the  $x$ -axis and thus experience the same illumination. To further simplify the analyses, an angle of

$$\eta = \arccos(\sin \theta |\sin \phi|) \quad (3.31)$$

is defined. It is the angle between the incident ray vector and the normal vector to the surface on the wall experiencing direct solar illumination.

The first case that is analyzed for the U-Groove Array is for high-angled illumination, at small zenith angles. It comes about when the bottom of the U-Groove Array receives direct solar illumination and the aspect ratio,  $N_{UG}$ , meets the condition  $1/N_{UG} > \tan \theta |\sin \phi|$ . For this case, the captured optical power densities on the illuminated and shaded walls are given by

$$\mathcal{P}_{\text{cap,UG,ill}} = \begin{cases} I_0 \cos \eta (1 + R(\theta))(1 - R(\eta)), & 2 \tan \theta |\sin \phi| \leq 1 / N_{\text{UG}} \\ I_0 \left( \cos \eta + (1 / N_{\text{UG}} - \tan \theta |\sin \phi|) \cos \theta R(\theta) \right) (1 - R(\eta)), & 2 \tan \theta |\sin \phi| > 1 / N_{\text{UG}} \end{cases}, \quad (3.32)$$

$$\mathcal{P}_{\text{cap,UG,shd}} = \begin{cases} 0, & 2 \tan \theta |\sin \phi| \leq 1 / N_{\text{UG}} \\ I_0 \cos \eta \frac{2 \tan \theta |\sin \phi| N_{\text{UG}} - 1}{\tan \theta |\sin \phi| N_{\text{UG}}} R(\eta) R(\theta) (1 - R(\eta)), & 2 \tan \theta |\sin \phi| > 1 / N_{\text{UG}} \end{cases}, \quad (3.33)$$

respectively. Here, the ill and shd subscripts denote solar cells on the directly illuminated and shadowed walls, respectively.

Since the row of solar cells on the bottom of the U-Groove Array consists of a discrete number of solar cells, which depends upon the aspect ratio, it is necessary to identify the distinct captured optical powers for each of them by dividing the total captured optical power on the row between these solar cells. It is first observed that any area of illumination on the bottom of the array will be adjacent to one of the walls. The two key parameters needed to calculate the captured optical power contributions for each solar cell are therefore the total captured optical power of the row of solar cells,  $P_B$ , and the area of illumination defined as a fraction of the bottom area,  $F_B$ . As this case involves both direct solar illumination on the bottom and a reflection onto the bottom off the illuminated wall, these parameters must be calculated for each of those sources of illumination. The results of these calculations are given by

$$P_B(1) = I_0 a^2 \left( \frac{1}{N_{\text{UG}}} - \tan \theta |\sin \phi| \right) \cos \phi (1 - R(\phi)), \quad (3.34)$$

$$F_B(1) = 1 - \tan \theta |\sin \phi| N_{\text{UG}}, \quad (3.35)$$

$$P_B(2) = I_0 a^2 \cos \eta R(\eta) (1 - R(\theta)), \quad (3.36)$$

$$F_B(2) = \tan \theta |\sin \phi| N_{\text{UG}}, \quad (3.37)$$

where the argument of the results is 1 for the direct solar illumination and 2 for the reflected illumination. The total captured optical power of the row of solar cells and the illuminated fraction of the bottom can be used to calculate a captured optical power contribution for each reflection on each solar cell of the row through the equation

$$\delta P_{\text{cap}}(w) = \sum_{i=1,2} \begin{cases} \frac{P_B(i)N_{UG}}{F_B(i)}, & w < \frac{F_B(i)}{N_{UG}} \\ \frac{P_B(i)(F_B(i) - wN_{UG} + N_{UG})}{F_B(i)}, & (w-1) < \frac{F_B(i)}{N_{UG}} < w \\ 0, & \frac{F_B(i)}{N_{UG}} < (w-1) \end{cases} \quad (3.38)$$

The variable  $w$  identifies the solar cell, beginning with  $w = 1$  on the side where the illuminated area is adjacent to the wall, which for this case is the directly illuminated wall. The captured optical power densities for the bottom solar cells can now be obtained by dividing the captured optical power by the solar cell's area, as per the equation

$$\mathcal{P}_{\text{cap,UG,btm}}(w) = \frac{\delta P_{\text{cap}}(w)}{a^2}. \quad (3.39)$$

The second case for the U-Groove Array's captured optical power density calculation occurs when there is no direct solar illumination onto the bottom of the array. This condition is defined from  $N_{UG}$  as being  $\tan(\theta)|\sin(\phi)| \geq 1/N_{UG}$ . In this case, as there is only one region of direct solar illumination and the number of reflections can become arbitrarily large, an iterated method is appropriate. As with the V-Groove Array, the illumination is fully defined by an incident power per solar cell on the illuminated side of the U-Groove, an incident ray vector, and an illuminated area defined by its upper and lower edges. The reflected power and reflected ray vector are calculated and used to project the illuminated area onto the opposing side of the U-Groove. The next iteration can then be carried out in the same manner. Three key intermediate variables are defined for each incidence of light onto a solar cell: the upper edge of the illuminated area as

a fraction of the wall's height,  $d_u$ ; the lower edge of the illuminated area as a fraction of the wall's height,  $d_l$ ; and the incident optical power per solar cell,  $P_{in}$ .

There are two special cases that apply to this iterated process. The first is that at some point light will reflect off the bottom of the U-Groove. This case is identified by  $d_l(r) < 0$ , where  $r$  indicates the iteration at which this occurs. The second special case is identical to that found in the V-Groove Array iteration, where illumination partially misses the opposing solar cell. Due to the relative simplicity of the calculations in this iterated process, both of these special cases will be represented in the following equations through case structures.

The variable of interest for this iterated calculation is the captured optical power contribution from each time light is incident onto a solar cell,  $\delta P_{cap}(i)$ , where  $i$  specifies the iteration during which this value is collected. This captured optical power contribution for each incidence is calculated from the intermediate variables listed above through the expression

$$\delta P_{cap}(i) = \begin{cases} P_{in}(i)(1 - R(\eta)) & i \neq r \\ P_{in}(i) \tan \theta |\sin \phi| N_{UG} (d_u(i) - d_l(i)R(\theta))(1 - R(\eta)) & i = r \end{cases}, \quad (3.40)$$

which includes an adjusted expression used for the iteration when light reflects off the bottom of the U-Groove Array.

For the first iteration,  $i = 1$ , the iterated variables are calculated according to

$$d_u(1) = 1, \quad (3.41)$$

$$d_l(1) = 1 - \frac{1}{\tan \theta |\sin \phi| N_{UG}}, \quad (3.42)$$

$$P_{in}(1) = I_0 a^2 (d_u(1) - d_l(1)) \cos \eta. \quad (3.43)$$

For each subsequent iteration, new values are calculated for the three iterated variables. These values follow the equations

$$d_1(i) = \begin{cases} d_1(i-1) - \frac{1}{\tan \theta |\sin \phi| N_{UG}} & i-1 < r \\ -d_1(i-1) & i-1 = r, \\ d_1(i-1) + \frac{1}{\tan \theta |\sin \phi| N_{UG}} & i-1 > r \end{cases} \quad (3.44)$$

$$d_u(i) = \min \left( d_1(i) + \frac{1}{\tan \theta |\sin \phi| N_{UG}}, 1 \right), \quad (3.45)$$

$$P_{in}(i) = \begin{cases} P_{in}(i-1)R(\eta) & i-1 \neq r, d_u(i) \neq 1 \\ P_{in}(i-1)R(\eta) \tan \theta |\sin \phi| N_{UG} (1 - d_1(i)) & i-1 \neq r, d_u(i) = 1 \\ P_{in}(i-1)R(\eta)R(\theta) & i-1 = r, d_u(i) \neq 1 \\ P_{in}(i-1)R(\eta)R(\theta) \tan \theta |\sin \phi| N_{UG} (1 - d_1(i)) & i-1 = r, d_u(i) = 1 \end{cases} \quad (3.46)$$

The iteration has two conditions upon which it will end: when the reflected light travels toward but misses the opposing solar cell, which is identified by  $d_1(i) > 1$ , and when the reflected light is negligible, which is identified by  $P_{in}(i) < P_{in}(1) \times 10^{-9}$ . Once one of these conditions has been reached, the collected optical power density for each solar cell in the array walls can be calculated by summing the captured optical power contributions onto the solar cells of each side, and dividing by the area of the solar cell, as per the equation

$$\mathcal{P}_{cap,UG,side}(s) = \frac{1}{a^2} \sum_{i \% 2 = s} \delta P_{cap}(i). \quad (3.47)$$

For the solar cells on the bottom of the U-Groove, two patches of reflected illumination will reach them. As with the previous case, the optical power captured by a row of solar cells and the fraction of the bottom that is illuminated need to be calculated. These can be found from the iterated variables at iteration  $i = r$ , through the equations

$$P_B(1) = -P_{in}(r)d_1(r) \tan \theta |\sin \phi| N_{UG} (1 - R(\theta)), \quad (3.48)$$

$$F_B(1) = -d_1(r) \tan \theta |\sin \phi| N_{UG}, \quad (3.49)$$

$$P_B(2) = P_{in}(r)d_u(r) \tan \theta |\sin \phi| N_{UG} R(\eta) (1 - R(\theta)), \quad (3.50)$$

$$F_B(2) = d_u(r) \tan \theta |\sin \phi| N_{UG}. \quad (3.51)$$

These values can be used in Equations 3.38-3.39 to calculate the captured optical power densities of each solar cell on the bottom of the U-Groove Array, with solar cell  $w = 1$  being adjacent to the directly illuminated wall if  $r$  is odd and adjacent to the shadowed wall if  $r$  is even.

#### 3.2.4.4: Conversion of Optical Power to Electrical Power

Once the captured optical power densities for each solar cell in any of the three geometric solar arrays have been calculated following the methods given above, these values must be converted into a generated electrical power density. The first step is to calculate the photovoltaic current, using the single-diode I/V Equation 3.7. This equation is modified slightly to become

$$I_{PV} = \max \left( I_{sc} \frac{\mathcal{P}_{cap}}{1000 \text{ W/m}^2} - I_{sat1} \left( e^{\frac{qV}{k_B T}} - 1 \right), 0 \right). \quad (3.52)$$

Here,  $1000 \text{ W/m}^2$  is the illumination irradiance for standard test conditions, for which  $I_{sc}$  is defined, and the restriction to positive values is due to the presence of blocking diodes. The temperature,  $T$ , is assumed to be  $25 \text{ }^\circ\text{C}$ , or  $298.15 \text{ K}$ , the temperature defined for standard test conditions.

The electrical power generated by each solar array is the sum of the products of voltage and current from each of its solar cells. In this analytical model, all solar cells in a given array are subject to an identical voltage, because each array has one MPPT unit, and this voltage is found by optimizing Equation 3.52 to yield the maximized electrical power. Once the maximum powers have been identified for the Flat-Panel

Array,  $P_{\text{gen,max,FP}}$ , V-Groove Array,  $P_{\text{gen,max,VG}}$ , and U-Groove Array,  $P_{\text{gen,max,UG}}$ , the powers are divided by the respective installation areas for the unit cells of each array, as previously shown in Table 3.1. This yields the respective generated electrical power densities for the Flat-Panel Array, V-Groove Array, and U-Groove Array:

$$\mathcal{P}_{\text{gen,FP}} = \frac{P_{\text{gen,max,FP}}}{a^2}, \quad (3.53)$$

$$\mathcal{P}_{\text{gen,VG}} = \frac{P_{\text{gen,max,VG}}}{2a^2 \sin v_{\text{VG}}}, \quad (3.54)$$

$$\mathcal{P}_{\text{gen,UG}} = \frac{P_{\text{gen,max,UG}} N_{\text{UG}}}{a^2}. \quad (3.55)$$

### 3.3: Simplified Simulation Results

In order to determine the relative effectiveness of the three solar arrays, the generated electrical power density and accumulated energy value density for the different arrays are calculated first for a single day with a prominent ‘‘Duck Curve’’, and then over the course of several years in order to determine overarching trends and evaluate the performance of each array.

In order to obtain results for the V-Groove Array and U-Groove Array that can be compared to each other and to the Flat-Panel Array, it is necessary to perform some level of optimization on the parameters of these arrays in order to select parameters to be tested. As previously noted, the V-Groove Array has two optimizable parameters that have not already been accounted for, the V-Angle ( $v_{\text{VG}}$ ) and the rotation angle ( $\rho_{\text{VG}}$ ). Similarly, the U-Groove Array has two optimizable parameters that have not been accounted for, the aspect ratio ( $N_{\text{UG}}$ ) and the rotation angle ( $\rho_{\text{UG}}$ ). As the purpose of this simulation was to be a quick validation of the arrays, the decision was made to fix the rotation angle at 0 for both arrays rather than optimizing it. As these two arrays were specifically selected to capture low-angle light from the east and west in their default  $\rho = 0$  orientation, it is highly likely that this orientation is very close to optimal.

Several variations of the V-Groove Array with differing V Angles and the U-Groove Array with differing aspect ratios were initially tested and compared according to the metric of yearly energy value density over the year of July 2016-June 2017. The optimal configurations were found to be the  $v_{VG} = 80^\circ$  V-Groove Array and the  $N_{UG} = 1/3$  U-Groove Array, which gave yearly energy value densities of 5.4978  $\$/(\text{m}^2 \cdot \text{year})$  and 5.5152  $\$/(\text{m}^2 \cdot \text{year})$ , respectively. It is these variations that are used for the ensuing analyses.

The single-day analysis is carried out for a date with a significant “Duck Curve” characteristic. The selected date is the spring equinox, being March 20, 2017. This is because March exhibits dramatic variations in electricity price over the course of a day and thus a strong susceptibility to the “Duck Curve”. Fig. 3.9 shows the average electricity price in US dollars across California as a function of the time of day on March 20, 2017. The characteristic low mid-day price and high early- and late-day prices of the “Duck Curve” can clearly be seen.

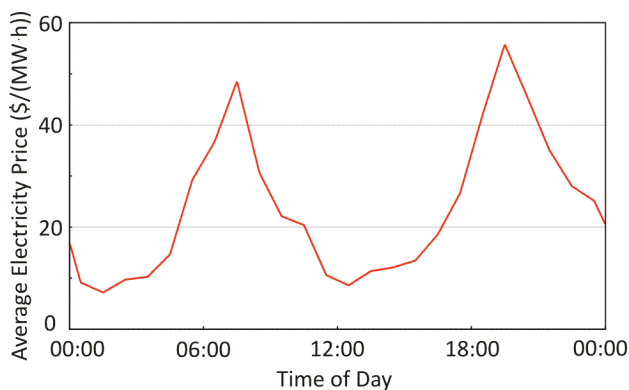


Fig. 3.9: Hourly electricity price on the sample day of March 20, 2017, demonstrating the distinctive “Duck Curve” profile. Reprinted with permission from the Royal Society of Chemistry.

Fig. 3.10 shows the generated electrical power density as a function of the time of day for the three solar arrays, at the prescribed date (March 20, 2017) and location ( $37^\circ$  north,  $120^\circ$  west). Results for the Flat-Panel Array, the V-Groove Array with  $v_{VG} = 80^\circ$ , and the U-Groove Array with  $N_{UG} = 1/3$  are plotted as solid curves against the left axis in green, red, and blue, respectively. The curves share a similar (bell) shape that is due to the varying capture cross-section of the arrays as the sun follows its trajectory over the course of the day. However, some differing characteristics can be observed. Notably, the V-Groove Array obtains

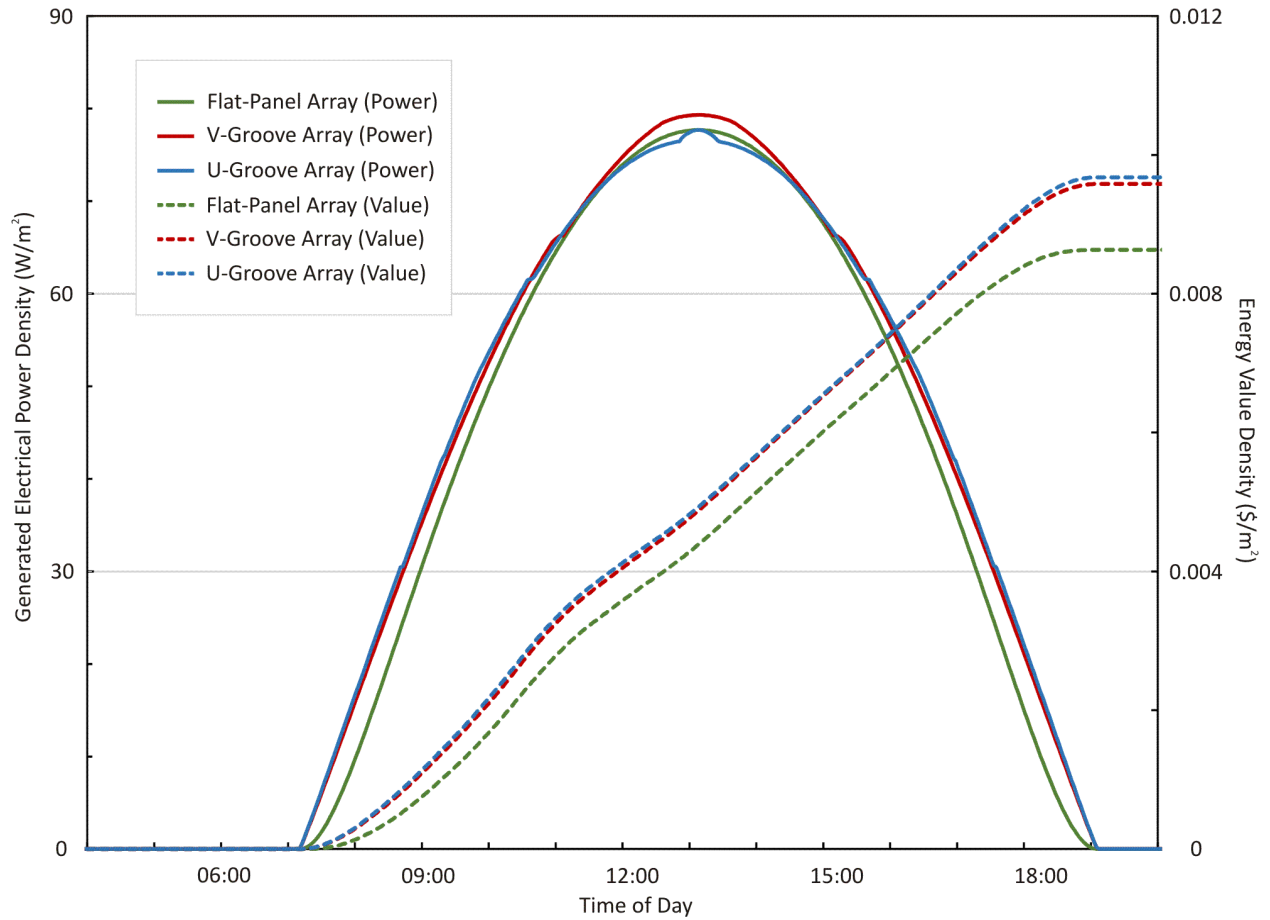


Fig. 3.10: Instantaneous power density and accumulated value density for the optimized configurations of the three arrays as a function of time on March 20, 2017. Reprinted with permission from the Royal Society of Chemistry.

the highest generated electrical power densities at mid-day hours, while the U-Groove Array obtains the highest generated electrical power densities during early- and late-day hours. The superiority of the V-Groove Array at mid-day hours is because of its angled solar cells, which let this array (and only this array) capture reflections when the sun is to the south, with small azimuth angles. The superiority of the U-Groove Array at early- and late-day hours is because of its vertical solar cells, which let this array (and the V-Groove Array to a lesser extent) capture reflections when the sun is to the east and west, with large zenith angles. Fig. 3.10 also shows the energy value density being accumulated as a function of the time of day for the solar arrays, at the prescribed date (March 20, 2017) and location ( $37^\circ$  north,  $120^\circ$  west). Results for the Flat-Panel Array, the V-Groove Array with  $\nu_{VG} = 80^\circ$ , and the U-Groove Array with  $N_{UG} = 1/3$  are plotted as dashed curves against the right axis in green, red, and blue, respectively. The curves approach

asymptotic values at the end of the day, which define the daily energy value densities for the three arrays. It is apparent here that the U-Groove Array and V-Groove Array outperform the Flat-Panel Array.

At the end of the day, the U-Groove Array and V-Groove Array have daily energy value densities of 0.00968  $\$/(\text{m}^2\text{-day})$  and 0.00958  $\$/(\text{m}^2\text{-day})$ , respectively, while the Flat-Panel Array has a daily energy value density of 0.00863  $\$/(\text{m}^2\text{-day})$ . This is due to the U-Groove and V-Groove Arrays' greater ability to capture incident optical power at the early- and late-day hours when the electricity price is high. Overall, the U-Groove Array exhibits the highest daily energy value density.

It is important to note that the above findings, and the improved performance levels of the U-Groove Array, manifest themselves during the spring, and to a lesser extent during the fall and winter, when the “Duck Curve” is the strongest. However, the majority of solar power is generated during the summer, when the mid-day electricity price is high due to the use of air conditioning. This would enhance the performance of the V-Groove Array. Thus, for fair comparison, it is necessary to compare the solar arrays over the span of a year. Such a process is carried out here, with the results collected over a period of six years. This extended data collection period is used to accommodate the growing prominence of the “Duck Curve” and identify relevant trends (if any).

Fig. 3.11 shows the normalized daily energy value density as a function of the date, spanning July 2012 to June 2018, for each solar array, at the prescribed location ( $37^\circ$  north,  $120^\circ$  west). The curves for the Flat-Panel Array, the V-Groove Array with  $\nu_{VG} = 80^\circ$ , and the U-Groove Array with  $N_{UG} = 1/3$  are shown in green, red, and blue, respectively. The results are normalized to compare performance levels and identify trends. The normalization is carried out with respect to results for an idealized Flat-Panel Array having a reflectance of zero. This idealized array is an effective baseline for comparison, but it should not be presumed to be a “perfect” structure. It does not necessarily yield the maximum generated electrical power density. This is because the diode losses are proportional to the silicon area that is not disconnected by the blocking diodes. As such, there can be situations in which the non-flat arrays absorb slightly less optical

power than the idealized Flat-Panel Array but they do so while experiencing far lower losses. This can have the non-flat arrays yield greater generated electrical powers than the idealized Flat-Panel Array.

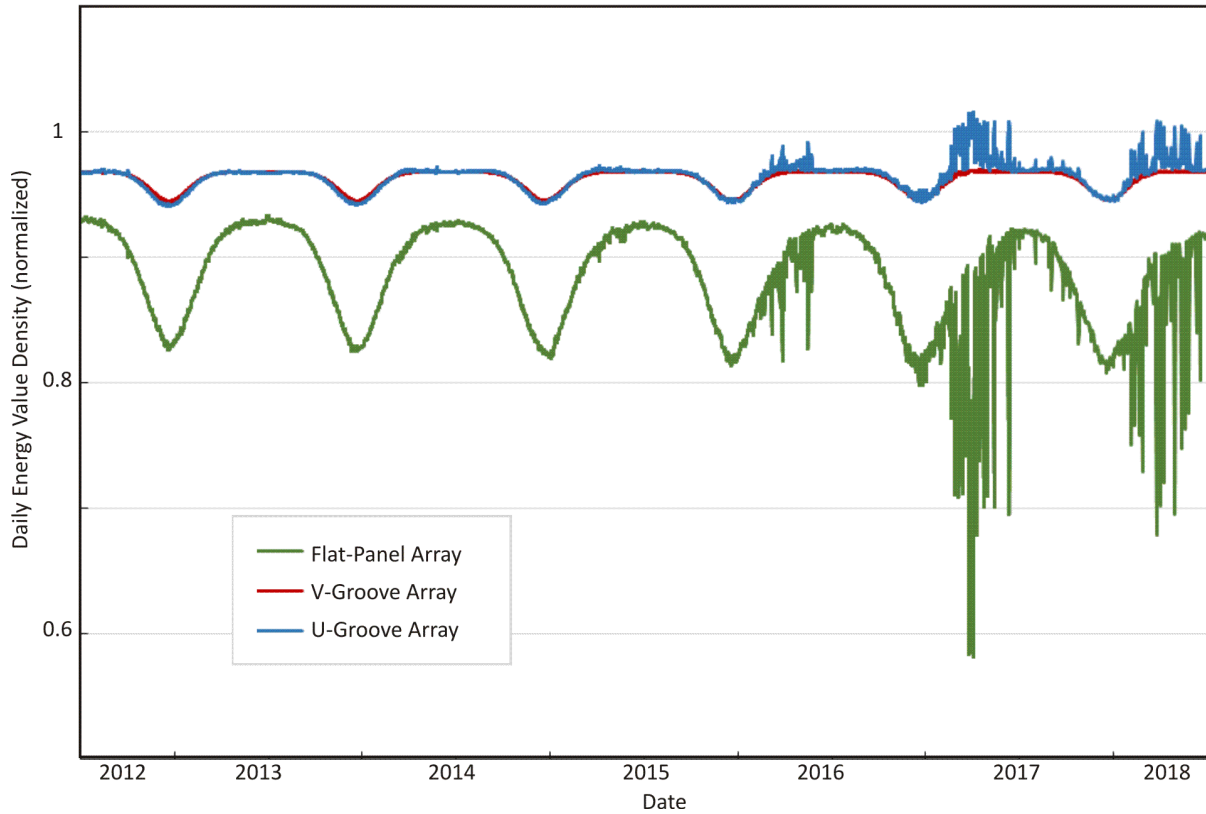


Fig. 3.11: Daily energy value densities for the optimal configurations of the three arrays, normalized to the case of a Flat-Panel Array with zero reflectance, for the period from July 1, 2012 to June 30, 2018. Reprinted with permission from the Royal Society of Chemistry.

Three key characteristics are evident in Fig. 3.11. First, the daily energy value density has a cyclical nature with a one-year period and stronger performance during the summer months. The reason for such a characteristic is self-evident. Second, the daily energy value density during the spring, and to a lesser extent the winter and fall, exhibits increasingly strong fluctuations. Such fluctuations come about from the “Duck Curve”, which manifests itself as dramatic changes in electricity prices over the course of a day according to the supply and demand of solar-generated power. Third, the “Duck Curve” yields its strongest effects on the performance of the Flat-Panel Array, which exhibits deep decreases in the normalized daily energy value density over 2016 (to a small extent), and 2017 and 2018 (to a greater extent). The V-Groove Array

does not exhibit such fluctuations. In stark contrast, the U-Groove Array exhibits increases in the normalized daily energy value density over 2016 (to a small extent), and 2017 and 2018 (to a greater extent). Such a result manifests itself here because all of the arrays experience the negative effects of the “Duck Curve” on the energy value density, including the idealized Flat-Panel Array that is used for normalization, but the U-Groove Array is able to minimize such effects and thereby maximize the energy value density.

The evolving influence of the “Duck Curve” can be quantified for the geometric solar arrays by summing their daily energy value densities over the course of a year to produce a yearly energy value density. The yearly energy value density is shown in Fig. 3.12 as a function of the year, spanning July 2012 to June 2018, for each of the solar arrays at the prescribed location ( $37^\circ$  north,  $120^\circ$  west). Curves for the Flat-Panel Array, the V-Groove Array with  $\nu_{VG} = 80^\circ$ , and the U-Groove Array with  $N_{UG} = 1/3$  are shown in green, red, and blue, respectively. The solid curves, plotted against the left-axis, correspond to unnormalized yearly energy value densities. The dashed curves, plotted against the right-axis, correspond to normalized yearly energy value densities, with respect to the idealized Flat-Panel Array having a reflectance of zero. The unnormalized results in the figure all show a downward trend in the yearly energy value densities for all three arrays over the six-year period. The similar downward trends are due to the resemblance of the generated electrical power density curves in Fig. 3.10, which show that all three arrays generate most of their power in the mid-day hours, and the increasing influence of the “Duck Curve”, which leads to lower electricity prices during those mid-day hours. The influence of the “Duck Curve” differs for the three arrays, however, and such differences are best seen following normalization. The normalized results in the figure show that the V-Groove Array and U-Groove Array far outperform the Flat-Panel Array and the levels at which they outperform the Flat-Panel Array are increasing. It is also clear that the V-Groove Array and U-Groove Array yielded similar performance in the past, but the U-Groove Array shows improved performance over that of the V-Groove Array in the latter three years. This is due to its greater capability in capturing optical power during early- and late-day hours, when the electricity prices are high, in tandem

with the growing influence of the “Duck Curve”. Should these trends continue, it is possible that the U-Groove Array will far outperform the other arrays in the future.

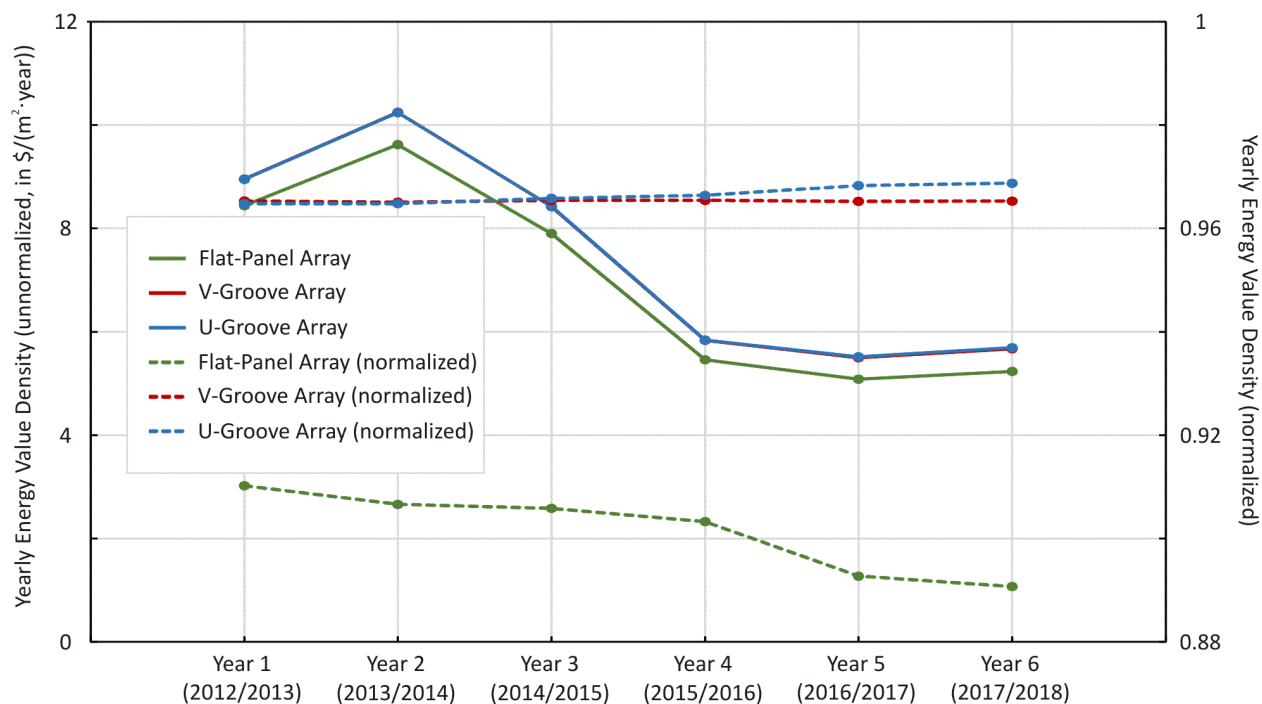


Fig. 3.12: Accumulated yearly energy value densities for the optimal configurations of the three arrays, plotted from July 1, 2012, to June 30, 2018. The solid curves are unnormalized and plotted against the left axis, while the dotted curves are normalized to a Flat-Panel Array with zero reflectance and plotted against the right axis. Note that the unnormalized V-Groove Array is difficult to see in this figure, as it is largely hidden by the very similar curve for the unnormalized U-Groove Array. Reprinted with permission from the Royal Society of Chemistry.

### 3.3.1: Discussion

The results of this preliminary study show strong support for the U-Groove Array in mitigating the effects of the “Duck Curve”, but there are several practical points that need to be discussed with respect to the underlying assumptions and the related findings.

Firstly, little thought was put into the location of any proposed value-optimized solar arrays. In terms of the geographical location, external factors such as weather conditions, due to frequent overcast days, or accessibility to the electricity grid should be considered. Such factors would impact the generated energy value density and were not factored into this study – given that it used an average location as well as an average of day-ahead marginal prices across the state of California.

Secondly, it is worth noting the practical issues of installing V-Groove and U-Groove Arrays – given that such arrays are designed here to be installed on rooftops. The vertical dimension of these arrays could have wind loading become a concern, even with the scaling factor set to 1, and so a robust support structure would be necessary. For the V-Groove Array, the design of the support structure is trivial because it, like the Angled-Panel Array, can use support structures beneath the arrays. For the U-Groove Array, the design is more challenging. This array benefits from having thin vertical walls, to maximize the active area of light collection, but such thin walls yield little support. Crossed struts could be used to enhance the support, but these struts would block some fraction of the incident light and reduce the effectiveness of the array. For sufficiently small walls, it may be possible for them to be supported primarily from within, but it is worth noting that additional shadowing losses may be inevitable in any practical U-Groove Array installation.

Additionally, it is useful to note how the metric of energy value density relates to the capital investment (installation) costs and the greater benefits to the general public. With respect to the capital investment costs, it must be noted that the defined energy value density is linked to the solar-generated revenue and so it does not take into account capital installation costs. Thus, there is an implicit assumption here that the installation costs do not vary to a great extent with the silicon area of the array, which would cause them to differ greatly between the different arrays investigated here. This assumption is valid more for smaller arrays, in sites with limited space, where the fixed costs of inverters and installation area outweigh the area-dependent cost of solar cells. If a more thorough economic evaluation with respect to the active silicon surface area were carried out for the arrays optimized in this work with respect to the installation area, we would see that the 1/3 U-Groove Array, which yields 8.76% more revenue and has 66.67% more silicon than the Flat-Panel Array, and the 80° V-Groove Array, which yields 8.37% more revenue and has 55.56% more silicon than the Flat-Panel Array, would likely not outperform the Flat-Panel Array. However, with respect to the benefits to the greater public, it is clear that the focus on optimizing energy value density yields clear advantages. This is because it directly confronts the challenge of energy capture during low-

supply and high-demand hours – by optimizing for improved matching between the generated electrical power and daily electricity price curves – and thus lessens the prominence of the “Duck Curve”.

## 4: Array Analysis with a Rigorous Simulation Approach

While the simplified simulation described in chapter 3 provided some useful initial insights into the performance of the U-Groove Array and V-Groove Array, its conclusions leave a lot to be desired. Therefore, this chapter introduces a more detailed simulation founded primarily around a shift from light interaction based in aggregate properties to a more rigorous model. In this simulation, the wavelength-dependence and polarization-dependence of light interactions will be addressed, where previously they were overlooked. Additionally, diffuse light will be accounted for, both originating from scattering during atmospheric propagation and originating from reflection off of textured surfaces. Further accuracy will be incorporated into the rigorous simulation through the use of a double-diode solar cell model with realistic ohmic resistance.

One important step that will be made with this simulation is the comparison of the Angled-Panel Array, which was previously discussed in section 3.1.2. While this array was neglected in the simplified simulation due to its optimization complexity, it is no longer reasonable to do so. This is due to the fact that the Angled-Panel Array represents the current photovoltaic industry standard, and any comparison that does not include it will therefore only provide results that are of limited practical value. With this array added to the comparison, it becomes possible to say whether the other compared arrays are viable alternatives that could see widespread implementation.

Another point of interest in this rigorous simulation is the definition of a new metric of optimization. The simplified simulation, being primarily focused on societal benefit rather than economic benefit, did not include the array costs in its metric of value density. However, it must be acknowledged that it is the economic benefit that primarily determines whether an array will see industry implementation. Notably, as was previously mentioned and will be examined in detail in the subsequent subsections, the Angled-Panel Array degenerates into a Flat-Panel Array under value density optimization, despite being the standard geometric solar array found in industry, confirming that results optimized for value density may not reflect

optimal selections within the photovoltaic industry. For this reason, a new metric, the Relative Profit Density, is introduced. The Relative Profit Density is defined as

$$\Pi_{\text{rel}} = Val_y - C_{\text{geo},y} g , \quad (4.1)$$

the difference between the generated value density used in chapter 3,  $Val_y$ , and a term which attempts to quantify how the costs of each array vary dependent on their complexity. More details on this metric are given in section 4.2.3.

Finally, it is worth noting that there were two iterations of the rigorous simulation performed. The first iteration contained some inaccuracies, and the results from it were ultimately discarded. This iteration will not be discussed in detail in this thesis. However, as will be noted occasionally in the following sections, the results of the first iteration were used to inspire certain design choices in the second iteration, with the accuracy of these choices being confirmed only after the completion of the second iteration.

#### 4.1: Experimental Derivation of Solar Cell Parameters

As with the previous simplified simulation, this rigorous simulation will use experimentally-seeded data in order to determine the core solar cell parameters. However, due to the decision to use a more accurate solar cell model here, the double-diode model with resistive losses as shown in Equation 2.2, several additional parameters are needed, and the values found for the simplified simulation cannot be reused.

The primary purpose of these experiments is to find and identify solar cell parameters to use in the simulation. As the simulation is intended to represent a generic commercial solar cell, rather than specifically the solar cells used in the experiments, the experimental parameters derived here have a high tolerance for error. Rather, the focus is on comparing both experimental values and values taken from the literature to verify whether either source contains significant errors that would negatively affect the results of the simulation. So long as the two correspond reasonably well, they can safely be assumed to represent a generic solar cell, and they can therefore be used in the simulation. In the case of significant discrepancies between experimental and literature-based results, the cause of these discrepancies must be investigated to

determine which source would be best for use in the simulation. For similar values, the experimental results will be preferentially used over the literature-based results, as this allows the experiments to serve a secondary purpose of providing additional validation for the final simulation by comparing results from each of them.

The parameters that will need to be identified are  $J_{\text{Sat}1}$ , the first saturation current density;  $J_{\text{Sat}2}$ , the second saturation current density;  $R_s$ , the series area-related resistance; and  $R_{\text{sh}}$ , the shut area-related resistance.

The second diode ideality factor,  $n_d$ , will be assumed to be 2.

The short-circuit current density,  $J_{\text{SC}}$ , is unfortunately no longer useful as a parameter due to the shift to wavelength dependence. Instead, it is necessary to switch to spectral responsivity,  $R_\lambda$ , defined as the wavelength-dependent ratio between the photocurrent and the absorbed optical power. The spectral responsivity can be calculated as

$$R_\lambda = IQE \frac{\lambda q}{hc}. \quad (4.2)$$

The internal quantum efficiency,  $IQE$ , is a wavelength-dependent measurement of the number of excited electrons produced per absorbed photon. Multiplying this by the wavelength accounts for the fact that the photon energy is inversely related to the wavelength, while the energy of an excited electron is constant.

Experimentally determining  $R_\lambda$  or  $IQE$  would be difficult, since these properties are wavelength-dependent, and a large number of data points would be needed. Instead, typical values from the literature will be used, and the assumption will be made that the  $IQE$  values from the experimental solar cells will be equivalent to a scaled version of these literature curves. As such, a normalized, literature-based  $R_\lambda$  will be calculated, and this result will then be scaled based on experimental results to match the solar cells used. The internal quantum efficiency curves for silicon solar cells from several sources ([60], [134]-[136]) were taken, and their results averaged to produce the internal quantum efficiency curve shown in Fig. 4.1. The internal quantum efficiency can be seen to be nearly 100% across much of the spectrum, dropping off in the near

infrared (due to the specificity of phonons needed for near-bandgap indirect excitation) and the near ultraviolet (since the high absorption here causes most photons to be absorbed above the diode junction, where the lack of an electric field leads to a higher chance of immediate recombination). Multiplying this by the wavelength and setting the maximum to 1 gives the normalized  $R_\lambda$  curve shown in Fig. 4.2. This curve can now be adjusted to match the optical power to the photocurrent observed experimentally.

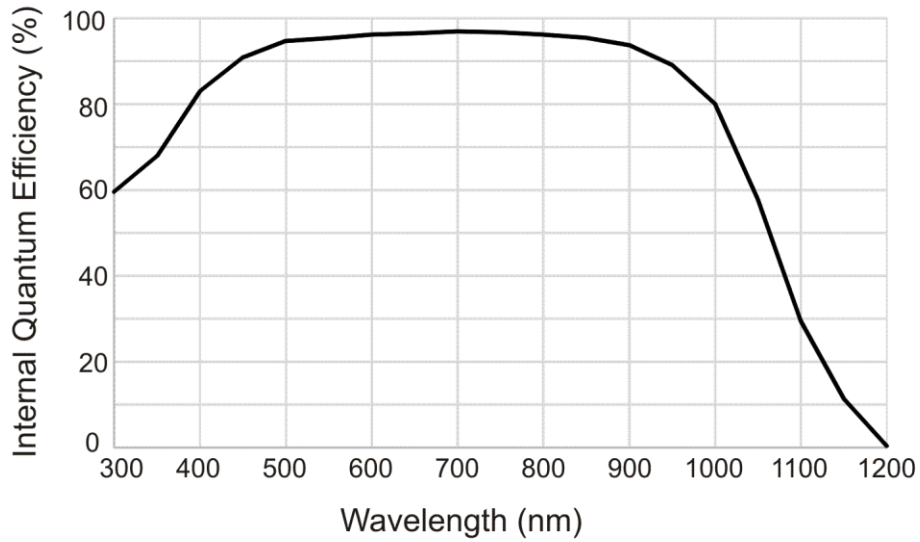


Fig. 4.1: Estimated silicon IQE curve derived from [60], [134]-[136].

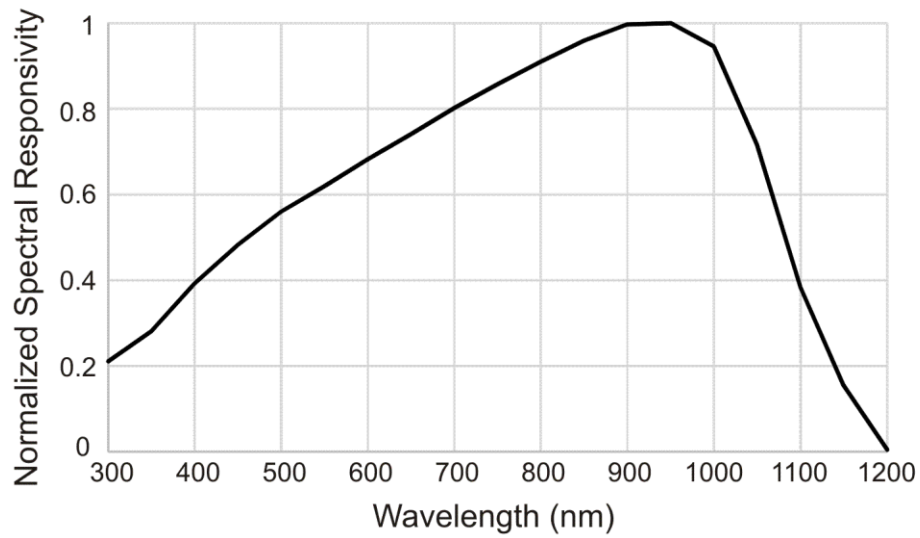


Fig. 4.2: Normalized spectral responsivity curve based on the IQE curve presented in Fig. 4.1.

The side length of the solar cells used,  $a$ , was assumed to be 78 mm for the simplified simulation in chapter 3. A more accurate measurement of this length was found to be 76.2 mm, which is the value that is used in the rigorous simulation.

The following two subsections detail the experiments run to evaluate the parameters listed above. The first subsection explains the simplified experiments used in the first iteration of the rigorous simulation, while the second subsection explains the more realistic experiments used in the second iteration of the rigorous simulation.

#### 4.1.1: Preliminary Analysis of Lab-Generated I/V Curves

Preliminary results for the solar cell parameters were obtained by curve-fitting the double-diode solar cell equation to lab-generated solar cell I/V curves. This experimental characterization was performed for the first iteration of the rigorous simulation, but was ultimately redone as described in the subsequent subsection. It is nonetheless included here, as the conclusions drawn from the values calculated here remain highly relevant to the research presented in this thesis.

The effects of varying different parameters in the double diode solar cell model are shown in Fig. 4.3. As can clearly be seen,  $J_{SC}$  and  $R_{sh}$  can be easily identified, as they are the primary parameters affecting the short-circuit current and the resistive slope above the elbow respectively. The other parameters are more difficult to directly discern. The two saturation currents are the primary parameters affecting the open-circuit voltage, but this is insufficient to individually identify them, as it is possible to maintain a constant open-circuit voltage by varying both parameters simultaneously. However, as seen in the dotted black line where both parameters are varied such that the open-circuit voltage remains constant, these parameters also determine the shape of the corner. This overlaps with solving for  $R_s$ , as the series resistance typically determines the slope of the curve below the elbow, which is also affected by the corner shape. Curve fitting is necessary to deconvolute the concurrent effects of these three variables.

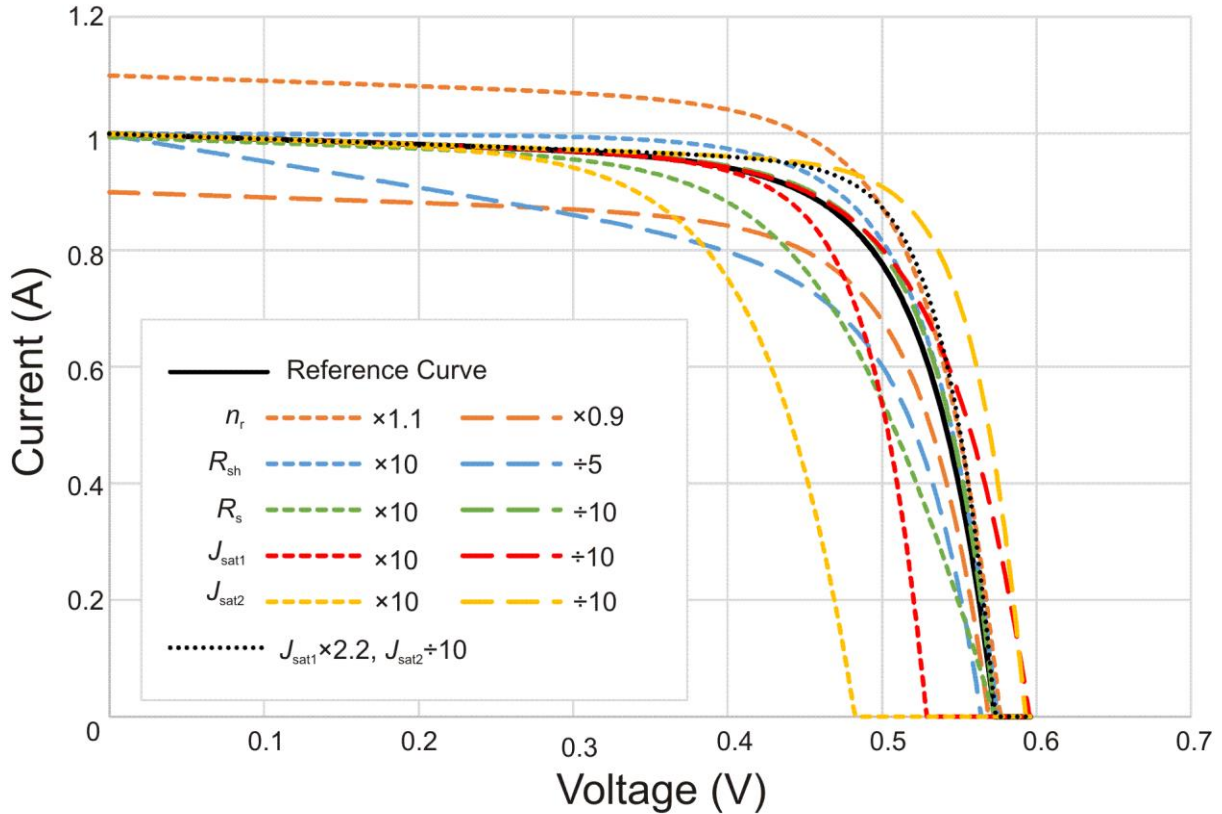


Fig. 4.3: The effects of varying solar cell parameters on the shape of the I/V curve, compared to a reference curve shown in black. The variations are generally by a factor of 10, with a few exceptions where the curve is too sensitive to that parameter. The dotted black line additionally shows both saturation currents being varied to cancel out their effects on the open-circuit voltage.

In order to obtain experimental I/V curves, an experimental measurement setup is necessary. This thesis uses a setup designed and originally used by T. Westgate for related research [78]. The setup is pictured in Fig. 4.4, with a schematic shown in Fig. 4.5. A simplified description of its operation is given here. A National Instruments USB-6008 DAQ generates two voltage signals, which are combined through a pair of operational amplifiers to generate a single, more sensitive voltage signal. This signal drives a MOSFET connecting the positive terminal of a solar cell to ground, effectively acting as a variable load on the solar cell. The solar cell terminal voltage is returned to the DAQ directly, while the solar cell current is measured across a small sensing resistor using an instrumentation amplifier. The DAQ is connected to a computer running a LabView program to vary the input voltage signal and measure the solar cell terminal voltage and current.

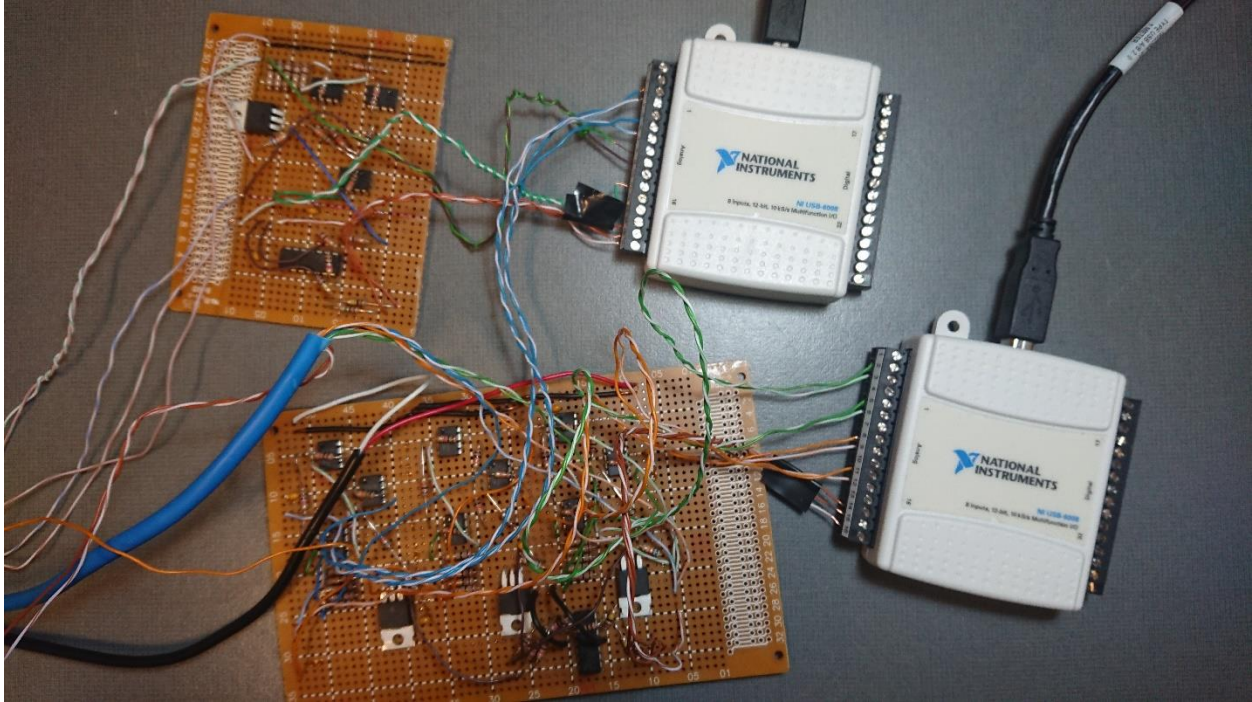


Fig. 4.4: The system for measuring solar cell I/V curves designed by T. Westgate.

Lab testing was performed on this setup using a halogen floodlamp as a light source. The spectral output of this source is shown in Fig. 4.6 compared to the standard AM1.5G spectrum. While both sources are broadband across the visible range, they otherwise do not bear a strong resemblance. This difference in spectra calls into question the accuracy of the  $R_{\lambda}$  scaling values that could be obtained through such an experiment, so that this value was ultimately derived using a different light source as explained below. The accuracy of other parameters is also potentially affected, should they exhibit a wavelength-dependence that is overlooked in this study. This was the primary motivation for ultimately redoing this experimental evaluation using natural sunlight, as described in the following subsection.

Three I/V curves were generated for this experiment using varying illumination levels and solar cells, and are shown in Fig. 4.7. These curves were then fit to the double diode solar cell equation in order to estimate the parameters. The curve fitting was set to minimize the sum of squares by varying one or two parameters at a time, down to a resolution of  $\sqrt[28]{10}$ , or 0.9035%. The parameters resulting from this curve fitting are displayed in Table 4.1.

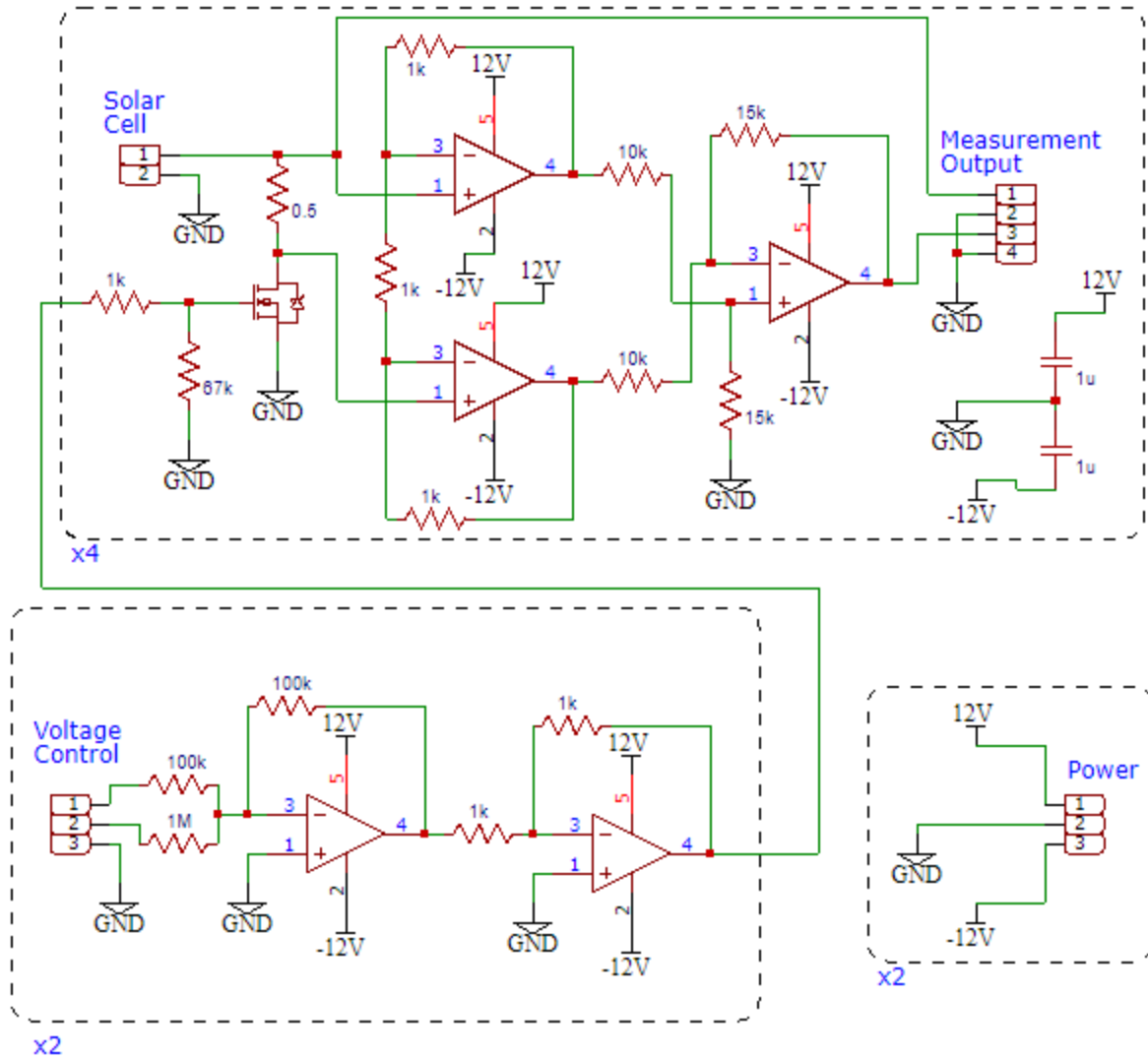


Fig. 4.5: The circuit schematic for the I/V curve measurement setup. The upper section is the measurement circuit, which is implemented four times for four solar cell channels (of which only three are used for this experiment). The solar cell is connected on the left, across a small current sense resistor and a MOSFET serving as a variable load. The voltage is output directly to the DAQ units, while the differential voltage across the current sense resistor is passed through an instrumentation amplifier to measure the current. The lower left circuit controls the variable load, while the lower right circuit is the voltage supply connection. Both of these are implemented twice, once per circuit board.

Table 4.1: The curve-fitting parameter results of the three tested lab-generated curves, along with the averaged values for each parameter to be used in simulation.

Experimental Curve	$J_{SC}$	$J_{Sat1}$	$J_{Sat2}$	$R_S$	$R_{Sh}$
#1	2.979 mA/cm <sup>2</sup>	612.9 fA/cm <sup>2</sup>	7.814 nA/cm <sup>2</sup>	92.9 Ωcm <sup>2</sup>	580.6 kΩcm <sup>2</sup>
#2	10.33 mA/cm <sup>2</sup>	2.279 pA/cm <sup>2</sup>	23.78 nA/cm <sup>2</sup>	31.94 Ωcm <sup>2</sup>	1.92×10 <sup>17</sup> Ωcm <sup>2</sup>
#3	7.647 mA/cm <sup>2</sup>	658.6 fA/cm <sup>2</sup>	4.201 nA/cm <sup>2</sup>	30.77 Ωcm <sup>2</sup>	37.71 kΩcm <sup>2</sup>
Averaged Results	-	636 fA/cm <sup>2</sup>	11.9 nA/cm <sup>2</sup>	31.4 Ωcm <sup>2</sup>	37.7 kΩcm <sup>2</sup>

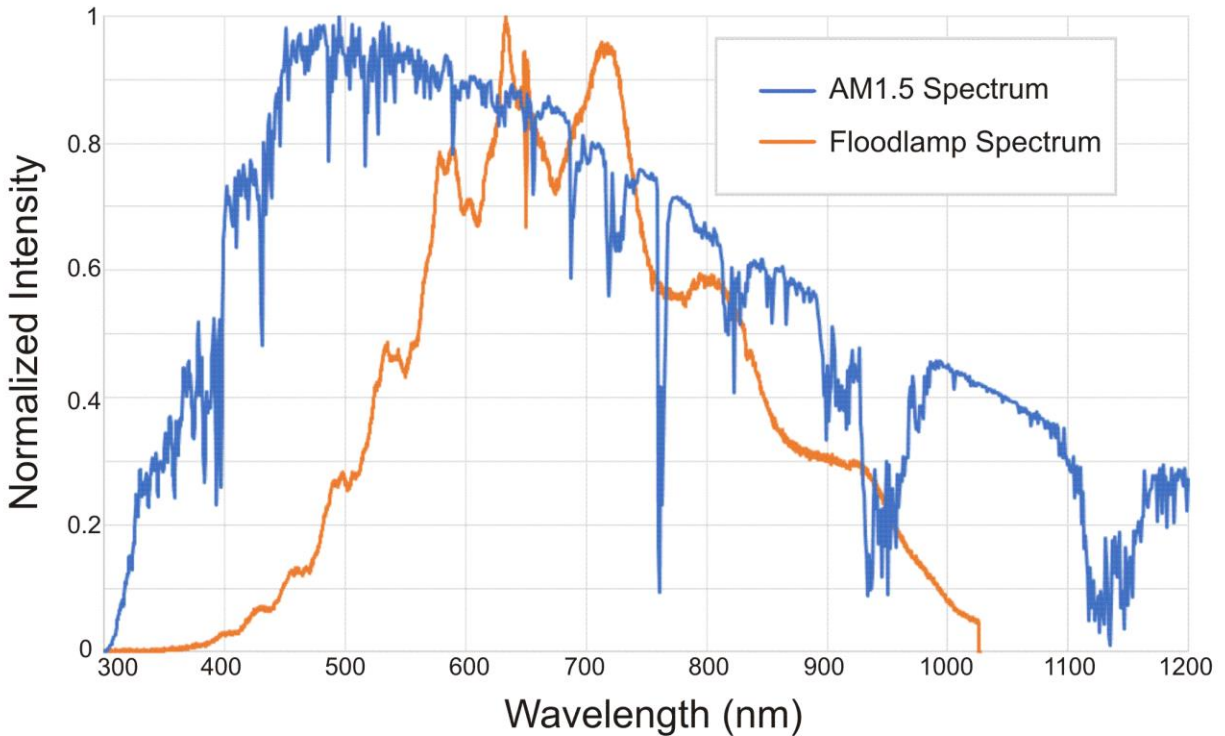


Fig. 4.6: A comparison of the halogen floodlamp spectrum, shown in orange, with the AM1.5 spectrum [118], shown in blue, with both spectra normalized. Note that the sharp IR cutoff of the floodlamp spectrum is a limitation of the spectrometer used, and is not characteristic of the floodlamp itself.

Some explanation of the values obtained is needed here. The  $J_{SC}$  values are not directly useful here, as the optical power was not measured during these tests; an additional test was required to calculate the value needed for the  $R_{\lambda}$  multiplication factor. The  $J_{Sat1}$  values were well-matched to values in the literature [129], [137], and similar across curves #1 and #3; however, curve #2 showed a significantly higher value here. This is likely due to the fact that curve #2 was generated using a solar cell that did not have the encapsulation and protective glass attached. It is probable that the encapsulation provided additional surface passivation, reducing the surface recombination and therefore the first saturation current, and validating the decision to use realistically-coated solar cells for this experiment.

The  $J_{Sat2}$  and  $R_{Sh}$  values both vary drastically between the different captures. Simulating these differing values, however, reveals that the variations do not have significant effects on the fit of the I/V curves. The effects of  $R_{Sh}$  are most noticeable in the low-voltage region of the I/V curve, which is cut off in these

captures due to the experimental setup, since the presence of a current sense resistor and a MOSFET with non-zero on-state drain-to-source resistance in series with the solar cell limits the minimum terminal voltage that can be measured. The fluctuations in  $J_{\text{Sat}2}$ , meanwhile, do not seem to have a significant effect on the I/V curve given the other measured parameters. Both fluctuations are therefore easily explainable as experimental noise. The two higher values for  $R_{\text{Sh}}$  are improbably large for a low-efficiency solar cell such as this one, but the lower value is similar to values reported in the literature [129]. All three  $J_{\text{Sat}2}$  values are much higher than those commonly reported in the literature [137]. This is, however, easily explainable, as literature values for this parameter are typically based on higher-grade solar cells where edge recombination is greatly minimized through passivated edges [129].

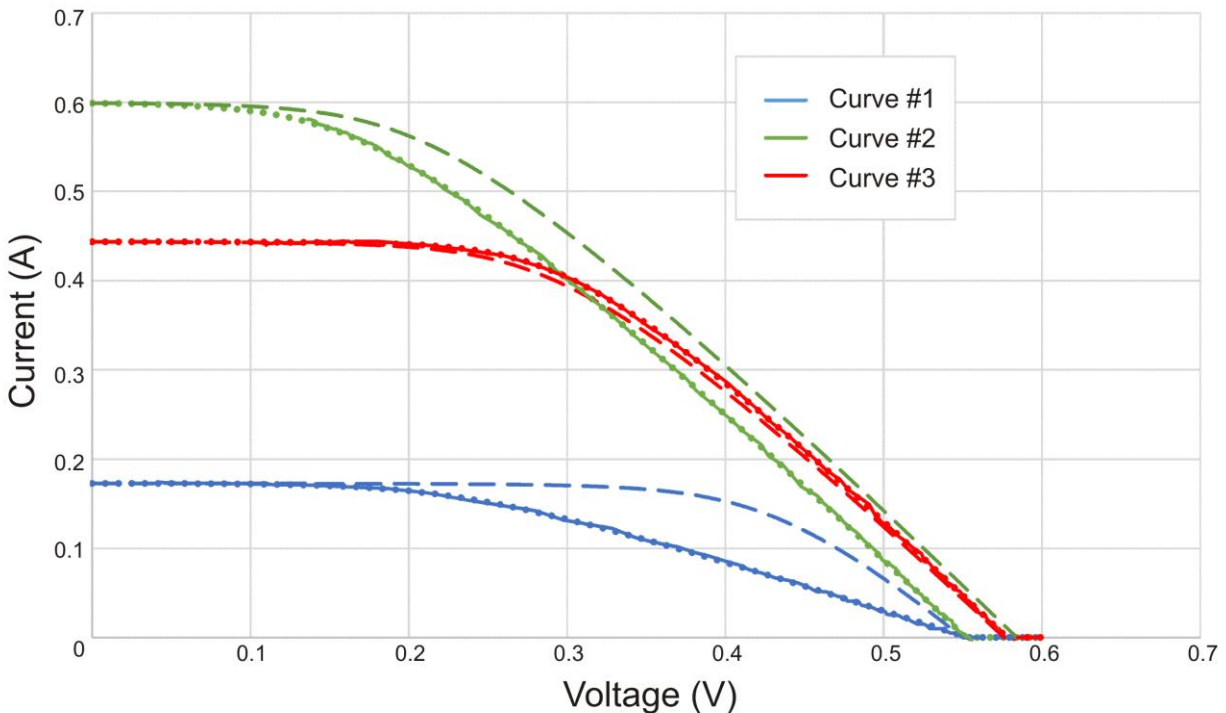


Fig. 4.7: The I/V curves derived from the preliminary lab experiments. Curves #1, #2 and #3 are shown in blue, green, and red respectively. The solid lines represent the experimental data; the dotted lines represent the curve-fit parameters; and the dashed lines represent the curves with final selected parameters. The large discrepancies between the experimental and final curves for the blue and green captures can be explained by excessive experimental series resistance and increased surface recombination, respectively.

The  $R_s$  values, too, are much higher than expected literature values [137], with the value from curve #1 being significantly greater than the other two. This result is easily explainable as experimental error. Series

resistance of any test incorporates the resistance of the testing setup as experimental error, including the solder connection between the solar cell and the tab wire, the resistance of the wires in the experimental setup, and most significantly here, the resistance of the connection between the solar cell and the measurement circuit. In these particular tests, this connection was performed with alligator clips for simplicity of setup. However, in hindsight, it is obvious that such a connection would introduce significant error to the  $R_S$  measurement.

Fig. 4.7 also shows simulated I/V curves using the calculated parameters to compare against the experimental curves. The dotted curves use the individually-calculated values, while the dashed curves use individually-calculated values for  $J_{SC}$  and otherwise the general values shown in Table 4.1, being the average value for  $J_{Sat2}$ , the average value overlooking the obvious outlier for  $J_{Sat1}$  and  $R_S$ , and the lowest value for  $R_{Sh}$ . For the experiment without excess series resistance or surface recombination, both sets of parameters fit well to the experimental measurement.

The additional experiment to determine the  $R_\lambda$  scaling factor,  $n_r$ , was performed under 532 nm monochromatic laser light, in an attempt to avoid the previously-mentioned bias due to the difference between the halogen floodlamp spectrum and the true solar spectrum. The wavelength of 532 nm is near the midpoint of the solar spectrum, and therefore a good choice of wavelength for this experiment. However, 532 nm laser light is typically produced by frequency doubling of 1064 nm laser light, and some of this near infrared light is still present in the laser beam and could affect the result. To avoid this, the beam was passed through a 335-610 nm bandpass filter, followed by a piece of translucent polystyrene to act as a diffuser, in order to spread the beam into a nearly constant illumination intensity over the entire solar cell. The results were calculated by measuring the solar cell short-circuit current using a multimeter, found to be 135  $\mu$ A, and the optical power on the solar cell, found to be 426  $\mu$ W, leading to a value of  $R_\lambda(532 \text{ nm}) = 0.317 \text{ A/W}$ . Applying this value to the normalized  $R_\lambda$  curve led to a scaling factor of  $n_r = 0.53$ . A major source of error in this calculation, however, is the extremely low optical power used for the characterization. A laser powerful enough to generate realistic solar intensities after diffusion would not be

practical to use here, and the low resulting current compounds the effect of experimental error due to the aforementioned series resistance of the experimental setup resulting in a non-zero terminal voltage. This value of 0.53 therefore has a high chance of not accurately representing the scale of the normalized  $R_s$  curve.

The high resistance of the testing equipment and the inaccurate spectrum of the light source used, together with the inaccuracies of using low optical power in the spectral responsivity experiment and the small sample of I/V curves tested, ultimately led to these solar cell parameters being recalculated. However, key findings from this experiment are still relevant to this research as a whole. The series resistance of the test setup needs to be minimized in order to determine an accurate value for the solar cell series resistance. The second saturation current will be much higher than predicted from the literature due to the high amount of edge recombination in mass-produced solar cells as compared to lab-prepared ones. And even ignoring optical properties, the inclusion of encapsulation on the solar cell affects its performance, as it acts as additional surface passivation for the solar cell, and is therefore necessary to obtain accurate experimental results. These conclusions are applied to the subsequent solar cell parameter experiments in order to improve their results.

#### 4.1.2: Collection and Analysis of Solar I/V Curves

Given the aforementioned problems with the lab-generated experiments, it was desirable to run an additional experiment under true conditions for the purpose of both accurately determining the solar cell parameters, and for comparison with the final results of the simulation to gauge its accuracy. To this end, ARIES, the Angled-panel Rooftop Illumination Experimental Setup, was designed. ARIES incorporates two unit cells from Angled-Panel Arrays with varying parameters and one unit cell from a Flat-Panel Array, and is intended to be placed on a rooftop to capture natural sunlight over the course of a day.

The choice to use only angled-panel and flat-panel arrays in ARIES is based entirely upon design complexity. Both of these arrays can be designed to require only a single solar cell per unit cell, and they

can therefore be experimentally implemented using only one solar cell. The V-Groove and U-Groove arrays, meanwhile, require a minimum of 2 and 3 solar cells per unit cell, respectively, making them more technically challenging to prototype.

The parameters selected for the two Angled-Panel Arrays were based on the results obtained from the first iteration of the rigorous simulation. The first one has a spacing of 7.8 cm and a tilt angle of  $6^\circ$ , while the second one has a spacing of 9.9 cm and a tilt angle of  $18^\circ$ . Note that both of these are much shallower than the typically-quoted guideline of having a tilt angle equal to the latitude, which for these California-optimized arrays should be  $37^\circ$ . The explanation and implications of this are discussed later, in section 4.3.2.

While only a single solar cell is necessary to evaluate each Angled-Panel Array, it is also necessary to replicate the row of solar cells in front of it in order to incorporate their role in shadowing the solar cell of interest. To this end, cardboard walls were constructed with an appropriate height and position within the setup to resemble these rows of solar cells. While the exact reflective behaviour of diffuse light in the space beneath the solar cells is not preserved by such an approximation, this setup is sufficiently accurate for the evaluations that are performed here.

The location selected for the ARIES experiment is the rooftop of a four-storey building at the University of British Columbia's Okanagan campus, in Kelowna, BC, Canada. The coordinates for this location are  $49.939^\circ$  N,  $119.394^\circ$  W. This location was selected for reasons of ease of access and is not entirely ideal for the ARIES experiment despite its location on a high and unobstructed roof, such as would be anticipated as an optimal location for these arrays as optimized here. Firstly, the location of this experiment is by necessity not California, having a similar longitude but a much more northern latitude than the simulated location. Due to this, the arc of the sun's path is much lower in the sky, resulting in a less-than-optimal power collection from the shallow Angled-Panel Arrays used. Secondly, the location of this experiment within the Okanagan Valley poses additional concerns, as large hills obstruct the horizon, such that accurate data collection very early and very late in the day is not possible. However, so long as the simulation is set

to represent comparable conditions, this data should be sufficient to validate the simulation's quality, and the measurement of solar cell parameters should not be affected by these concerns.

The complete ARIES system is shown in Fig. 4.8 installed on the rooftop. The solar cells from the three measured arrays are connected to the measurement circuit described in section 4.1.1, and the resulting data is recorded by a laptop computer. The experiment was run over the course of the day on November 8, 2018, during which data was captured at 5-minute intervals. Technical errors led to the loss of the majority of the mid-morning data, but data for the key time period around sunrise as well as for a prolonged period lasting from the middle of the day until sunset was collected successfully, which was judged to be sufficient to not require additional days of experiments. Weather conditions were ideal throughout much of this capture period, although scattered clouds began appearing around 3:00 PM and may have periodically shielded the experiment.

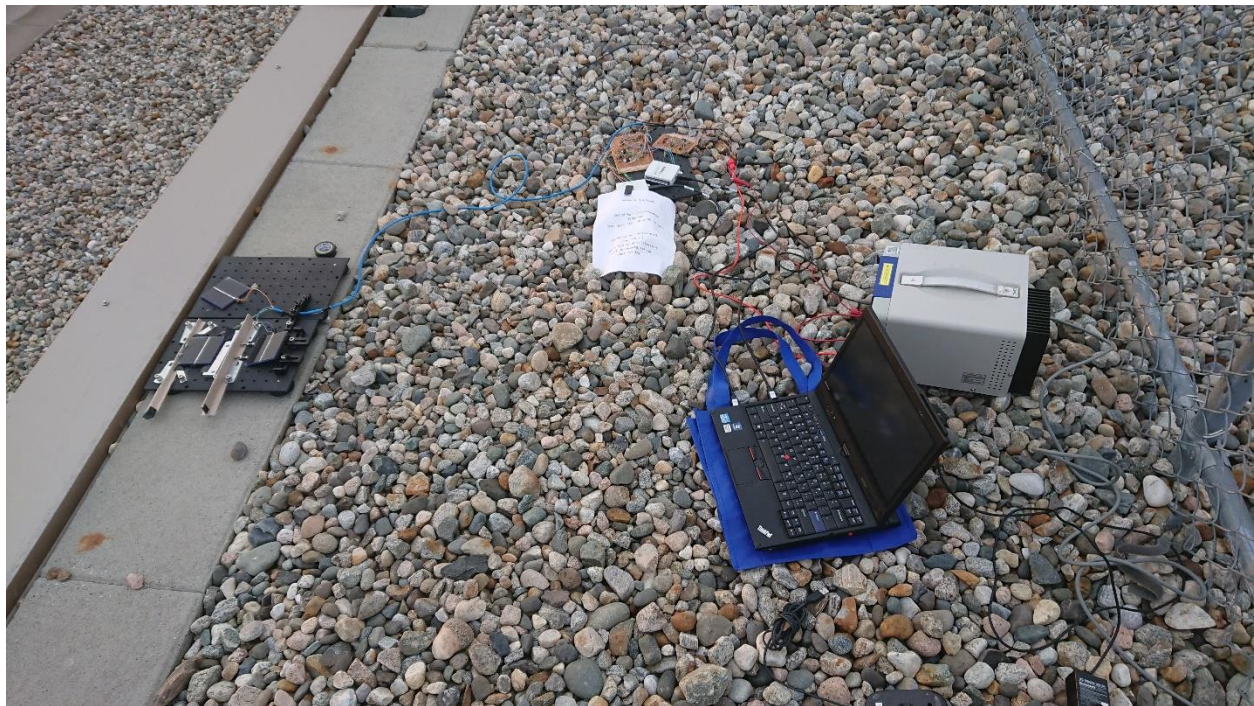


Fig. 4.8: The ARIES experimental setup. The three simulated arrays are shown to the left, with the Flat-Panel Array furthest from the camera. The upper centre of the image shows the I/V curve measuring circuit described in section 4.1.1, with the power supply and computer controlling it shown to the right.

The electrical power captured by the ARIES experiment as a function of time is shown in Fig. 4.9. The aforementioned cloud cover is clearly visible as dips in the curve after 3:00 PM. Additionally, the curve appears rather flattened through the middle of the day. This is unfortunately a symptom of excessive series resistance. Although efforts were taken to reduce this resistance for the ARIES experiment by properly soldering the circuit's electrical connections, the trend of near-constant generated electrical power beyond a certain incident optical power threshold is strongly indicative that this value is still not low enough. Examining the individual data point I/V curves confirms this, as a back-of-the-envelope calculation based on the slope of the curve after the elbow shows that the series resistance is still approximately  $30 \Omega\text{cm}^2$ , the value obtained in the previous experiment in section 4.1.1.

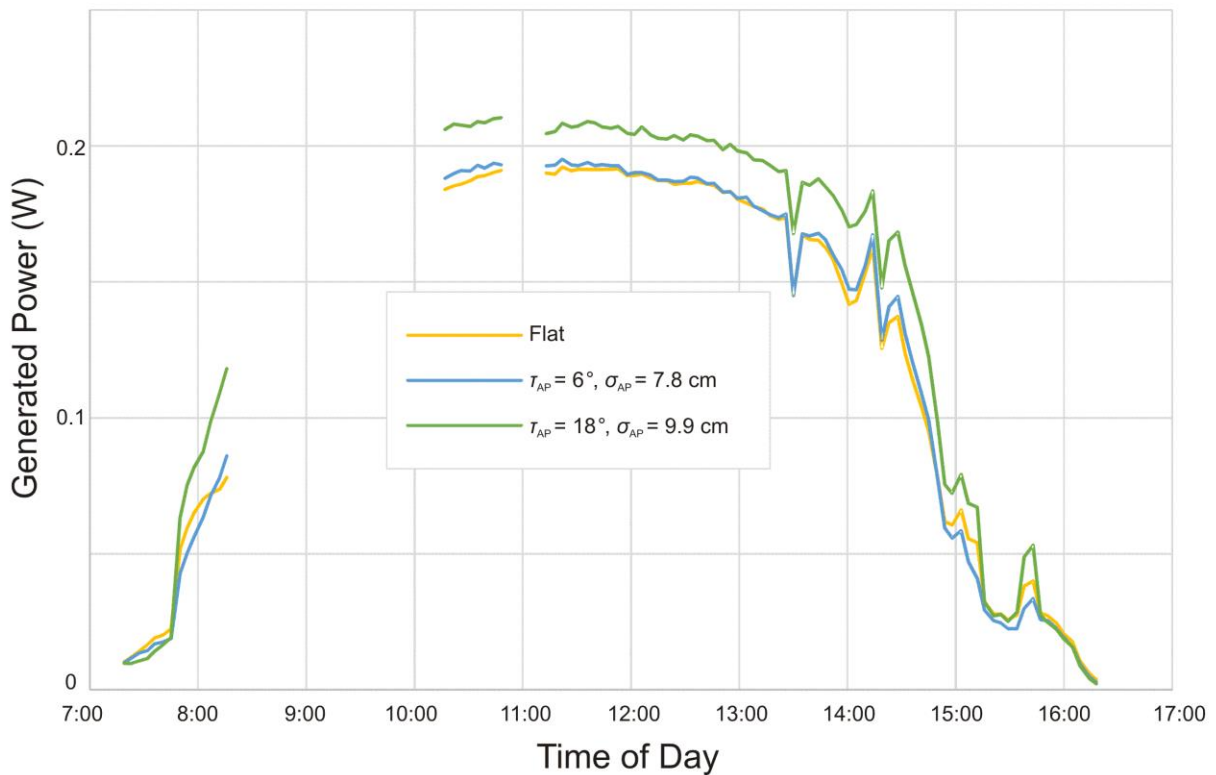


Fig. 4.9: The power captured by each array over the course of the day for the three arrays in the ARIES experiment.

Based on the results of the previous experiment, it can be concluded that experimentally determining the shunt resistance is similarly futile. Examining the slope of the I/V curves before the elbow shows it to be negligible and frequently obscured by experimental noise. While curve fitting to find a value for this would

still be possible, it was ultimately decided that the value determined in section 4.1.1 for shunt resistance could still be used here. Given the significantly-increased sample size of 276 I/V curves from this experiment, as compared to 3 from the previous experiment, the presence of an additional curve-fitting parameter would also result in a substantial increase in required processing time, so additional benefit is obtained here from the use of the previously-calculated parameter.

Therefore, the values of  $R_S$  and  $R_{Sh}$  from section 4.1.1 were applied to the double diode I/V curve equation, which was then curve-fit to the 276 data point I/V curves from the ARIES experiments to find estimated values for  $J_{SC}$ ,  $J_{Sat1}$ , and  $J_{Sat2}$  for each. The results of this curve fitting are shown in Figs. 4.10-4.12.

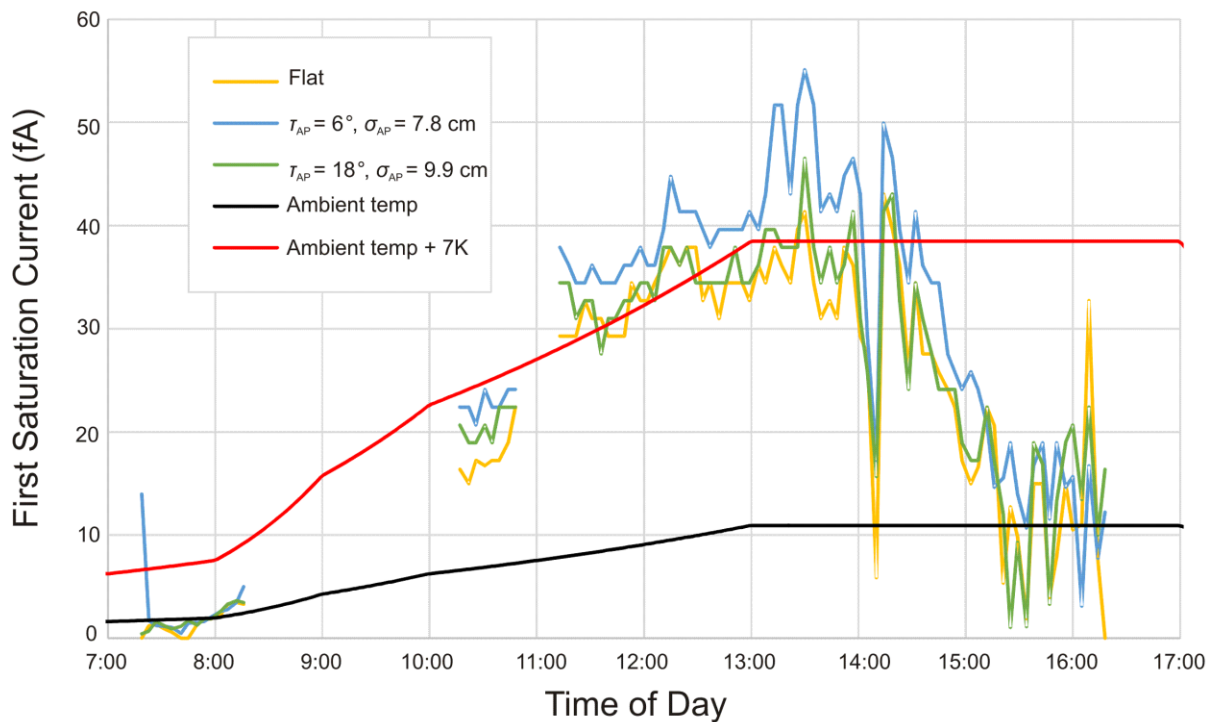


Fig. 4.10: The curve-fit values for the first saturation current obtained from the ARIES experiments. The black and red lines show simulated results at ambient temperature and at 7 K above ambient temperature respectively, scaled to match the experimental data.

The results of the curve fitting for  $J_{Sat1}$ , shown in Fig. 4.10, show an interesting trend. This value seems to follow a curve approximately mimicking that of the generated power over the course of the day. However, the value does not correspond directly to the power, as the peak is shifted significantly towards the end of the day. This variation is ultimately due to temperature dependence. While the air temperature was already

used to determine the junction thermal voltage, the first saturation current itself is also strongly dependent on temperature, according to the equation

$$J_{\text{Sat1}} \propto T^3 e^{-\frac{E_g}{k_B T}}, \quad (4.3)$$

obtained from [138]. Fig. 4.10 also shows a curve representing the possible variation of the first saturation current at the ambient temperature, which corresponds well to the early-morning data points as well as the late-day cloudy data points. To explain the significantly-higher mid-day data points, a second curve, corresponding to the ambient temperature with additional heating of 7 K, is shown. This would be the result of the heating of the solar cell above ambient temperature due to both the infrared portion of the incident direct solar illumination and the subsequent resistive and relaxation losses of the absorbed light being released as heat. This curve fits well to the measured experimental data through the middle of the day.

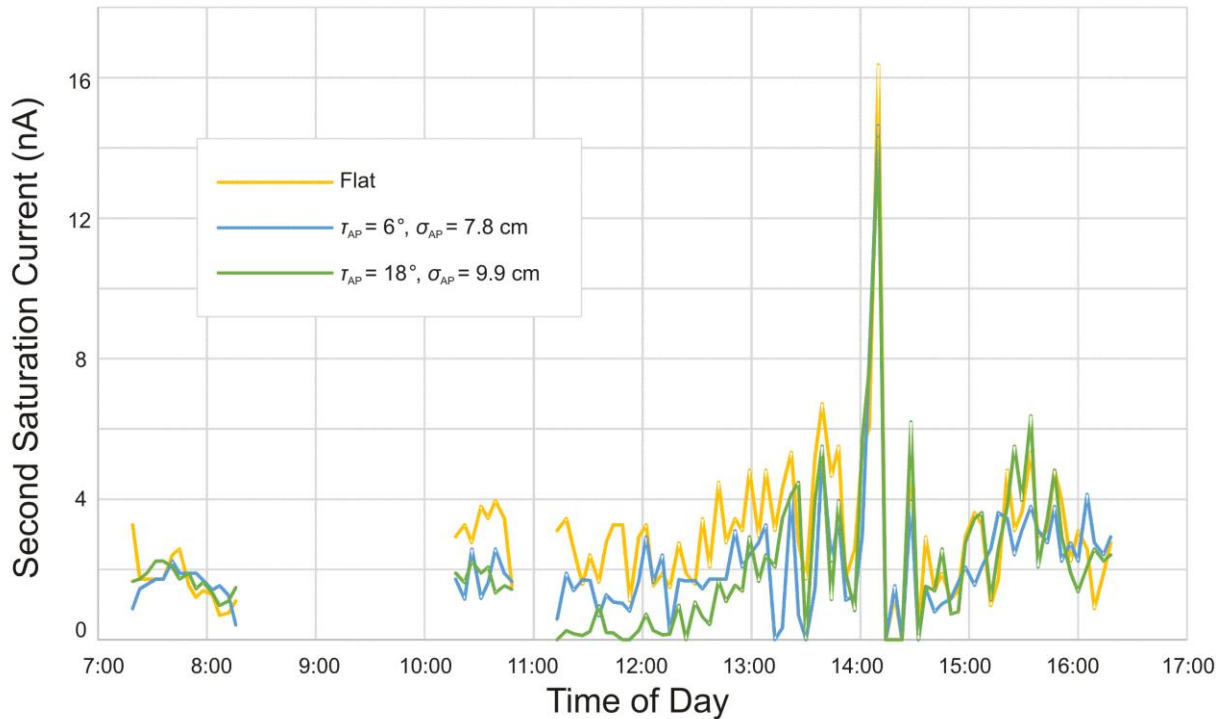


Fig. 4.11: The curve-fit values for the second saturation current obtained from the ARIES experiments.

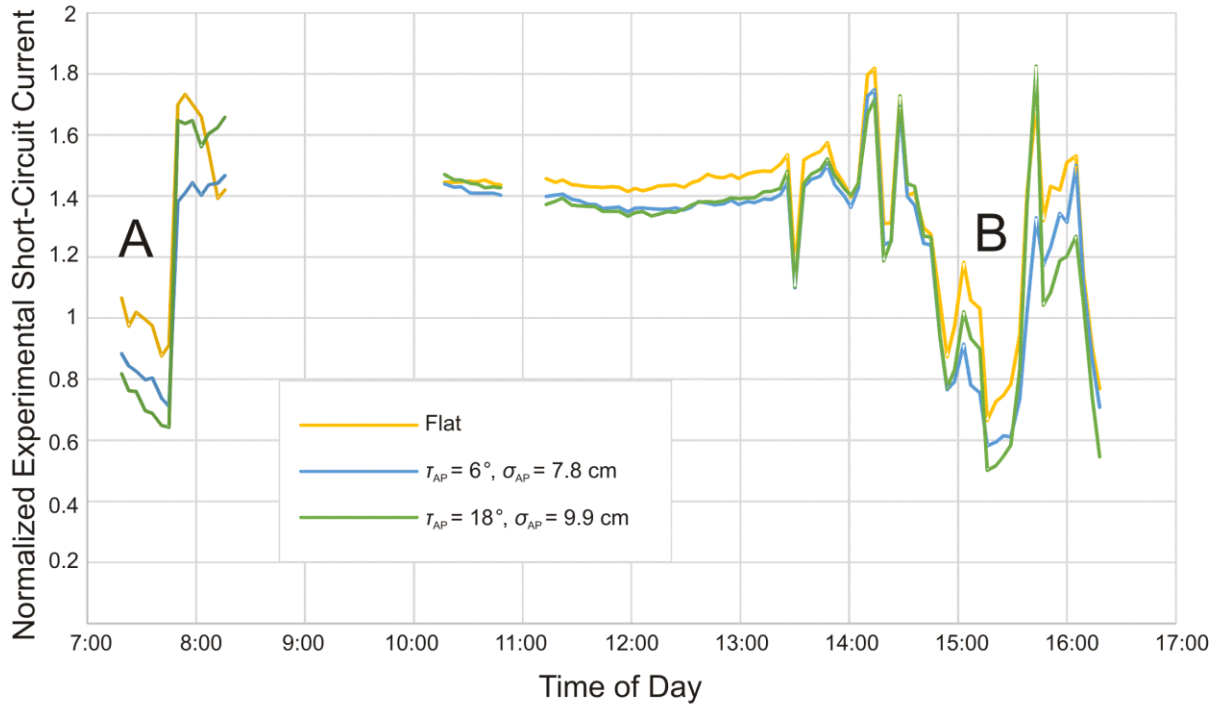


Fig. 4.12: The curve-fit values for the photocurrent obtained from the ARIES experiment, normalized to the simulated photocurrent using the spectral responsivity scaling factor previously obtained in section 4.1.1. Shadowing from hills and from afternoon clouds are indicated by A and B, respectively.

The fitted curves in Fig. 4.10 correspond to a saturation current at  $T_0 = 273.15 \text{ K}$  of  $6.25 \text{ fA/cm}^2$ . This value can be used, together with the temperature-dependence ratio established in Equation 4.3, to determine the first saturation current at an arbitrary temperature. Mapping this to  $25^\circ \text{ C}$  gives a value of  $471 \text{ fA/cm}^2$ , which is comparable to those seen in the literature [129], [137]. The two important conclusions drawn here are that temperature dependence of the first saturation current is highly significant, and resistive heating of the solar cell also has a significant effect on its performance.

The second parameter plotted in Fig. 4.11 is the second saturation current. Unlike the first saturation current, it is much harder to find any clear pattern here. A simple test of plotting I/V curves with varying second saturation currents shows that under these experimental conditions, the effect of varying the second saturation current is minor, and the large fluctuations seen here are likely experimental noise. A small rise in the middle of the day can still be observed, likely reflecting the temperature dependence of the second saturation current. This is given as

$$J_{\text{Sat2}} \propto T^{\frac{3}{2}} e^{-\frac{E_g}{2k_B T}} \quad (4.4)$$

in [139], which is much smaller than the variation for the first saturation current but is still significant. Given that the temperature on the day of the experiment began at  $-7\text{ }^\circ\text{C}$ , and was steady at  $3\text{ }^\circ\text{C}$  across most of the day, with an estimated solar cell temperature with resistive heating of  $10\text{ }^\circ\text{C}$  in the middle of the day, the average value of the second saturation current across the day is assumed to apply at  $3\text{ }^\circ\text{C}$ . This value is found to be  $2.348\text{ nA/cm}^2$ . Converting this to  $T_0 = 273.15\text{ K}$  using Equation 4.4 gives a value of  $1.775\text{ nA/cm}^2$ , while converting this to  $25\text{ }^\circ\text{C}$  gives a value of  $15.4\text{ nA/cm}^2$ , which is again comparable with those found in the literature [129].

Fig. 4.12 shows the short-circuit currents measured for the three experimental solar cells. These are normalized against simulated short-circuit currents based on the array configurations as well as the actual position of the sun, using the spectral responsivity scaling value of  $n_r = 0.53$  obtained in section 4.1.1. A few regions of this graph are obvious outliers and were overlooked during this scaling. The early-morning region marked as (A) had the sun hidden behind the hills, while the late-afternoon region marked as (B) had partial cloud cover. The remaining experimental results are nearly constant at 1.4, suggesting that the selected scaling value is 40% too low. This scaling value was therefore increased to  $n_r = 0.742$ .

The question of what to do about  $R_S$  must still be addressed. Although both this and the experiment in section 4.1.1 agreed on a value around  $30\text{ }\Omega\text{cm}^2$ , this is much higher than values given in the literature, and it must be concluded that this is a failing of the experiment and not indicative of the solar cells themselves. While this experiment improved the connection between the solar cells and the measurement circuit by soldering it, the resistance of the lengthy test wires themselves as well as the resistance of the solder paste connection between the solar cell bus bars and the tab wire are both questionable. Given the size of the solar cells used,  $30\text{ }\Omega\text{cm}^2$  corresponds to only  $0.52\text{ }\Omega$  in the measurement path, which could easily be introduced by these sources. It can, however, be assumed that although the standards of industrial solar

cells often fall below those used in laboratory conditions, dedicated methods for joining solar cells into a module would produce much better results than those seen here.

As previously discussed, this simulation will therefore use values from the literature to represent the series resistance. Values for industrial solar cells are typically near  $1 \Omega\text{cm}^2$  [129]. A slightly higher value of  $3 \Omega\text{cm}^2$  was ultimately selected, a reduction of an order of magnitude from the measured values, to account for further resistance within the wiring. Series resistance is also known to vary with temperature, but as the selected value is approximate and the variation is not as large as those of the saturation currents, this will not be represented in the subsequent simulation.

All five solar cell parameters have therefore been adequately determined using a combination of the results of the ARIES experiment, the results of the preliminary lab experiments, and literature-derived values, and can safely be assumed to represent a typical monocrystalline silicon solar cell. The experiment's secondary purpose, to validate the results of the rigorous simulation, will be shown in section 4.3.1, after the rigorous simulation itself has been thoroughly explained.

## 4.2: Design of the Rigorous Simulation

This section takes a detailed look at the design of the rigorous simulation and the ways in which it differs from the simplified simulation presented in chapter 3. The first step in designing a more rigorous simulation is to challenge some of the fundamental assumptions that were made in the design of the simplified simulation. In particular, the location and temperature selected for the simplified simulation were both highly generalized. The use of more realistic values for these two quantities could improve the accuracy of the rigorous simulation. Additionally, as the Angled-Panel Array was not included in the simplified simulation, the applicability of certain assumptions made there to this array must be considered.

The previous simulation used a location central to California, and averaged electricity prices over the entirety of the state. Such an implementation is rather inaccurate due to the simple fact that solar generation is not evenly distributed across the entire state. The northern coast of California, for example, experiences

a typically overcast climate, which is not particularly amenable to photovoltaic generation. However, the relative isolation of communities in this region increases the cost of electricity transmission, thereby raising the electricity price and skewing the state-averaged price higher than that which would be seen at most photovoltaic generation sites [98].

Commercial solar generation within the state of California is primarily located in the southern half of the Central Valley, as well as the southern interior desert [140]. While this study is not focused on large-scale generation, these locations demonstrate where optimal conditions for solar generation will be located within the state. Additionally, regions with significant amounts of commercial solar generation are likely to experience a more severe “Duck Curve” effect, and therefore receive greater benefits from value-based optimization metrics.

The location ultimately selected for this study is  $35^{\circ}\text{N}$ ,  $119^{\circ}\text{W}$ , near the city of Bakersfield, California. This location is on the border of multiple solar generation hotspots, and also in close proximity to the urban areas of greater Los Angeles, where rooftop solar generation such as that proposed in this study would be optimal. Instead of being averaged over the entirety of the state, only pricing data from within the area bounded by  $34^{\circ}\text{N}$ ,  $118^{\circ}\text{W}$ ,  $36^{\circ}\text{N}$ , and  $120^{\circ}\text{W}$  was used to generate the electricity prices for this study. These values were found by gathering price node names and coordinates from CAISO’s real-time price map [141], and matching these against the node names and historical day-ahead locational marginal price data previously obtained from OASIS [98]. The effect that limiting the area in such a manner has on the pricing data used is shown in Appendix A. As with the simplified simulation, these values were then averaged with negative numbers treated as zero. Unlike in the simplified simulation, however, the values were not time-interpolated. For this simulation, the economic performance of the arrays is of greater interest than their societal benefit (which would be represented by a smooth price curve), and a constant price for every hour is more likely to exist in an actual power purchase agreement than a constantly-varying price.

One important consideration to make here is the applicability of the negligible end-effect assumption to the Angled-Panel Array, as this array was not considered when the assumption was originally made for the

simplified simulation. It was previously stated that this assumption relies partially on the fact that the sun will not typically be on the southern horizon. However, as the Angled-Panel Array has grooves running in an east-west direction rather than north-south, the corresponding conditions would have the sun on the eastern or western horizon, conditions which do happen frequently.

The key to solving this problem lies in the fact that the end effect applies primarily to direct solar illumination, and in the conditions mentioned above, the incidence of direct solar illumination onto the solar cells of the Angled-Panel Array will be at an extremely shallow angle. It is therefore likely that most direct solar illumination will be reflected off the solar cells rather than absorbed, and therefore the absorption of direct solar illumination will be less significant than the absorption of diffuse light from the rest of the sky. This is aided by the fact that the Angled-Panel Array has only a single side covered with solar cells, so it is impossible for direct solar illumination to propagate down the groove through multiple specular reflections, as it can only experience diffuse reflection off the back of the solar cells and the ground between them. Due to these observations, it can be concluded that the end effect can still be ignored for the Angled-Panel Array even if it is not as insignificant as for the other arrays.

Given the strong dependence on temperature observed during the ARIES experiment, the use of a single standard test condition value for temperature is no longer viable. In order to provide a somewhat accurate estimate of daily temperature, the monthly-averaged daily maximum and minimum temperatures were collected from the National Oceanic and Atmospheric Administration's Online Weather Data service [142]. This data was collected for two weather stations, Sandberg and Bakersfield Airport, selected to be near and approximately equidistant in opposite directions from the previously selected simulation coordinates. Data was collected for the 6-year period from 2013 to 2018, and then averaged to give a monthly estimated high and low temperature. Based on observations of daily temperature curves in that region, the decision was made to place the low temperature at 6:00 AM, and the high temperature at 1:00 PM. Details of the conversion of these values into a temperature curve, and the subsequent addition of solar cell resistive heating temperature, are expanded upon in section 4.2.4.

Unfortunately, the vastly increased complexity of the rigorous simulation means that certain tradeoffs need to be made to ensure that the simulation runtime does not become unfeasibly long. To this end, saving and reuse of intermediate variables at several points of the simulation will be introduced to reduce the number of calculations required. In order for this strategy to be successful, the input parameters must be quantized enough for identical conditions to be replicated frequently. This is in addition to the quantization necessarily introduced through the use of continuous spectra. Such quantization will be noted and justified wherever it occurs throughout the subsequent simulation design. Additionally, the length of the simulation was decreased to five years by removing the year of July 1, 2012-June 30, 2013, since the simplified simulation did not show that the extended length was useful.

To summarize these starting parameters and assumptions for the rigorous simulation, the location is still taken as a rooftop with unobstructed horizons, but is moved to the location of 35°N, 119°W. The array is again assumed to be sufficiently large relative to its structures to minimize end effects, and to have a height limited to one solar cell's side length. Temperature is approximated as linearly transitioning between a minimum value at 6:00 AM and a maximum value at 1:00 PM. Quantization of various intermediate steps in the simulation will be used to facilitate the reuse of calculations. The assumptions for the solar cells' electrical connections as well as the array section to be simulated remain the same as was previously discussed in section 3.1.5.

The following subsections provide an explanation of the rigorous simulation and the details of its design. The calculation of atmospheric direct and diffuse light is explained first, followed by the optical behaviour of the four arrays. More detail is given on the metric of relative profit density, and the calculations used to convert optical power to relative profit density are then explained.

#### 4.2.1: A Model for Atmospheric Light

The simulation design must begin with a representation of the illumination, both direct and diffuse, which enters the solar arrays. For the simplified simulation, this was represented by an aggregate number for the

direct solar illumination while the diffuse sky light was ignored, but for this simulation, a more detailed representation is necessary.

For direct solar illumination, this representation begins with the AM0 and AM1.5D spectra previously obtained from [118]-[119] and shown in Fig. 2.5. All absorption and scattering processes act on direct solar illumination as an exponential decay based on the transmission path through the atmosphere, and therefore the air mass. However, this only holds true if the solar spectrum is quantized into differential elements small enough that the absorption and scattering of each element is approximately constant. This is a simple condition to meet for most scattering and absorption processes. Molecular absorption, however, typically occurs in narrow bands, and may therefore have its accuracy compromised if the differential elements are not sufficiently small [143].

The spectra used here have 1 nm steps between data points and run from 300 nm to 1200 nm. Light below 300 nm is almost entirely blocked by the atmosphere, while light above 1200 nm does not undergo absorption for the silicon bandgap. The 1 nm step is on the order of the features of the most significant molecular absorption band in the visible spectrum, the 760 nm oxygen A-band [144], so while this step size is not ideally small, it should be sufficiently small to minimize the error of using exponential decay to calculate air-mass-dependent absorption. Ultimately, the step size was determined by practical concerns, as it was the resolution of the spectral data obtained from [118]-[119].

Given the presence of two direct solar illumination spectra with established air mass values and the assumption of exponential decay based on propagation distance for any specified wavelength, it becomes possible to define a general expression for the direct solar illumination spectrum as a function of air mass,

$$S_{\lambda,D}(AM) = \frac{S_{\lambda,D}(1.5)^{\frac{AM}{1.5}}}{S_{\lambda,D}(0)^{\frac{AM}{1.5}-1}}. \quad (4.5)$$

In order to use this equation, the air mass must also be calculated, which is done based on the zenith angle using the equation

$$AM = \frac{1.002432 \cos^2(\theta) + 0.148386 \cos(\theta) + 0.0096467}{\cos^3(\theta) + 0.149864 \cos^2(\theta) + 0.0102963 \cos(\theta) + 0.000303978}, \quad (4.6)$$

obtained from [145].

The calculation of a diffuse light spectrum is a much more challenging conundrum. The AM1.5Diff spectrum can be easily found, but diffuse light does not exponentially decay with the air mass. Regardless of the angle of incident direct solar illumination, the volume of atmosphere near the solar generating array in which scattering can occur remains constant. At higher zenith angles, the direct solar illumination passing through this volume becomes less intense as some of it will already pass through a substantial portion of the atmosphere before reaching this volume, reducing the amount of sunlight available to be scattered accordingly. Additionally, the steeper angle of scattering required for this high-angled light to reach the ground reduces the quantity of Mie-scattered light that will be incident on the solar generating array. Generally, it can be assumed that while the intensity of diffuse light will decrease with increasing zenith angle, it will do so less quickly than the exponential decay seen for direct solar illumination.

The selection of a formula to relate diffuse light intensity and zenith angle is complicated by the fact that illumination at sunrise and sunset is a major point of interest to this work. Many approximate formulas for diffuse light intensity exist, but they share the common characteristic of becoming zero when the zenith angle is equal to  $\pi/2$  rad. Obviously, this is not entirely accurate, as the sky does not instantly become completely dark when the sun sets. Data sets for the diffuse light intensity with the sun near the horizon also exist, but generally do not extend into the middle of the day. For this simulation to have sufficient accuracy here, it becomes necessary to combine these two types of formulas.

For low-zenith (midday) diffuse light, the formula used is

$$I_{\text{diff}} = 39.78 \text{ W/m}^2 \times \cos^{0.35}(\theta) + 2.6 \text{ W/m}^2 \times \cos^{0.66}(\theta)(1000B - 12)^{0.81}. \quad (4.7)$$

This formula was obtained from [146], and includes as a parameter the Schuepp Turbidity Coefficient,  $B$ , which relates to the real-time particulate content of the atmosphere. Based on the values given in [147], a constant  $B$  equal to 0.08 was selected.

For high-zenith (horizon) diffuse light, the data collected by [148], specifically the data for sky brightness around sunset at Sacramento Peak, NM, was used for curve fitting. An approximate equation was found to fit the zenith data point, and was then checked against all other data points to verify that it was well-representative of the sky as a whole. This fitted equation is

$$I_{\text{diff}} = (1.64 - \theta)^{1.8}. \quad (4.8)$$

Under this equation, the sky stays illuminated until the sun is 0.07 rad ( $4^\circ$ ) below the horizon. Beyond this point, any remaining light should not be sufficient to activate the solar cells.

The horizon diffuse light equation as given here is not properly scaled, and needed to be adjusted to match the midday diffuse light equation. A zenith value of 1.53 rad was chosen to join the equations as their scaled slopes were approximately equal at this point. The complete diffuse light intensity equation is therefore

$$I_{\text{diff}} = \begin{cases} 39.78 \text{ W/m}^2 \times \cos^{0.35}(\theta) + 79.3059 \text{ W/m}^2 \times \cos^{0.66}(\theta), & \theta \leq 1.53 \text{ rad} \\ 1200.2 \text{ W/m}^2 \times (1.64 \text{ rad} - \theta)^{1.8}, & 1.53 \text{ rad} < \theta \leq 1.64 \text{ rad} \\ 0, & \theta > 1.64 \text{ rad} \end{cases} \quad (4.9)$$

At this point, some assumptions must be made to successfully determine the diffuse light spectrum at an arbitrary zenith angle. The variation in both time and space of diffuse light has previously been discussed in section 2.2.1. To calculate the diffuse light spectrum in a simplified manner, these variations will be ignored, and it will be assumed that the spectral distribution of diffuse sky light is always equal to the AM1.5Diff spectrum, with only the intensity varying, and with that variation being uniform across the sky. With these assumptions, the diffuse sky light spectrum can be obtained by taking the AM1.5Diff spectrum, normalizing it, and multiplying the result by Equation 4.9.

#### 4.2.2: Optical Power with Diffuse and Polarized Light

Given this more advanced simulation, the simplified assumption of a single number for solar cell reflectance must be challenged. The solar cell is a complex multi-layered system, and the following calculations attempt to give a more detailed explanation of its optical properties.

The reflectance of direct (specular) light off the front glass surface of the solar cell can be calculated using the Fresnel equations, as was done in the simplified simulation. Unlike with that simulation, however, S- and P-polarized light are kept separate here and calculated as

$$R_{g,S}(\lambda, \theta_i) = \left( \frac{\cos(\theta_i) - n_g \sqrt{1 - \frac{\sin^2(\theta_i)}{n_g^2}}}{\cos(\theta_i) + n_g \sqrt{1 - \frac{\sin^2(\theta_i)}{n_g^2}}} \right)^2, \quad (4.10)$$

$$R_{g,P}(\lambda, \theta_i) = \left( \frac{\sqrt{1 - \frac{\sin^2(\theta_i)}{n_g^2}} - n_g \cos(\theta_i)}{\sqrt{1 - \frac{\sin^2(\theta_i)}{n_g^2}} + n_g \cos(\theta_i)} \right)^2, \quad (4.11)$$

based on the incident angle of light,  $\theta_i$ , and the wavelength-dependent refractive index of glass,  $n_g$ , which was previously shown in Fig. 2.6. It can be assumed that direct solar illumination is initially unpolarized, and subsequent polarization of the specular light can be tracked.

An additional equation can be derived for the reflectance of diffuse light off the air-glass interface. Given that the diffuse light is assumed to be Lambertian, the amount of diffuse light hitting the glass at a given incident angle would be proportional to the product of the sine and cosine of that angle from the normal, with the sine term representing the total solid angle area at that angle, and the cosine term representing the projection of the light into the plane of the glass. With this in mind, it is possible to average the reflection over the entire hemisphere, generating a diffuse reflectance equation of

$$R_{g,D}(\lambda) = \int_0^{\pi/2} \left( R_{g,S}(\lambda, \theta_i) + R_{g,P}(\lambda, \theta_i) \right) \cos(\theta_i) \sin(\theta_i) d\theta_i. \quad (4.12)$$

A factor of 2 is added out here, cancelling the 0.5 from averaging the specular reflectances, in order to normalize the result so it equals 1 if both specular reflectance terms are equal to 1. This equation is built on the assumption that the diffuse light is Lambertian at the surface of the glass. While this light can typically be accurately assumed to be Lambertian at its source, it is unlikely that said source covers the entire hemisphere visible from the surface of the glass, except in certain specific cases such as the diffuse sky light incident on a Flat-Panel Array. The calculation of diffuse reflection based on the location and shape of the source relative to the reflective surface would provide more accurate results, but such an implementation would be much more complex and require the reflection to be individually calculated every time it is used.

Specular reflectance off the inside of the glass interface can be calculated similarly. Although it will not be used directly, as this model assumes that the anti-reflection coating does not produce any specular reflections, it will be used to build subsequent diffuse reflectance terms. The unpolarized reflectance term for specular light off the inside of the glass interface is

$$R_{gi,Spec} = \min \left( \frac{1}{2} \left( \frac{n_g \cos(\theta_i) - \sqrt{1 - n_g^2 \sin^2(\theta_i)}}{n_g \cos(\theta_i) + \sqrt{1 - n_g^2 \sin^2(\theta_i)}} \right)^2 + \frac{1}{2} \left( \frac{n_g \sqrt{1 - n_g^2 \sin^2(\theta_i)} - \cos(\theta_i)}{n_g \sqrt{1 - n_g^2 \sin^2(\theta_i)} + \cos(\theta_i)} \right)^2, 1 \right). \quad (4.13)$$

This can then be used to build the diffuse reflectance off the inside of the glass, which is calculated as

$$R_{gi,D}(\lambda) = \int_0^{\pi/2} 2R_{gi,Spec}(\lambda, \theta_i) \cos(\theta_i) \sin(\theta_i) d\theta_i. \quad (4.14)$$

Similarly, absorptance can be defined for the various layers of the solar cell. This begins with the absorption coefficients of the materials,  $\alpha$ , which are derived from the extinction coefficients,  $\kappa$ , given in Fig. 2.6, as

$$\alpha = \frac{4\pi\kappa}{\lambda}. \quad (4.15)$$

The absorptance of specular light in the glass layer as a function of the incident angle of the light before it enters the glass is given as

$$A_{g,Spec} = 1 - e^{-\frac{\alpha_g t_g}{\cos\left(\arcsin\left(\frac{\sin(\theta_i)}{n_g}\right)\right)}}. \quad (4.16)$$

This equation requires the thickness of the glass layer,  $t_g$ , which was measured to be 3.05 mm.

As with the reflectances, the absorptance of diffuse light entering the glass from the air can be found by multiplying the specular light by double the sine and cosine of the angle, to account for relative density of directions and projection of the light onto the glass surface, and integrating the result. This results in

$$A_{ag,D} = \int_0^{\pi/2} 2A_{g,Spec}(\theta_i) \sin(\theta_i) \cos(\theta_i) d\theta_i. \quad (4.17)$$

As the diffuse light transmitting upwards through the glass is assumed to be Lambertian within the glass, rather than being converted to Lambertian after entering the glass, its formula is very similar, but does not convert the path length term to account for refraction through the interface:

$$A_{g,D} = \int_0^{\pi/2} 2 \left( 1 - e^{-\frac{\alpha_g t_g}{\cos(\theta_i)}} \right) \sin(\theta_i) \cos(\theta_i) d\theta_i. \quad (4.18)$$

One additional quantity must be calculated for diffuse light in the glass layer. Initially Lambertian light that internally reflects off the glass-air interface will no longer have a Lambertian profile, as the steeper light paths are disproportionately likely to be reflected. Therefore, the absorptance of initially diffuse light originating from the glass-silicon interface before reflecting internally off the glass-air interface is calculated as

$$A_{\text{gi,D}} = \int_0^{\pi/2} \left( 1 - e^{\frac{-\alpha_g t_g}{\cos(\theta_i)}} \right) \frac{2R_{\text{gi,Spec}}(\theta_i) \cos(\theta_i) \sin(\theta_i)}{R_{\text{gi,D}}} d\theta_i. \quad (4.19)$$

Taking the ratio between the specular and diffuse reflectances off the inside of the glass gives the normalized amount of light that reflects at a specific angle.

Finally, the calculation of absorptance in silicon follows much the same pattern as the glass absorptances. However, here the reflectance of the silicon-aluminum interface must be considered. As the light passing through this interface is minimal, this interface will be assumed to be a perfect specular reflector for simplicity. This means that the path length for light through the silicon layer can simply be doubled to account for the path in both directions. The total absorptance in this layer is therefore

$$A_{\text{Si}} = \int_0^{\pi/2} 2 \left( 1 - e^{\frac{-2\alpha_{\text{Si}} t_{\text{Si}}}{\cos(\theta_i)}} \right) \sin(\theta_i) \cos(\theta_i) d\theta_i, \quad (4.20)$$

calculated using the thickness of the silicon layer,  $t_{\text{Si}}$ , which was found to be 176  $\mu\text{m}$  based on Fig. 3.7.

Similarly, the reflectance off the glass-silicon interface has yet to be considered. Given that this is highly dependent on the anti-reflective coating used, using wavelength-dependent values from the literature is unnecessarily complicated for a negligible gain in accuracy, and an experimental measurement is not possible due to the difficulty of determining non-specular hemispherical wavelength-dependent reflectance from a specular source, including the effects of the glass refractive index but not of its front interface. Therefore, a flat value will be used for this reflectance, based on typical literature reflectance values [60], of

$$R_{\text{ARC}} = 0.05. \quad (4.21)$$

In order to reduce the complexity of the simulation, the reflectance and absorptance values shown above are calculated once and then reused as needed. For this, the incident angle of light must be quantized, which is done by rounding it to the nearest 2°.

Using these values the total reflective behaviour of the solar cell can be calculated. As the anti-reflective coating is assumed to diffuse all light that passes through or reflects off it, specular reflections occur only off the front surface, and are calculated as

$$P_{S,out} = P_{S,in} R_{g,S}(\lambda, \theta_i), \quad (4.22)$$

$$P_{P,out} = P_{P,in} R_{g,P}(\lambda, \theta_i), \quad (4.23)$$

The total diffuse reflectance is more complex, but can still be calculated using the sum of infinite geometric series to represent multiple internal reflections within the solar cell structure. The end result of this is calculated as

$$P_{D,out} = P_{D,in} R_{g,D} + \frac{\left[ \left[ P_{D,in} (1 - R_{g,D}) (1 - A_{ag,D}) + P_{S,in} (1 - R_{g,S}) (1 - A_{g,Spec}) + P_{P,in} (1 - R_{g,P}) (1 - A_{g,Spec}) \right] \times (1 - R_{gi,D}) (1 - A_{g,D}) \left[ (1 - R_{ARC})^2 (1 - A_{Si}) + R_{ARC} - R_{ARC}^2 (1 - A_{Si}) \right] \right]}{\left[ R_{ARC}^2 R_{gi,D} (1 - A_{gi,D}) (1 - A_{Si}) (1 - A_{g,D}) - (1 - R_{ARC})^2 R_{gi,D} (1 - A_{Si}) (1 - A_{gi,D}) (1 - A_{g,D}) \right] - R_{ARC} (1 - A_{Si}) - R_{ARC} (1 - A_{gi,D}) R_{gi,D} (1 - A_{g,D}) + 1} \quad (4.24)$$

The power absorbed by the silicon can similarly be calculated as

$$P_{abs,Si} = A_{Si} (1 - R_{ARC}) \times \frac{\left[ P_{D,in} (1 - R_{g,D}) (1 - A_{ag,D}) + P_{S,in} (1 - R_{g,S}) (1 - A_{g,Spec}) + P_{P,in} (1 - R_{g,P}) (1 - A_{g,Spec}) \right]}{\left[ R_{ARC}^2 R_{gi,D} (1 - A_{gi,D}) (1 - A_{Si}) (1 - A_{g,D}) - (1 - R_{ARC})^2 R_{gi,D} (1 - A_{Si}) (1 - A_{gi,D}) (1 - A_{g,D}) \right] - R_{ARC} (1 - A_{Si}) - R_{ARC} (1 - A_{gi,D}) R_{gi,D} (1 - A_{g,D}) + 1} \quad (4.25)$$

As this simulation introduces the use of polarization for the specular light, it is also necessary to define an equation for the transfer of polarization between two surfaces. This is most easily calculated using vectors.

The S-polarization direction of light on each surface can be found by taking the cross product of the surface normal vector and the light propagation vector. The amount of S-polarized light from the first side that remains S-polarized when incident on the second side is proportional to the square of the cosine of the angle

between the two surfaces' S-polarization directions. As the two polarization directions are rotationally symmetric, the percentage of P-polarized light that remains P-polarized must be equal to the percentage of S-polarized light that remains S-polarized. The polarization of light on the second surface can therefore be calculated as

$$P_{S,2} = P_{S,1} \frac{\hat{n}_1 \times \vec{l} \cdot \hat{n}_2 \times \vec{l}}{|\hat{n}_1 \times \vec{l}| |\hat{n}_2 \times \vec{l}|} + P_{P,1} \left[ 1 - \frac{\hat{n}_1 \times \vec{l} \cdot \hat{n}_2 \times \vec{l}}{|\hat{n}_1 \times \vec{l}| |\hat{n}_2 \times \vec{l}|} \right], \quad (4.26)$$

$$P_{P,2} = P_{P,1} \frac{\hat{n}_1 \times \vec{l} \cdot \hat{n}_2 \times \vec{l}}{|\hat{n}_1 \times \vec{l}| |\hat{n}_2 \times \vec{l}|} + P_{S,1} \left[ 1 - \frac{\hat{n}_1 \times \vec{l} \cdot \hat{n}_2 \times \vec{l}}{|\hat{n}_1 \times \vec{l}| |\hat{n}_2 \times \vec{l}|} \right], \quad (4.27)$$

where the surface normal vectors are denoted by  $\hat{n}$  and the light propagation vector is denoted by  $\vec{l}$ .

The calculation of zenith and azimuth angles as a function of the time and date is mainly unchanged from what was used for the simplified simulation, in Equations 3.9-3.15. However, the zenith angle calculation has been updated with the introduction of atmospheric refraction, which serves to decrease the apparent zenith angle of the sun when it is near the horizon. The formula used for this is

$$\theta_{\text{apparent}} = \theta - 2.967 \times 10^{-4} \text{ rad} \times \cot \left( \frac{\pi}{2} - \theta + \frac{0.003138 \text{ rad}^2}{1.66 \text{ rad} - \theta} \right), \quad (4.28)$$

which was taken from [149] and converted to radians.

Additionally, to allow for the increased reuse of the calculated generated electrical power, both the zenith and the azimuth have been quantized. The zenith angle is rounded to the nearest  $1/3^\circ$ , or 0.0058 rad. This value was chosen to be less than the angular diameter of the Sun ( $0.53^\circ$ ) so that the position error is less than the error inherent in considering the sun to be a columnated source.

The quantization of the azimuth angle is slightly more complex. Near the horizon, the azimuth angle is more significant, while overhead a small change in the sun's position can lead to a very large change in the

azimuth angle. To maintain sufficient accuracy in the crucial high-zenith locations while avoiding excessive resolution in the low-zenith locations that could lead to reduced reuse of values and inconsistent position error, a dynamic azimuth quantization is required. The azimuth value is therefore rounded to be

$$\phi_{\text{quantized}} \in n \frac{\pi}{2 \times \text{ceiling}(270 \sin(\theta))}, \quad (4.29)$$

where  $n$  is an integer. With this formula, the azimuth angle has the same resolution as the zenith angle at the horizon, is always 0 at the zenith, and can always take on the values of 0 and  $\pm\pi/2$  rad so long as the zenith angle is non-zero.

While the configurable array parameters are primarily accounted for in the following subsections analyzing the incident light for each array, the rotation angle,  $\rho$ , can be introduced in a more simplified manner by merely subtracting it from the azimuth. All references to the azimuth throughout the following subsections refer to this effective azimuth.

#### 4.2.2.1: The Flat-Panel Array

The calculation of specular light absorption for the Flat-Panel Array is essentially unchanged from the specular light absorption presented in section 3.2.4.1. The primary difference is that the absorption calculation is replaced with the more advanced one given in Equation 4.25.

Due to the lack of inter-cell reflections, the management of diffuse light for the Flat-Panel Array is similarly simple. The intensity of diffuse sky light is directly equal to the intensity of diffuse light incident on the solar cell, and can be immediately used in Equation 4.25. The reflection generated here can be discarded, as none of it will be re-incident onto the array.

#### 4.2.2.2: The V-Groove Array

The specular light calculation for the V-Groove Array builds upon the calculation previously explained in section 3.2.4.3. Two main improvements are used here over that calculation. The first is that, rather than

the simple angle-dependent reflectance calculation used previously, the advanced reflection calculation presented in Equation 4.25 is used. This allows the reflected light to maintain its polarization, and also enables the calculation of reflected diffuse light, the values of which are saved and used in the following diffuse light calculation. The second improvement is in the transmission of specular light between the sides of the V-Groove Array, where the polarization projection calculations given in Equations 4.26-4.27 are used to correctly map polarization from one surface of the array onto the other.

The diffuse light calculation for the V-Groove Array begins with the diffuse sky light intensity that was calculated in Equation 4.9. In order to calculate diffuse light for both this and the following two complex arrays, the solar cells are split into small diffuse-reflecting elements, where the illumination is assumed to be constant on each of them. Unfortunately, the number of diffuse elements ultimately proved to have a severely detrimental effect on the runtime of the simulation, and this value therefore had to be highly restricted for the full five-year simulation. For this reason, only ten diffuse-reflecting elements were used per solar cell.

For a given diffuse-reflecting element, the amount of diffuse sky light falling on it can be determined based on the fact that since the sky is treated as a Lambertian source, the light from the sky falling on a given point is proportional to the area of the sky visible from that point. Additionally, the projection of the light onto the surface must be accounted for by multiplying this by the cosine of the angle between the light propagation direction and the surface normal. As the array is assumed to be infinite in one dimension, the visible sky can be taken as a rectangle that is infinite in one dimension. By converting this into spherical coordinates, a region of visible sky is bounded only by two constant values of the azimuthal angle. This makes it simple to apply the cosine from the normal term, integrate over the visible area, and normalize the result to the limiting case of an entire visible hemisphere of sky, in which the light intensity on the surface would be expected to be equal to the light intensity of the sky. The resulting formula is

$$I_{\text{diff,surf}} = I_{\text{diff,sky}} \times 0.5 |\sin(\theta_1) - \sin(\theta_2)|. \quad (4.30)$$

The two angles in this formula,  $\theta_1$  and  $\theta_2$ , represent the angles between the normal direction and the edges of the V-Groove Array. Applying this to a diffuse-reflecting element at distance  $d$  from the upper edge of the array gives

$$I_{\text{diff,surf}} = I_{\text{diff,sky}} \times 0.5 \left( 1 - \frac{d - 2 \sin^2 \left( \frac{\nu_{\text{VG}}}{2} \right) a S_{\text{VG}}}{\sqrt{d^2 + 4 \sin^2 \left( \frac{\nu_{\text{VG}}}{2} \right) a^2 S_{\text{VG}}^2 - 4d \sin^2 \left( \frac{\nu_{\text{VG}}}{2} \right) a S_{\text{VG}}}} \right). \quad (4.31)$$

The same formula can be used to calculate the amount of diffuse light reflected off one diffuse-reflecting element that is incident onto another diffuse-reflecting element. For a source element at distance  $d_1$  from the vertex of the V-Groove Array, the light transmitted onto a destination element at distance  $d_2$  from the vertex of the V-Groove Array on the opposite wall is found by

$$I_{\text{diff,2}} = I_{\text{diff,1}} \times 0.5 \left( \frac{\frac{d_2 - \left( d_1 - \frac{\delta}{2} \right) \cos(\nu_{\text{VG}})}{\sqrt{d_2^2 + \left( d_1 - \frac{\delta}{2} \right)^2 - 2d_2 \left( d_1 - \frac{\delta}{2} \right) \cos(\nu_{\text{VG}})}}}{\frac{d_2 - \left( d_1 + \frac{\delta}{2} \right) \cos(\nu_{\text{VG}})}{\sqrt{d_2^2 + \left( d_1 + \frac{\delta}{2} \right)^2 - 2d_2 \left( d_1 + \frac{\delta}{2} \right) \cos(\nu_{\text{VG}})}}} \right), \quad (4.32)$$

where  $\delta$  represents the width of a diffuse-reflecting element.

With these formulas, the calculation of diffuse light is simple, if somewhat simulation-intensive. The diffuse sky light incident on every diffuse-reflecting element is calculated using Equation 4.31, and the absorbed power and diffusely-reflected intensity are found using Equations 4.24-4.25. This diffusely-reflected light is added to the diffusely-reflected light from the specular light calculation. The coupling between each pair of diffuse-reflecting elements is then found using Equation 4.32, and the reflected light is mapped onto the new diffuse-reflecting elements. This process of calculating the absorbed and reflected light and then

mapping the reflected light onto new diffuse-reflecting elements is then repeated until the maximum instantaneous intensity drops below  $10^{-5}$  times the original maximum intensity, at which point the remaining diffuse light is assumed to be insignificant.

#### 4.2.2.3: The U-Groove Array

The specular light calculation for the U-Groove Array builds upon the calculation previously explained in section 3.2.4.3. As with the V-Groove Array, the primary differences in the treatment of specular light are the use of the advanced reflection calculation presented in Equations 4.24-4.25, as well as the separation of light by polarization direction and the use of the polarization projection calculations given in Equations 4.26-4.27 for each transit of specular light between faces within the U-Groove Array.

Diffuse light calculations for the U-Groove Array build upon the calculations previously established for the V-Groove Array. The calculation begins by mapping the diffuse sky light onto each surface of the array, based upon Equation 4.30. For the walls of the array, this can be calculated as

$$I_{\text{diff,surf}} = I_{\text{diff,sky}} \times 0.5 \left( 1 - \frac{x}{\sqrt{x^2 + W_{\text{UG}}^2}} \right), \quad (4.33)$$

where  $x$  is the distance from the upper edge of the wall to the diffuse-reflecting element. For the bottom of the array, this can be calculated as

$$I_{\text{diff,surf}} = I_{\text{diff,sky}} \times 0.5 \left( \sin \left( \arctan \left( \frac{W_{\text{UG}} - y}{H_{\text{UG}}} \right) \right) - \sin \left( \arctan \left( \frac{-y}{H_{\text{UG}}} \right) \right) \right), \quad (4.34)$$

where  $y$  is the distance from either wall to the diffuse-reflecting element.

The diffuse sky light incident on each surface is subjected to the reflection and absorption calculations, and the resulting reflection is added to the diffuse reflection from the specular calculation. Next, the diffuse light from each surface must be mapped onto each other surface, using the equations

$$I_{\text{diff,side}} = I_{\text{diff,bottom}} \times 0.5 \left[ \frac{H_{\text{UG}} - x}{\sqrt{(H_{\text{UG}} - x)^2 + \left(y - \frac{\delta}{2}\right)^2}} - \frac{H_{\text{UG}} - x}{\sqrt{(H_{\text{UG}} - x)^2 + \left(y + \frac{\delta}{2}\right)^2}} \right], \quad (4.35)$$

$$I_{\text{diff,side1}} = I_{\text{diff,side2}} \times 0.5 \left( \sin \left( \arctan \left( \frac{x_1 - x_2 + \frac{\delta}{2}}{W_{\text{UG}}} \right) \right) - \sin \left( \arctan \left( \frac{x_1 - x_2 - \frac{\delta}{2}}{W_{\text{UG}}} \right) \right) \right), \quad (4.36)$$

$$I_{\text{diff,bottom}} = I_{\text{diff,side}} \times 0.5 \left[ \frac{y}{\sqrt{y^2 + \left(H_{\text{UG}} - x - \frac{\delta}{2}\right)^2}} - \frac{y}{\sqrt{y^2 + \left(H_{\text{UG}} - x + \frac{\delta}{2}\right)^2}} \right], \quad (4.37)$$

where  $y$  is specifically measured from the side where the other diffuse reflecting element is located. The reflection and absorption calculation is then repeated. The diffuse light is repeatedly mapped and then reflected until the maximum diffuse intensity is less than  $10^{-5}$  times the original maximum intensity, at which point the remaining reflected light is assumed to be insignificant and the light absorbed by the silicon layer on each iteration is summed.

#### 4.2.2.4: The Angled-Panel Array

To calculate the optical behaviour of the Angled-Panel Array, one issue still needs to be solved. This array has the backs of the solar cells visible, as well as the ground below the array. The reflective behaviour of both of these surfaces needs to be defined for this calculation. It would be desirable for both of these surfaces to be strongly reflective. Any light absorbed here would not contribute to the power generation of the array, but would still contribute to heating of the structure, lowering the efficiency of the solar cells. While the resistive heating calculation used in this simulation is not advanced enough for this effect to be seen, for an actual solar installation, having these surfaces reflect light back into space would be preferable to having them absorb it.

At the same time, the use of specularly reflecting surfaces here would require special consideration in manufacturing for the backs of the solar cells, and likely significant additional material and cost for the ground. A diffusely-reflecting surface is much more practical in terms of installation cost. Therefore, these surfaces are assumed to be covered in white paint. Reflectance values for white paint in the literature are around 75% [150], which is the value that will be used in this calculation.

Unlike for the other three arrays, the specular light behaviour of the Angled-Panel Array has not yet been established. This must therefore be done here. This is begun by determining the direct solar illumination incident onto each surface of the array, which is done by calculating the zenith angle projected into the xz-plane:

$$\theta_{xz} = \arctan(\tan(\theta)\cos(\phi)). \quad (4.38)$$

The following five cases for illumination can then be defined based on this value. In the first case, we have

$$-\frac{\pi}{2} < \theta_{xz} \leq -\arccos\left(\frac{\sin(\tau_{AP})H_{AP}}{\sqrt{\sigma_{AP}^2 + H_{AP}^2 + 2\sigma_{AP}H_{AP}\cos(\tau_{AP})}}\right). \quad (4.39)$$

In this case, the back of the solar cell is partially illuminated, from the top edge down to a point

$$x = \frac{-\sigma_{AP}\cos(\theta_{xz})}{\cos(\tau_{AP} - \theta_{xz})}. \quad (4.40)$$

In the second case, we have

$$-\arccos\left(\frac{\sin(\tau_{AP})H_{AP}}{\sqrt{\sigma_{AP}^2 + H_{AP}^2 + 2\sigma_{AP}H_{AP}\cos(\tau_{AP})}}\right) < \theta_{xz} \leq \tau_{AP} - \frac{\pi}{2}. \quad (4.41)$$

In this case, the back of the solar cell is fully illuminated, and the ground between the solar cells is partially illuminated, from the back of the solar cells to a point

$$y = \sigma_{AP} + \frac{H_{AP} \cos(\tau_{AP} - \theta_{xz})}{\cos(\theta_{xz})}. \quad (4.42)$$

In the third case, we have

$$\tau_{AP} - \frac{\pi}{2} < \theta_{xz} < \tau_{AP} - \frac{\pi}{2} + \arccos\left(\frac{2H_{AP}^2 + \sigma_{AP}^2 - 2H_{AP}\sigma_{AP}\cos(\tau_{AP})}{2H_{AP}\sqrt{H_{AP}^2 + \sigma_{AP}^2 - 2H_{AP}\sigma_{AP}\cos(\tau_{AP})}}\right). \quad (4.43)$$

In this case, the front of the solar cell is fully illuminated, and the ground between the solar cells is partially illuminated, from the front of the solar cells to a point

$$y = \sigma_{AP} - \frac{H_{AP} \cos(\theta_{xz} - \tau_{AP})}{\cos(\theta_{xz})}. \quad (4.44)$$

In the fourth case, we have

$$\tau_{AP} - \frac{\pi}{2} + \arccos\left(\frac{2H_{AP}^2 + \sigma_{AP}^2 - 2H_{AP}\sigma_{AP}\cos(\tau_{AP})}{2H_{AP}\sqrt{H_{AP}^2 + \sigma_{AP}^2 - 2H_{AP}\sigma_{AP}\cos(\tau_{AP})}}\right) \leq \theta_{xz} < \frac{\pi}{2}. \quad (4.45)$$

In this case, the front of the solar cell is partially illuminated, from the top of the solar cells to a point

$$x = \frac{\sigma_{AP} \cos(\theta_{xz})}{\cos(\theta_{xz} - \tau_{AP})}. \quad (4.46)$$

The fifth case corresponds to the sun below the horizon, in which case no surfaces are illuminated.

For each illuminated surface, the light intensity must be projected onto that surface. The equations for this are

$$I_{\text{spec,back}} = I_{\text{spec,sky}} \times (-\sin(\theta)\cos(\phi)\sin(\tau_{AP}) - \cos(\theta)\cos(\tau_{AP})), \quad (4.47)$$

$$I_{\text{spec,bottom}} = I_{\text{spec,sky}} \times \cos(\theta), \quad (4.48)$$

$$I_{\text{spec,front}} = I_{\text{spec,sky}} \times (\sin(\theta) \cos(\phi) \sin(\tau_{\text{AP}}) + \cos(\theta) \cos(\tau_{\text{AP}})). \quad (4.49)$$

The direct solar illumination on the bottom and back of the solar cells can be multiplied by 75% to represent the diffuse reflectance and then used directly in the diffuse light calculations. The direct solar illumination on the front of the solar cells, however, is then calculated as diffuse and specular reflections and absorption using Equations 4.22-4.25. The polarization of this direct reflection does not need to be tracked, as it will not be incident on a specularly-reflecting surface, but the location of the reflected illuminated spot must be determined.

The upper and lower edges of this illuminated spot on the back of the opposing solar cells, as measured from their upper edge, can be found as

$$x_{\text{upper}} = x - 2\sigma_{\text{AP}} \cos(\tau_{\text{AP}}), \quad (4.50)$$

$$x_{\text{lower}} = 2x - 2\sigma_{\text{AP}} \cos(\tau_{\text{AP}}), \quad (4.51)$$

where  $x$  is the distance between the lower end of the illuminated region on the front of the solar cells and the top of those solar cells. As these two surfaces are parallel, the intensity stays the same and can be used directly for the diffuse light calculation. Only the region between 0 and  $H$  is actually on the solar cells, so light falling outside this region can be ignored.

If  $x_{\text{lower}}$  is larger than  $H$ , some of the reflected light falls onto the space between solar cells. This illuminated region can be defined by the borders

$$y_{\text{farther}} = \frac{H_{\text{AP}} \sin\left(\theta_{\text{xz}} + \frac{\pi}{2} - \tau_{\text{AP}}\right)}{\sin\left(2\tau_{\text{AP}} - \theta_{\text{xz}} - \frac{\pi}{2}\right)}, \quad (4.52)$$

$$y_{\text{closer}} = y_{\text{farther}} \left( 1 - \frac{x}{H_{\text{AP}}} \right). \quad (4.53)$$

If this region extends beyond  $\sigma$ , the further part will be blocked by the opposing solar cells. As the surfaces are not parallel, the light intensity then has to be projected onto the illuminated spot as

$$I_{\text{bottom}} = I_{\text{front}} \times \frac{x}{y_{\text{farther}} - y_{\text{closer}}}. \quad (4.54)$$

As there are no repeated specular reflections, an iterated process is unnecessary to define the specular light. With the specular intensity onto each diffusely-scattering surface defined, it is now possible to multiply this by 75% to represent the diffuse reflectance and use the resulting values in the diffuse light calculations.

Using the diffuse light equations derived in section 4.2.2.2, the diffuse sky light falling onto each diffuse-reflecting element can be calculated for all three surfaces of the geometric solar array. For the face of the solar cells,

$$I_{\text{diff,surf}} = I_{\text{diff,sky}} \times 0.5 \left( 1 - \frac{x - \sigma_{\text{AP}} \cos(\tau_{\text{AP}})}{\sqrt{x^2 + \sigma_{\text{AP}}^2 - 2x\sigma_{\text{AP}} \cos(\tau_{\text{AP}})}} \right), \quad (4.55)$$

where  $x$  is the distance between the diffuse-reflecting element and the upper edge of the solar cell. For the ground between the solar cells,

$$I_{\text{diff,surf}} = I_{\text{diff,sky}} \times 0.5 \left( \sin \left( \arctan \left( \frac{y + H_{\text{AP}} \cos(\tau_{\text{AP}})}{H_{\text{AP}} \sin(\tau_{\text{AP}})} \right) \right) - \sin \left( \arctan \left( \frac{y - \sigma_{\text{AP}} + H_{\text{AP}} \cos(\tau_{\text{AP}})}{H_{\text{AP}} \sin(\tau_{\text{AP}})} \right) \right) \right), \quad (4.56)$$

where  $y$  is the distance between the diffuse-reflecting element and the bottom of the solar cell facing towards the diffuse-reflecting element. For the back of the solar cells,

$$I_{\text{diff,surf}} = I_{\text{diff,sky}} \times 0.5 \left( 1 - \frac{x + \sigma_{\text{AP}} \cos(\tau_{\text{AP}})}{\sqrt{x^2 + \sigma_{\text{AP}}^2 + 2x\sigma_{\text{AP}} \cos(\tau_{\text{AP}})}} \right), \quad (4.57)$$

where  $x$  is the distance between the diffuse-reflecting element and the upper edge of the solar cell.

Once the diffuse sky light intensity on each surface is calculated, the reflection and absorption calculations from Equations 4.24-4.25 are applied to the light on the front of the solar cell, while the flat 75% reflectance is applied to light on the other two surfaces. This reflected light is then added to the diffuse reflected light from the specular light calculations. The diffuse light reflected from each surface is then coupled onto the other two surfaces. Due to the asymmetric shape of this array's groove, this calculation is somewhat more complex than the equivalent calculations for the V-Groove Array and the U-Groove Array. They are given as

$$I_{\text{diff,back}} = I_{\text{diff,bottom}} \times 0.5 \left[ \frac{H_{\text{AP}} - x - \left( \sigma_{\text{AP}} - y - \frac{\delta}{2} \right) \cos(\tau_{\text{AP}})}{\sqrt{(H_{\text{AP}} - x)^2 + \left( \sigma_{\text{AP}} - y - \frac{\delta}{2} \right)^2 - 2(H_{\text{AP}} - x) \left( \sigma_{\text{AP}} - y - \frac{\delta}{2} \right) \cos(\tau_{\text{AP}})}} - \frac{H_{\text{AP}} - x - \left( \sigma_{\text{AP}} - y + \frac{\delta}{2} \right) \cos(\tau_{\text{AP}})}{\sqrt{(H_{\text{AP}} - x)^2 + \left( \sigma_{\text{AP}} - y + \frac{\delta}{2} \right)^2 - 2(H_{\text{AP}} - x) \left( \sigma_{\text{AP}} - y + \frac{\delta}{2} \right) \cos(\tau_{\text{AP}})}} \right], \quad (4.58)$$

$$I_{\text{diff,bottom}} = I_{\text{diff,back}} \times 0.5 \left[ \frac{\sigma_{\text{AP}} - y - \left( H_{\text{AP}} - x - \frac{\delta}{2} \right) \cos(\tau_{\text{AP}})}{\sqrt{(\sigma_{\text{AP}} - y)^2 + \left( H_{\text{AP}} - x - \frac{\delta}{2} \right)^2 - 2(\sigma_{\text{AP}} - y) \left( H_{\text{AP}} - x - \frac{\delta}{2} \right) \cos(\tau_{\text{AP}})}} - \frac{\sigma_{\text{AP}} - y - \left( H_{\text{AP}} - x + \frac{\delta}{2} \right) \cos(\tau_{\text{AP}})}{\sqrt{(\sigma_{\text{AP}} - y)^2 + \left( H_{\text{AP}} - x + \frac{\delta}{2} \right)^2 - 2(\sigma_{\text{AP}} - y) \left( H_{\text{AP}} - x + \frac{\delta}{2} \right) \cos(\tau_{\text{AP}})}} \right], \quad (4.59)$$

$$I_{\text{diff,bottom}} = I_{\text{diff,front}} \times 0.5 \left( \frac{y + \left( H_{\text{AP}} - x - \frac{\delta}{2} \right) \cos(\tau_{\text{AP}})}{\sqrt{y^2 + \left( H_{\text{AP}} - x - \frac{\delta}{2} \right)^2 + 2y \left( H_{\text{AP}} - x - \frac{\delta}{2} \right) \cos(\tau_{\text{AP}})}} - \frac{y + \left( H_{\text{AP}} - x + \frac{\delta}{2} \right) \cos(\tau_{\text{AP}})}{\sqrt{y^2 + \left( H_{\text{AP}} - x + \frac{\delta}{2} \right)^2 + 2y \left( H_{\text{AP}} - x + \frac{\delta}{2} \right) \cos(\tau_{\text{AP}})}} \right), \quad (4.60)$$

$$I_{\text{diff,front}} = I_{\text{diff,bottom}} \times 0.5 \left( \frac{H_{\text{AP}} - x + \left( y - \frac{\delta}{2} \right) \cos(\tau_{\text{AP}})}{\sqrt{(H_{\text{AP}} - x)^2 + \left( y - \frac{\delta}{2} \right)^2 + 2(H_{\text{AP}} - x) \left( y - \frac{\delta}{2} \right) \cos(\tau_{\text{AP}})}} - \frac{H_{\text{AP}} - x + \left( y + \frac{\delta}{2} \right) \cos(\tau_{\text{AP}})}{\sqrt{(H_{\text{AP}} - x)^2 + \left( y + \frac{\delta}{2} \right)^2 + 2(H_{\text{AP}} - x) \left( y + \frac{\delta}{2} \right) \cos(\tau_{\text{AP}})}} \right), \quad (4.61)$$

$$I_{\text{diff,back}} = I_{\text{diff,front}} \times 0.5 \left( \sin \left( \arctan \left( \frac{x_b - x_f + \frac{\delta}{2} + \sigma_{\text{AP}} \cos(\tau_{\text{AP}})}{\sigma_{\text{AP}} \sin(\tau_{\text{AP}})} \right) \right) - \sin \left( \arctan \left( \frac{x_b - x_f - \frac{\delta}{2} + \sigma_{\text{AP}} \cos(\tau_{\text{AP}})}{\sigma_{\text{AP}} \sin(\tau_{\text{AP}})} \right) \right) \right), \quad (4.62)$$

$$I_{\text{diff,front}} = I_{\text{diff,back}} \times 0.5 \left( \sin \left( \arctan \left( \frac{x_b - x_f + \frac{\delta}{2} + \sigma_{\text{AP}} \cos(\tau_{\text{AP}})}{\sigma_{\text{AP}} \sin(\tau_{\text{AP}})} \right) \right) - \sin \left( \arctan \left( \frac{x_b - x_f - \frac{\delta}{2} + \sigma_{\text{AP}} \cos(\tau_{\text{AP}})}{\sigma_{\text{AP}} \sin(\tau_{\text{AP}})} \right) \right) \right). \quad (4.63)$$

The reflection and absorption calculations are repeatedly run with these coupling calculations until the maximum intensity is less than  $10^{-5}$  times the original maximum intensity, at which time the accumulated absorption of the front side of the solar cells can be calculated.

#### 4.2.3: Relative Profit Density as a Metric for Array Performance

It was previously mentioned that the use of generated value density as an optimization metric does not reflect the actual economic viability of the solar arrays, due to the fact that it does not consider installation costs. In order to define a more practical metric for optimization, the profit of the array is defined as

$$\Pi = Val_y l A - C. \quad (4.64)$$

The total profit is the difference between the total value (defined as the product of the value density  $Val_y$ , the lifespan  $l$ , and the area  $A$ ) and the cost  $C$ .

Using profit as a metric for analysis is similar to what is often done in LCOE analyses [88]. In such analyses, the total lifetime cost is divided by the total lifetime energy produced, to determine the cost per kWh of electricity produced. This value is often used to compare solar generation to other forms of electricity generation [151] or to evaluate the economic benefits of solar generation [152]. However, LCOE analyses are typically very high-level, and overlook the time-varying value of electricity. While such an analysis may be appropriate for determining the benefits of solar generation under a constant-price power-purchase agreement, performing a similar analysis geared towards time-of-use rates or societal value requires this approach to be extended from comparing dollars spent and energy generated to comparing dollars spent and dollars earned.

For the sake of this analysis, the cost can be further divided into several categories depending on its relationship to the area,

$$\Pi = Val_y l A - C_{\text{fix}} - C_{\text{area}} A - C_{\text{geo}} g A. \quad (4.65)$$

The variable  $C_{\text{fix}}$  is the fixed cost, incorporating all costs that are not dependent on the size of the array. In practice, all costs will scale with the array's size to some extent, but some costs such as permits and grid interconnection may be largely independent of the array size unless that size gets sufficiently large, and economies of scale reduce the cost of various aspects of installation as the array gets larger [153]. These effects may therefore be considered to be fixed costs. The variable  $C_{\text{area}}$  is the area-dependent cost, incorporating all costs that are directly dependent on the area of the array. Notably, these costs are ones that do not vary between different arrays, such as land use cost, electronics cost, and some aspects of the installation and maintenance costs. The variable  $C_{\text{geo}}$  is the geometry-dependent cost, incorporating all costs that are dependent on the solar cell area of the array. These costs therefore scale with both the size of the array and its complexity, such that arrays with higher aspect ratios will generally see greater effects of geometry-dependent costs. The costs of the solar cells, the support structure, and some of the installation and maintenance costs fall into this category. The geometry factor,  $g$ , is defined as the ratio of the silicon area to the installation area for a unit cell, and is used to modify the geometry-dependent cost here.

Previously, the majority of results obtained from this research were defined to be yearly densities. This same definition can be applied to the profit to obtain the yearly profit density

$$\Pi_y = Val_y - \frac{C_{\text{fix}}}{lA} - \frac{C_{\text{area}}}{l} - \frac{C_{\text{geo}}g}{l}. \quad (4.66)$$

While comprehensive, this metric has the undesirable trait of containing three poorly-known costs whose values would need to be determined before it could be used. However, one point worth noting is that the fixed and area-dependent cost terms are not dependent on the type of array used. As the goal of this research is to compare the different types of arrays, the value of these terms is therefore irrelevant to this comparison. By taking only the geometry-dependent terms of the yearly profit density equation, the relative profit density can be found:

$$\Pi_{\text{rel}} = Val_y - \frac{C_{\text{geo}}g}{l}. \quad (4.67)$$

It is still necessary to find an approximate value for the geometry-dependent cost. Using the installation price breakdown from [80], and assuming that the geometry-dependent cost includes the photovoltaic modules, the structural components, half the supply and tax costs, and half the installation costs, a value of 0.9 \$/W can be found. This cost breakdown does not include maintenance costs, which must be considered in this analysis, so this cost is rounded up to 1 \$/W to compensate. Assuming an average 17% efficiency [153] and standard test conditions of 1000 W/m<sup>2</sup>, this value translates to 170 \$/m<sup>2</sup>. For the purpose of this study, it is beneficial to represent the geometry-dependent cost density as a yearly value, represented by  $C_{\text{geo,y}}$ . Given the established lifespan of 25 years, this value becomes 6.8 \$/m<sup>2</sup>/y.

This value is a very rough estimate, and is likely to decrease over time. Therefore, results should be collected at multiple values of the geometry-dependent cost. Values ranging from a realistic 7 \$/m<sup>2</sup>/y down to 0 \$/m<sup>2</sup>/y (which is identical to the value density metric used in chapter 3) will therefore be used for the geometry-dependent cost, and the relative profit density will be optimized separately for each value.

#### 4.2.4: Conversion of Optical Power to Relative Profit Density

To accurately determine the power collected by each geometric solar array, the time-dependent solar cell temperature must be determined. The monthly estimated maximum and minimum ambient temperatures were previously determined in section 4.2, which also established the times for maximum and minimum temperature as being 1:00 PM and 6:00 AM respectively. The temperature was then linearly interpreted between these points to find intervening temperatures. A more rounded curve, such as a stretched sinusoid, might have been more realistic here, but it would have unnecessarily complicated this value, which already experiences significant and unavoidable error due to the temperature's strong dependence on the weather conditions. What is, however, worth noting is that the temperature is dependent on the sun's position rather than strictly the time. Therefore, during daylight savings time, the maximum and minimum temperature times are adjusted to 2:00 PM and 7:00 AM, respectively, to compensate for this.

The resistive heating of the solar cells must also be accounted for. Reference [81] shows resistive heating to be linearly related to light intensity, and to range from 12 to 30 K at 1000 W/m<sup>2</sup> dependent on the wind speed. A value of 25 K, near the upper end of this range, is selected. As 1000 W/m<sup>2</sup> is considered to be the standard test condition light intensity under AM1.5 conditions, and the intensity of AM0 light is taken to be 1366 W/m<sup>2</sup>, a simplified light intensity can be calculated based on the air mass. As high precision is not required here, exponential decay can be applied to the light intensity even though it is given as an aggregate quantity rather than being divided by wavelength. The resulting equation is

$$T_{SC} = T_{amb} + 25 \text{ K} \left( \frac{1000 \text{ W/m}^2}{1366 \text{ W/m}^2} \right)^{\left( \frac{AM}{1.5} - 1 \right)}. \quad (4.68)$$

The conversion of optical power to electrical power is done through solving the double diode solar cell equation, which is produced here in full:

$$I_{PV} = n_R P_{Opt} R_{\lambda, norm} - \frac{J_{Sat1,0} a^2}{T_0^3 e^{\frac{-E_g}{k_B T_0}}} T^3 e^{\frac{q \left( V_{PV} + \frac{I_{PV} R_S}{a^2} \right) - E_g}{k_B T}} - \frac{J_{Sat2,0} a^2}{T_0^{3/2} e^{\frac{-E_g}{2k_B T_0}}} T^{3/2} e^{\frac{q \left( V_{PV} + \frac{I_{PV} R_S}{a^2} \right) - E_g}{2k_B T}} - \frac{V_{PV} a^2 + I_{PV} R_S}{R_{Sh}}. \quad (4.69)$$

This equation is based on Equation 2.2, with a few key changes. The temperature dependence of the two saturation currents that was introduced in section 4.1.2 has been added, and the -1 terms that are subtracted from the exponential terms have been removed. This is a common simplification, as the effect of these terms is negligible at typical system voltages, and in this case it allows for additional simplification by combining the temperature dependence exponential with the voltage exponential. The solar cell parameters used here have previously been defined in section 4.1.2, such that this equation contains only four variables: photovoltaic current, voltage, optical power, and temperature.

Due to the complexity of solving this equation, it is desirable to reuse the results rather than recalculate them for every data point. In order to do so, the variables are quantized as previously discussed. The photocurrent, being the product of the optical power, the normalized optical responsivity, and the

responsivity scaling factor represented in the first term, is rounded to a step size of 5 mA. The photovoltaic voltage is rounded to a step size of 1 mV. The temperature is rounded to a step size of 1.16 K (which is equivalent to a thermal voltage step size of 100  $\mu$ V).

Given an established temperature and a previously-determined photocurrent, Equation 4.69 can be used to derive the I/V curve of the solar cell. The I/V curve can then be converted into a generated value density in a similar manner to what was done in section 4.2.4.4, by limiting the minimum current to 0, taking the maximum of the product of current and voltage, dividing this by the unit cell area, and multiplying the result by the electricity price at that time.

The generated value density can then be converted to relative profit density by subtracting from it the geometry-dependent cost density. As the geometry dependence is array-specific, equations for each type of array are shown here:

$$\Pi_{\text{rel,FP}} = Val_{y,\text{FP}} - C_{\text{geo},y} , \quad (4.70)$$

$$\Pi_{\text{rel,VG}} = Val_{y,\text{VG}} - \frac{C_{\text{geo},y}}{\sin\left(\frac{V_{\text{VG}}}{2}\right)} , \quad (4.71)$$

$$\Pi_{\text{rel,UG}} = Val_{y,\text{UG}} - C_{\text{geo},y} (2N_{\text{UG}} + 1) , \quad (4.72)$$

$$\Pi_{\text{rel,AP}} = Val_{y,\text{AP}} - C_{\text{geo},y} N_{\text{AP}} . \quad (4.73)$$

These values can then be compared to determine the relative economic performance of both differing types of arrays and differing configurations of these arrays.

### 4.3: Results

With the simulation framework complete, it can be applied to the varying arrays and configurations in order to draw conclusions about the use of value-based metrics. In this section, the results of the ARIES

experiment are used to validate the quality of the simulation, and the simulation is then used to identify optimal configurations for each array at each geometry-dependent cost density value. The relative profit densities of these optimal configurations are then compared to determine an optimal array at each geometry-dependent cost density value, and analyze the benefits of using value-based metrics for array optimization.

#### 4.3.1: Experimental Validation of the Simulation

The results from the rooftop experiment performed in section 4.1.2 are used here as a comparison against the rigorous simulation in order to test its accuracy. Several minor modifications to the simulation were made to keep its test conditions similar to those seen in the rooftop experiment. The simulation coordinates were shifted to match the experimental ones, the estimated daily temperature curve was replaced with time-interpolated temperature data from the date and location of the experiment, and the series resistance was increased to the  $30 \Omega\text{cm}^2$  seen in the experiment. With these adjustments in place, the outputs of the simulation should match the results of the experiment.

Fig. 4.13 shows a comparison between the experimental and simulated photocurrents. The curves match well across most of the day, with the experimental curves dropping lower in the early morning, due to the sun being blocked by hills, and the afternoon, due to cloud shadowing. Interestingly, the early afternoon also shows several significant spikes above the simulated curve. It is possible that the presence of clouds that do not directly obscure the sun could increase the amount of diffuse light falling on the solar cells, or that reflected light from another building reached the experiment during these times.

Fig. 4.14 shows a comparison between the experimental and simulated first saturation current curves. Two simulated curves are shown. The upper one is the curve used in the California simulations, representing 25 K resistive heating at STC. The lower curve, representing 10 K resistive heating at STC, is a much closer match to the experimental data. Although there was some mild wind on the day of the experiment, which would have been compounded by the experimental location on a tall, unobstructed building, this by itself is insufficient to explain this significantly-reduced resistive heating. Additionally, the fact that the solar

cells were disconnected for most of the day, only operating briefly while each data point was calculated, would be expected to further increase the resistive heating seen by the solar cells, as during the disconnected times the solar cells would receive the same amount of sunlight while experiencing open-circuit conditions, effectively forcing their efficiency to zero. There are a few possible explanations for this behaviour, and the true cause is likely a combination of them. The cold ambient conditions at the test site could have reduced the resistive heating below what would be expected for a desert environment. The study used to determine resistive heating [81] does provide support both for alpine conditions having reduced resistive heating, and for winter conditions increasing the wind-dependence of resistive heating. Secondly, although the solar cells were encapsulated, they were not packaged into a module like industrial solar cells would be. This free-standing nature would have made it easier for them to lose heat to the environment, reducing their resistive heating.

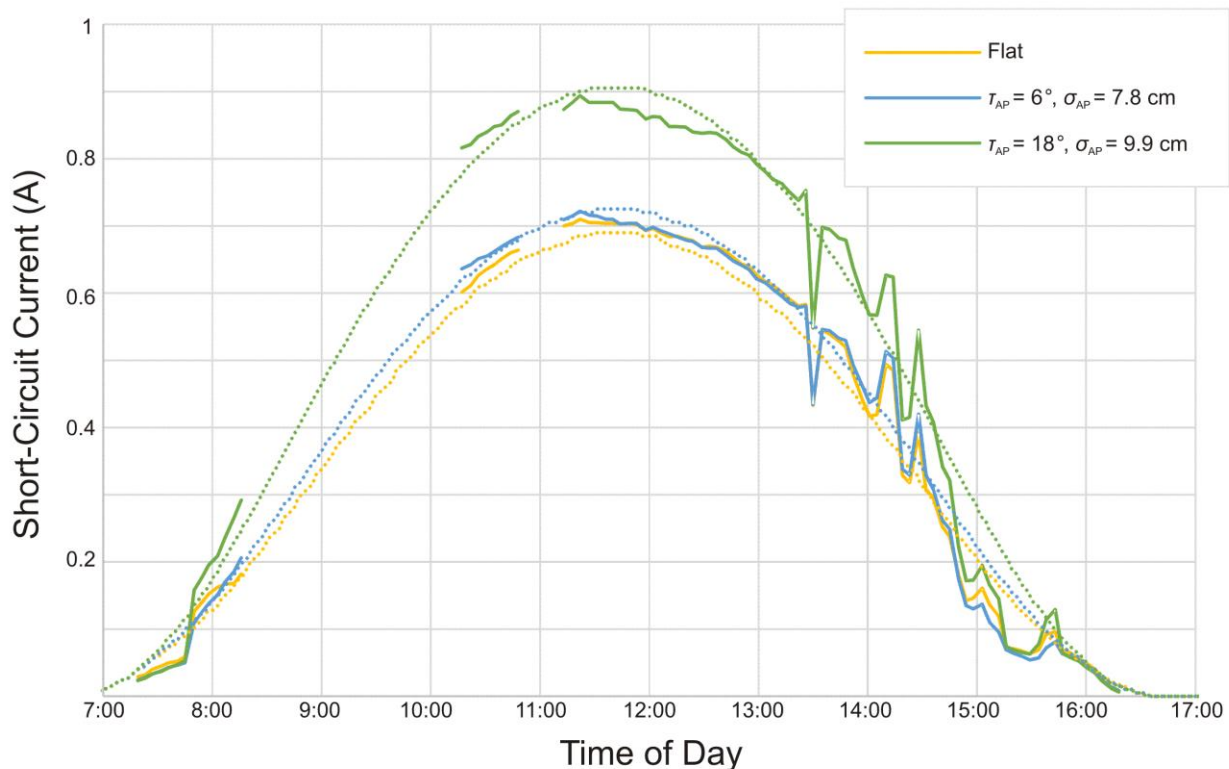


Fig. 4.13: A comparison of the experimental photocurrents obtained in the ARIES experiment, shown as solid lines, against the simulated photocurrents under identical conditions, shown as dotted lines.

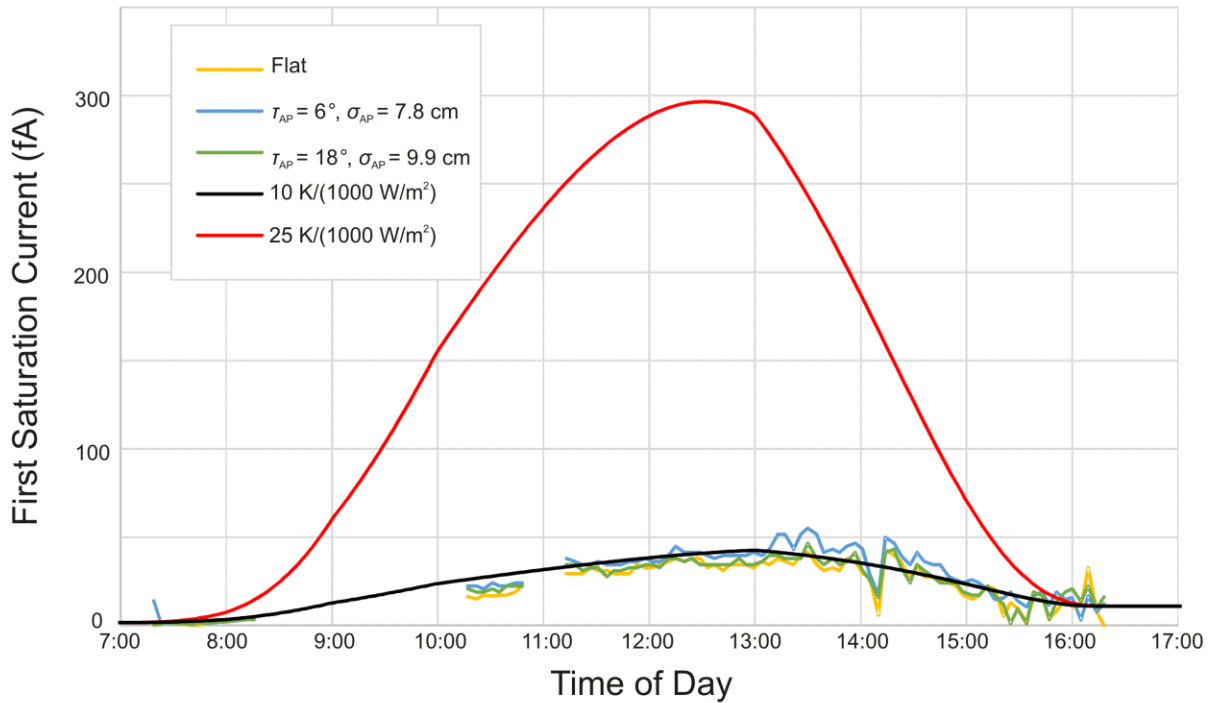


Fig. 4.14: A comparison of the experimental first saturation currents obtained from the ARIES experiment against simulated first saturation currents given a solar cell resistive heating of 10 K/(1000 W/m<sup>2</sup>) and 25 K/(1000 W/m<sup>2</sup>)

Fig. 4.15 shows a comparison between the experimental and simulated second saturation current curves. The 10 K resistive heating curve matches well to the experimental data at the start and end of the day, but exceeds it in the middle of the day. Given the large scale of the noise present in this capture, it is unclear how much of this deviation is legitimate, and what could be causing it.

Fig. 4.16 shows a comparison between the experimental and simulated power curves. Initially, these two curves fit poorly together. Comparisons of I/V curves at several of the data points on each power curve led to the conclusion that the experimental series resistance of 30 Ωcm<sup>2</sup> was too high. By reducing this to 26 Ωcm<sup>2</sup>, the strong correlation seen in this figure was obtained. Additionally, Fig. 4.16 shows simulated power curves under zero direct solar illumination. It was expected that these curves would match well to both the early hours before the sun rose above the obstructing hills, and the afternoon hours when the sun was obscured by clouds. In both of these cases, it can be seen that the simulated values slightly exceed the experimental ones. This is likely due to the limitations of the experimental model. By giving the simulated

Angled-Panel Arrays a length of only one solar cell, and replacing the solar cell in front of each row by a vertical wall, much of these arrays' diffuse light-trapping ability is lost. Additionally, while care was taken to ensure that the three arrays were not directly shadowed by each other or surrounding environmental features, both of these could still contribute to blocking diffuse light.

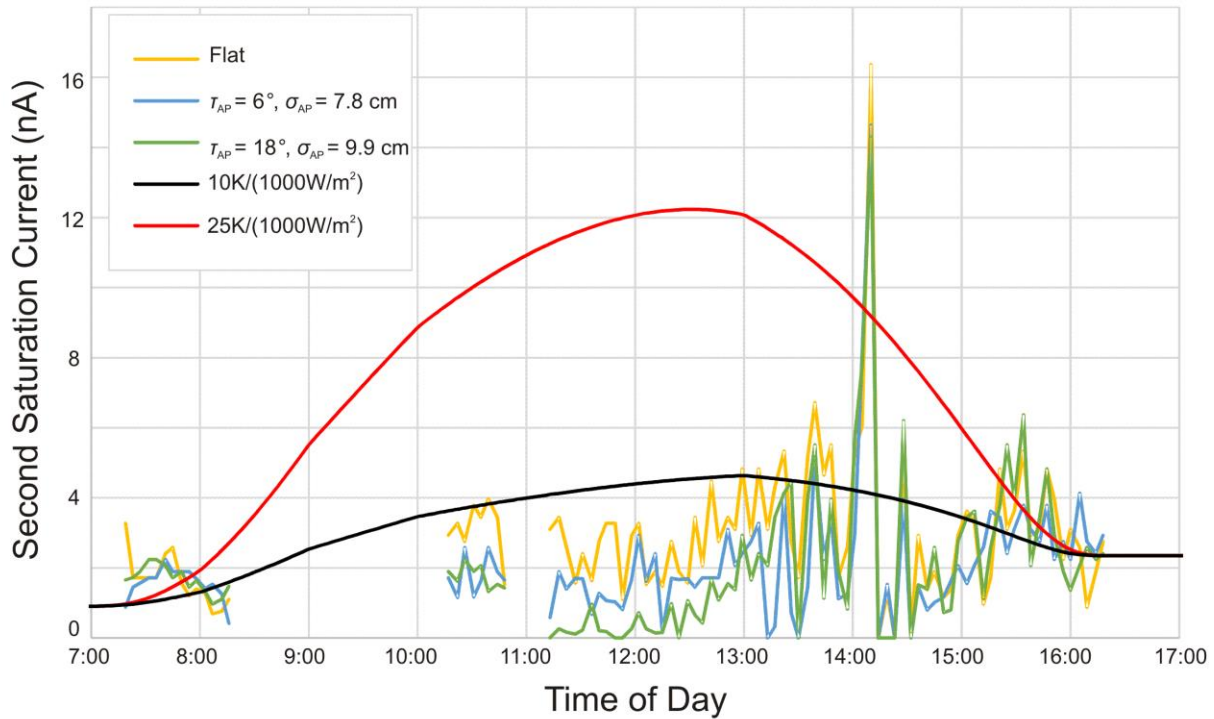


Fig. 4.15: A comparison of the experimental second saturation currents obtained from the ARIES experiment against simulated second saturation currents given a solar cell resistive heating of 10 K/(1000 W/m<sup>2</sup>) and 25 K/(1000 W/m<sup>2</sup>)

The comparison of the simulated data to the experimental data does raise some concerns about the accuracy of the solar cell parameters obtained from the ARIES experiment. The series resistance value used during the optimization used to find the two saturation currents has been seen to be inaccurate, calling into question the accuracy of the saturation current values. Additionally, the unusually low value of the second saturation current during the day has not been adequately explained. Despite these concerns, the values shown here match closely enough that the simulation can be assumed to be a good representation of a solar cell, even if it does not precisely match the solar cells used for the experiment.

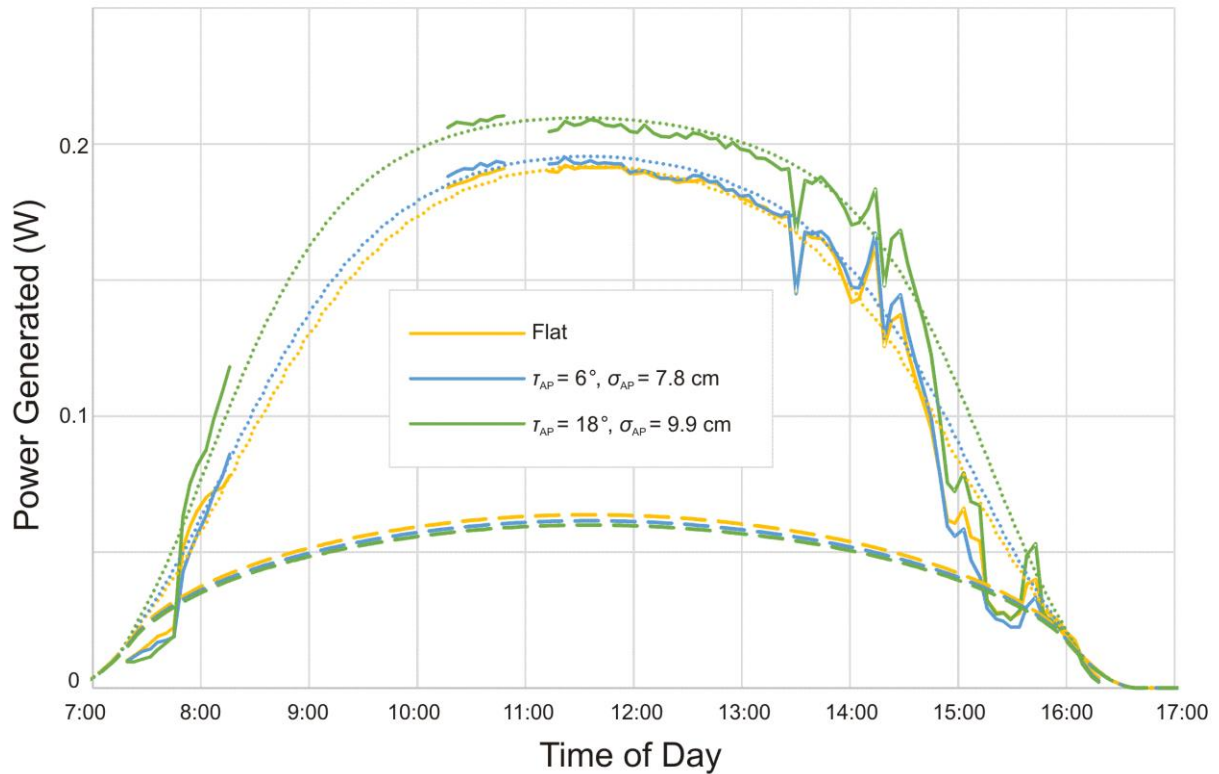


Fig. 4.16: A comparison of the experimental solar cell electrical powers obtained from the ARIES experiment, represented by solid lines, against simulated electrical powers with and without incident direct solar illumination, represented by dotted and dashed lines respectively.

#### 4.3.2: Array Optimization under the Relative Profit Density Metric

As the metric of optimization now contains a variable parameter, the arrays were optimized for values of  $C_{\text{geo},y}$  ranging from 0 to 7  $\$/\text{m}^2/\text{y}$  in steps of 0.5  $\$/\text{m}^2/\text{y}$ . As with the simplified simulation, the value of the array rotation,  $\rho$ , is initially left as zero to simplify the optimization. However, this simplification will then be examined to determine how valid it is. The arrays were optimized for each year of the five year study. The full results of this optimization are shown in Appendix C. This section focuses on the optimization for the final year of the study.

Fig. 4.17 shows the optimized value of  $v_{\text{VG}}$  as a function of  $C_{\text{geo},y}$ . When the geometric cost is zero, the relative profit density is expected to be equal to the value density used for the simplified simulation. However, in this case, the V-Groove Array has a much narrower optimal V-angle, being  $31^\circ$  rather than the  $80^\circ$  seen previously. This is primarily due to the introduction of diffuse light to the simulation. The ability

of an array to trap diffuse light is greatly heightened when the array incorporates tall, narrow geometries. Therefore, when the cost of additional solar cells is negligible, narrow structures tend to dominate.

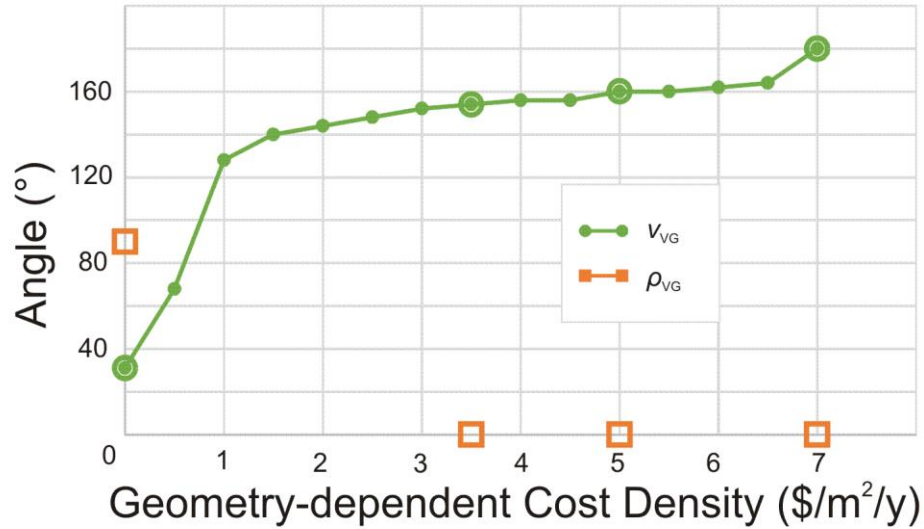


Fig. 4.17: The optimal configuration of the V-Groove Array at varying values of  $C_{\text{geo},y}$ . The solid line represents the detailed analysis run with a fixed  $\rho_{\text{VG}}$ , while outlined points represent investigations where  $\rho_{\text{VG}}$  was left free to vary.

As the geometric cost increases, the optimal V-angle increases quickly, before stabilizing around 150°. Shallow V-Grooves of this type would require minimal additional solar cells compared to a Flat-Panel Array, but their tilted faces would prove beneficial in capturing high-value light in the morning and evening. When the geometry-dependent cost density reaches 7 \$/m<sup>2</sup>/y, this effect is no longer sufficient to justify the additional silicon cost, and the V-Groove Array degenerates into a Flat-Panel Array.

Fig. 4.18 shows the optimized value of  $N_{\text{UG}}$  as a function of  $C_{\text{geo},y}$ . The optimization of the U-Groove Array presented a significant challenge in this simulation due to the behaviour of this array as the geometry-dependent cost increases. The array is expected to degenerate into a Flat-Panel Array under such conditions. However, the means in which it does so is by having the aspect ratio approach zero, which causes the spacing between walls to become infinite. An increased spacing leads to increased array complexity and thereby increased simulation time. It becomes impractical to find an optimal width beyond a certain point.

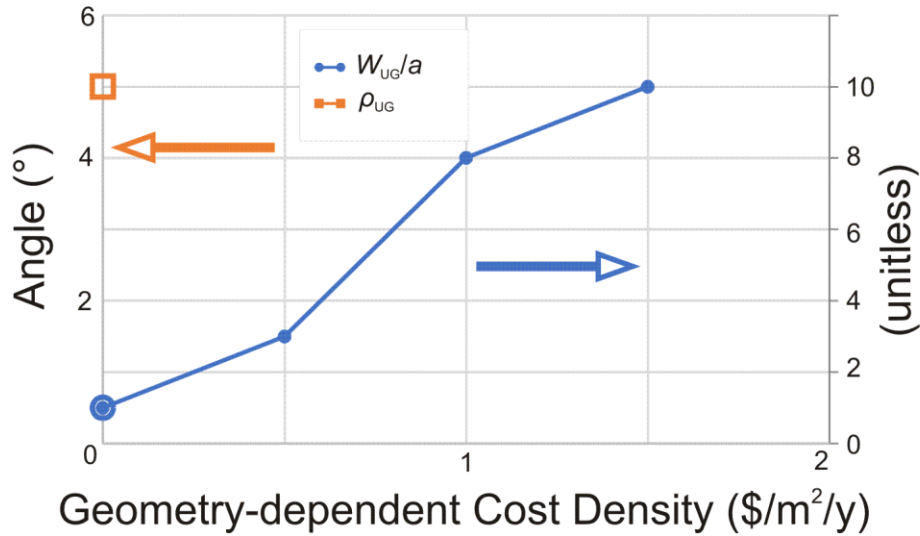


Fig. 4.18: The optimal configuration of the U-Groove Array at varying values of  $C_{\text{geo},y}$ . The solid line represents the detailed analysis run with a fixed  $\rho_{\text{VG}}$ , while the outlined points represent investigations where  $\rho_{\text{VG}}$  was left free to vary. Note that the actual value of  $W_{\text{UG}}/a$  at  $C_{\text{geo},y} = 1.5$   $\$/\text{m}^2/\text{y}$  is at least 10, but could be as high as 99.

To work around this problem, the width of the U-Groove Array was restricted to be less than or equal to 10 solar cell side lengths for optimization. A single data point with  $W_{\text{UG}}/a = 100$  was also used. At zero geometry-dependent cost, a U-Groove Array of aspect ratio 1 is optimal, which is again narrower than the aspect ratio 1/3 structure found in the simplified simulation. Values for  $C_{\text{geo},y} = 0.5$  and 1  $\$/\text{m}^2/\text{y}$  were found as well. At  $C_{\text{geo},y} = 1.5$   $\$/\text{m}^2/\text{y}$ , the optimal aspect ratio lies somewhere between 1/10 and 1/100. At  $C_{\text{geo},y} = 2$   $\$/\text{m}^2/\text{y}$  and above, all simulated U-Groove Array geometries, including the  $W_{\text{UG}}/a = 100$  one, were outperformed by the Flat-Panel Array. While an optimal and non-degenerate U-Groove Array may well exist at these values, it would need to be impractically large.

Fig. 4.19 shows the optimized values of  $\sigma_{\text{AP}}$  and  $\tau_{\text{AP}}$  as functions of  $C_{\text{geo},y}$ . It was mentioned earlier that under the conditions presented in the simplified simulation, an Angled-Panel Array would degenerate into a Flat-Panel Array. This plot, however, shows that for zero geometry-dependent cost, the optimal Angled-Panel Array in fact has a fairly large tilt angle and very narrow spacing. As with the other two arrays, this geometry is ideal for trapping diffuse light. It is likely that in the absence of diffuse light, the Angled-Panel Array would degenerate at these conditions, as this array is not capable of trapping specular light.

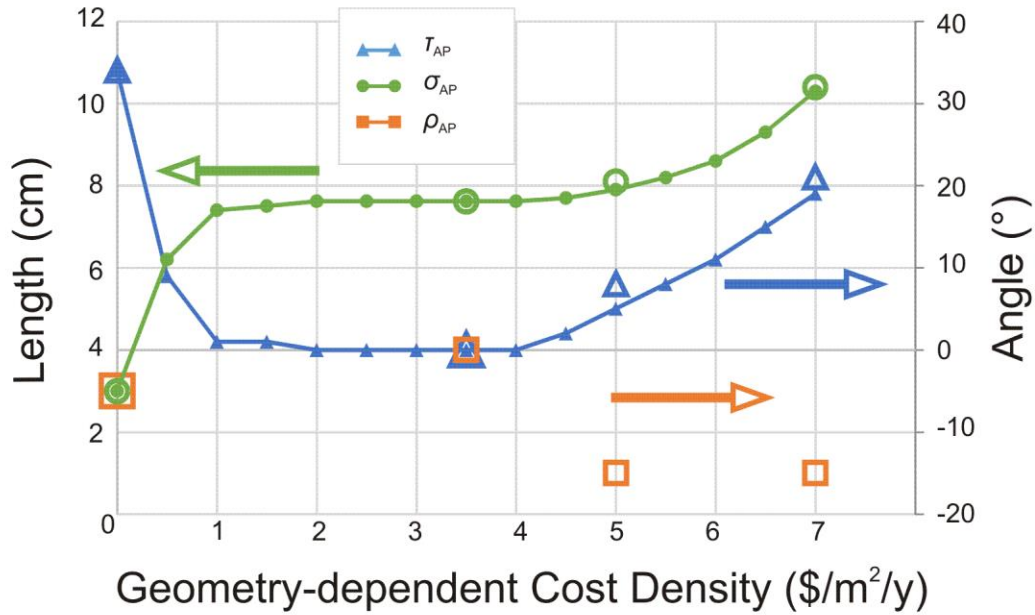


Fig. 4.19: The optimal configuration of the Angled-Panel Array at varying values of  $C_{geo,y}$ . Solid lines represent the detailed analysis run with a fixed  $\rho_{AP}$ , while outlined points represent investigations where  $\rho_{AP}$  was left free to vary.

As the geometry-dependent cost increases, the Angled-Panel Array does in fact degenerate into a Flat-Panel Array for values of  $C_{geo,y}$  between 2 and 4  $\$/m^2/y$ . Above this, both the spacing and angle start to increase, although the angle remains relatively shallow over the entire range of tested geometry-based cost density values.

To verify the suitability of the assumption that zero rotation is optimal, several arrays had their rotation varied to track the effect on geometry-dependent profit density. This test used all non-degenerate array geometries at  $C_{geo,y}$  values of 0, 3.5, and 7  $\$/m^2/y$ , being the mid- and endpoints of the tested range, as well as 5  $\$/m^2/y$ , the importance of which will be discussed in the following subsection. The results from this testing are plotted alongside the optimal configurations with zero rotation in Figs. 4.17-4.19. Almost all of these tested arrays had a maximum geometry-dependent profit density that was within  $10^\circ$  of  $\rho = 0$  with less than a 0.1% improvement over that value. The three exceptions to this are examined here.

The narrow V-Groove Array optimized to zero geometry-dependent cost density has an optimal rotation angle of  $\rho_{VG} = 90^\circ$ , an improvement of 5.8%, having both the largest magnitude of optimal rotation and

magnitude of rotational improvement of any of the tested arrays. This may be due to the fact that while a very narrow V-Groove Array does provide a nearly-normal surface for low-angle light to be incident on, it is best suited for trapping high-angle light directly incident onto the solar cells. Under standard conditions, when the array's grooves run north-south, this property is not significantly utilized. However,  $\rho_{VG} = 90^\circ$  corresponds to a complete rotation of the array's orientation, resulting in an east-west V-Groove Array that would have improved trapping of midday direct solar illumination, an effect that seems to outweigh the collection of low-angle high-value light for sufficiently narrow geometries.

A less notable rotation dependence is visible in the high- $C_{geo,y}$  Angled-Panel Arrays. Both of these arrays have an optimal rotation of  $\rho_{AP} = -15^\circ$ , with non-negligible improvements of 0.5% for the  $C_{geo,y} = 5$   $\$/m^2/y$  case and 3.7% for the  $C_{geo,y} = 7$   $\$/m^2/y$  case. This fits with what is seen in the literature, where southwest-facing Angled-Panel Arrays are often used in situations where electricity price peaks in the afternoon [154], as is commonly seen with the "Duck Curve". The rotation seen here is smaller than typical, which may be due to the fact that the "Duck Curve" produces bimodal, rather than strictly shifted, price curves, where the morning price may be high enough that more extreme rotations would be negatively affected by losing out on collecting electricity during the morning. It can also be noted that the rotationally-optimized Angled-Panel Array configuration has slightly steeper angles and wider spacings than the optimal configuration with zero rotation. The reason for this effect is likely rooted in the increased correlation between directly incident sunlight and high electricity prices when the array is rotated, which results in the optimal configuration being more strongly tilted to better face the sun, and more widely spaced to offset the self-shadowing inherent in increased tilt angles.

#### 4.3.3: The Cost-Dependent Viability of Solar Arrays

As with the simplified simulation, the results of the rigorous simulation are presented by first focussing on a single day of interest, and then expanding the conclusions to incorporate an extended span of data. In this case, the extended span is five years beginning July 1, 2013, rather than the six years beginning July 1,

2012 that was previously used. This change was made as the extended range did not yield any additional useful insight during the simplified simulation.

The day selected for detailed analysis is March 20, 2018. Due to the short simulation length needed for this day, the quantization is reduced drastically compared to the year-long captures. The threshold at which optical power is considered to be insignificant is decreased from  $10^{-5}$  times the initial optical power to  $10^{-7}$  times the initial optical power, and the incident angle for specular reflection is rounded to  $1^\circ$  rather than  $2^\circ$ . The number of diffuse reflecting elements per solar cell is increased from 10 to 20. Additionally, the exact values for the zenith, azimuth, and temperature are used rather than quantizing them.

Fig. 4.20 shows a comparison of instantaneous optical power on each solar cell of the optimal arrays at  $C_{\text{geo},y} = 0, 5, \text{ and } 7 \text{ \$/m}^2/\text{y}$ , an intermediate step that was overlooked during the simplified simulation. The comparative performance of the various arrays can clearly be seen here. The widely-spaced Angled-Panel Array has the highest performance by a significant margin, which is offset by the large spacing between rows, making it ideal for applications with high geometry-dependent costs. The shallow Angled-Panel Array and V-Groove Array are both similar to the Flat-Panel Array that they closely resemble, with the former having higher mid-day performance, and the latter's two solar cells peaking at different times and having noticeably increased power in the early morning and late evening, which are the only times inter-cell direct reflections are possible with such a shallow V-Angle. The three low geometry-dependent cost arrays have noticeably lower optical powers per solar cell due to their closely-spaced solar cells. The U-Groove Array has all of its solar cells distinctly peaking at different times during the day and collecting a low but nearly constant power throughout the rest of the day due to the collection of diffuse light. The V-Groove Array experiences similar low power levels throughout the day on its north-facing solar cell, and a much larger bell-shaped intensity curve on its south-facing solar cell. The narrow Angled-Panel Array, has a similar bell-shaped curve, with a value intermediate to the two solar cells of the narrow V-Groove Array.

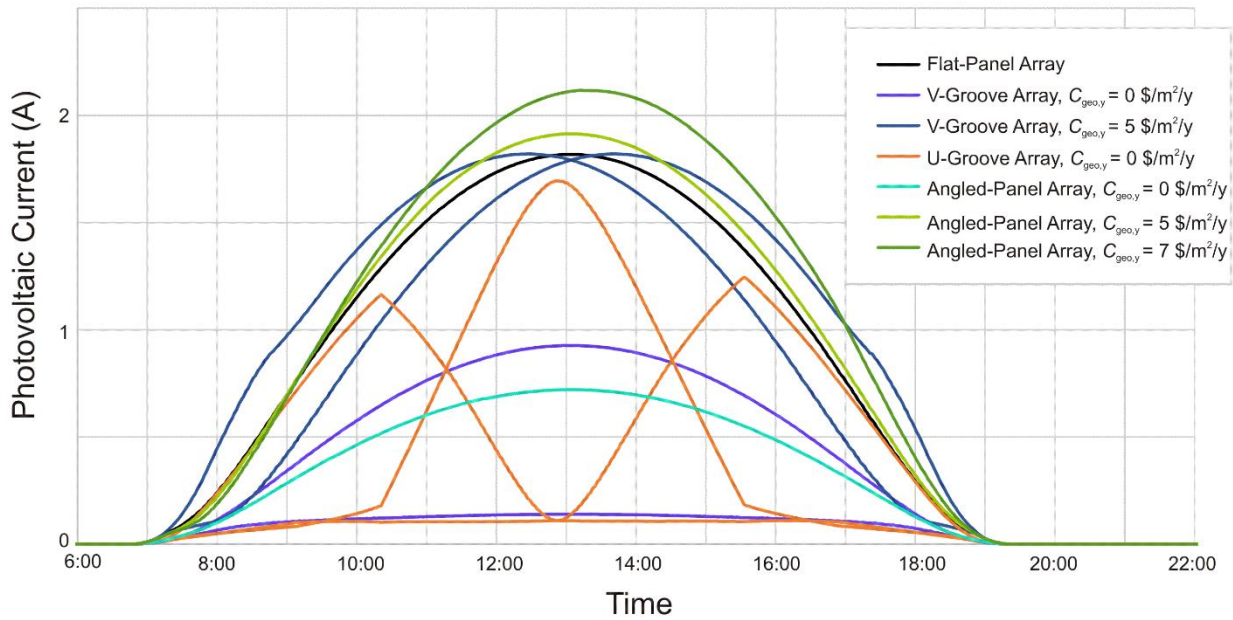


Fig. 4.20: The photocurrent collected by each solar cell of the array configurations optimized to  $C_{geo,y} = 0, 5, \text{ and } 7 \text{ \$/m}^2/\text{y}$  on March 20, 2018.

Fig. 4.21 shows a comparison of the generated electrical power densities of the same arrays. Due to the switch from absolute values to densities, the order of the curves has reversed, with the low geometry-dependent cost arrays now having the highest values. The narrow V-Groove Array stands out as having the highest performance in the middle of the day. The U-Groove Array slightly outperforms it in the morning and evening, but falls behind it in the middle of the day. The same distinctive double peaks that were seen in the simplified simulation can be observed here, although their height is now skewed due to the slight rotation introduced during optimization. The narrow Angled-Panel Array can be seen to have significantly higher power density than the Flat-Panel Array, but it still falls well below the two other low geometry-dependent cost arrays. Both of the shallow-angle arrays are similar enough in performance to the Flat-Panel Array to be difficult to distinguish from it in this plot. The widely-spaced Angled-Panel Array falls well below the Flat-Panel Array due to the increased space between rows reducing the power density. As expected, the peak of this curve is slightly later in the day than the other arrays with similar power profiles. This indicates that the rotation of the array is allowing it to gain some power during the afternoon and

evening, at the expense of power during the morning and midday. The similar rotation in the shallow Angled-Panel Array is not obvious here, as the shallow tilt angle makes it much less sensitive to rotation.

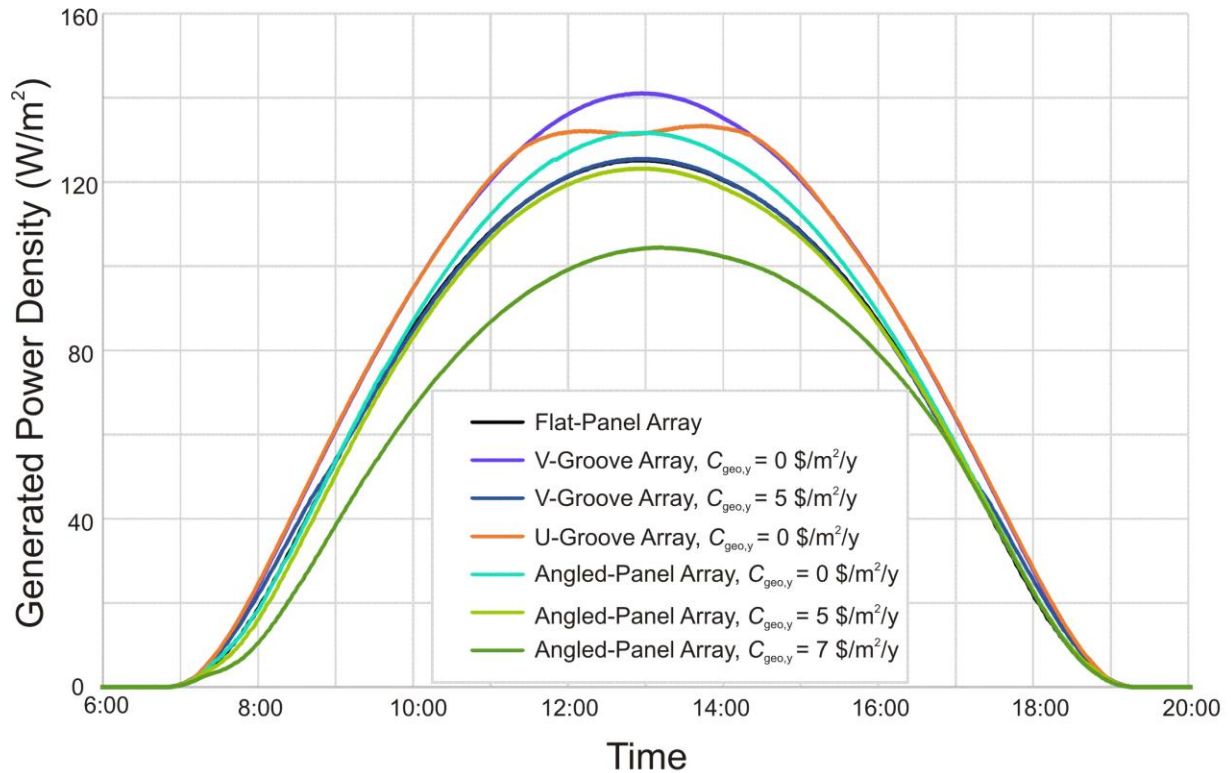


Fig. 4.21: The generated electrical power density of each of the array configurations optimized to  $C_{geo,y} = 0, 5,$  and  $7$  \$/m²/y on March 20, 2018. The Flat-Panel Array is difficult to distinguish in this figure, being nearly identical to the V-Groove Array at  $C_{geo,y} = 5$  \$/m²/y during the middle of the day and the Angled-Panel Array at  $C_{geo,y} = 0$  \$/m²/y during the morning and evening.

This daily capture can also serve to validate the use of the various quantization measures to simplify the simulation. Fig. 4.22 shows a comparison of the high-accuracy generated electrical power curve for the Angled-Panel Array at  $C_{geo,y} = 5$  \$/m²/y against the highly-quantized curve for the same value. Some noise can clearly be seen on the quantized curve, particularly in the middle of the day, but generally the two curves fit together well enough to trust the conclusions drawn from the highly-quantized version of the simulation. The normalized RMS error for the non-zero portion of this curve is 0.28%.

Moving on to longer-term trends, Fig. 4.23 shows the daily relative profit densities for the optimal configurations of the Angled-Panel Array, V-Groove Array, and U-Groove Array at  $C_{geo,y}$  values of 0, 5,

and 7  $\$/\text{m}^2/\text{y}$ . As was done in the simplified simulation, these results are normalized against the results of the Flat-Panel Array. However, in this case, since relative profit density can be negative during periods of low photovoltaic generation, the normalization was performed as the absolute improvement over a Flat-Panel Array, rather than the percentage relative to an idealized Flat-Panel Array.

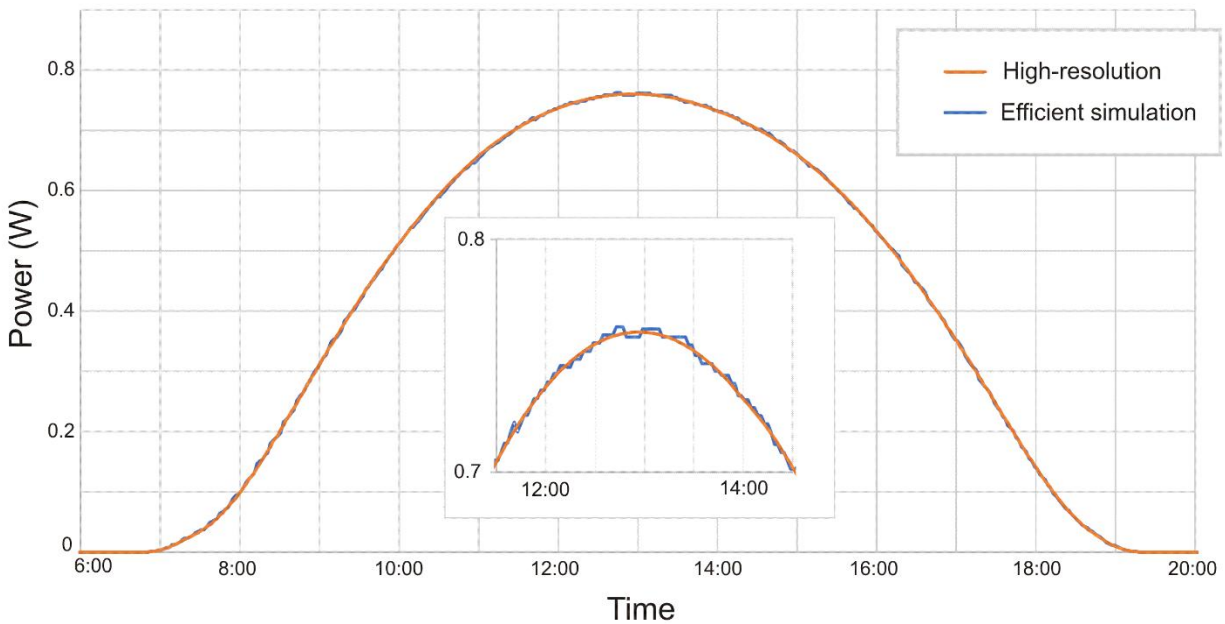


Fig. 4.22: A comparison of the generated power of the Angled-Panel Array optimized to  $C_{\text{geo},y} = 5 \text{ \$/m}^2/\text{y}$  on March 20, 2018, shown in orange at high-resolution settings and in blue at high-simulation-efficiency settings. The inset shows a closer view of the mid-day period to illustrate the quantization noise introduced at high-simulation-efficiency settings.

The majority of the curves shown here demonstrate a clear seasonal cycle, with the exception of the shallow V-Groove Array, whose performance is nearly identical to that of the Flat-Panel Array. The noise caused by the “Duck Curve” can be clearly seen during the spring of the later years.

The three arrays configured for  $C_{\text{geo},y} = 0 \text{ \$/m}^2/\text{y}$  demonstrate very similar profiles, with significantly increased relative profit densities during the summer, and slightly increased relative profit densities during the winter. This result can be expected; as these arrays rely on light trapping, their performance increases the most during the summer when more light is available.

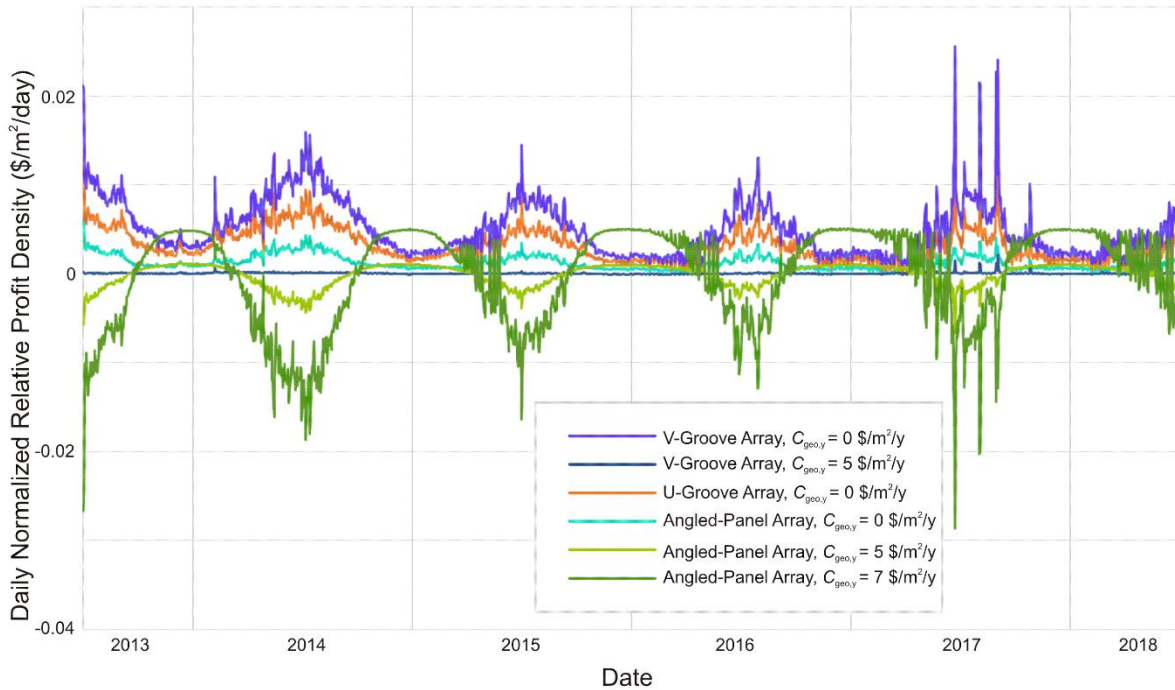


Fig. 4.23: The daily relative profit densities of the optimal array configurations at  $C_{\text{geo},y}$  values of 0, 5, and 7  $\$/\text{m}^2/\text{y}$ , over the five-year period of study. Curves shown here are normalized by subtracting the relative profit densities of a Flat-Panel Array at the same  $C_{\text{geo},y}$  value.

The two wider-spaced Angled-Panel Arrays conversely experience the opposite trend, with improved performance during the winter, and worse performance than the Flat-Panel Array during the summer. This unusual trend is likely due to the gaps between rows in these arrays. The spacing of these arrays is optimally large, to avoid self-shadowing during the winter, but this allows some direct solar illumination during the summer to fall on the space between the rows, greatly reducing its collection efficiency. While both the direction of incidence and the reflection-capturing behaviour of the Flat-Panel Array are poor, such an array at least has the benefit that all direct solar illumination will be incident on a photovoltaic surface, which is not true for the Angled-Panel Array.

To provide a detailed comparison of the four arrays at current conditions, Fig. 4.24 shows the relative profit density improvement of each array as compared to the Flat-Panel Array over the year of July 2017-June 2018. At low geometry-dependent cost densities, the V-Groove Array is seen to dominate, with the U-Groove Array close behind it. This is a reversal of the trend seen with the simplified simulation, where the

U-Groove Array slightly outperformed the V-Groove Array. This reversal is likely due to the introduction of diffuse light, the capture of which is related to the aspect ratio of the arrays. The U-Groove Array requires more solar cells per unit area, and therefore higher losses, for a given aspect ratio than the V-Groove Array does, reducing its effectiveness at trapping diffuse light. When rotation is taken into consideration, the improvement of the V-Groove Array increases substantially, greatly outperforming the U-Groove Array thanks to its improved ability to trap direct solar illumination.

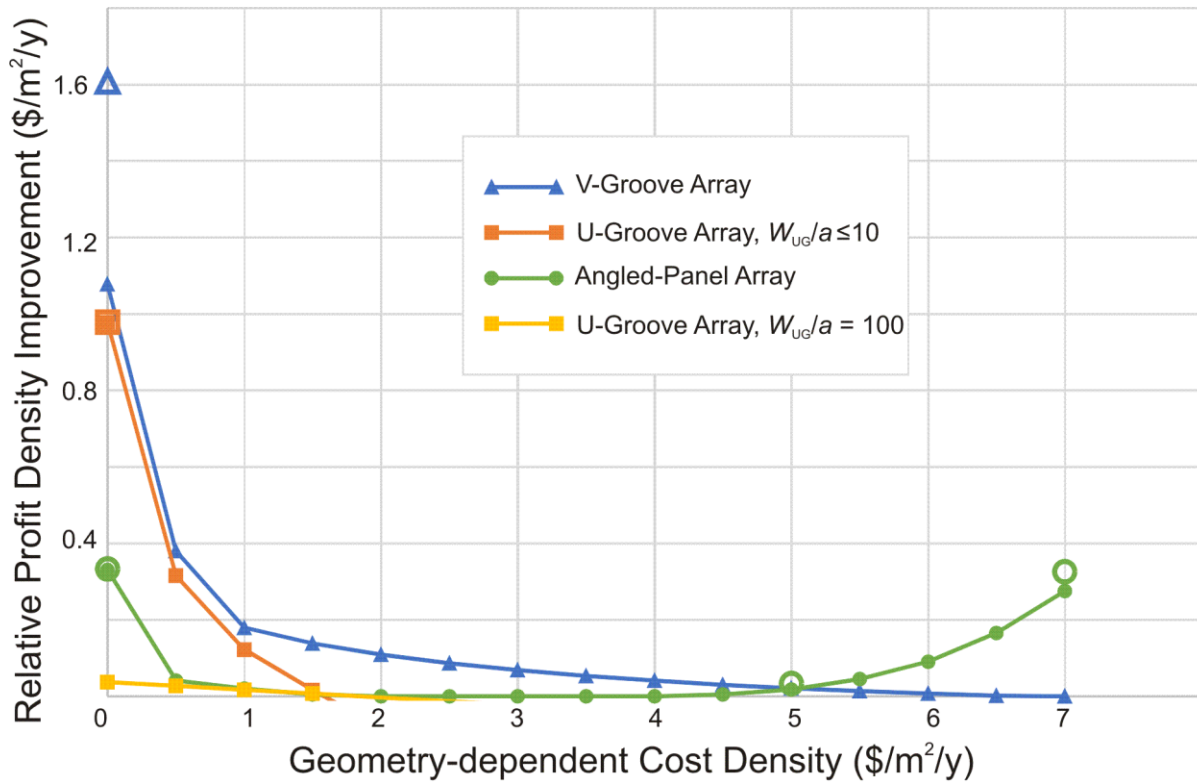


Fig. 4.24: Relative profit density improvement over the Flat-Panel Array as a function of  $C_{geo,y}$  for optimal configurations of the three other arrays. Solid lines represent the optimal configurations with fixed  $\rho$  values, while outlined points represent the optimal configurations with optimized  $\rho$  values.

The curve shown for the U-Groove Array is limited to widths of 10 solar cell side lengths or less. A curve for the 100-width U-Groove Array is also shown, demonstrating that while a wider U-Groove Array does increase the range over which the U-Groove Array outperforms the Flat-Panel Array, this improvement greatly suffers from diminishing returns, and would generally not be practical.

The improved performance of the Angled-Panel Array at low geometry-dependent cost densities due to light trapping can also be seen here, although it falls well short of the values for the V-Groove Array and U-Groove Array. At high geometry-dependent cost densities, the performance of the Angled-Panel Array can be seen to improve again, eventually surpassing the V-Groove Array around  $C_{\text{geo},y} = 5 \text{ \$/m}^2/\text{y}$ , which is the reason for this point's inclusion in earlier analyses. This point, which will be referred to from here on as the crossover point, represents the geometry-dependent cost density at which the V-Groove Array and Angled-Panel Array have equivalent performance. Note that the improvement in the Angled-Panel Array's performance when rotation is allowed shifts the crossover point slightly left to smaller values of  $C_{\text{geo},y}$ . However, as the improvement of the Angled-Panel Array optimized to  $C_{\text{geo},y} = 5 \text{ \$/m}^2/\text{y}$  under rotational optimization is not particularly substantial, this shift is not expected to be large.

Similar crossover points can be found for the five years of the study, as demonstrated in Appendix B. The locations of these crossover points are summarized in Table 4.2. The results appear to be strongly correlated to the electricity price, similar to what was previously observed with the yearly value density in Fig. 3.12. In order to confirm this correlation, the location of the crossover point is plotted against average yearly electricity price in Fig. 4.25. The two quantities do appear to be somewhat linked. However, there are obviously other factors influencing the location of the crossover point, given that the electricity price jumped substantially over the past year without the crossover point moving significantly.

Table 4.2: Value of the geometry-dependent cost density at the crossover point for the five years of the study if rotation is fixed at zero. Allowing rotation to vary would likely result in a slight reduction in all these values.

<b>Year</b>	<b><math>C_{\text{geo},y}</math> at Crossover Point</b>
2013-2014	6.65 $\text{\$/m}^2/\text{y}$
2014-2015	5.75 $\text{\$/m}^2/\text{y}$
2015-2016	4.44 $\text{\$/m}^2/\text{y}$
2016-2017	5.03 $\text{\$/m}^2/\text{y}$
2017-2018	5.05 $\text{\$/m}^2/\text{y}$

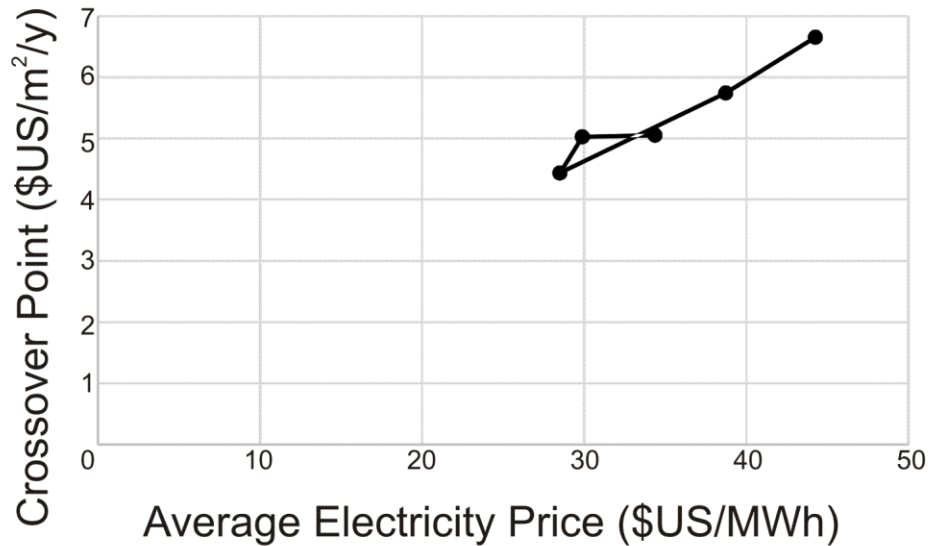


Fig. 4.25: A comparison of the value of  $C_{\text{geo},y}$  at the crossover point and the average electricity price over the five year period studied. A strong correlation between the two values can be seen.

#### 4.3.4: Discussion

For the July 2017-June 2018 year, at a value of  $C_{\text{geo},y} = 7 \text{ \$/m}^2/\text{y}$ , the optimal array and configuration according to this simulation is an Angled-Panel Array with a row separation of 10.4 cm (or 136% of the solar cell width, if the array's scale were to be increased), a tilt angle of  $21^\circ$  from horizontal, and a rotation angle of approximately  $15^\circ$  west of south. This fits well to the industry standard array being an Angled-Panel Array facing slightly west to reduce the effect of the “Duck Curve”. However, the rule-of-thumb guideline for Angled-Panel Array angle has it equal to the latitude [155], which would be  $35^\circ$ , substantially greater than the optimal value at  $C_{\text{geo},y} = 7 \text{ \$/m}^2/\text{y}$  of  $21^\circ$ . This is an interesting result, as it suggests that this guideline is not applicable to the circumstances measured in this simulation. The most likely reason for this discrepancy is the presence of multiple rows of solar cells. Investigations into the validity of this assumption typically do not include a spacing parameter [155]-[157], and it can therefore be assumed that such investigations apply to a single, standalone solar panel rather than a large array. When assembled into an array, larger values for  $\tau_{\text{AP}}$  would result in increased shadowing between solar cells, reducing the efficiency of the solar cells. Therefore, lower angles would be preferable for large arrays. The optimal tilt angle can additionally be seen to be closely linked to the value of  $C_{\text{geo},y}$ , with higher geometry-dependent cost densities

leading to larger optimal tilt angles. It is important to bear in mind that the selection of the current geometry-dependent cost density as being equal to 7  $\$/\text{m}^2\text{y}$  was an estimate without rigorous support, which this analysis has left clear is both approximate and easily adjustable. The infrastructure costs associated with photovoltaic generation are also falling over time, and it is possible the latitude-based estimate is founded in historically-higher values of  $C_{\text{geo,y}}$ . It is also worth noting that the optimal tilt angle at  $C_{\text{geo,y}} = 7 \text{ \$/m}^2\text{/y}$  has varied greatly over the past five years, due in part to long-term fluctuations in electricity price. Any one of these effects could have influenced additional inaccuracies in either the latitude-based estimate or the optimal values derived here.

One trend that can, however, be clearly predicted, is that the value of  $C_{\text{geo,y}}$  is decreasing over time. The primary cost associated with geometry-dependence, the cost of the photovoltaic modules themselves, has been consistently decreasing, and although that rate of decrease has slowed significantly recently, the downward trend still persists [80]. As this value drops, shallower and more closely-spaced Angled-Panel Arrays will become optimal. If the decrease continues far enough to reach the crossover point, the V-Groove Array will surpass the Angled-Panel Array as the optimal geometric solar array.

However, this simplified statement does not present the entire picture. While the geometry-dependent cost density may be decreasing, the crossover point is also moving. This trend has been shown to be linked to the average price of electricity, but this study does not extend to the prediction of long-term electricity price trends. Complicating this, while the geometry-dependent cost density is primarily relevant when the geometric solar array is first installed, the crossover point location remains relevant to its performance over the array's entire lifespan, so long-term predictions are required to determine its effect. Additionally, investigation into the additional factors affecting the crossover point is still needed before its future trends can be predicted to any accurate extent.

Furthermore, the electricity price used here can itself be called into question, as it is founded on the broad and generally inaccurate assumption that photovoltaically-generated electrical energy sold to the power grid is sold at the day-ahead locational marginal grid electricity price, with no further subsidies or

incentives. The significant inaccuracies of this assumption are made obvious by how large the geometry-dependent cost density is relative to the generated value density, even though it should represent only a fraction of the total cost. For the Flat-Panel Array, the value generated in the past year is 8.0633  $\$/\text{m}^2/\text{y}$ , which is not significantly greater than the estimated 6.8  $\$/\text{m}^2/\text{y}$  of the geometry-dependent cost density, indicating that under the conditions simulated here, none of the geometric solar arrays would ultimately prove to be financially profitable. Essentially, the motion of the crossover point cannot be predicted to any significant extent based on this research, limiting the ability of the results presented here to support recommendations for the development of future geometric solar arrays.

While the U-Groove Array looked like a promising geometric structure based on the results of the simplified simulation, the detailed analysis presented here reveals that once installation costs and diffuse light are taken into account, the array's performance improvements are insufficient to make up for its increased complexity. Ultimately, while it remains a novel and interesting idea, the U-Groove Array is unlikely to prove useful for photovoltaic generation in the near future, at least in the case of crystalline silicon photovoltaics.

Despite the vast improvement seen between the first, simplified, simulation and the second, rigorous, simulation, there are some assumptions remaining that could have negatively affected the results. The assumptions made about the geometry-dependent cost density and the sale price of electricity have been discussed above. Additionally, the use of quantization and reusing intermediate results, while necessary for this analysis, may be avoidable through further optimization of the simulation or a shift to more dedicated simulation hardware. The assumptions of ideal aluminum reflectance, wavelength-independent ARC reflectance, and a single MPPT and inverter rather than a micro-inverter system, while made for practical reasons, are difficult to justify in hindsight. Diffuse sky light was heavily simplified in this analysis, with its spectral distribution assumed to be independent of both time and location in the sky and its intensity was derived from joining two models without sufficient investigation into their compatibility. A more realistic treatment of the weather, and the effects of cloud cover, accurate temperature variation, and resistive heating

based on wind speed, would also be warranted. Ultimately, the treatment of all diffuse light as Lambertian may also warrant major adjustments to the simulation method. While the results presented in this study can be assumed to be generally accurate, there are still numerous ways in which they could be improved to more precisely match what would be encountered in a true commercial photovoltaic generating array.

## 5: Conclusion

With global warming becoming an imminent crisis, a shift away from the use of fossil fuels for electricity generation is desperately needed. Solar generation has been taking centre stage in this shift due to its low environmental impact and highly flexible location requirements. For large-scale solar generating facilities, concentrating solar power is becoming known as the best option. However, these flexible location requirements combined with significant scalability have led to the proliferation of small-scale, distributed photovoltaic generation.

Despite its benefits, solar generation still faces significant challenges. One of the most important of these relates to the daily cycle of solar generation and its effect on electricity supply and demand. Electricity supply is typically scaled to match electricity demand, but at high penetration levels of solar generation, the electricity supply tends to increase during the day, and other forms of electricity generation are proving inadequate at compensating for this. The resulting mismatch in supply and demand results in extreme fluctuations in electricity price and the potential for instability in the power grid. The ultimate solution to this problem is likely through the use of energy storage, but short-term solutions are necessary to allow time for sufficient development in energy storage technology.

This thesis served to introduce a value-based metric in lieu of the standard power-based metric. This metric was used to carry out performance analyses of various geometric solar arrays and their configurations with the goal of identifying the ideal array and implementation under present conditions. We commented on how the ideal array and its implementation may differ in the future based on trends in infrastructure and electricity price.

A metric of geometry-dependent profit density was introduced, being the difference between the annual value generated and the annually-distributed installation and maintenance costs that are found to be proportional to the active area of the array, rather than its installation area, both presented per unit area. Under the estimated conditions, for the year from July 2017 to June 2018, the array and configuration found

to maximize this metric was an Angled-Panel Array with the rows of panels raised at a height of  $21^\circ$  from horizontal and facing  $15^\circ$  west of south, with a spacing between the rows equal to 1.36 times their height.

Predicting how well this ideal array and implementation will hold up in the future is beyond the scope of this research. If installation costs decrease and electricity prices increase, the ideal implementation of the Angled-Panel Array will develop a shallower tilt angle and narrower spacing, approaching the limiting case of a Flat-Panel Array. However, before this would completely degenerate, the ideal array will switch from being the Angled-Panel Array to the V-Groove Array, specifically a shallow configuration with an internal angle around  $160^\circ$  and panels facing directly east and west. While the installation costs are known to be decreasing, albeit slowly, electricity prices have fluctuated dramatically over the course of the study, and the prediction of their future trends would require significant additional research. Additionally, while installation costs are only relevant when a solar generating array is first constructed, electricity prices continue to be relevant over its entire lifespan. Therefore, further research would be required to extend the results collected here into future predictions and recommendations.

Future work on this topic could involve the continued refinement of the methods and data presented in this thesis. Several potential inaccuracies with the simulation used were pointed out in section 4.3.4, and these could be changed to improve the results obtained. Additionally, the rotation of the arrays was not as well studied as the other implementation parameters, being instead largely overlooked by this study and only investigated at a few specific data points. Further optimization would be warranted here to test the validity of observed trends.

While this work focused on crystalline silicon solar cells, their status as the dominant type of photovoltaics may be changing. Although the role of economies of scale and existing manufacturing infrastructure means that any such change will likely only become significant over longer timescales, it is nonetheless possible that the analyses developed here would prove beneficial when applied to different types of photovoltaics. Thin-film photovoltaics in particular, given their low installation cost and low efficiency, have been shown to benefit from light-trapping structures, and are currently the main use for the V-Groove Array. Applying

value-based optimization to thin-film photovoltaics could reveal more effective geometrical arrangements to use them in, particularly given that the restrictions to flat, square solar cells could then be waived. Additionally, the significant low-light performance of dye-sensitized solar cells could lend itself well to the geometric arrangements studied here by improving the overall performance in low-light high-value conditions, as well as by increasing the efficiency when sunlight is split between a large number of solar cells in a complex geometric structure.

One further avenue for additional research is the collection of supporting experimental data. While the ARIES experiment was helpful to derive the solar cell parameters and validate the simulation, long-term experimental data for additional arrays and implementations collected in a location that is more similar to the targeted location for this study would nonetheless be valuable to further quantify the accuracy of the simulation and identify any inaccuracies that might need to be addressed.

In summary, the use of a value-based metric to optimize geometric solar arrays has led to the conclusion that the current industry standard geometric solar array, consisting of rows of angled solar panels facing slightly west of south, is ideal under present conditions for both economic profit and to reduce the impact of daily electricity price fluctuations caused by high penetration of solar generation, although a shallower tilt angle than that which is typically recommended would be preferable when implemented as a large array. Suggestions were given for how this work could be extended to accurately predict how this research will change in the future. This would aid decision making for the best geometric solar arrays to construct for future photovoltaic applications.

## Bibliography

- [1] *Paris Agreement to the United Nations Framework Convention on Climate Change (UNFCCC)*, December 2015, Paris, France.
- [2] S. Chu and A. Majumdar, “Opportunities and challenges for a sustainable energy future,” *Nature*, vol. 488, no. 7411, pp. 294, 2012.
- [3] M. B. Hayat, D. Ali, K. C. Monyake, L. Alagha and N. Ahmed, “Solar energy—A look into power generation, challenges, and a solar-powered future,” *Int. J. Energy Res.*, vol. 43, no. 3, pp. 1049-1067, 2019.
- [4] M. A. Green, “Silicon photovoltaic modules: a brief history of the first 50 years,” *Prog Photovoltaics Res Appl*, vol. 13, no. 5, pp. 447-455, 2005.
- [5] J. Jean, P. R. Brown, R. L. Jaffe, T. Buonassisi and V. Bulović, “Pathways for solar photovoltaics,” *Energy & Environmental Science*, vol. 8, no. 4, pp. 1200-1219, 2015.
- [6] J. S. Price, A. J. Grede, B. Wang, M. V. Lipski, B. Fisher, K. Lee, J. He, G. S. Brulo, X. Ma and S. Burroughs, “High-concentration planar microtracking photovoltaic system exceeding 30% efficiency,” *Nature Energy*, vol. 2, no. 8, pp. 17113, 2017.
- [7] S. Rühle, “Tabulated values of the Shockley–Queisser limit for single junction solar cells,” *Solar Energy*, vol. 130, pp. 139-147, 2016.
- [8] S. Essig, C. Allebé, T. Remo, J. F. Geisz, M. A. Steiner, K. Horowitz, L. Barraud, J. S. Ward, M. Schnabel and A. Descoedres, “Raising the one-sun conversion efficiency of III–V/Si solar cells to 32.8% for two junctions and 35.9% for three junctions,” *Nature Energy*, vol. 2, no. 9, pp. 17144, 2017.
- [9] T. K. Todorov, D. M. Bishop and Y. S. Lee, “Materials perspectives for next-generation low-cost tandem solar cells,” *Solar Energy Mater. Solar Cells*, vol. 180, pp. 350-357, 2018.
- [10] K. Chopra, P. Paulson and V. Dutta, “Thin-film solar cells: an overview,” *Prog Photovoltaics Res Appl*, vol. 12, no. 2-3, pp. 69-92, 2004.
- [11] Y. Peter and M. Cardona, *Fundamentals of Semiconductors: Physics and Materials Properties*. Springer Science & Business Media, 2010.
- [12] A. H. Munshi, N. Sasidharan, S. Pinkayan, K. L. Barth, W. Sampath and W. Ongsakul, “Thin-film CdTe photovoltaics—The technology for utility scale sustainable energy generation,” *Solar Energy*, vol. 173, pp. 511-516, 2018.
- [13] M. Green, E. Dunlop, D. Levi, J. Hohl-Ebinger, M. Yoshita and A. Ho-Baillie, “Solar Cell Efficiency Tables (version 54),” *Prog Photovoltaics Res Appl*, vol. 27, pp. 565-575, 2019.

- [14] O. O. Ogbomo, E. H. Amalu, N. Ekere and P. Olagbegi, "A review of photovoltaic module technologies for increased performance in tropical climate," *Renewable and Sustainable Energy Reviews*, vol. 75, pp. 1225-1238, 2017.
- [15] S. Hegedus, "Thin film solar modules: the low cost, high throughput and versatile alternative to Si wafers," *Prog Photovoltaics Res Appl*, vol. 14, no. 5, pp. 393-411, 2006.
- [16] S. Amarakoon, C. Vallet, M. A. Curran, P. Haldar, D. Metacarpa, D. Fobare and J. Bell, "Life cycle assessment of photovoltaic manufacturing consortium (PVMC) copper indium gallium (di) selenide (CIGS) modules," *The International Journal of Life Cycle Assessment*, vol. 23, no. 4, pp. 851-866, 2018.
- [17] D. Liu, D. Han, M. Huang, X. Zhang, T. Zhang, C. Dai and S. Chen, "Theoretical study on the kesterite solar cells based on  $\text{Cu}_2\text{ZnSn}(\text{S}, \text{Se})_4$  and related photovoltaic semiconductors," *Chinese Physics B*, vol. 27, no. 1, pp. 018806, 2018.
- [18] S. Zhuk, A. Kushwaha, T. K. Wong, S. Masudy-Panah, A. Smirnov and G. K. Dalapati, "Critical review on sputter-deposited  $\text{Cu}_2\text{ZnSnS}_4$  (CZTS) based thin film photovoltaic technology focusing on device architecture and absorber quality on the solar cells performance," *Solar Energy Mater. Solar Cells*, vol. 171, pp. 239-252, 2017.
- [19] A. L. Greenaway, J. W. Boucher, S. Z. Oener, C. J. Funch and S. W. Boettcher, "Low-Cost Approaches to III-V Semiconductor Growth for Photovoltaic Applications," *ACS Energy Letters*, vol. 2, no. 10, pp. 2270-2282, 2017.
- [20] A. W. Bett, S. P. Philipps, S. Essig, S. Heckelmann, R. Kellenbenz, V. Klinger, M. Niemeyer, D. Lackner and F. Dimroth, "Overview about technology perspectives for high efficiency solar cells for space and terrestrial applications," in *28th European Photovoltaic Solar Energy Conference and Exhibition*, 2013, pp. 1-6.
- [21] G. Conibeer, "Third-generation photovoltaics," *Materials Today*, vol. 10, no. 11, pp. 42-50, 2007.
- [22] M. A. Green and A. Ho-Baillie, "Perovskite solar cells: the birth of a new era in photovoltaics," *ACS Energy Letters*, vol. 2, no. 4, pp. 822-830, 2017.
- [23] J. Alberola-Borràs, R. Vidal and I. Mora-Seró, "Evaluation of multiple cation/anion perovskite solar cells through life cycle assessment," *Sustainable Energy & Fuels*, vol. 2, no. 7, pp. 1600-1609, 2018.
- [24] Y. Chen, L. Zhang, Y. Zhang, H. Gao and H. Yan, "Large-area perovskite solar cells—a review of recent progress and issues," *RSC Advances*, vol. 8, no. 19, pp. 10489-10508, 2018.
- [25] S. Holliday, Y. Li and C. K. Luscombe, "Recent advances in high performance donor-acceptor polymers for organic photovoltaics," *Progress in Polymer Science*, vol. 70, pp. 34-51, 2017.
- [26] M. Igarashi, M. F. Budiman, W. Pan, Y. Hoshi, W. Hu, M. E. Syazwan, K. Sawano, N. Usami and S. Samukawa, "High efficiency quantum dot solar cells using 2-dimensional 6.4-nm-

- diameter si nanodisk with SiC interlayer,” in *2012 38th IEEE Photovoltaic Specialists Conference*, 2012, pp. 003195-003199.
- [27] H. Choi, C. Nahm, J. Kim, C. Kim, S. Kang, T. Hwang and B. Park, “Toward highly efficient quantum-dot-and dye-sensitized solar cells,” *Current Applied Physics*, vol. 13, pp. S2-S13, 2013.
- [28] H. J. Snaith and L. Schmidt-Mende, “Advances in liquid-electrolyte and solid-state dye-sensitized solar cells,” *Adv Mater*, vol. 19, no. 20, pp. 3187-3200, 2007.
- [29] P. Selvaraj, H. Baig, T. K. Mallick, J. Siviter, A. Montecucco, W. Li, M. Paul, T. Sweet, M. Gao and A. R. Knox, “Enhancing the efficiency of transparent dye-sensitized solar cells using concentrated light,” *Solar Energy Mater. Solar Cells*, vol. 175, pp. 29-34, 2018.
- [30] A. Goodrich, P. Hacke, Q. Wang, B. Sopori, R. Margolis, T. L. James and M. Woodhouse, “A wafer-based monocrystalline silicon photovoltaics road map: Utilizing known technology improvement opportunities for further reductions in manufacturing costs,” *Solar Energy Mater. Solar Cells*, vol. 114, pp. 110-135, 2013.
- [31] D. M. Powell, R. Fu, K. Horowitz, P. A. Basore, M. Woodhouse and T. Buonassisi, “The capital intensity of photovoltaics manufacturing: barrier to scale and opportunity for innovation,” *Energy & Environmental Science*, vol. 8, no. 12, pp. 3395-3408, 2015.
- [32] K. Rajkanan, R. Singh and J. Shewchun, “Absorption coefficient of silicon for solar cell calculations,” *Solid-State Electronics*, vol. 22, no. 9, pp. 793-795, 1979.
- [33] S. Philipps and W. Warmuth, “Photovoltaics report—Fraunhofer ISE,” *Fraunhofer Institute for Solar Energy Systems ISE, Freiburg Im Breisgau, Germany*. Accessed: Sep, vol. 15, 2018.
- [34] S. Xiao and S. Xu, “High-efficiency silicon solar cells—materials and devices physics,” *Critical Reviews in Solid State and Materials Sciences*, vol. 39, no. 4, pp. 277-317, 2014.
- [35] T. Saga, “Advances in crystalline silicon solar cell technology for industrial mass production,” *NPG Asia Materials*, vol. 2, no. 3, pp. 96, 2010.
- [36] H. Sai, T. Matsui and K. Matsubara, “Key Points in the Latest Developments of High-Efficiency Thin-Film Silicon Solar Cells,” *Physica Status Solidi (a)*, vol. 214, no. 12, pp. 1700544, 2017.
- [37] F. Haug and C. Ballif, “Light management in thin film silicon solar cells,” *Energy & Environmental Science*, vol. 8, no. 3, pp. 824-837, 2015.
- [38] A. E. Morishige, F. D. Heinz, H. S. Laine, J. Schön, W. Kwapil, B. Lai, H. Savin, M. C. Schubert and T. Buonassisi, “Moving Beyond p-Type mc-Si: Quantified Measurements of Iron Content and Lifetime of Iron-Rich Precipitates in n-Type Silicon,” *IEEE Journal of Photovoltaics*, vol. 8, no. 6, pp. 1525-1530, 2018.
- [39] J. Cotter, J. Guo, P. Cousins, M. Abbott, F. Chen and K. Fisher, “P-type versus n-type silicon wafers: prospects for high-efficiency commercial silicon solar cells,” *IEEE Trans. Electron Devices*, vol. 53, no. 8, pp. 1893-1901, 2006.

- [40] M. Tao, "Substitution of silver electrode with an abundant metal—A fundamental study," in *2011 37th IEEE Photovoltaic Specialists Conference*, 2011, pp. 002947-002951.
- [41] O. Von Roos, "A simple theory of back surface field (BSF) solar cells," *J. Appl. Phys.*, vol. 49, no. 6, pp. 3503-3511, 1978.
- [42] N. L. Chang, A. Ho-Baillie, S. Wenham, M. Woodhouse, R. Evans, B. Tjahjono, F. Qi, C. M. Chong and R. J. Egan, "A techno-economic analysis method for guiding research and investment directions for c-Si photovoltaics and its application to Al-BSF, PERC, LDSE and advanced hydrogenation," *Sustainable Energy & Fuels*, vol. 2, no. 5, pp. 1007-1019, 2018.
- [43] K. Yoshikawa, H. Kawasaki, W. Yoshida, T. Irie, K. Konishi, K. Nakano, T. Uto, D. Adachi, M. Kanematsu and H. Uzu, "Silicon heterojunction solar cell with interdigitated back contacts for a photoconversion efficiency over 26%," *Nature Energy*, vol. 2, no. 5, pp. 17032, 2017.
- [44] M. M. Desa, S. Sapeai, A. Azhari, K. Sopian, M. Y. Sulaiman, N. Amin and S. H. Zaidi, "Silicon back contact solar cell configuration: A pathway towards higher efficiency," *Renewable and Sustainable Energy Reviews*, vol. 60, pp. 1516-1532, 2016.
- [45] M. S. Farhan, E. Zalnezhad, A. R. Bushroa and A. A. D. Sarhan, "Electrical and optical properties of indium-tin oxide (ITO) films by ion-assisted deposition (IAD) at room temperature," *International Journal of Precision Engineering and Manufacturing*, vol. 14, no. 8, pp. 1465-1469, 2013.
- [46] M. Cudzinovic and B. Sopori, "Control of back surface reflectance from aluminum alloyed contacts on silicon solar cells," in *Conference Record of the Twenty Fifth IEEE Photovoltaic Specialists Conference-1996*, 1996, pp. 501-503.
- [47] H. K. Raut, V. A. Ganesh, A. S. Nair and S. Ramakrishna, "Anti-reflective coatings: A critical, in-depth review," *Energy & Environmental Science*, vol. 4, no. 10, pp. 3779-3804, 2011.
- [48] Y. Matsumoto, J. A. Urbano, M. Ortega, E. Barrera and G. Romero-Paredes, "Towards cost-effective antireflective-coating and surface-texturing," in *2012 38th IEEE Photovoltaic Specialists Conference*, 2012, pp. 000258-000264.
- [49] J. Schmidt, R. Peibst and R. Brendel, "Surface passivation of crystalline silicon solar cells: Present and future," *Solar Energy Mater. Solar Cells*, vol. 187, pp. 39-54, 2018.
- [50] E. E. Perl, C. Lin, W. E. McMahon, D. J. Friedman and J. E. Bowers, "Ultrabroadband and wide-angle hybrid antireflection coatings with nanostructures," *IEEE Journal of Photovoltaics*, vol. 4, no. 3, pp. 962-967, 2014.
- [51] Z. Ge, P. Rajbhandari, J. Hu, A. Emrani, T. P. Dhakal, C. Westgate and D. Klotzkin, "Enhanced omni-directional performance of copper zinc tin sulfide thin film solar cell by gradient index coating," *Appl. Phys. Lett.*, vol. 104, no. 10, pp. 101104, 2014.
- [52] W. H. Southwell, "Gradient-index antireflection coatings," *Opt. Lett.*, vol. 8, no. 11, pp. 584-586, 1983.

- [53] F. Bouquet, "Glass as encapsulation for low-cost photovoltaic solar arrays," *Journal of Solar Energy Engineering*, vol. 103, no. 3, pp. 221-232, 1981.
- [54] C. Peike, I. Hädrich, K. Weiß and I. Dürr, "Overview of PV module encapsulation materials," *Photovoltaics International*, vol. 19, pp. 85-92, 2013.
- [55] A. Nadia, N. A. M. Isa and M. K. M. Desa, "Advances in solar photovoltaic tracking systems: A review," *Renewable and Sustainable Energy Reviews*, vol. 82, pp. 2548-2569, 2018.
- [56] H. Mousazadeh, A. Keyhani, A. Javadi, H. Mobli, K. Abrinia and A. Sharifi, "A review of principle and sun-tracking methods for maximizing solar systems output," *Renewable and Sustainable Energy Reviews*, vol. 13, no. 8, pp. 1800-1818, 2009.
- [57] J. Gordon and H. J. Wenger, "Central-station solar photovoltaic systems: field layout, tracker, and array geometry sensitivity studies," *Solar Energy*, vol. 46, no. 4, pp. 211-217, 1991.
- [58] W. Xiao, N. Ozog and W. G. Dunford, "Topology study of photovoltaic interface for maximum power point tracking," *IEEE Trans. Ind. Electron.*, vol. 54, no. 3, pp. 1696-1704, 2007.
- [59] A. Nadia, N. A. M. Isa and M. K. M. Desa, "Advances in solar photovoltaic tracking systems: A review," *Renewable and Sustainable Energy Reviews*, vol. 82, pp. 2548-2569, 2018.
- [60] Y. Du, W. Tao, Y. Liu, Z. Le and M. Zhang, "Cell-to-Module Variation of Optical and Photovoltaic Properties for Monocrystalline Silicon Solar Cells with Different Texturing Approaches," *ECS Journal of Solid State Science and Technology*, vol. 6, no. 5, pp. P332-P338, 2017.
- [61] A. Ingenito, O. Isabella and M. Zeman, "Nano-cones on micro-pyramids: modulated surface textures for maximal spectral response and high-efficiency solar cells," *Prog Photovoltaics Res Appl*, vol. 23, no. 11, pp. 1649-1659, 2015.
- [62] C. Chang, P. Yu, M. Hsu, P. Tseng, W. Chang, W. Sun, W. Hsu, S. Hsu and Y. Chang, "Combined micro-and nano-scale surface textures for enhanced near-infrared light harvesting in silicon photovoltaics," *Nanotechnology*, vol. 22, no. 9, pp. 095201, 2011.
- [63] J. Oh, H. Yuan and H. M. Branz, "An 18.2%-efficient black-silicon solar cell achieved through control of carrier recombination in nanostructures," *Nature Nanotechnology*, vol. 7, no. 11, pp. 743, 2012.
- [64] W. Zhou, M. Tao, L. Chen and H. Yang, "Microstructured surface design for omnidirectional antireflection coatings on solar cells," *J. Appl. Phys.*, vol. 102, no. 10, pp. 103105, 2007.
- [65] D. Macdonald, A. Cuevas, M. J. Kerr, C. Samundsett, D. Ruby, S. Winderbaum and A. Leo, "Texturing industrial multicrystalline silicon solar cells," *Solar Energy*, vol. 76, no. 1-3, pp. 277-283, 2004.
- [66] J. Zhao, A. Wang, M. A. Green and F. Ferrazza, "19.8% efficient "honeycomb" textured multicrystalline and 24.4% monocrystalline silicon solar cells," *Appl. Phys. Lett.*, vol. 73, no. 14, pp. 1991-1993, 1998.

- [67] J. Kettle, N. Bristow, T. K. Sweet, N. Jenkins, dos Reis Benatto, Gisele A, M. Jørgensen and F. C. Krebs, “Three dimensional corrugated organic photovoltaics for building integration; improving the efficiency, oblique angle and diffuse performance of solar cells,” *Energy & Environmental Science*, vol. 8, no. 11, pp. 3266-3273, 2015.
- [68] H. Zhen, K. Li, Z. Huang, Z. Tang, R. Wu, G. Li, X. Liu and F. Zhang, “Inverted indium-tin-oxide-free cone-shaped polymer solar cells for light trapping,” *Appl. Phys. Lett.*, vol. 100, no. 21, pp. 213901, 2012.
- [69] Y. Xia, L. Hou, K. Ma, B. Wang, K. Xiong, P. Liu, J. Liao, S. Wen and E. Wang, “Pyramid shape of polymer solar cells: a simple solution to triple efficiency,” *J. Phys. D*, vol. 46, no. 30, pp. 305101, 2013.
- [70] D. Yu, M. Yin, L. Lu, H. Zhang, X. Chen, X. Zhu, J. Che and D. Li, “High-Performance and Omnidirectional Thin-Film Amorphous Silicon Solar Cell Modules Achieved by 3D Geometry Design,” *Adv Mater*, vol. 27, no. 42, pp. 6747-6752, 2015.
- [71] B. Myers, M. Bernardi and J. C. Grossman, “Three-dimensional photovoltaics,” *Appl. Phys. Lett.*, vol. 96, no. 7, pp. 071902, 2010.
- [72] D. Shin, N. Chang, Y. Wang and M. Pedram, “Reconfigurable three dimensional photovoltaic panel architecture for solar-powered time extension,” in *2015 IEEE/ACM International Symposium on Low Power Electronics and Design (ISLPED)*, 2015, pp. 273-278.
- [73] J. Li, M. Chong, L. Yang, J. Xu, X. Duan, M. Gao, F. Wang, H. Liu, L. Bian and X. Chi, “A new technique for boosting efficiency of silicon solar cells,” *Solar Energy Mater. Solar Cells*, vol. 86, no. 4, pp. 585-591, 2005.
- [74] S. Rim, S. Zhao, S. R. Scully, M. D. McGehee and P. Peumans, “An effective light trapping configuration for thin-film solar cells,” *Appl. Phys. Lett.*, vol. 91, no. 24, pp. 243501, 2007.
- [75] J. Yoon, K. Kang, S. Kim and J. Kim, “Effect of oblique incidence angle of sunlight on the optimized folding angle of V-shaped organic solar cells,” *Current Applied Physics*, vol. 15, no. 4, pp. 446-451, 2015.
- [76] B. V. Andersson, U. Wuerfel and O. Inganäs, “Full day modelling of V-shaped organic solar cell,” *Solar Energy*, vol. 85, no. 6, pp. 1257-1263, 2011.
- [77] S. Sista, Z. Hong, L. Chen and Y. Yang, “Tandem polymer photovoltaic cells—current status, challenges and future outlook,” *Energy & Environmental Science*, vol. 4, no. 5, pp. 1606-1620, 2011.
- [78] T. Westgate, “A novel photovoltaic device for improvements in solar energy collection,” M.A.Sc. thesis, University of British Columbia, Kelowna, BC, 2019.
- [79] M. Bernardi, N. Ferralis, J. H. Wan, R. Villalon and J. C. Grossman, “Solar energy generation in three dimensions,” *Energy & Environmental Science*, vol. 5, no. 5, pp. 6880-6884, 2012.

- [80] R. Fu, R. M. Margolis and D. J. Feldman, *US Solar Photovoltaic System Cost Benchmark: Q1 2018*, 2018.
- [81] M. Koehl, M. Heck, S. Wiesmeier and J. Wirth, "Modeling of the nominal operating cell temperature based on outdoor weathering," *Solar Energy Mater. Solar Cells*, vol. 95, no. 7, pp. 1638-1646, 2011.
- [82] R. Faranda, S. Leva and V. Maugeri, "MPPT techniques for PV systems: Energetic and cost comparison," in *2008 IEEE Power and Energy Society General Meeting-Conversion and Delivery of Electrical Energy in the 21st Century*, 2008, pp. 1-6.
- [83] S. Narendiran, "Grid tie inverter and MPPT-A review," in *2013 International Conference on Circuits, Power and Computing Technologies (ICCPCT)*, 2013, pp. 564-567.
- [84] A. S. Mundada, E. W. Prehoda and J. M. Pearce, "US market for solar photovoltaic plug-and-play systems," *Renewable Energy*, vol. 103, pp. 255-264, 2017.
- [85] R. E. Pawluk, Y. Chen and Y. She, "Photovoltaic electricity generation loss due to snow—A literature review on influence factors, estimation, and mitigation," *Renewable and Sustainable Energy Reviews*, vol. 107, pp. 171-182, 2019.
- [86] S. A. Said, G. Hassan, H. M. Walwil and N. Al-Aqeeli, "The effect of environmental factors and dust accumulation on photovoltaic modules and dust-accumulation mitigation strategies," *Renewable and Sustainable Energy Reviews*, vol. 82, pp. 743-760, 2018.
- [87] W. Kessler, "Comparing energy payback and simple payback period for solar photovoltaic systems," in *E3S Web of Conferences*, 2017, pp. 00080.
- [88] S. B. Darling, F. You, T. Veselka and A. Velosa, "Assumptions and the levelized cost of energy for photovoltaics," *Energy & Environmental Science*, vol. 4, no. 9, pp. 3133-3139, 2011.
- [89] G. R. Timilsina, L. Kurdgelashvili and P. A. Narbel, "Solar energy: Markets, economics and policies," *Renewable and Sustainable Energy Reviews*, vol. 16, no. 1, pp. 449-465, 2012.
- [90] California Public Utilities Commission, "California net energy metering ratepayer impacts evaluation," *California Public Utilities Commission*, 2013.
- [91] N. R. Darghouth, G. Barbose and R. Wiser, "The impact of rate design and net metering on the bill savings from distributed PV for residential customers in California," *Energy Policy*, vol. 39, no. 9, pp. 5243-5253, 2011.
- [92] T. Couture and Y. Gagnon, "An analysis of feed-in tariff remuneration models: Implications for renewable energy investment," *Energy Policy*, vol. 38, no. 2, pp. 955-965, 2010.
- [93] G. Gowrisankaran, S. S. Reynolds and M. Samano, "Intermittency and the value of renewable energy," *Journal of Political Economy*, vol. 124, no. 4, pp. 1187-1234, 2016.
- [94] J. Feher, "A comparison of siting factors for various electricity-generating technologies," in *Proc., Intersoc. Energy Convers. Eng. Conf.:(United States)*, 1984.

- [95] M. Li, J. Pan, Q. Su and Y. Niu, "Analyzing sensitivity of power system wind penetration to thermal generation flexibility," in *2017 13th IEEE Conference on Automation Science and Engineering (CASE)*, 2017, pp. 1628-1632.
- [96] S. Borenstein, "The market value and cost of solar photovoltaic electricity production," 2008.
- [97] M. Hartner, A. Ortner, A. Hiesl and R. Haas, "East to west—The optimal tilt angle and orientation of photovoltaic panels from an electricity system perspective," *Appl. Energy*, vol. 160, pp. 94-107, 2015.
- [98] California ISO, "Open-Access Same-Time Information System". [Online]. Available: oasis.caiso.com. [Accessed: Sept. 2018].
- [99] P. Palensky and D. Dietrich, "Demand side management: Demand response, intelligent energy systems, and smart loads," *IEEE Transactions on Industrial Informatics*, vol. 7, no. 3, pp. 381-388, 2011.
- [100] A. Henriot, "Economic curtailment of intermittent renewable energy sources," *Energy Econ*, vol. 49, pp. 370-379, 2015.
- [101] R. J. Bass, W. Malalasekera, P. Willmot and H. K. Versteeg, "The impact of variable demand upon the performance of a combined cycle gas turbine (CCGT) power plant," *Energy*, vol. 36, no. 4, pp. 1956-1965, 2011.
- [102] M. K. Chang, J. D. Eichman, F. Mueller and S. Samuelsen, "Buffering intermittent renewable power with hydroelectric generation: A case study in California," *Appl. Energy*, vol. 112, pp. 1-11, 2013.
- [103] E. Baker, M. Fowle, D. Lemoine and S. S. Reynolds, "The economics of solar electricity," *Annu.Rev.Resour.Econ.*, vol. 5, no. 1, pp. 387-426, 2013.
- [104] B. Dunn, H. Kamath and J. M. Tarascon, "Electrical energy storage for the grid: a battery of choices," *Science*, vol. 334, no. 6058, pp. 928-935, Nov 18, 2011.
- [105] V. Jülch, "Comparison of electricity storage options using levelized cost of storage (LCOS) method," *Appl. Energy*, vol. 183, pp. 1594-1606, 2016.
- [106] E. Naswali, C. Alexander, H. Han, D. Naviaux, A. Bistrika, A. von Jouanne, A. Yokochi and T. K. Brekken, "Supercapacitor energy storage for wind energy integration," in *2011 IEEE Energy Conversion Congress and Exposition*, 2011, pp. 298-305.
- [107] T. Grube, L. Doré, A. Hoffrichter, L. E. Hombach, S. Raths, M. Robinius, M. Nobis, S. Schiebahn, V. Tietze and A. Schnettler, "An option for stranded renewables: electrolytic-hydrogen in future energy systems," *Sustainable Energy & Fuels*, vol. 2, no. 7, pp. 1500-1515, 2018.
- [108] H. Ibrahim, A. Ilinca and J. Perron, "Energy storage systems—Characteristics and comparisons," *Renewable and Sustainable Energy Reviews*, vol. 12, no. 5, pp. 1221-1250, 2008.

- [109] D. L. Hartmann, *Global Physical Climatology*. Newnes, 2015/03.
- [110] C. Cornaro and A. Andreotti, "Influence of Average Photon Energy index on solar irradiance characteristics and outdoor performance of photovoltaic modules," *Prog Photovoltaics Res Appl*, vol. 21, no. 5, pp. 996-1003, 2013.
- [111] G. Severino, *The Structure and Evolution of the Sun*. Cham, Switzerland: Springer Nature, 2017.
- [112] F. Kasten and A. T. Young, "Revised optical air mass tables and approximation formula," *Appl. Opt.*, vol. 28, no. 22, pp. 4735-4738, 1989.
- [113] B. E. Schaefer, "Astronomy and the limits of vision," *Vistas in Astronomy*, vol. 36, pp. 311-361, 1993.
- [114] R. Bird, "Terrestrial solar spectral modeling," *Solar Cells*, vol. 7, no. 1-2, pp. 107-118, 1982.
- [115] G. Aher and V. Agashe, "Determination of atmospheric turbidity at Pune," 1998.
- [116] A. A. Kokhanovsky, *Aerosol Optics: Light Absorption and Scattering by Particles in the Atmosphere*. Springer Science & Business Media, 2008.
- [117] C. Riordan and R. Hulstron, "What is an air mass 1.5 spectrum? (solar cell performance calculations)," in *IEEE Conference on Photovoltaic Specialists*, 1990, pp. 1085-1088.
- [118] ASTM International. *ASTM G173-03(2012) Standard Tables for Reference Solar Spectral Irradiances: Direct Normal and Hemispherical on 37° Tilted Surface*. West Conshohocken, PA, ASTM International, 2012
- [119] ASTM International. *ASTM E490-00a(2014) Standard Solar Constant and Zero Air Mass Solar Spectral Irradiance Tables*. West Conshohocken, PA; ASTM International, 2014.
- [120] R. Kittler and S. Darula, "Scattered sunlight determining sky luminance patterns," *Renewable and Sustainable Energy Reviews*, vol. 62, pp. 575-584, 2016.
- [121] V. P. Galileiskii, A. I. Elizarov, D. V. Kokarev and A. M. Morozov, "The formation of the sky brightness with horizon position of the sun," in *21st International Symposium Atmospheric and Ocean Optics: Atmospheric Physics*, 2015, pp. 96803L.
- [122] R. Penndorf, "Angular mie scattering," *Josa*, vol. 52, no. 4, pp. 402-408, 1962.
- [123] M. N. Polyanskiy, "Refractive index database," *refractiveindex.info*. [Online]. Available: <https://refractiveindex.info>. [Accessed: Mar. 12, 2019].
- [124] P. Sánchez-Illescas, P. Carpena, P. Bernaola-Galván, M. Sidrach-de-Cardona, A. Coronado and J. Álvarez, "An analysis of geometrical shapes for PV module glass encapsulation," *Solar Energy Mater. Solar Cells*, vol. 92, no. 3, pp. 323-331, 2008.
- [125] P. Campbell and M. A. Green, "Light trapping properties of pyramidally textured surfaces," *J. Appl. Phys.*, vol. 62, no. 1, pp. 243-249, 1987.

- [126] M. Cudzinovic and B. Sopori, "Control of back surface reflectance from aluminum alloyed contacts on silicon solar cells," in *Conference Record of the Twenty Fifth IEEE Photovoltaic Specialists Conference-1996*, 1996, pp. 501-503.
- [127] S. Mukherjee, K. Miao, A. Paul, N. Neophytou, R. Kim, J. Geng, M. Povolotskyi, T. C. Kubis, A. Ajoy, B. Novakovic, J. Fonseca, H. Ilatikhameneh, S. Steiger, M. McLennan, M. Lundstrom, and G. Klimeck, "Band Structure Lab," *nanoHUB*, 2015. [Online]. Available: <https://nanohub.org/resources/bandstrlab>. [Accessed: Apr. 25, 2019].
- [128] S. A. Kalogirou, *Solar Energy Engineering: Processes and Systems*. Academic Press, 2013.
- [129] O. Breitenstein, "Understanding the current-voltage characteristics of industrial crystalline silicon solar cells by considering inhomogeneous current distributions," *Opto-Electronics Review*, vol. 21, no. 3, pp. 259-282, 2013.
- [130] M. Hasan and S. Parida, "An overview of solar photovoltaic panel modeling based on analytical and experimental viewpoint," *Renewable and Sustainable Energy Reviews*, vol. 60, pp. 75-83, 2016.
- [131] S. Harb, M. Kedia, H. Zhang and R. S. Balog, "Microinverter and string inverter grid-connected photovoltaic system—A comprehensive study," in *2013 IEEE 39th Photovoltaic Specialists Conference (PVSC)*, 2013, pp. 2885-2890.
- [132] G. A. Kopp, S. Farquhar and M. J. Morrison, "Aerodynamic mechanisms for wind loads on tilted, roof-mounted, solar arrays," *J. Wind Eng. Ind. Aerodyn.*, vol. 111, pp. 40-52, 2012.
- [133] F. Meillaud, A. Shah, C. Droz, E. Vallat-Sauvain and C. Miazza, "Efficiency limits for single-junction and tandem solar cells," *Solar Energy Mater. Solar Cells*, vol. 90, no. 18-19, pp. 2952-2959, 2006.
- [134] C. SINGH and S. H. Kumar, *Anti-Reflection and Light Trapping in c-Si Solar Cells*. Springer, 2018.
- [135] D. Saynova, V. Mihailetchi, L. Geerligs and A. Weeber, "Comparison of high efficiency solar cells on large area n-type and p-type silicon wafers with screen-printed aluminum-alloyed rear junction," in *2008 33rd IEEE Photovoltaic Specialists Conference*, 2008, pp. 1-5.
- [136] A. G. Aberle, W. Zhang and B. Hoex, "Advanced loss analysis method for silicon wafer solar cells," *Energy Procedia*, vol. 8, pp. 244-249, 2011.
- [137] E. Meyer, "Extraction of saturation current and ideality factor from measuring Voc and Isc of photovoltaic modules," *International Journal of Photoenergy*, vol. 2017, 2017.
- [138] P. Singh and N. M. Ravindra, "Temperature dependence of solar cell performance—an analysis," *Solar Energy Mater. Solar Cells*, vol. 101, pp. 36-45, 2012.

- [139] N. Veissid and A. M. De Andrade, "The I-V silicon solar cell characteristic parameters temperature dependence. An experimental study using the standard deviation method," *Tenth E.C. Photovoltaic Solar Energy Conf.*, pp. 43-47, 1991.
- [140] R. R. Hernandez, M. K. Hoffacker, M. L. Murphy-Mariscal, G. C. Wu and M. F. Allen, "Solar energy development impacts on land cover change and protected areas," *Proc. Natl. Acad. Sci. U. S. A.*, vol. 112, no. 44, pp. 13579-13584, Nov 3, 2015.
- [141] California ISO, "Market price maps". [Online]. Available: [caiso.com/pricemap](http://caiso.com/pricemap). [Accessed: Sept. 2018].
- [142] National Weather Service Forecast Office, "NOAA Online Weather Data". [Online]. Available: [w2.weather.gov/climate](http://w2.weather.gov/climate). [Accessed: May 2019].
- [143] B. Leckner, "The spectral distribution of solar radiation at the earth's surface—elements of a model," *Solar Energy*, vol. 20, no. 2, pp. 143-150, 1978.
- [144] D. Wark and D. Mercer, "Absorption in the atmosphere by the oxygen "A" band," *Appl. Opt.*, vol. 4, no. 7, pp. 839-845, 1965.
- [145] A. T. Young, "Air mass and refraction," *Appl. Opt.*, vol. 33, no. 6, pp. 1108-1110, 1994.
- [146] S. Becker, "Calculation of direct solar and diffuse radiation in Israel," *International Journal of Climatology: A Journal of the Royal Meteorological Society*, vol. 21, no. 12, pp. 1561-1576, 2001.
- [147] J. T. Peterson, E. C. Flowers and J. H. Rudisill III, "Atmospheric turbidity across the Los Angeles basin," *J. Appl. Meteorol.*, vol. 17, no. 4, pp. 428-435, 1978.
- [148] M. Koomen, C. Lock, D. Packer, R. Scolnik, R. Tousey and E. Hulburt, "Measurements of the brightness of the twilight sky," *Josa*, vol. 42, no. 5, pp. 353-356, 1952.
- [149] T. Saemundsson, "Atmospheric refraction," *Sky and Telescope*, vol. 72, pp. 70, 1986.
- [150] W. Coblentz, "The diffuse reflecting power of various substances," *J. Wash. Acad. Sci.*, vol. 2, no. 19, pp. 447-451, 1912.
- [151] N. Lazard, "Lazard's Levelized Cost of Energy Analysis—Version 9.0," 2016.
- [152] G. Liu, M. Rasul, M. Amanullah and M. Khan, "Techno-economic simulation and optimization of residential grid-connected PV system for the Queensland climate," *Renewable Energy*, vol. 45, pp. 146-155, 2012.
- [153] G. Barbose, N. Darghouth, D. Millstein, S. Cates, N. DiSanti and R. Widiss, *Tracking the Sun IX: The Installed Price of Residential and Non-Residential Photovoltaic Systems in the United States*, 2016.

- [154] S. Borenstein, "The market value and cost of solar photovoltaic electricity production," 2008.
- [155] M. Lave and J. Kleissl, "Optimum fixed orientations and benefits of tracking for capturing solar radiation in the continental United States," *Renewable Energy*, vol. 36, no. 3, pp. 1145-1152, 2011.
- [156] M. Hartner, A. Ortner, A. Hiesl and R. Haas, "East to west—The optimal tilt angle and orientation of photovoltaic panels from an electricity system perspective," *Appl. Energy*, vol. 160, pp. 94-107, 2015.
- [157] I. H. Rowlands, B. P. Kemery and I. Beausoleil-Morrison, "Optimal solar-PV tilt angle and azimuth: An Ontario (Canada) case-study," *Energy Policy*, vol. 39, no. 3, pp. 1397-1409, 2011.

## Appendix A

The day-ahead locational marginal electricity prices collected from OASIS have been used extensively in this research. However, due to the significant amount of data involved, only small excerpts of this data have been shown in the main chapters of this work. Although the data used cannot be presented in full here, this appendix presents an overview of the data used.

Figs. A.1-A.5 show the monthly-averaged daily price curve of the restricted pricing area used in the rigorous simulation of chapter 4. Each figure shows one year of the five year data set used for the rigorous simulation.

Fig. A.6 compares the monthly-averaged daily price curve of the restricted pricing area against the monthly-averaged daily price curve of the entire state of California, which was used in the simplified simulation of chapter 3. The two price curves are compared for four key months over the final year of the study.

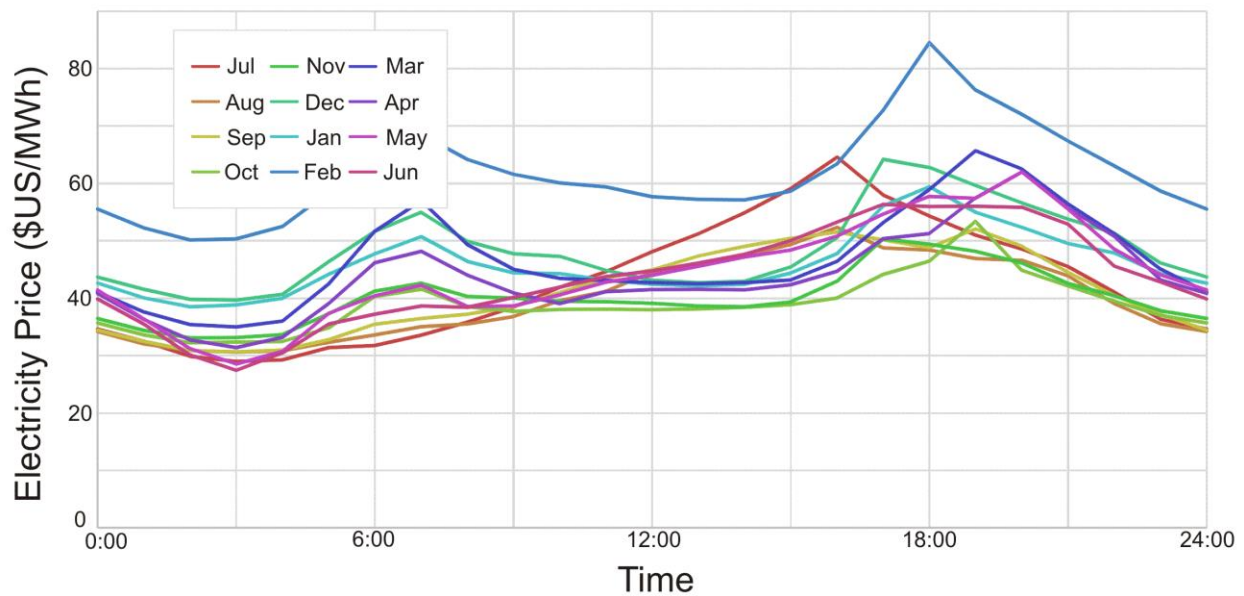


Fig. A.1: The monthly-averaged day-ahead hourly locational marginal pricing, for the year of July 1, 2013-June 30, 2014, in the region bounded by 34°N, 36°N, 118°W, and 120°W.

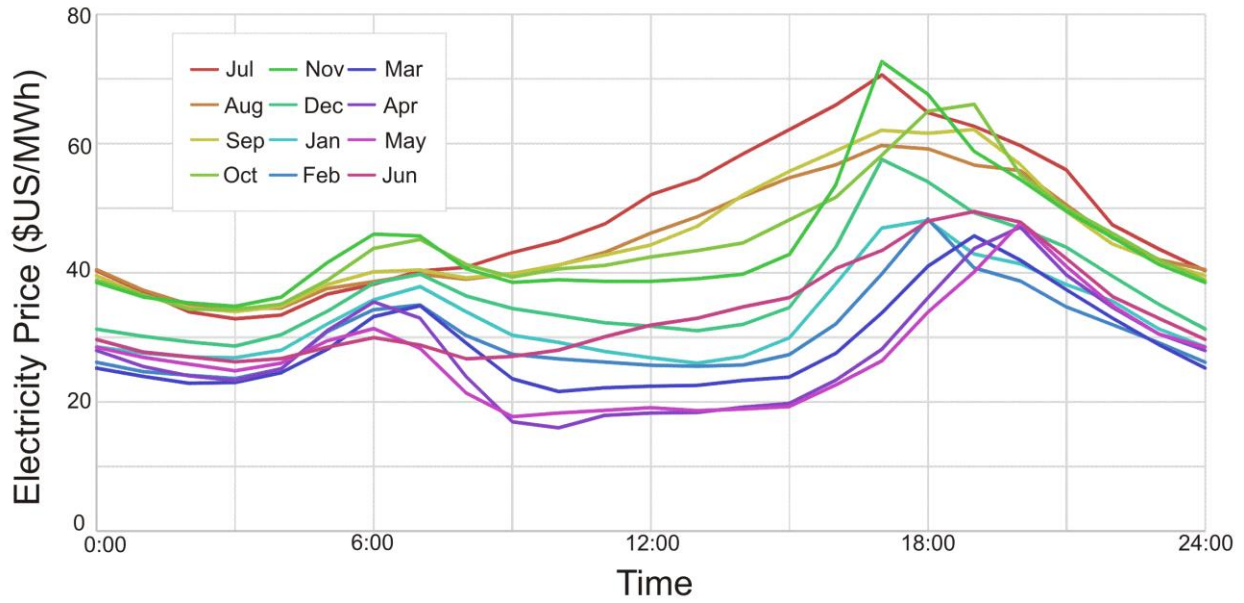


Fig. A.2: The monthly-averaged day-ahead hourly locational marginal pricing, for the year of July 1, 2014-June 30, 2015, in the region bounded by 34°N, 36°N, 118°W, and 120°W.

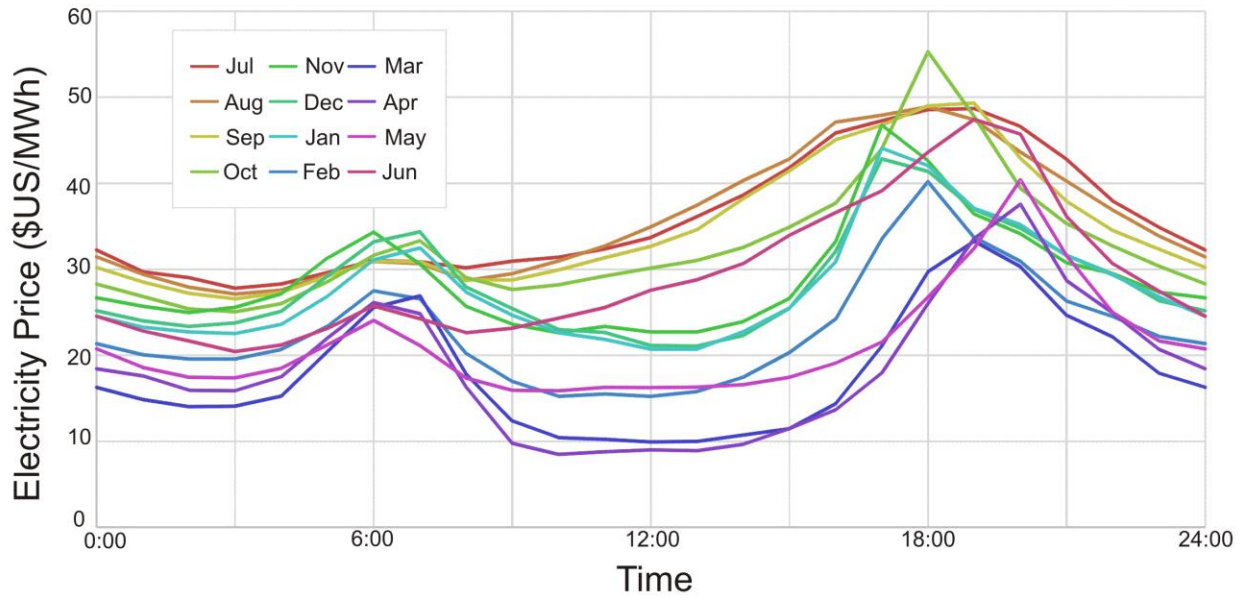


Fig. A.3: The monthly-averaged day-ahead hourly locational marginal pricing, for the year of July 1, 2015-June 30, 2016, in the region bounded by 34°N, 36°N, 118°W, and 120°W.

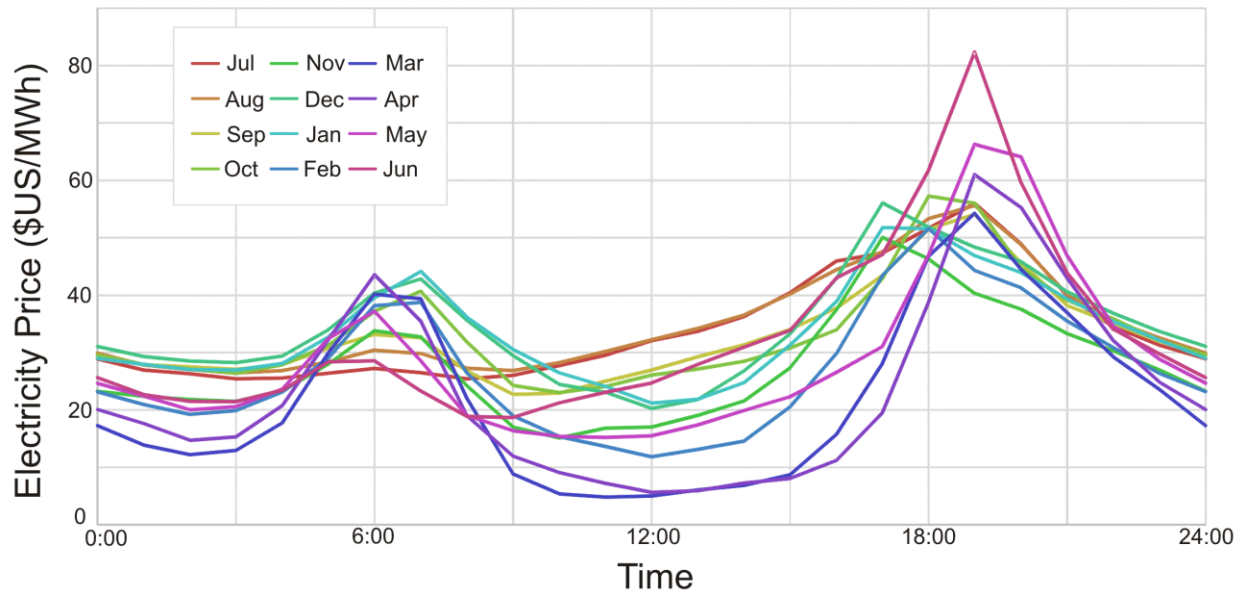


Fig. A.4: The monthly-averaged day-ahead hourly locational marginal pricing, for the year of July 1, 2016-June 30, 2017, in the region bounded by 34°N, 36°N, 118°W, and 120°W.

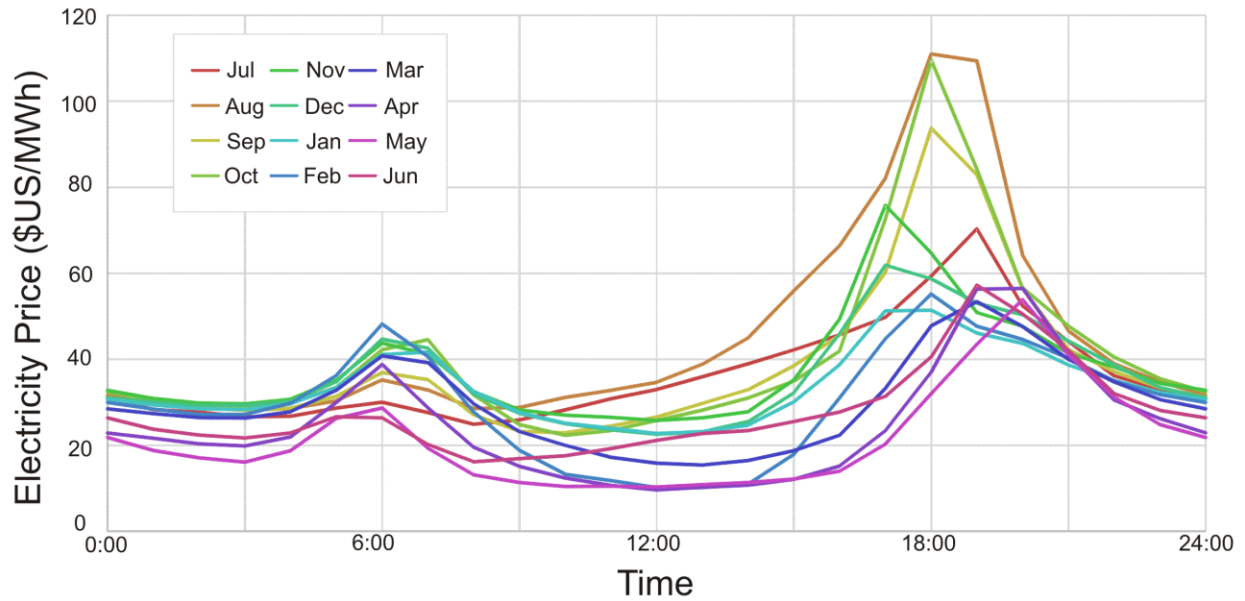


Fig. A.5: The monthly-averaged day-ahead hourly locational marginal pricing, for the year of July 1, 2017-June 30, 2018, in the region bounded by 34°N, 36°N, 118°W, and 120°W.

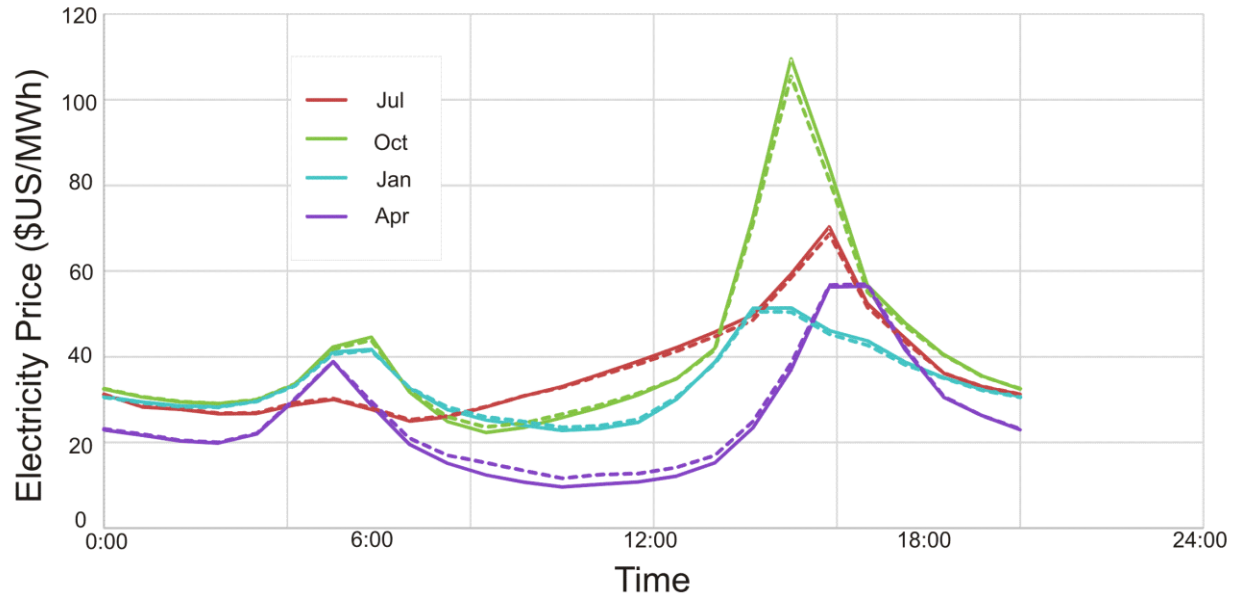


Fig. A.6: The monthly-averaged day-ahead hourly locational marginal pricing, for four months of the year of July 1, 2017-June 30, 2018. This figure compares data averaged over the entire state of California, represented by dotted lines, to data collected in the region bounded by 34°N, 36°N, 118°W, and 120°W, represented by solid lines. The accentuation of the Duck Curve effect in a region with large quantities of solar generation is clearly visible.

## Appendix B

Optimization of the three geometric solar arrays based on relative profit density and using the rigorous simulation was carried out for all five years of the study. The body of this thesis concerned itself with the optimizations for the most recent year of the study, July 1, 2017-June 30, 2018. These optimized results were used to generate plots of relative profit density as a function of geometry-dependent cost density for each array, and identify the value of  $C_{\text{geo},y}$  at which the V-Groove Array becomes the optimal geometric solar array.

This appendix presents similar plots for the other four years of the study. These figures compare arrays optimized for each year of the study in terms of their performance during that year, in order to show how these findings have changed over the course of the study.

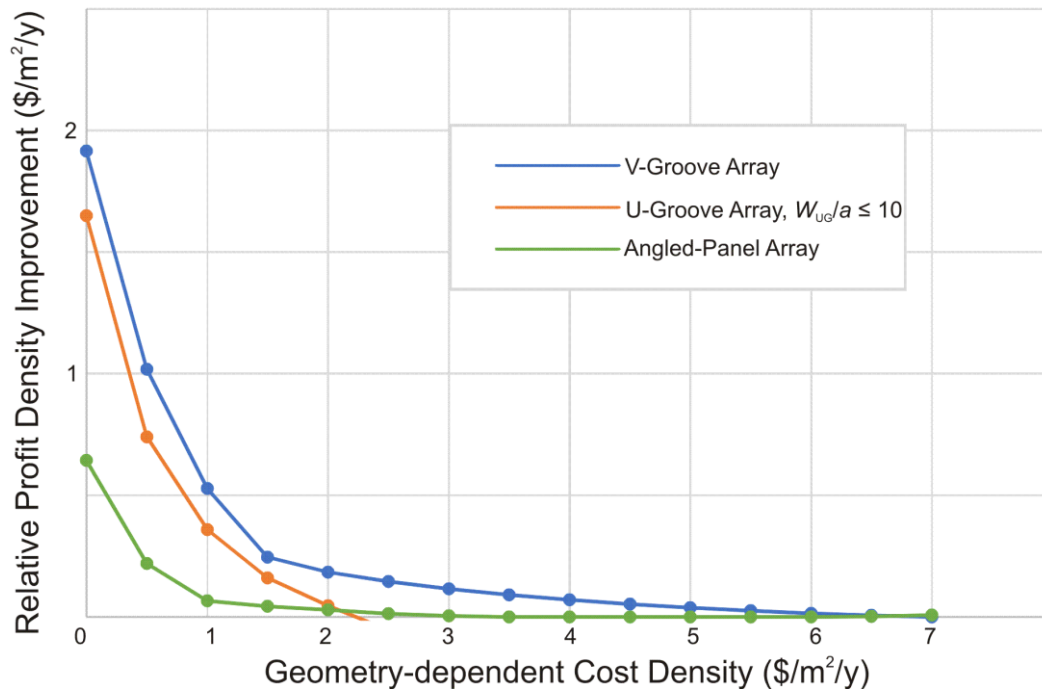


Fig. B.1: Relative profit density improvement over the Flat-Panel Array as a function of  $C_{\text{geo},y}$  for optimal configurations of the three other arrays, for the year of July 1, 2013 to June 30, 2014.

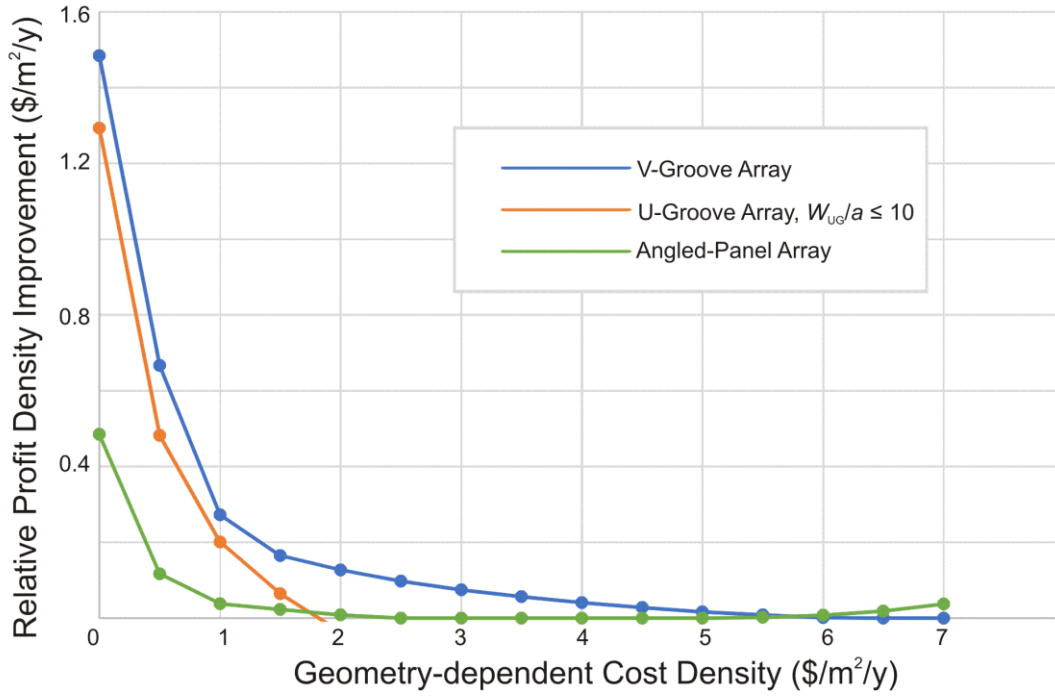


Fig. B.2: Relative profit density improvement over the Flat-Panel Array as a function of  $C_{\text{geo},y}$  for optimal configurations of the three other arrays, for the year of July 1, 2014 to June 30, 2015.

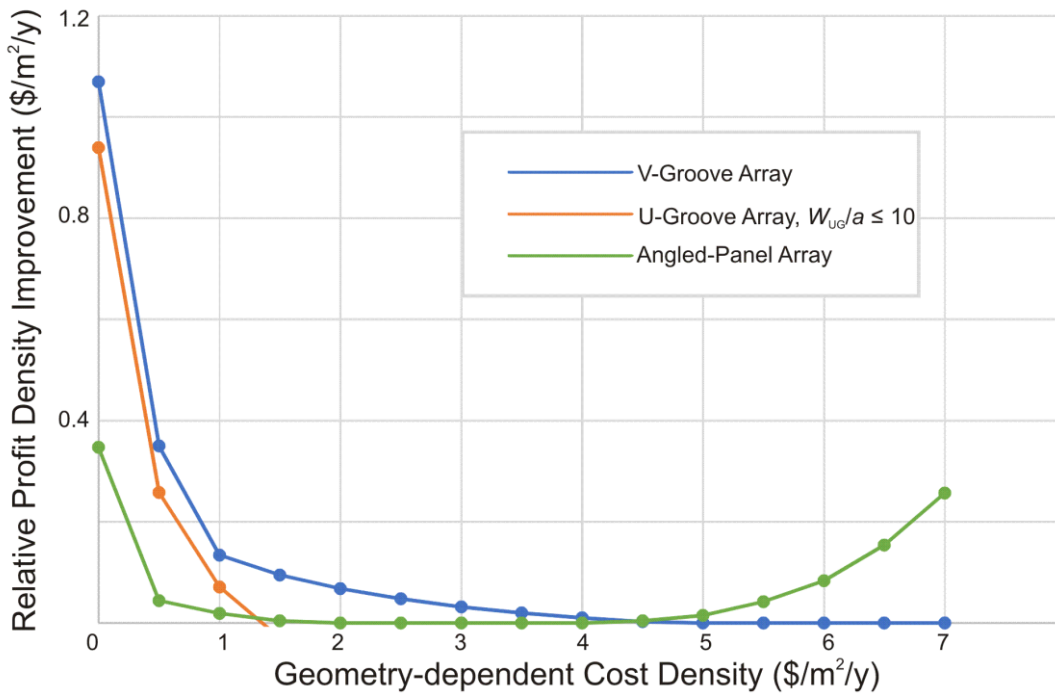


Fig. B.3: Relative profit density improvement over the Flat-Panel Array as a function of  $C_{\text{geo},y}$  for optimal configurations of the three other arrays, for the year of July 1, 2015 to June 30, 2016.

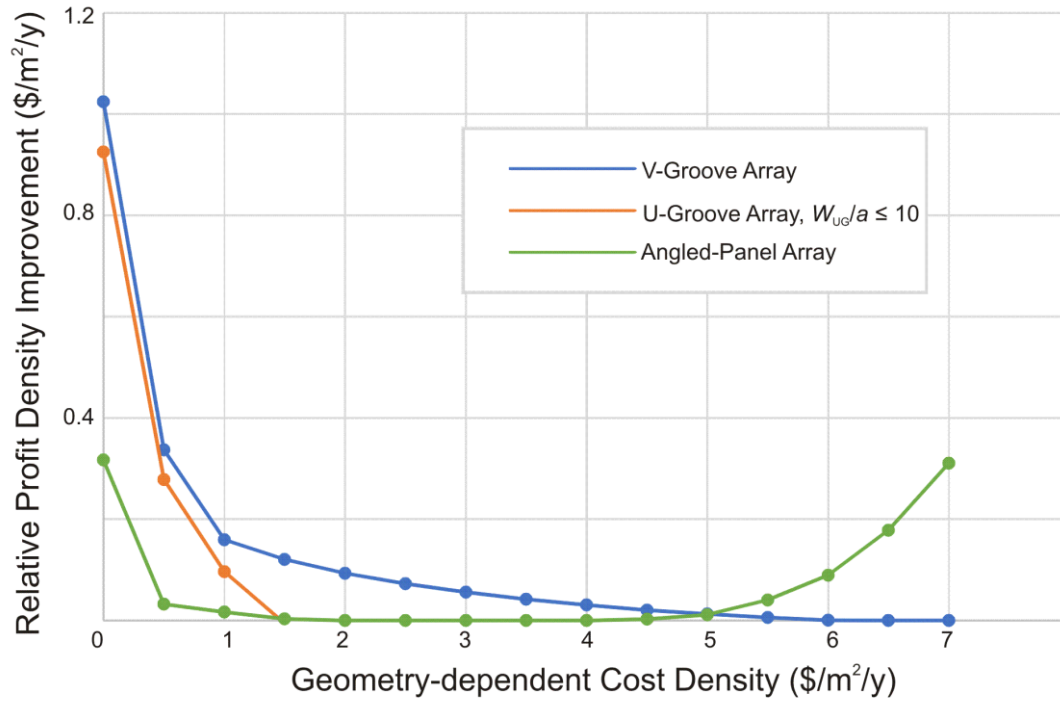


Fig. B.4: Relative profit density improvement over the Flat-Panel Array as a function of  $C_{geo,y}$  for optimal configurations of the three other arrays, for the year of July 1, 2016 to June 30, 2017.

## Appendix C

This appendix collects data on the key array configurations found during the optimization procedure of section 4.3.2. Specifically, all array configurations that were found to be optimal under any combination of year and geometry-dependent cost density are presented in the tables below.

Table C.1: Relative profit density of the Flat-Panel Array, in  $\$/\text{m}^2/\text{y}$ , as a function of the year and geometry-dependent cost density, in  $\$/\text{m}^2/\text{y}$

$C_{\text{geo},y}$	<b>2013-2014</b>	<b>2014-2015</b>	<b>2015-2016</b>	<b>2016-2017</b>	<b>2017-2018</b>
0	14.3758	11.1655	8.0222	7.6167	8.0633
0.5	13.8758	10.6655	7.5222	7.1167	7.5633
1	13.3758	10.1655	7.0222	6.6167	7.0633
1.5	12.8758	9.6655	6.5222	6.1167	6.5633
2	12.3758	9.1655	6.0222	5.6167	6.0633
2.5	11.8758	8.6655	5.5222	5.1167	5.5633
3	11.3758	8.1655	5.0222	4.6167	5.0633
3.5	10.8758	7.6655	4.5222	4.1167	4.5633
4	10.3758	7.1655	4.0222	3.6167	4.0633
4.5	9.8758	6.6655	3.5222	3.1167	3.5633
5	9.3758	6.1655	3.0222	2.6167	3.0633
5.5	8.8758	5.6655	2.5222	2.1167	2.5633
6	8.3758	5.1655	2.0222	1.6167	2.0633
6.5	7.8758	4.6655	1.5222	1.1167	1.5633
7	7.3758	4.1655	1.0222	0.6167	1.0633

Table C.2: Optimal V-Angle of the V-Groove Array without rotation, in degrees, as a function of the year and geometry-dependent cost density, in  $\$/m^2/y$

$C_{geo,y}$	2013-2014	2014-2015	2015-2016	2016-2017	2017-2018
0	31	31	31	31	31
0.5	52	58	68	71	68
1	71	81	130	130	128
1.5	115	130	140	140	140
2	130	140	146	144	144
2.5	140	144	150	150	148
3	143	148	154	152	152
3.5	147	150	156	155	154
4	150	152	160	156	156
4.5	152	156	162	160	156
5	154	156	180	160	160
5.5	156	160	180	162	160
6	158	162	180	164	162
6.5	160	180	180	180	164
7	180	180	180	180	180

Table C.3: Optimal relative profit density of the V-Groove Array without rotation, in  $\$/m^2/y$ , as a function of the year and geometry-dependent cost density, in  $\$/m^2/y$

$C_{geo,y}$	2013-2014	2014-2015	2015-2016	2016-2017	2017-2018
0	16.2908	12.65	9.0917	8.6412	9.1411
0.5	14.8941	11.3323	7.8716	7.4535	7.9439
1	13.9034	10.4377	7.1563	6.7759	7.2426
1.5	13.1205	9.8302	6.6167	6.2373	6.701
2	12.5592	9.292	6.0896	5.7098	6.172
2.5	12.0214	8.7632	5.5698	5.189	5.6494
3	11.4911	8.2402	5.054	4.6723	5.1315
3.5	10.9663	7.7216	4.5419	4.1585	4.6166
4	10.4457	7.2059	4.0322	3.647	4.1043
4.5	9.9285	6.6932	3.5247	3.1372	3.5931
5	9.4135	6.182	3.0222	2.6295	3.0846
5.5	8.9012	5.6738	2.5222	2.1227	2.5769
6	8.39	5.1664	2.0222	1.6168	2.0703
6.5	7.8819	4.6655	1.5222	1.1167	1.5646
7	7.3758	4.1655	1.0222	0.6167	1.0633

Table C.4: Optimal width of the U-Groove Array without rotation, normalized to the solar cell side length, as a function of the year and geometry-dependent cost density, in  $\$/\text{m}^2/\text{y}$

$C_{\text{geo},y}$	2013-2014	2014-2015	2015-2016	2016-2017	2017-2018
0	1	1	1	1	1
0.5	2	2	3	4	3
1	4	5	9	8	8
1.5	7	$\geq 10, < 100$	$> 10$	$> 10$	$\geq 10, < 100$
2	$\geq 10, < 100$	$> 10$	$> 100$	$> 100$	$> 100$
2.5	$> 100$	$> 100$	$> 100$	$> 100$	$> 100$

Table C.5: Optimal relative profit density of the U-Groove Array without rotation, in  $\$/\text{m}^2/\text{y}$ , as a function of the year and geometry-dependent cost density, in  $\$/\text{m}^2/\text{y}$ , including only widths of 1-10, 100, and infinite times the solar cell side length.

$C_{\text{geo},y}$	2013-2014	2014-2015	2015-2016	2016-2017	2017-2018
0	16.0255	12.4589	8.9612	8.5419	9.0414
0.5	14.6159	11.1477	7.7798	7.3947	7.8788
1	13.7338	10.3665	7.0931	6.713	7.1856
1.5	13.0358	9.7295	6.5228	6.1208	6.5798
2	12.4218	9.1666	6.0222	5.6167	6.0633
2.5	11.8758	8.6655	5.5222	5.1167	5.5633

Table C.6: Optimal Tilt Angle of the Angled-Panel Array without rotation, in degrees, as a function of the year and geometry-dependent cost density, in  $\$/\text{m}^2/\text{y}$

$C_{\text{geo},y}$	2013-2014	2014-2015	2015-2016	2016-2017	2017-2018
0	36	36	36	32	34
0.5	14	10	9	4	9
1	9	1	1	1	1
1.5	1	1	1	1	1
2	1	1	0	0	0
2.5	1	0	0	0	0
3	1	0	0	0	0
3.5	0	0	0	0	0
4	0	0	0	0	0
4.5	0	0	2	2	2
5	0	0	5	5	5
5.5	0	2	8	7	8
6	0	2	10	12	11
6.5	2	4	14	16	15
7	2	6	18	21	19

Table C.7: Optimal spacing of the Angled-Panel Array without rotation, in mm, as a function of the year and geometry-dependent cost density, in  $\$/\text{m}^2/\text{y}$

$C_{\text{geo,y}}$	2013-2014	2014-2015	2015-2016	2016-2017	2017-2018
0	28	28	28	30	30
0.5	53	59	62	67	62
1	62	74	74	74	74
1.5	74	74	75	75	75
2	74	74	76.2	76.2	76.2
2.5	74	76.2	76.2	76.2	76.2
3	75	76.2	76.2	76.2	76.2
3.5	76.2	76.2	76.2	76.2	76.2
4	76.2	76.2	76.2	76.2	76.2
4.5	76.2	76.2	77	77	77
5	76.2	76.2	79	79	79
5.5	76.2	77	82	82	82
6	76.2	77	85	89	86
6.5	77	78	92	98	93
7	77	80	100	111	103

Table C.8: Optimal relative profit density of the Angled-Panel Array without rotation, in  $\$/\text{m}^2/\text{y}$ , as a function of the year and geometry-dependent cost density, in  $\$/\text{m}^2/\text{y}$

$C_{\text{geo,y}}$	2013-2014	2014-2015	2015-2016	2016-2017	2017-2018
0	15.0196	11.6504	8.3692	7.9335	8.3937
0.5	14.0954	10.7821	7.5663	7.1489	7.6044
1	13.4421	10.2033	7.0409	6.6334	7.0832
1.5	12.9189	9.6885	6.5262	6.1195	6.5684
2	12.404	9.1736	6.0222	5.6167	6.0633
2.5	11.8891	8.6655	5.5222	5.1167	5.5633
3	11.3795	8.1655	5.0222	4.6167	5.0633
3.5	10.8758	7.6655	4.5222	4.1167	4.5633
4	10.3758	7.1655	4.0222	3.6167	4.0633
4.5	9.8758	6.6655	3.5263	3.119	3.5682
5	9.3758	6.1655	3.0368	2.6277	3.0808
5.5	8.8758	5.6676	2.5637	2.1566	2.6086
6	8.3758	5.1728	2.1056	1.7058	2.1537
6.5	7.878	4.6837	1.6761	1.2949	1.729
7	7.3832	4.2028	1.2789	0.9274	1.339

Table C.9: Results of the rotation-dependent analysis of the V-Groove Array.

$C_{\text{geo,y}} (\$/\text{m}^2/\text{y})$	$\nu_{\text{VG}} (^\circ)$	$\rho_{\text{VG}} (^\circ)$	$\Pi_{\text{rel}} (\$/\text{m}^2/\text{y})$
0	31	90	9.6701
3.5	154	0	4.6166
5	160	0	3.0846
7	180	N/A	1.0616

Table C.10: Results of the rotation-dependent analysis of the U-Groove Array.

$C_{\text{geo,y}} (\$/\text{m}^2/\text{y})$	$W_{\text{UG}}/a$	$\rho_{\text{VG}} (^\circ)$	$\Pi_{\text{rel}} (\$/\text{m}^2/\text{y})$
0	1	5	9.0418

Table C.11: Results of the rotation-dependent analysis of the Angled-Panel Array.

$C_{\text{geo,y}} (\$/\text{m}^2/\text{y})$	$\sigma_{\text{AP}} (\text{mm})$	$\tau_{\text{AP}} (^\circ)$	$\rho_{\text{AP}} (^\circ)$	$\Pi_{\text{rel}} (\$/\text{m}^2/\text{y})$
0	30	34	-5	8.3967
3.5	76.2	0	N/A	4.5633
5	81	8	-15	3.0966
7	104	21	-15	1.389